Proceedings of the 18th International Conference on Biomedical Applications of

ELECTRICAL IMPEDANCE TOMOGRAPHY

Edited by Alistair Boyle, Ryan Halter, Ethan Murphy and Andy Adler

June 21-24, 2017
Thayer School of Engineering at Dartmouth
Hanover, New Hampshire, USA

This document is the collection of papers accepted for presentation at the
18th International Conference on Biomedical Applications of Electrical Impedance Tomography.

Funding for this conference was made possible (in part) by 1 R13 EB024401-01 from the National Institute of Biomedical Imaging and Bioengineering. The views expressed in written conference materials or publications and by speakers and moderators do not necessarily reflect the official policies of the Department of Health and Human Services; nor does mention of trade names, commercial practices, or organizations imply endorsement by the U.S. Government.

Printed in USA

DOI: 10.5281/zenodo.557093

Thayer School of Engineering at Dartmouth
14 Engineering Drive
Hanover, New Hampshire
USA
engineering.dartmouth.edu
thayer.receptionist@dartmouth.edu
(603) 646-2230

eit2017.org

Table of Contents

Acceleration of EIT Image Reconstruction on GPUs

Andrea Borsic[1], Michael G Crabb[2] and William RB Lionheart[2]

[1]NE Scientific LLC, MA, USA, aborsic@ne-scientific.com

[2]School of Mathematics, University of Manchester, UK, michael.crabb@manchester.ac.uk

Abstract: Graphic Processing Units (GPU) are highly parallel architectures used in scientific computing to achieve substantial speed gains. This manuscript reports results from acceleration of EIT image reconstruction using GPUs, with gains of up to 24 times compared to EIDORS Version 3.8 running on a modern CPU under MATLAB. These gains enable a more interactive reconstruction on dense 3D meshes.

1 Introduction

A current trend in biomedical EIT research is the use of dense 3D FEM meshes in forward modelling to better represent the anatomy of interest. In part this trend is driven by approaches where CT, MRI, or Ultrasound images are used to build accurate models. Use of optical scanners for capturing the body shape has also been demonstrated [1]. The anatomically accurate meshes that result from these modelling approaches typically have between 100K and 300K nodes and 500K to 1M tetrahedral mesh elements. Non-linear image reconstruction on meshes of this size requires currently in excess of tens of minutes, therefore limiting the interactive exploration of data. The use of GPUs for accelerating EIT reconstruction has therefore been considered promising for some time [2]. In this manuscript computational speed-ups are reported for a complete implementation of EIT reconstruction on GPUs.

2 Methods

A forward solver implementing the complete electrode model, routines for computing the Jacobian matrix, routines for estimating the conductivity update with the Newton Raphson method, and with the PD-IPM framework [3] have been implemented on a GPU using the Thrust, CUSP, cuBlas, cuSparse libraries and a number of custom CUDA kernels. This low-level implementation compiles under Windows and Linux operating systems and results in a dynamic linked library (DLL). To facilitate the use, the DLL has been wrapped with Python/NumPy, exposing the functionality of the library to the high level Python language, resulting in a computation environment for EIT not too dissimilar to MATLAB. EIDORS [4] Version 3.8 was used as a reference implementation to test the GPU library against. Firstly the GPU library was tested for accuracy. It was verified that all the output from the relevant routines agreed to the outputs from EIDORS to 6 decimal places.

Secondly 3 meshes with 29K, 79K, and 190K nodes were generated in order to evaluate the performance of the GPU implementation against EIDORS running on a CPU. For each of these three meshes used for forward solving, 3 levels of coarse discretization were setup, resulting in 900, 3100, and 7275 parameters to estimate.

EIDORS timing data was collected under MATLAB Version 2016b on Ubuntu Linux 16.04 64bit on a computer with an Intel Core-i7 4790K CPU running at 4.0GHz, and 16GB of RAM. An inhomogeneous conductivity was used to generate synthetic measurements, which were later reconstructed with the Newton-Raphson algorithm, set to perform 6 iterations. The same setup was used for the GPU Library, which was run on the same computer, using an NVIDIA GTX TITAN Black GPU with 6GB of RAM. The same coarse-to-fine interpolation and regularization matrices were used to run the two algorithms. Table 1 reports speed-gain results. Time gains are very modest on the smaller mesh (1.42 to 2.49) as the setup and communication times on the GPU are significant compared to the overall reconstruction time. Timing results on the intermediate Mesh_2 (79K nodes) show increased benefit of GPU acceleration. On the larger Mesh_3 gains are significant, and range between 16.5 to 24.5 times depending on coarse resolution. Specifically the six non-linear reconstruction steps completed in 43 to 63 seconds on the GPU, depending on the coarse resolution level, and in 17 minutes in EIDORS on the CPU.

3 Conclusions

Use of GPU enables more interactive EIT image reconstruction. Further speed gains are expected from optimization of the current GPU library as well as when the upcoming Pascal family of GPUs are released.

References

[1] Forsyth, J., et al. "*Optical breast shape capture and finite-element mesh generation for electrical impedance tomography*" Physiological measurement 32.7, 2011.

[2] Borsic, A., E. A. Attardo, and R. J. Halter. "*Multi-GPU Jacobian accelerated computing for soft-field tomography*" Physiological measurement 33.10, 2012.

[3] Borsic, A., and A. Adler. "*A primal–dual interior-point framework for using the L1 or L2 norm on the data and regularization terms of inverse problems*" Inverse Problems 28.9, 2012.

[4] *Adler, Andy, et al. "EIDORS Version 3.8." Proc. of the 16th Int. Conf. on Biomedical Applications of Electrical Impedance Tomography. 2015.*

Table 1: Speed gains for three different forward mesh densities and for three different level of coarse discretisation. GPU speed gains are limited for small meshes, but significant (16 to 24 times) for dense meshes.

	Mesh_2 29K Nodes	**Mesh_2 79K nodes**	**Mesh_3 190K nodes**
900 Inv. Parameters	2.49 speed gain	8.20 speed gain	24.46 speed gain
3,100 Inv. Parameters	1.42 speed gain	5.12 speed gain	18.02 speed gain
7,275 Inv. Parameters	N/A	5.09 speed gain	16.55 speed gain

Towards Efficient Iterative Absolute EIT

Henry FJ Tregidgo[1,2], Michael G Crabb[1], William RB Lionheart[1]

[1]University of Manchester, Manchester, UK.
[2]henry.tregidgo@manchester.ac.uk

Abstract: One factor limiting the use of absolute reconstructions in 3D lung EIT is the computational cost of iterative algorithms. We show how the programming experience of the Finite Element and Research Software Engineering communities can be applied to these algorithms, resulting in a speed up of reconstructions in EIDORS 3.8 [1]. We also outline a combination of absolute and difference imaging to provide fast pseudo-absolute imaging.

1 Introduction

In situations where 3D absolute EIT could be useful the high cost of iterative inversion can be prohibitive. A large proportion of time taken is in the solution of a sparse linear system representing the forward problem [2]. We present simple software refinements to improve performance of this linear solve in Matlab. We also address refinements in construction of the Jacobian, coarse-to-fine and Laplace-prior matrices.

For purposes such as parameter fitting and control of ventilation, absolute reconstruction is only required for calibration [3]. For situations where calibration of absolute values is required at multiple time steps, we present a combination of absolute and difference imaging to provide a fast pseudo-absolute reconstruction.

2 Reconstruction Steps

Errors in floating point arithmetic can produce small asymmetries even when using seemingly symmetric constructions of the system matrix. For example the factorisation of the FEM system matrix for piecewise linear elements into mesh and conductivity dependent components [4] as performed in EIDORS. This asymmetry, shown in Figure 1, can cause checks in default sparse linear solvers to incorrectly choose slower non-symmetric algortithms. In particular the UMFPACK algorithm is chosen over CHOLMOD by MATLAB's `mldivide` function, resulting in worse performance.

We demonstrate how symmetry correction can drastically reduce the sparse linear solve time as shown in Table 1. We additionally detail other software engineering refinements to speed up construction of the Jacobian, coarse-to-fine and Laplace-prior matrices. These include vectorisation of operations, replacement of `find` operations with `sort` functions and reduction of complexity through further use of symmetry.

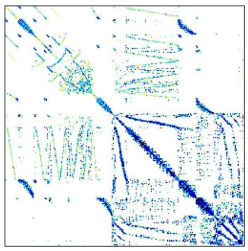

Figure 1: Sparsity pattern for the antisymmetric system matrix error component using first order elements. Entries are of order 10^{-12}.

3 Pseudo-absolute Reconstruction

We propose using additional imaging modalities to produce a segmented mesh of the thorax [5, 6] and performing a very low dimensional absolute reconstruction of a single frame on this mesh. The absolute values are then incorporated into the conductivity Jacobian for further difference imaging. This results in improved residual data-fit and only requires a small additional offline processing time. Using the 46k node mesh from Table 1 for a simulated domain with 64 electrodes and 5 level set regions required an additional 2 minutes elapsed time with the improvements from the previous section.

4 Conclusions

By ensuring conditions are met for the use of the optimal linear solvers, and reducing the dimensionality of the iterative inversion, significant speed-ups are available and pseudo-absolute reconstructions are possible.

5 Acknowledgements

The authors would like to thank A. Boyle and A. Adler for their help in confirming these efficiency savings in EIDORS.

References

[1] Adler A, Boyle A, Crabb MG, et al. In *Proc. 16th Int. Conf. Biomed. Applications of EIT*. 2015
[2] Boyle A, Borsic A, Adler A. *Physiol Meas* **33**(5):787, 2012
[3] Tregidgo HFJ, Crabb MG, Lionheart W. In *Proc. 16th Int. Conf. Biomed. Applications of EIT*, 96. 2015
[4] Vavasis SA. *SIAM J on Numerical Analysis* **33**(3):890–916, 1996
[5] Crabb M, Davidson J, Little R, et al. *Physiol Meas* **35**(5):863, 2014
[6] Grychtol B, Lionheart WR, Bodenstein M, et al. *Medical Imaging, IEEE Transactions on* **31**(9):1754–1760, 2012

Table 1: Time comparisons for symmetric and non-symmetric linear solve on two meshes of the same thorax segmentation. Timings are given in both CPU and elapsed time as measured on a 2.8GHz Intel Core i7 with 16 GB 1.6 GHz DDR3 RAM.

N. nodes	Unsymmetric (CPU time s)	Symmetric (CPU time s)	Speedup (CPU time ×)	Unsymmetric (elapsed time s)	Symmetric (elapsed time s)	Speedup (elapsed time ×)
46k	9.83	3.47	2.83	6.55	1.09	6.03
190k	281.06	91.45	3.07	146.77	28.01	5.24

Rotational electrical impedance tomography with few electrodes

Mari Lehti-Polojärvi[1*], Olli Koskela[1*], Aku Seppänen[2], Edite Figueiras[3] and Jari Hyttinen[1]

[1]BioMediTech Institute and Faculty of Biomedical Sciences and Engineering, Tampere University of Technology, Tampere, Finland, mari.lehti@tut.fi, olli.koskela@tut.fi

[2]Department of Applied Physics, University of Eastern Finland, Kuopio, Finland

[3] International Iberian Nanotechnology Laboratory, Braga, Portugal

* with equal contribution

Abstract: In multimodal applications, electrodes used in electrical impedance tomography (EIT) should cover only part of the object surface to allow the use of other probes. We propose to use a rotational setup with only eight electrodes. To obtain a proof of concept of this method, we measured gelatin phantoms with resistive inclusions. The results proof the method provides images of good quality.

1 Introduction

Placing EIT electrodes so that they cover only a limited portion of the object surface would save space for other probes, enabling multimodal imaging. For this purpose, we propose a method applying eight fixed electrodes around a rotating object. Our goal is to use this method for monitoring cell cultures in a cylindrical hydrogel scaffold.

Aim of this study is to demonstrate the effectiveness of the proposed method by phantom measurements.

2 Methods

2.1 Rotational setup

We used two sets of four electrodes placed symmetrically on opposite sides of the object as is shown in Fig. 1. Each set covered one quarter of the sample boundary (90 degrees). To be able to rotate the object while keeping the electrodes fixed, we used a thin layer of aqueous solution between the object and the electrodes.

2.2 Rotational reconstruction

For each rotated measurement position, we defined a linear mapping of the conductivity distribution from initial position to the rotated coordinates. These mappings were incorporated into the forward model of EIT. Inverse of this model was used to reconstruct the conductivity distribution within the object, corresponding to the set of voltage measurements in these rotated measurement positions. All computations were performed in MATLAB with an adaption of the open source EIDORS package. [1]

2.3 Experiments

Cylindrical gelatin phantoms were measured before and after adding resistive inclusions with different sizes. The phantoms were manually rotated and measurements recorded every 5.6-degree turn, providing data from 64 different angles. The measurements were done in a 16-electrode tank (used previously for example in [2]) where eight electrodes were insulated and eight were in use. The measurement device was KIT4, presented in [3]. All measured phantoms were constant along the height of the tank, thus analysis in two dimension is adequate.

3 Results

Difference mode reconstructions of one of the experiments are shown in Fig. 1. Rotational data from the object enhances image quality.

4 Conclusions

This study demonstrates that rotational EIT provides good image quality even with limited electrode coverage on the object. We anticipate this method could create new applications of EIT imaging.

5 Acknowledgements

Financial support has been provided by Jane and Aatos Erkko foundation, Instrumentarium Science foundation, Tekes Human Spare Parts project and Academy of Finland. Authors would like to thank Tuomo Savolainen and Panu Kuusela (University of Eastern Finland) for the help in the laboratory measurements.

References

[1] A Adler, W Lionheart, *PhysiolMeas*, 27: S25–S42, 2006

[2] D Liu, V Kolehmainen, S Siltanen, A Laukkanen, A Seppänen, *Inverse Problems and Imaging,* 9: 211-229, 2015

[3] J Kourunen, T Savolainen, A Lehikoinen, M Vauhkonen and L Heikkinen, *MeasSciTechnol*, 20, 2009

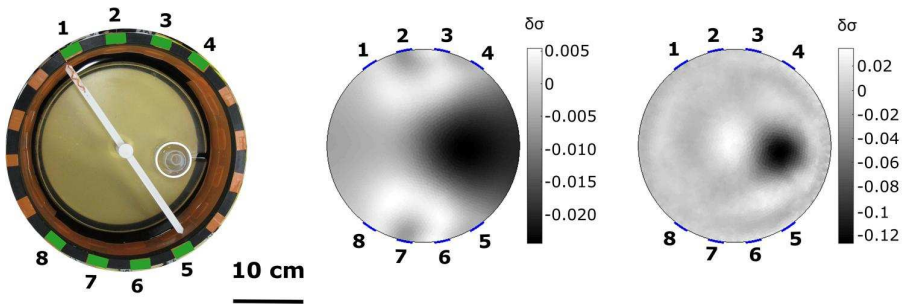

Figure 1: A photo of the measured object (left) and corresponding reconstructions using data from 1 (middle) and 64 (right) rotational positions. Setup includes a tank with eight electrodes in use (numbers 1-8), a platform for rotation (white), aqueous solution around a rotating gelatin object and a resistive plastic tube (white circle).

Spatio-Temporal Regularization over Many Frames

Alistair Boyle

University of Ottawa, Ottawa, Canada, aboyle2@uottawa.ca

Abstract: Regularizing over both spatial and temporal spaces for EIT data can lead to very large matrices which can be challenging to compute. The Kronecker product identity may be leveraged with the Conjugate Gradient method to construct a system of equations that scales linearly with the number of data frames collected and reconstruction parameters.

1 Introduction

Gauss-Newton methods are generally used to reconstruct an Electrical Impedance Tomography (EIT) conductivity image for a single frame of data. Multiple frames of data may be reconstructed together and have regularization applied across them, leading to spatio-temporal regularization.

2 Gauss-Newton

The Gauss-Newton iterative update (GN-update) is

$$\mathbf{x}_{n+1} = (\mathbf{J}_2 + \lambda\mathbf{R}_2)^{-1}\left(\mathbf{J}^\mathsf{T}\mathbf{W}\mathbf{b} + \lambda\mathbf{R}_2(\mathbf{x}_* - \mathbf{x}_n)\right) \quad (1)$$

where $\mathbf{J}_2 = \mathbf{J}^\mathsf{T}\mathbf{W}\mathbf{J}$ and $\mathbf{R}_2 = \mathbf{R}^\mathsf{T}\mathbf{R}$. New parameters $\mathbf{x}_{n+1}$ are calculated using results from iteration n and with a prior estimate $\mathbf{x}_*$, where the Jacobian $\mathbf{J}$ is calculated based on $\mathbf{x}_n$, the measurements are weighted by an inverse noise covariance matrix $\mathbf{W}$, and the reconstruction is regularized by $\mathbf{R}$ with a hyperparameter λ controlling regularization strength.

Following [1], the GN-update (1) may be expanded as a block-diagonal matrix to handle many frames in a time-series of data and reconstruct these frames simultaneously while applying regularization across time. Entries in the time series are assigned an exponential smoothing $\mathbf{\Gamma}$, so that adjacent frames are assumed to be strongly correlated. The same spatial regularization $\mathbf{R}$ is applied to every frame's reconstruction.

$$\mathbf{I}\otimes\mathbf{J} = \begin{bmatrix}\mathbf{J} & & \\ & \mathbf{J} & \\ & & \mathbf{J}\end{bmatrix} \qquad \mathbf{\Gamma}\otimes\mathbf{R} = \begin{bmatrix}\mathbf{R} & \mathbf{R} & \mathbf{R} \\ \mathbf{R} & \mathbf{R} & \mathbf{R} \\ \mathbf{R} & \mathbf{R} & \mathbf{R}\end{bmatrix} \quad (2)$$

The GN-update becomes

$$\begin{aligned}\mathrm{vec}(\mathbf{X}_{n+1}) = \big((\mathbf{I}\otimes\mathbf{J})^\mathsf{T}(\mathbf{I}\otimes\mathbf{W})(\mathbf{I}\otimes\mathbf{J}) + \\ \lambda(\mathbf{\Gamma}\otimes\mathbf{R})^\mathsf{T}(\mathbf{\Gamma}\otimes\mathbf{R})\big)^{-1} \\ \big((\mathbf{I}\otimes\mathbf{J})^\mathsf{T}(\mathbf{I}\otimes\mathbf{W})\mathrm{vec}(\mathbf{B}) + \\ \lambda(\mathbf{\Gamma}\otimes\mathbf{R})^\mathsf{T}(\mathbf{\Gamma}\otimes\mathbf{R})\mathrm{vec}(\mathbf{X}_* - \mathbf{X}_n)\big) \quad (3)\end{aligned}$$

where $\mathbf{X}$ denotes the reconstruction parameters joined into a matrix with one column per frame and the vec() operator reshapes this matrix into a single column vector. The measurements $\mathbf{B}$ are treated similarly. Using Kronecker product identities, (3) may be written

$$\begin{aligned}\mathrm{vec}(\mathbf{X}_{n+1}) = (\mathbf{I}\otimes\mathbf{J}_2 + \lambda\mathbf{\Gamma}_2\otimes\mathbf{R}_2)^{-1} \\ \big(\mathbf{I}\otimes(\mathbf{J}^\mathsf{T}\mathbf{W})\mathrm{vec}(\mathbf{B}) + \lambda\mathbf{\Gamma}_2\otimes\mathbf{R}_2\mathrm{vec}(\mathbf{X}_* - \mathbf{X}_n)\big) \quad (4)\end{aligned}$$

where $\mathbf{\Gamma}_2 = \mathbf{\Gamma}^\mathsf{T}\mathbf{\Gamma}$. This formulation can result in very large, dense matrices $\mathbf{I}\otimes\mathbf{J}_2$. The Wiener filter form, as suggested in [1], may help though it still gives the large dense matrices.

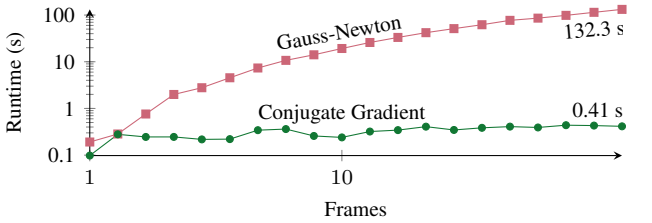

Figure 1: Runtime for a 16 electrode 2D Finite Element mesh (1600 elements) for 1 to 20 frames of 208 measurements using Gauss Newton (GN) (4) and Conjugate Gradient (CG) (7); CG scales to many frames of measurement data while GN runs exponentially slower as more frames are added

3 Conjugate Gradient

The Conjugate Gradient (CG) update [2] efficiently calculates the inverse in (4) by iterative evaluation of

$$\begin{aligned}(\mathbf{I}\otimes\mathbf{J}_2 + \lambda\mathbf{\Gamma}_2\otimes\mathbf{R}_2)\mathrm{vec}(\mathbf{X}_{n+1}) = \\ \mathbf{I}\otimes(\mathbf{J}^\mathsf{T}\mathbf{W})\mathrm{vec}(\mathbf{B}) + \lambda\mathbf{\Gamma}_2\otimes\mathbf{R}_2\mathrm{vec}(\mathbf{X}_* - \mathbf{X}_n) \quad (5)\end{aligned}$$

A key identity of the Kronecker product may be used to significantly reduce the computational requirements

$$\mathrm{vec}(\mathbf{AXB}) = \mathrm{vec}(\mathbf{C}) = (\mathbf{B}^\mathsf{T}\otimes\mathbf{A})\mathrm{vec}(\mathbf{X}) \quad (6)$$

which transforms (5) into

$$\begin{aligned}\mathrm{vec}(\mathbf{J}_2\mathbf{X}_{n+1} + \lambda\mathbf{R}_2\mathbf{X}_{n+1}\mathbf{\Gamma}_2^\mathsf{T}) = \\ \mathrm{vec}\left(\mathbf{J}^\mathsf{T}\mathbf{W}\mathbf{B} + \lambda\mathbf{R}_2(\mathbf{X}_* - \mathbf{X}_n)\mathbf{\Gamma}_2^\mathsf{T}\right) \quad (7)\end{aligned}$$

where, by judicious choice in the order of operations, one can maintain a minimal storage footprint. Note that in the GN solution, solving (5) would result in the same very large matrices as (4), while for CG the Kronecker products do not need to be expanded.

The CG method typically computes the solution $\mathbf{X}_{n+1}$ to a certain precision. For ill-posed problems, the accuracy of the parametrization is limited by measurement noise and regularization. Stopping the conjugate gradient iterations early avoids getting trapped in fruitless iterations. Rigorously CG stopping criteria for EIT CG-updates have been developed in [3], but were heuristically found in this work through plotting of the CG error estimates. Halting CG iterations when the algorithm started to oscillate gave nearly identical results.

4 Discussion

Spatio-temporal regularization combining the techniques described in this work, the Kronecker product identities and the Conjugate Gradient method, may be brought together to tackle previously uncomputable EIT data sets.

References

[1] Dai T, Soleimani M, et al. *Med Biol Eng Comput* **46**(9):889–899, 2008

[2] Shewchuk J. An introduction to the conjugate gradient method without the agonizing pain. Tech. rep., Carnegie Mellon University, 1994

[3] Rieder A. *SIAM J Numer Anal* **43**(2):604–622, 2006

Image reconstruction in Lorentz force Electrical Tomography

Nick Polydorides

School of Engineering, University of Edinburgh, Edinburgh, UK, npolydor@ed.ac.uk

Abstract: We describe an algorithm for electrical conductivity reconstruction from Lorentz force Electrical Impedance Tomography data. The inverse problem is formulated in three iterations, beginning with the recovery of the curl of the currents within the body, and subsequently reconstructing the current density and the conductivity. Subject to the appropriate acoustic modulation the method yields quantitative, stable and high resolution imaging.

1 Introduction

Lorentz Force Electrical Impedance Tomography (LFEIT) [1], also known as Magneto-Acousto-Electric Tomography[2], has recently emerged as an alternative modality that can yield, in principle, noise-robust, high-resolution, quantitative conductivity imaging. The technique is primarily destined for early stage cancer detection coupling the resolution of ultrasound imaging and the sensitivity of EIT to small cancer lesions. The LFEIT measurements are acquired on a pair of electrodes attached to the boundary of a conductive body Ω, homogeneous in density ρ and speed of sound c, whilst in a static magnetic field with strength $\mathbf{B}$. An ultrasound wave is then driven into the body perturbing the conductive tissue which in turn yields an interior Lorentz force current, leading to Ohmic currents and potentials. The measurement admits a simpler expression via its adjoint model. If $\mathbf{v} = \frac{1}{\rho}\operatorname{grad}\varphi$ for a velocity potential φ (satisfying the wave equation) and $\mathbf{J}^a$ is the current density of the boundary adjoint source corresponding to the measurement electrodes then the measurement is approximately

$$M(t) \approx -\frac{1}{\rho}\int_\Omega \mathrm{d}\mathbf{r}\,\mathbf{B}\cdot\big(\varphi(t)\,\operatorname{curl}\mathbf{J}^a(t)\big), \qquad (1)$$

where the sought conductivity information is encoded into $\operatorname{curl}\mathbf{J}^a = -\operatorname{grad}\sigma\times\operatorname{grad}w$ with w the adjoint potential.

2 Image reconstruction

We outline the image reconstruction algorithm for reconstructing the conductivity σ from LFEIT data captured on two pairs of electrodes. In this context, quantitative imaging requires, in addition, two impedance measurements on the same electrodes. The image reconstruction process, as originally suggested in [2] involves 3 iterated inverse problems, in principle all stable, subject to having sufficient data. We outline these stages that take LFEIT data to the interior curl of the adjoint current densities, then the curls to the currents and finally reconstructing the conductivity from the currents.

2.1 Reconstructing the adjoint curl

If the acoustic velocity potential is focused at a point within the region, say through linear phased array-based ultrasound focusing, repeating the measurements for three orthogonal magnetic field directions yields a representation of the curl there.

2.2 Reconstructing the adjoint current density

Having reconstructed $\operatorname{curl}\mathbf{J}^a$ on a dense grid of points within the domain we can then compute the current density from the solenoidal condition $\operatorname{div}\mathbf{J}^a = 0$ and the fact that the current density is a smooth, continuous field that can be expressed as a sum of a solenoidal and a conservative field $\mathbf{J}^a = \operatorname{curl}\mathbf{K} - \operatorname{grad}\phi$ for a unique combination of $\mathbf{K}$ and ϕ.

2.3 Reconstructing the conductivity

The final step of the reconstruction process is a current-density impedance imaging imaging problem, for which we develop an adaptation of the J-substitution algorithm [3] to exploit the information on the recovered vector field $\mathbf{J}^a$. As current density resolves the conductivity distribution up to a multiplicative constant, having two distinct currents and their respective impedance measurements (i.e. say on three electrodes) provides the necessary information to image the conductivity. The results shown below were obtained with simulated data containing 5% additive noise. To make the comparison between target and image more profound we plot the logarithm of the images at the same cross section of a 3D phantom.

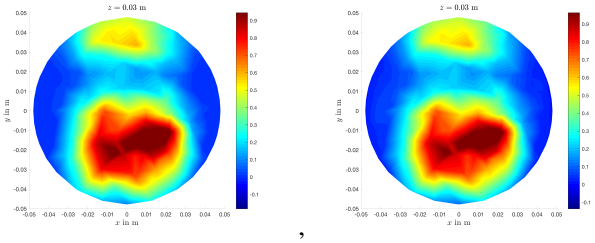

Figure 1: Cross section of the logarithm of the conductivity in the target (left) and reconstruction (right) form an ellipsoidal breast phantom at height $z = 3$ cm. Note the very small reconstruction error.

3 Conclusions

Our numerical results support the claim that despite the complicated experiment setup of LFEIT, image reconstruction is stable and the images provide adequate spatial resolution for medical diagnosis.

References

[1] P. Gransland-Mongrain, J-l. Mari, J-Y. Chapelon and C. Lafon *IRBM* 34(4-5), p. 357-360, 2013.

[2] L Kunyansky *Inverse problems*, 28, 2012.

[3] O. Kwon, EJ. Woo, JR. Yoon and JK. Seo, *IEEE Trans Biomed Eng.*, 49(2), p.160–167, 2002.

Fused-data Transrectal EIT incorporating Biopsy Electrodes

Ethan K. Murphy[1], Xiaotian Wu[1], and Ryan J Halter[1,2]

[1]Thayer School of Engineering, Dartmouth College, Hanover, NH, USA, ethan.k.murphy@dartmouth.edu

[2]Geisel School of Medicine, Dartmouth College, Hanover, NH, USA

Abstract: This work explores fusing transrectal electrical impedance tomography (TREIT) data from the top surface of an ultrasound probe and 4 electrodes from a biopsy needle measured at different positions to produce an improved reconstruction. Sensitivity analysis and measured tank experiments are used to validate the approach. This fused-data TREIT method has significant promise for improving prostate cancer screening.

1 Introduction

Detecting prostate cancer non-invasively is clinically challenging. Low threshold PSA-based screening has a high sensitivity, but low specificity due to numerous benign reasons for elevated levels [1]. Men with elevated levels of PSA are typically subject to image-guided biopsy protocol for more accurate diagnosis. Unfortunately, numerous investigators report that transrectal ultrasound (TRUS)-guided biopsies miss 10-30% of all cancers [1]. A number of ex vivo studies have shown that electrical properties show significant differences between benign and cancerous tissues [2], and there has been prior work in developing transrectal electrical impedance tomography (TREIT) algorithms [3] that include a biopsy needle electrode [4]. This study builds on [4] by fusing TREIT and biopsy electrodes measurements from different positions to increase the sensitivity far from the TRUS probe.

2 Methods

The fusion approach is based on a standard Gauss-Newton algorithm using a regularization scheme optimized for open domains [5]. In the experiment illustrated in Fig. 1A the TRUS probe with biopsy electrode is held fixed while a tank and two metal inclusions are rotated 0 to 340° in 20° steps. The biopsy electrodes are approximately 37 mm in front of the TRUS probe and are at the same depth as the inclusions.

The fusion process utilizes a single finite element method (FEM) mesh that has the TRUS probe and biopsy needle encoded within the domain. The mesh constructed in gmsh has ~500k nodes and ~3M elements. Corresponding to each tank rotation the mesh is rotated to yield the same relative geometry as the experiment and the Jacobian is calculated using a dual mesh approach. The dual mesh approach maps the fine (and dense) FEM mesh onto a much coarser set of nodes in which the reconstruction is actually performed. The same set of coarse nodes is used for each rotation, i.e. the coarse nodes remain fixed while the FEM mesh rotates. There are 1,778 coarse nodes in a cylindrical region extending from 25 to 50 mm in front of the TRUS probe with a radius of 10 mm. The measurements and Jacobians are concatenated so the problem can be solved as if it were a standard EIT problem [6].

A difference reconstruction using this fused data approach is shown in Fig. 1B. The yellow 'blocks' represent coarse nodes that are > 0.85 the maximum of the reconstruction, i.e. it represents the reconstructed metal inclusions. We used a Tikhonov factor of 1e5 and tetrapolar patterns that had 2 electrodes on the biopsy needle and 2 electrodes from the TREIT electrode array, as these patterns were agreed well with simulation on a blank tank and gave a large region of sensitivity based on an analysis of the Jacobian.

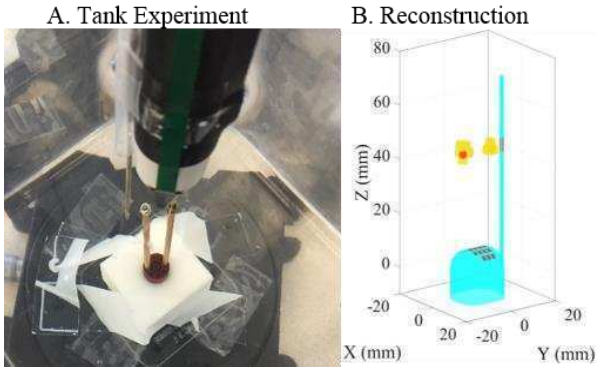

Figure 1: A. Downward view of TRUS probe with TREIT array (in green), biopsy needle and electrode on the left, and two metal inclusions in a saline filled tank on a rotation stage, and B. a difference reconstruction that fused the rotated datasets where the yellow represents nodes that are > 0.85 the maximum, the red spheres represent the true solutions of the inclusions, and the blue surface are faces of the FEM mesh.

3 Conclusions

This work presents a proof of principle difference reconstruction from tank experiment that shows that fused data in this TREIT with biopsy electrode is possible. In ongoing work more general rotations and translations of the probe and biopsy needle are being considered, which are further important steps to bringing this technique into a clinical setting.

4 Acknowledgements

This work was supported in part by the U.S. National Institutes of Health under Grant 1R01CA143020–01A1 and DoD CDMRP Grant W81XWH-15-1-0102.

References

[1] Campbell's Urology, 9th ed, P. Walsh, Editor. 2007, Saunders: Philadelphia
[2] R. J. Halter, et al., IEEE Trans. Bio. Eng., 54:,1321-1327, 2007.
[3] A. Borsic, et al., Phys. Meas., 30:S1-S18, 2009.
[4] Y. Wan, et al., 34th Annual Intern. Conf IEEE EMBS, 6220-6223, Sept. 2012.
[5] E.K. Murphy, A. Mahara, R.J. Halter, IEEE Trans Med. Imag., 35:1593-1603, 2016.
[6] E.K. Murphy, A. Mahara, R.J. Halter, IEEE Trans Med. Imag., 36:892-903, 2017.

Convergence of finite element approximation in electrical impedance tomography

Erfang Ma[1]

[1]Department of Mathematical Sciences, Xi'an Jiaotong-Liverpool University, Suzhou, Jiangsu Province, China,
erfang.ma@xjtlu.edu.cn

Abstract: For electrical impedance tomography (EIT) with the complete electrode model, we prove that the estimated voltages on the electrodes by the finite element method (FEM) converge pointwisely to the true ones as the sizes of elements in the underlying mesh approach zero.

1 Introduction

Assume the conductivity distribution σ of a convex polygonal region Ω is of interest. L electrodes are placed on the boundary of Ω. For $i = 1, 2, ..., L$, I_i is the amount of current flowing into the region through the i-th electrode; U_i is the voltage on the i-th electrode; e_i is the part of boundary of Ω that is covered by the i-th electrode; z_i is the contact impedance underneath the i-th electrode. $U = (U_1, U_2, ..., U_L)^T \in R^L$. The potential distribution over Ω is denoted by u which is assumed to belong to Sobolev space $H^1(\Omega)$. $H \stackrel{\text{def}}{=} H^1(\Omega) \otimes R^L$ i.e., the Cartesian product of $H^1(\Omega)$ and R^L.

Given the above assumptions, the weak formulation [1] for the boundary value problem of EIT is to find $[(u, U)]$ in the quotient space H/R such that

$$a([(u,U)],[(v,V)]) = \langle \ell, [(v,V)] \rangle \quad \text{for all } [(v,V)] \in H/R, \tag{1}$$

where

$$a([(u,U)],[(v,V)]) \stackrel{\text{def}}{=} \int_\Omega \sigma \nabla u \cdot \nabla v \mathrm{d}\Omega + \sum_{i=1}^{L} \frac{1}{z_i} \int_{e_i} (u-U)(v-V)\mathrm{d}s, \tag{2}$$

$$\langle \ell, [(u,U)] \rangle \stackrel{\text{def}}{=} \sum_{i=1}^{L} U_i I_i. \tag{3}$$

The space H/R is associated with two different norms:

$$\|[(u,U)]\|_{H/R} \stackrel{\text{def}}{=} \inf_{c \in R} \left(\|u - c\|_{H^1(\Omega)} + \|U - c\|_{R^L} \right), \tag{4}$$

$$\|[(u,U)]\|_a \stackrel{\text{def}}{=} \sqrt{a\left([(u,U)],[(u,U)]\right)}. \tag{5}$$

2 Methods

Assume $H_h^1(\Omega)$ is a finite element space for $H^1(\Omega)$ based on a triangularization $\mathcal{T}_h$ of domain Ω. Here h is a discretization parameter. The $(u_h, U_h) \in H_h \stackrel{\text{def}}{=} H_h^1(\Omega) \otimes R^L$ is a finite element solution. The $[(u_h, U_h)]$ is the element in the quotient space H_h/R that corresponds to (u_h, U_h). We claim

$$\lim_{h \to 0} \inf_{c \in R} \|U - U_h + c\|_{R^L} = 0. \tag{6}$$

Proof. According to the density argument [2] and the interpolation theory for Sobolev space [3], for any $\epsilon > 0$, we can find a h and $[(I_h v, U)] \in H_h/R$ such that

$$\lim_{h \to 0} \|[(u,U)] - [(I_h v, U)]\|_{H/R} < \epsilon \tag{7}$$

where $v \in H^2(\Omega)$ and $I_h v \in H_h^1(\Omega)$ is the interpolation of v by a piecewise polynomial of degree one. This gives

$$\lim_{h \to 0} \inf_{[(v_h, V_h)] \in H_h/R} \|[u,U] - [(v_h, V_h)]\|_{H/R} = 0. \tag{8}$$

On the other hand, the Galerkin orthogonality [3] and the ellipticity [1] of the bilinear form (2) lead to

$$\|[(u,U)] - [(u_h,U_h)]\|_{H/R} \le C \inf_{[(v_h,V_h)] \in H_h/R} \|[(u,U)] - [(v_h,V_h)]\|_{H/R}, \tag{9}$$

for some constant C. From (8) and (9),

$$\lim_{h \to 0} \|[(u,U)] - [(u_h,U_h)]\|_{H/R} = 0. \tag{10}$$

The (10) and (4) give (6). □

3 Conclusions

For EIT, the finite element approximation for the voltages on the electrodes converge to the true ones as the size of elements in the underlying mesh tend to zero.

4 Acknowledgements

This work is supported by a research development fund from Xi'an Jiaotong-Liverpool University.

References

[1] E Somersalo, M Cheney, D Isaacson *SIAM J Appl Math*, 52:1023–1042, 1992

[2] PG Ciarlet *The Finite Element Method for Elliptic Problems* SIAM: Philadelphia, 2002

[3] D Braess *Finite Elements: Theory, fast solver and applications in solid mechanics* CUP: New York, 2007

EIT in Multimodal Imaging for Avoiding Biopsies of False Positive Results in Mammography

P. Robert Kotiuga[1]

[1]Boston University, ECE Dept., 8 St. Mary's Str., Boston, MA, USA, prk@bu.edu

Abstract: EIT, in the context of false positives in mammography is considered where repeated negative results of biopsies can lead patients to avoid future mammograms. Our approach is to consider the conditional probabilities associated with use of EIT in conjunction to mammography, not for increasing the overall rate of detection of breast cancer, but for maintaining the best possible rate of cancer detection with fewer biopsies.

Introduction

Although EIT is a notoriously ill-conditioned problem, it has distinct advantages over other imaging modalities and it has made a place for itself in several multimodal medical imaging contexts. For example, forced lung ventilation in respiratory medicine where continuous monitoring of lung volume can be achieved for "lung protective ventilation strategy", without resorting to repeated x-ray exposure[1]. Another context is cancer imaging where knowledge of the conductivity of tissue can help discard false positives. However, in the application of EIT to cancer imaging, the ill-conditioning of EIT and coregistration of data from different imaging modalities becomes a critical issue. Coregistration is particularly difficult to achieve in the context of mammography. By focusing on three dimensional reality of mammography, the eigenfunctions of the Dirichlet to Neumann(D-N), map as a means to deal with both ill conditioning and coregistration, the present work offers a means to reduce the number of false positives that require a follow-up biopsy. The drawback of the proposed work is that it requires a more personalized approach, and considerably more preparation on the part of the patient. Thus, it only makes sense for those with a history of false positives being discovered by means of a biopsy. This classic example of a "false positive paradox"[2] can deter people from having follow-up mammograms.

1 Methods

Key aspects to the proposed approach are:

1) Dealing with the underlying ill-conditioning in a manner that reflects the 3D reality of the problem. Specifically, despite the fact that EIT requires vastly more data as one goes up in dimension, one also has to take advantage of the fact that the conditioning of EIT also gets better as dimension increases[3]. This is counterintuitive to many in the field who feel it is necessary to first demonstrate EIT in lower-dimensional contexts which require less data.
2) The conditioning of EIT can also be improved dramatically by reformulating EIT in terms of "Euclidean Dirac operators" and not in terms of the Laplace operator[4]. This aspect is best understood in terms of a "generalized Calderon problem" for self-adjoint elliptic operators. The underlying principles and the spectral theory of their associated "D-N" maps will be sketched in the extended paper.
3) Exploitation of generic properties of the eigenfunctions of the D-N map as a means to a personalized electrode configuration for coregistration of EIT data.
4) Articulating, the improvement in the conditioning and data acquisition in the context of a Bayesian framework where the conditional probabilities associated with avoiding a biopsy depends on the amount of coregistered data acquired.

2 Conclusions

This paper to considers the conditional probabilities associated with use of EIT in conjunction to mammography, not for increasing the overall rate of detection of breast cancer, but for maintaining the best possible rate of cancer detection with increased patient engagement and fewer biopsies. The underlying Bayesian model takes into account the dependence of the conditioning of the EIT problem as a function of dimension, and other aspects which affect conditioning.

3 Acknowledgements

The author is indebted Bill Loinheart for encouraging a broader exploitation of geometric insights in EIT practice.

References

[1] I. Frerichs, et. al., Chest electrical tomography examination, data analysis, terminilogy, clinical use and recommendations: Consensus statement of the Translational EIT development study group review. Thorax Online First, published on October 4, 2016 as 10.1136/thoraxjnl-2016-208357.

[2] B. L. Madison, Mathematical Proficiency for Citizenship, Chapter 8 in, A.H. Schoenfeld (Ed.), Assessing Mathematical Proficiency, MSRI Monograph No. 53, Camb U. Press, 2007

[3] P. R. Kotiuga, A Rationale for Pursuing EIT and MREIT in 3-D based on Weyl Asymptotics and Problem Conditioning. EIT 2008 Conference, Dartmouth College, Hannover NH, June 16-18, 2008.

[4] Kotiuga, P.R., Metric Dependent Aspects of Inverse Problems and Functionals Based Helicity. Journal of Applied Physics, 70(10), May 1993, pp. 5437-5439.

Direct Absolute EIT Imaging on Experimental Data

Sarah Hamilton[1]

[1]Department of Mathematics, Statistics and Computer Science, Marquette University, Milwaukee, WI, USA,
sarah.hamilton@mu.edu

Abstract: A direct reconstruction algorithm [1, 2] for 2D Absolute Admittivity EIT imaging is presented and demonstrated on experimental tank data for the first time. The key benefit of the method is that it does not require any simulated reference data Λ_1 or Λ_{ref}. The method is based on the D-bar methodology which uses a tailor-made nonlinear Fourier transform of the measured boundary voltage/current data Λ_γ to uniquely recover the admittivity $\gamma = \sigma + i\omega\epsilon$ of the interior.

1 Introduction

In Electrical Impedance Tomography (EIT) electrical measurements are taken on electrodes at the body's surface, and a mathematical inverse problem is solved to recover the internal conductivity/admittivity of the body. The most common solution methods solve an optimization problem to minimize the error between measured and predicted data (e.g. voltage/current data) therefore requiring a finely-tuned forward model. By contrast, D-bar methods solve the inverse problem directly without repeated forward solutions.

D-bar methods are based on using a nonlinear Fourier transform of the Dirichlet-to-Neumann (voltage-to-current-density) data that is tailor-made for the EIT problem. The conductivity/admittivity is then recovered from the transformed data by solving a $\overline{\partial}_k$ (D-bar) equation in the transformed variable k. While there are multiple D-bar methods for EIT, they all have the same basic form:

$$\text{Current/Voltage data} \longrightarrow \text{Scattering data} \longrightarrow \text{Conductivity/ Admittivity}$$

2 Methods

Here we use a specific D-bar method that is based on introducing an auxiliary parameter $k \in \mathbb{C}$ and transforming two special complex geometrical optics (CGO) solutions u_1 and u_2 of the admittivity equation

$$\nabla \cdot \gamma(z)\nabla u(z,k) = 0, \quad z \in \Omega \subset \mathbb{R}^2 \tag{1}$$

into a first-order matrix system of CGOs:

$$[-D_k + Q(z)]\, M(z,k) = 0 \tag{2}$$

where $D_k M = \begin{bmatrix} \bar\partial_z & 0 \\ 0 & \partial_z \end{bmatrix} M - ik \begin{bmatrix} 1 & 0 \\ 0 & -1 \end{bmatrix} \begin{bmatrix} 0 & M_{12} \\ M_{21} & 0 \end{bmatrix}$ and $Q(z) = \begin{bmatrix} 0 & -\frac{1}{2}\partial_z \log\gamma(z) \\ -\frac{1}{2}\bar\partial_z \log\gamma(z) & 0 \end{bmatrix}$. These CGO solutions satisfy a D-bar equation in the transform variable k

$$\overline{\partial}_k M(z,k) = M(z,\bar k) \begin{bmatrix} e(z,\bar k) & 0 \\ 0 & e(z,-k) \end{bmatrix} S(k), \tag{3}$$

from which the admittivity γ can be recovered.

This work uses a 'Born'-approximation to the scattering data $S(k)$ that can be computed directly from the measured data Λ_γ via:

$$\begin{aligned} S_{12}(k) &= \tfrac{i}{4\pi} \textstyle\int_{\partial\Omega} e^{-i\bar k z} \left(\Lambda_\gamma + i\partial_\tau\right) \left(\frac{e^{-ikz}}{-ik}\right) ds(z) \\ S_{21}(k) &= -\tfrac{i}{4\pi} \textstyle\int_{\partial\Omega} e^{i\bar k z} \left(\Lambda_\gamma - i\partial_\tau\right) \left(\frac{e^{ikz}}{ik}\right) ds(z), \end{aligned} \tag{4}$$

where ∂_τ denotes the tangential derivative operator: $\partial_\tau f(z) = \nabla f(z) \cdot \tau$ and the asymptotic behaviors of $u_1 \sim \frac{e^{ikz}}{ik}$ and $u_2 \sim \frac{e^{-ik\bar z}}{-ik}$ are used [1, 2].

Figure 1 demonstrates the method on archival experimental tank data taken on RPI's ACT3 EIT system, and compares the results to those from the traditional formulation [3] for difference and absolute imaging for the first-order system D-bar method (2).

3 Conclusions

A D-bar method that does not require any simulated measurement data Λ_1 to form absolute EIT images is presented and demonstrated on experimental data for the first time. The method is non-iterative, trivially parallelizable, and holds for both conductivity-only as well as admittivity imaging. If only the conductivity is desired, symmetries in the underlying CGO system (2) can be exploited reducing the computational load by a factor of 1/2 leading to an even faster solution.

4 Acknowledgements

The experimental data was provided by the EIT lab at RPI, for which we express our thanks.

References

[1] C.N.L. Herrera, *PhD Thesis*, Escola Politécnica da Universidade de São Paulo, 2012.

[2] C.N.L. Herrera, M.F.M Vallejo, J.L. Mueller, R.G. Lima *IEEE TMI*, 34(1): 267-274, 2015.

[3] S.J. Hamilton, C.N.L. Herrera, J.L. Mueller, A. Von Hermann *Inverse Problems* 28: 095005, 2012.

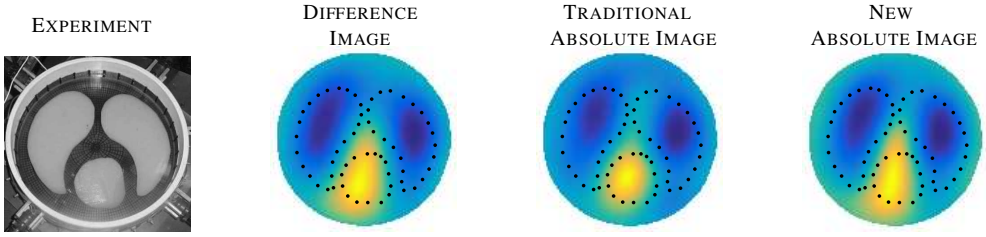

Figure 1: Comparison of D-bar methods on experimental data. Note that the difference image requires $\Lambda_\gamma - \Lambda_{\text{ref}}$, the traditional absolute image [3] requires $\Lambda_\gamma - \Lambda_1$ where Λ_1 is simulated, however the new absolute image (right) only requires the measured data Λ_γ.

EIT reconstruction regularized by Total Generalized Variation

Bo Gong, Benjamin Schullcke, Sabine Krueger-Ziolek, Knut Moeller

Institute of technical Medicine (ITeM), VS-Schwenningen, Germany, Bo.Gong@hs-furtwangen.de

Abstract: EIT reconstructions with Total Variation (TV) regularization promote solutions with sparse first order derivation. Consequentially, the sharp boundaries between different tissues can be approximated. However, TV regularization may induce blocky images which are not realistic in clinical applications. To reduce such blocky artefacts, we applied the Total Generalized Variation (TGV) for regularization. TGV employs higher order differential operators over the finite element mesh.

1 Introduction

We focus on the linearized time difference lung EIT reconstruction. The image reconstruction intends to solve the conductivity changes Δs from the measured voltage differences dV between two time steps. This is an ill-posed inverse problem which needs regularizations to confine the solution space. Mathematically, the following regularized optimization problem is solved:

$$\Delta s := \mathrm{argmin}_{\Delta s} \|J \cdot \Delta s - dV\|_2^2 + \lambda \cdot R(\Delta s) \quad (1)$$

where J is the Jacobian matrix, $R(\Delta s)$ is the regularization term and λ is the regularization parameter.

One type of regularization term is TV regularization. It is the ℓ_1 norm of the first order derivation of underlying conductivity distribution over the domain. Because of the ℓ_1 norm in TV regularization, the TV regularized EIT reconstruction promotes a solution with sparse discrete derivation of the underlying solution. Consequentially, TV regularization identifies the sparse sharp interfaces between different tissues and promotes block-wise constant image reconstruction. As a side effect, the reconstructed images often contain the blocky artefacts. To reduce these blocky artefacts, higher order differential operators are considered in regularization, such as the total generalized variation regularization TGV [1].

2 Methods

EIT images are reconstructed under the finite element mesh (FEM) framework. An FEM can be endowed with an undirected weighted graph structure: $G := \{V, E, A\}$, which contains three components: a set V that consists of the indexed vertices, a set of edges E and a weighted adjacency matrix A. Explicitly, each finite element in FEM is identified as a vertex in V and two vertexes v_i and v_j in V are connected by an edge $e_{ij} \in E$ if the corresponding two finite elements share a common boundary. A weight a_{ij} which equals the area of the shared boundary is attributed on each edge e_{ij}. These weights are saved as the (i,j)-th entry of the adjacency matrix A. The differential operator of the functions over the undirected graph is indeed the weighted indication matrix D:

$$D_{e_{ij},v_k} := \begin{cases} a_{ij} & if \quad i = k \\ -a_{ij} & if \; j = k \\ 0 & else \end{cases} \quad (2).$$

With this formulation, the TV regularization on the graph structured FEM framework is represented by: $R_{TV}(\Delta s) := \|D \cdot \Delta s\|_1$. On the other hand, following [2], the total generalized variation operator is defined by:

$$\mathrm{R_{TGV}}(\Delta s) := \min_q \alpha \cdot \|\mathrm{D} \cdot \Delta s - q\|_1 + (1-\alpha)\|\mathrm{D^T} \cdot q\|_1. \quad (3)$$

Intuitively, $q \in \mathcal{R}^{|E|}$ is an approximation of the first order derivation of Δs and $D^T \cdot q$ is an approximation of the second order derivation of Δs. Under the TGV regularization, the reconstruction is to solve the follow optimization problem:

$$\Delta s = argmin_{\Delta s, q} \|J \cdot \Delta s\|_2^2 + \lambda \cdot (\alpha \cdot \|D \cdot \Delta s - q\|_1 + (1-\alpha)\|D^T \cdot q\|_1). \quad (4)$$

We solve this problem by Split Bregmann iterations [3].

3 Conclusions

The performance of different regularization methods has been compared by 2.5D simulations (Fig. 1). The simulated voltage difference was added with 10% white noise. The common parameters for TV and TGV regularizations are same and were heuristically chosen. It can be observed that the reconstruction with TGV regularization recovers the piecewise linear conductivity distribution. However, TGV regularization fails to smooth out the overshoots introduced by the fidelity term. This leads to the artefacts at the interfaces between contrasts.

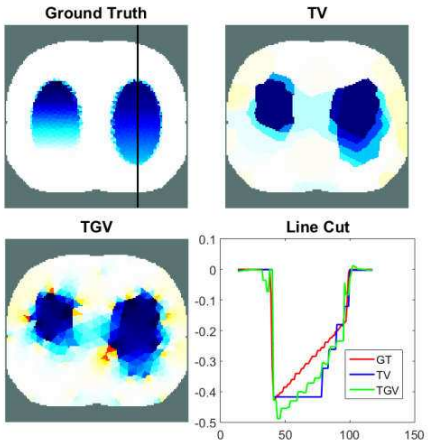

Figure 1: Example reconstructions with different regularization methods. The reconstructed Δs located on a vertical line cut (black line in Ground Truth) are demonstrated in the lower right plot.

4 Acknowledgements

This work was supported by the BMBF grant no. 03FH038I3 (MOSES).

References

[1] K Bredies, K Kunisch, and T Pock SIAM J. Imaging Sci., 3(3), pp. 492–526
[2] S Ono, I Yamada, and I Kumazawa Conf ICASSP, 2015
[3] T Goldstein, S Osher SIAM J. Imaging Sci., 2(2), 323–343.

The sensitivity in time domain EIT

M. G. Crabb[1] and W. R. B. Lionheart[1]

[1]School of Mathematics, University of Manchester, Manchester, UK, michael.crabb@manchester.ac.uk

Abstract: A formula for the sensitivity with respect to conductivity and permittivity changes is derived for the EIT forward problem with time domain boundary data. We demonstrate that at multiplexing, regions of high permittivity behave like interior current sources, and increased sensitivity to conductive changes is observed.

1 Methods: Time domain EIT

We consider a time-dependent equation to model transient behaviour e.g. at multiplexing [1]. Assume linear constitutive relations $D = \epsilon E$ and $J = \sigma E$ in Maxwell's equations, and neglecting magnetic induction

$$\nabla \cdot (\sigma \nabla u(x,t) + \epsilon \nabla \dot{u}(x,t)) = 0 \quad x \in \Omega, \tag{1}$$

where $E = \nabla u$. Denote $j(t) = (\sigma \nabla u(t) + \epsilon \nabla \dot{u}(t)) \cdot n|_{\partial\Omega}$ the current density applied on $\partial\Omega$ and assume both $u(t)|_{\partial\Omega}$ and $\dot{u}(t)|_{\partial\Omega}$ are measured. Note that the quasi-static approximation assumes a fixed frequency ω and harmonic current j, giving

$$\nabla \cdot ((\sigma + \mathrm{i}\omega\epsilon)\nabla u(x,\omega)) = 0. \tag{2}$$

Unique recovery of the complex admittivity $\sigma + \mathrm{i}\omega\epsilon$ from (complex) boundary data is known [2] but is highly unstable.

1.1 Transient sensitivity and effective current source

In a similar manner to [3] we consider two conductivities σ and $\sigma + \delta\sigma$ with same applied current j. To 1^{st} order in $\delta\sigma$

$$\nabla \cdot (\delta\sigma \nabla u) + \nabla \cdot (\sigma \nabla \delta u) + \nabla \cdot (\epsilon \nabla \delta \dot{u}) = 0.$$

Multiplying by u, integrating over Ω, using divergence theorem and assuming $\delta\sigma$ is compactly supported gives

$$\int_\Omega \nabla u \cdot (\sigma \nabla \delta u + \epsilon \nabla \delta \dot{u}) + \int_\Omega \delta\sigma \nabla u \cdot \nabla u = \int_{\partial\Omega} u \delta j$$

Eliminating δu and using $\int_\Omega \delta u \nabla \cdot (\sigma \nabla u + \epsilon \nabla \dot{u}) = 0$

$$\int_{\partial\Omega} \delta u (\sigma \nabla u + \epsilon \nabla \dot{u}) \cdot n = \int_\Omega \nabla \delta u \cdot (\sigma \nabla u + \epsilon \nabla \dot{u}).$$

Now using $\delta j = 0$ gives

$$\int_{\partial\Omega} \delta u j = -\int_\Omega \delta\sigma \nabla u \cdot \nabla u + O(||\delta\sigma||^2_\infty),$$

and by symmetry the analogous formula for ϵ perturbation is

$$\int_{\partial\Omega} \delta \dot{u} j = -\int_\Omega \delta\epsilon \nabla \dot{u} \cdot \nabla \dot{u} + O(||\delta\epsilon||^2_\infty).$$

Let $L_p = \nabla \cdot (p\nabla)$, then (1) is $L_\sigma u + L_\epsilon \dot{u} = 0$ and applying Green's operator $G_\epsilon := L_\epsilon^{-1}$, gives $\dot{u} + G_\epsilon L_\sigma u = 0$. The exponential of this operator is well-defined since $G_\epsilon L_\sigma$ is a pseudo-differential operator of order 0. Assuming current source switched off at $t = 0$, we have to leading order

$$u(x,t) = \exp(-G_\epsilon L_\sigma t) u(x,0). \tag{3}$$

This formula is a continuum analogue of a parallel RC circuit with an applied current source switched off at $t = 0$, which results in a transient current $I(t) = I_0 \exp(-t/RC)$.

2 Results

To simulate $u(x,t)$ we expand $u(x,t) = \sum_\omega u(x,\omega) e^{\mathrm{i}\omega t}$, where for each ω $u(x,\omega)$ satisfies (2). A square wave time domain current $I(t)$ is decomposed into Fourier modes $\tilde{I}(\omega)$, and the quasi-static problem with boundary data $\tilde{I}(\omega)$ is solved using a piecewise linear FEM, and the resulting $u(x,\omega)$ is summed weighted by $e^{i\omega t}$.

For the k^{th} time step, i^{th} measurement pair (u,v), we have discretised conductivity and permittivity Jacobian

$$J^\sigma_{ijk} = \int_{E_j} \nabla u(:,k) \cdot \nabla v(:,k), \; J^\epsilon_{ijk} = \int_{E_j} \nabla \dot{u}(:,k) \cdot \nabla \dot{v}(:,k).$$

At each k, the singular value decomposition (SVD) $J = U\Sigma V^T$ is computed, where the columns of V, $\{v_i\}_{i=1}^N$, form a basis for discretised model space and U is a diagonal matrix of singular values. The singular vectors associated with largest singular vectors give the largest components in data. Consequently a perturbation $\delta\sigma = \sum \delta_i \chi_i$, means that $\delta = \sum_{i=1}^T (\delta^T v_i) v_i$, $T \leq N$, is the effective observable perturbation when singular values below a noise level T are rejected.

A unit disc mesh is generated in EIDORS with 16 electrodes with a disc inclusion centred at $(0.3, 0.3)$ and radius 0.3. A square wave current is applied using a skip 5 electrode current excitation and voltage measurement protocol. The background is set to $(\sigma, \epsilon) = (1, 0.01)$ and the inclusion set to $(\sigma, \epsilon) = (1, 1)$. The transient and conductive Jacobians are computed as above, the SVD computed and used to represent an effective conductive perturbation of amplitude $\sigma = 2$ supported in the permittive inclusions in Figure 1.

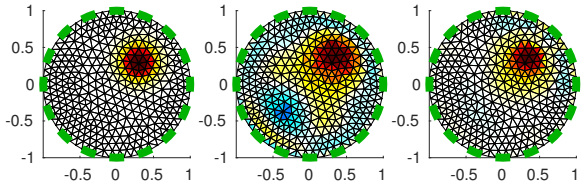

Figure 1: Left - true conductive perturbation. Middle and Right - effective perturbation expanded using DC and transient singular vectors resp., both rejecting singular vectors below 38dB noise level.

3 Conclusion

A sensitivity formula for EIT with time-dependent boundary data is derived. We demonstrate permittive regions have greater sensitivity to conductivity changes at multiplexing since these regions act like interior current sources.

References

[1] MG Crabb, P Green, P Wright, WRB Lionheart *Multiplexing and transient estimates in lung EIT instruments Conf. 16th ICEBI & 17th EIT*, p.110, Stockholm, Sweden, 2016

[2] E Francini *Recovering a complex coefficient in a planar domain from the Dirichlet-to-Neumann map* Inverse Problems 16(1) 2000

[3] AP Calderón, *On an inverse boundary value problem* Comput. Appl. Math. vol. 25, no. 2-3, 2006

EIT guided PEEP titration in ARDS: preliminary results of a prospective study

Yeong-Long Hsu[1], Mei-Yun Chang[1], Hou-Tai Chang[1*], Knut Möller[2] and Zhanqi Zhao[2]

[1] Division of Chest Medicine, Far Eastern Memorial Hospital, Taipei, Taiwan, *houtai38@gmail.com

[2] Institute of Technical Medicine, Furtwangen University, Villingen-Schwenningen, Germany

Abstract: The efficacy of PEEP titration in ARDS patients guided by EIT is examined prospectively. Optimal PEEP was defined according to the regional overdistension and collapse. Patients who received treatments prior to the study were explored retrospectively as control group. Individual PEEP titration was set at low inflation point of the quasi-static pressure-volume curve. Preliminary results showed higher optimal PEEP and PaO_2/FiO_2 increase in EIT group.

1 Introduction

Clinical studies indicate that chest EIT is able to monitor ventilation distribution at the bedside and may help to develop lung protective ventilation strategies [1]. Acute respiratory distress syndrome (ARDS) is the sudden failure of the respiratory system and is associated with a high mortality rate (27–45% from mild to severe) [2]. An adequate positive end-expiratory pressure (PEEP) and low tidal volume are critical to reduce the mortality rate [3]. EIT-guided PEEP titration for ECMO-treated ARDS patients showed promising results [4]. Further prospective outcome studies comparing EIT-guided and conventional PEEP titration are warranted. Preliminary results of a running prospective study are presented in this abstract.

2 Method

ARDS patients from year 2016 were studied retrospectively as control group. Individual PEEP titration was set at low inflation point (LIP) of the quasi-static pressure-volume curve [5]. New ARDS patients were prospectively included for EIT-guided group (PulmoVista 500, Dräger Medical, Lübeck, Germany). Optimal PEEP was defined according to the regional overdistension and collapse [6].

Patients in both groups were ventilated with EVITA 4 (Dräger Medical, Lübeck, Germany) with low tidal volume (6 ml/kg predicted body weight). Fraction of inspired oxygen (F_iO_2,) and partial pressure of arterial oxygen (PaO_2) were measured directly before and 2 hours after PEEP titration. In EIT group, the EIT data were recorded at 20 Hz and reconstructed with EIT Data Analysis Tool 6.3 (Dräger Medical, Lübeck, Germany). Offline analysis of regional compliance was achieved using a customized software compiled with MATLAB (MathWorks, Natick, MA, USA).

3 Preliminary results

Up to now, 5 ARDS patients were titrated with EIT. Records of 30 patients titrated with pressure-volume curve were retrospectively analyzed. Fig. 1 showed the curves of regional overdistension and collapse. Intersection of the curves marked the optimal PEEP level. Table 1 summarized the optimal PEEP in each group and the corresponding PaO_2/FiO_2 increase 2 hours after PEEP titration. Data are presented in median (interquartile range).

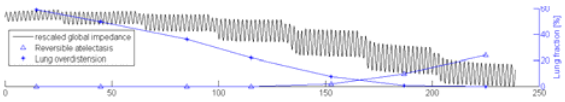

Figure 1: Global impedance (black) curve during PEEP titration in one patient measured with EIT. Regional overdistension (stars) and regional collapse (triangles) were calculated for each PEEP step.

Table 1: Parameters summary of PEEP titration

	EIT group	Control group
optimal PEEP	18 (3)	15 (4)
PaO_2/FiO_2 increase	127 (101)	28 (113)
increase percentage	125% (92)	26% (112)

Increase percentage was referenced to the values before PEEP optimization.

4 Discussion and conclusion

This is a running prospective study using EIT to titrate PEEP in ARDS patients. Based on the preliminary results, PEEP selected in EIT group were higher than that in the control group. This coincided with a previous animal study [7]. The off-line analysis time of the EIT data was ~5 minutes after the end of a PEEP titration, which is acceptable in clinical practice. However, due to the small number of the subjects included in the EIT group, no statistical significance was found. Interquartile ranges were relatively high, which may be due to the mixture of mild moderate and severe ARDS patients in both groups. By further increasing the number of subjects in the EIT group and the retrospective control group, division of the groups according to the severity levels may increase the comparability. Further outcome parameters such as ventilator days, ICU days, weaning successful rate, APACHE II index will be explored.

The preliminary results show that our protocol is feasible and the PEEP titration guided by EIT might lead to a better clinical outcome in ARDS patients.

References

[1] I Frerichs, *et al*. *Thorax*, 72: 83-93, 2017
[2] VM Ranieri, *et al*. *JAMA*, 307: 2526-33, 2012
[3] MB Amato, *et al*. *N Engl J Med*, 372:747-55, 2015
[4] G Franchineau, *et al*. *Am J Respir Crit Care Med*, in press 2017
[5] GM Albaiceta, *et al*. *Curr Opin Crit Care*, 14:80-6, 2008
[6] E Costa, *et al*. *Intensive Care Med,* 35: 1132-37, 2009
[7] GK Wolf, *et al*. *Crit Care Med,* 41: 1296-304, 2013

Pulsatile Perfusion Imaging of Premature Neonates using SMS-EIT

Tzu-Jen Kao[1], Jonathan Newell[2], David Isaacson[2], Gary Saulnier[2], Bruce Amm[1], Greg Boverman[1], Rakesh Sahni[3], Marilyn Weindler[3], David Chong[3], David DiBardino[3], David Davenport[1], Jeffrey Ashe[1]
[1]Diagnostics, Imaging and Biomedical Technologies, GE Global Research Center, Niskayuna, NY 12309, USA,
[2]Rensselaer Polytechnic Institute, Troy, NY 12180, USA, [3]Columbia University Medical Center, New York, NY 10032, USA

Abstract: The aim of this study was to investigate the perfusion signals in premature infants. Five pre-term newborns, (3 males and 2 females, mean (standard deviation, SD) gestational age: 32.6 (0.89) weeks; mean birth weight: 1821 (547.36) g, mean postnatal age: 8.40 (5.03) days), were studied in the Neonatal Intensive Care Unit (NICU) at Columbia University Medical Center. One-hour impedance measurements were made at 18.3 frames/sec with 16-bit precision. Impedance images were reconstructed and displayed in real-time and further analyzed off-line. Frame-by-frame images of pulsatile perfusion were clearly demonstrated without averaging, filtering or contrast agents. The expected phase shift between the pulsatile perfusion waveform in the heart region and in the lung regions was clearly seen. The peak magnitude of the pulsatile signal in the lung region was about half that in the heart region.

1 Introduction

Interest in the clinical use of EIT for monitoring lung function is growing rapidly [1]. But monitoring regional pulmonary perfusion is an unmet clinical need and a technical challenge especially in the neonatal population in which other imaging techniques are rarely used [2].

2 Methods and Results

Impedance measurements were made for one hour intervals at 18.3 frames/sec with 16-bit precision using the GE Simultaneous Multi-Source-EIT (SMS-EIT) prototype system [3]. The time-series results in Figures 1 are power waveforms, computed from the first cosine pattern current amplitude multiplied by the real part of the corresponding voltages. Perfusion images were reconstructed during a breathing pause, and regions of interest were selected in the lung and heart fields as shown in Figure 2. Frame-by-frame pulsatile perfusion images were reconstructed in Figure 3 (same scale for different time frames) and Figure 4 (different scale for each subjects).

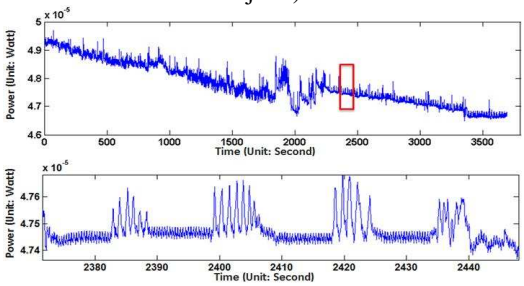

Figure 1: The power waveforms during the entire 60-minute recordings had significant drift (top). A suitable segment of this signal was selected by hand for detailed analysis (bottom).

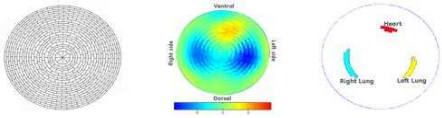

Figure 2: Reconstruction mesh, orientation of the impedance images and Regions of Interest (ROI) of the mesh.

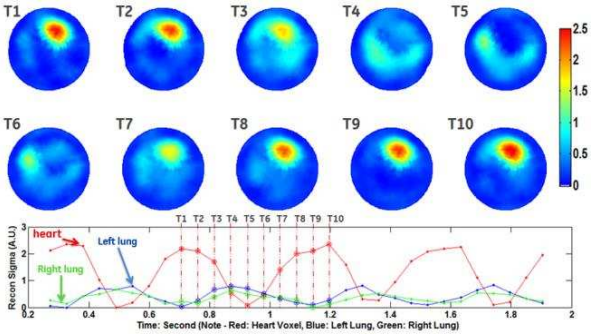

Figure 3: Top: Frame by frame reconstructed regional pulsatile perfusion images in the same color scale. The subject's heart rate is about 140 bpm. **Bottom:** Red denotes conductivity change in the heart region; blue denotes the left lung region and green denotes the right lung region.

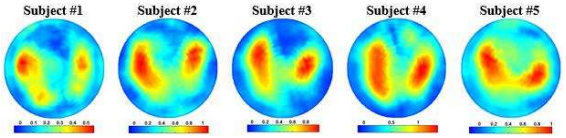

Regional Perfusion	subject #1	subject #2	subject #3	subject #4	subject #5
Heart Region	0.801	1.045	1.291	1.957	2.355
Left Lung Region	0.408	0.531	0.636	0.989	0.784
Right Lung Region	0.419	0.543	0.501	0.938	0.728

Figure 4: Top: Reconstructed regional pulsatile perfusion image at the end of systole for 5 subjects. **Bottom:** The comparison of the amplitude of pulsatile perfusion signal in different regions.

3 Conclusions

We have demonstrated the ability of the GE SMS-EIT prototype system to create real-time ventilation and pulsatile perfusion images with impedance data from pre-term neonates. The peak-to-peak magnitude of the pulsatile perfusion signal in the heart region was about 2.2 times that seen in the lung regions, using this 2-D reconstruction algorithm. The phase shift between the perfusion signal in the heart and lungs is clearly observed in Figure 3, and agrees with expectations from normal physiology.

4 Acknowledgement

This research was supported by Grant 1R01HL 109854 from the National Institutes of Health. The content is solely the responsibility of the authors and does not necessarily represent the official views of the National Institutes of Health.

References

[1] A Adler, B Grychtol, R Bayford *PhysioMeas*, 36:1067–1074,2015
[2] Caples S M and, Hubmayr R D. 2003 Respiratory monitoring tools in the intensive care unit *Critical Care*. 2003; 9:230–235
[3] Kao T-J et al 2014 Real-time 3D electrical impedance imaging for ventilation and perfusion of the lung with lateral decubitus position Proc. of the IEEE 36th Conf. of the EMBC (Chicago)

Regional Air Distributions in Porcine Lungs using High-performance Electrical Impedance Tomography System

Geuk Young Jang[2], Hun Wi[2], Young Bok Kim[1], Tong In Oh[1] and Eung Je Woo[1]

[1]Department of Medical Engineering, Graduate school, Kyung Hee University, Seoul, Korea, ejwoo@khu.ac.kr

[2]Department of Biomedical Engineering, Graduate school, Kyung Hee University, Yongin, Korea

Abstract: There have been many studies to find optimal ventilator values using EIT (electrical impedance tomography). In this study, we generated the strain images during PEEP maneuver at porcine.

1 Introduction

Ventilator induced lung injury (VILI) is one of the major issues in intensive care patients with mechanical ventilator [1]. For lung protective mechanical ventilation needed optimal ventilation settings. Pulmonary assisted ventilation using EIT monitoring is one of the methods of ventilator assist.

Lung strain in the lung is the primary determinants of ventilator induced lung injury [2]. Clinical equivalent of lung strain as the ratio of lung volume change to the end expiratory lung volume. With this concept to analyse the effects of mechanical ventilation on the lungs is a new way to design optimal ventilation for intensive care patients. EIT can measure strain distribution of lung from tidal volume and expiratory lung volume in real time.

2 Methods

2.1 Experimental Setup

We used a KHU Mark2.5 16-channel multi-frequency parallel EIT system [3]. Current injection pattern used adjacent protocol at 10 kHz and frame rate was 50 frames/s. For PEEP maneuver, Mechanical ventilator (Hamilton-G5, Hamilton Medical, Switzerland) was used. After experiment, we scan boundary shape using 3D scanner (Sense, 3D SYSTEMS, USA) for real shape reconstruction model.

2.2 Reconstruction Algorithm

We used a correlation based fidelity-embedded regularization (FER) method for robust image reconstructions against motion artifacts [4]. Subject-specific reconstruction models were used for reduce geometric modeling errors [5].

2.3 Experimental Protocol

Initial ventilator setup included TV of 10 ml/kg (or 10 cmH2O in pressure mode), RR(respiration rate) of 20 breaths/min and PEEP of 5 cmH2O. In PEEP maneuver, the value of PEEP was increased from 5 to 25 cmH20 and then decreased to 5 cmH20 again.

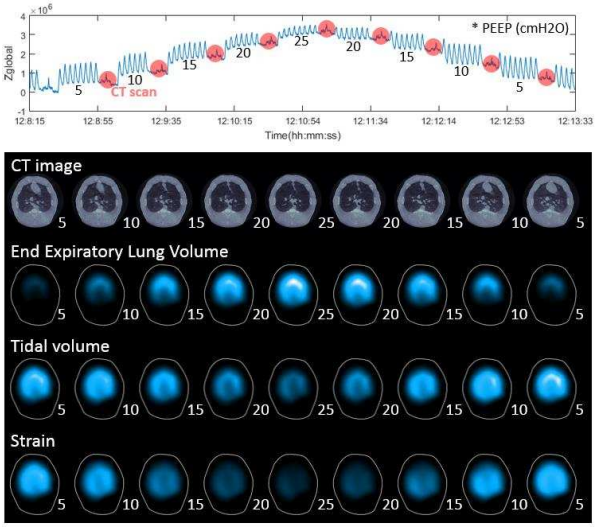

Figure 1: Global impedance change and EIT reconstruction images (EELV, TV and Strain) with CT image during PEEP maneuver

3 Conclusions

We reconstruct the functional EIT images (end expiratory lung volume, tidal volume) and CT images measured in each PEEP stage. Strain distribution image was calculated by end expiratory lung volume and tidal volume ratio. We plan to evaluate the strain image in disease model.

4 Acknowledgements

Research supported by Korean Health Technology R&D Project, Ministry of Health and Welfare, Republic of Korea (HI14C0743).

References

[1] MBF. Amato et al, New England Journal of Medicine, vol. 338, pp. 347-54, 1998.

[2] G. F. Nieman et al, Intensive Care Medicine Experimental, 4:16, 2016

[3] H. Wi et al, IEEE Trans. Biomed. Circ. Syst., vol. 8, pp. 119–128, 2014.

[4] K. H. Lee, E. J. Woo, J. K. Seo *Conf 16th ICEBI & 17th EIT*, p.103, Stockholm, Sweden, Jun 2016.

[5] AR. Lupton-Smith et al, Pediatr Pulmonol, vol. 49, pp. 764–71, 2014.

Effect of variable pressure support ventilation on ventilation distribution: preliminary results of a prospective study

Songqiao Liu[1], Haibo Qiu[1*], Knut Möller[2] and Zhanqi Zhao[2]

[1] Department of Critical Care Medicine, Zhongda Hospital, Nanjing, China, * haiboq2000@163.com

[2] Institute of Technical Medicine, Furtwangen University, Villingen-Schwenningen, Germany

Abstract: The efficacy of variable pressure support ventilation (vPSV) in ARDS patients is examined prospectively using EIT. Regional distribution of tidal ventilation and of changes in end expiratory lung volume (ΔEELV) were compared to that during traditional PSV. Preliminary results showed positive ΔEELV during vPSV and ventilation redistribution towards dorsal regions in most of the patients.

1 Introduction

Pressure support ventilation (PSV) is one of the most widely used modes to assist spontaneous breathing [1]. A fixed driving pressure is applied to support spontaneous breathing, which may result in a relatively low tidal volume variability [2]. Previous studies have demonstrated that adding variable tidal volumes by means of variable pressure support levels (vPSV) may improve lung function and reduce pulmonary inflammatory response [3-5]. EIT allows continuous monitoring of the regional distribution of tidal ventilation (TV) and changes in end expiratory lung volume (ΔEELV) [6]. A recent case report had showed an increase of ΔEELV during vPSV compared to traditional PSV in a patient with cardiac arrest [7]. We have started a prospective self-control study to validate efficacy of vPSV in patients with acute respiratory distress syndrome (ARDS). Preliminary results of this ongoing study are presented in this abstract.

2 Method

ARDS patients who are scheduled to wean from ventilators are studied prospectively. We compared EIT data recorded during PSV (V300, Dräger Medical, Lübeck, Germany; positive end-expiratory pressure 5 cmH_2O, pressure support 5-10 cmH_2O decided by attending physicians) with those obtained after 20 minutes on vPSV (pressure variability range 30%). For comparison, the rest of the ventilator settings remained. EIT data were recorded at 20 Hz and reconstructed with EIT Data Analysis Tool 6.3 (Dräger Medical, Lübeck, Germany). Same baselines were selected for both PSV and vPSV periods. Offline analysis of ΔEELV, TV changes, center of ventilation (CoV) [8] and global inhomogeneity index (GI) [9] were achieved using a customized software compiled with MATLAB (MathWorks, Natick, MA, USA).

3 Preliminary results

Up to now, 8 ARDS patients were studied. Fig. 1 showed ΔEELV and ΔTV of one patient during PSV and vPSV. Table 1 summarized the EIT parameters quantifying ventilation distribution. Data are presented in median (interquartile range). Five patients had a positive ΔEELV. Six patients had a redistribution towards ventral regions.

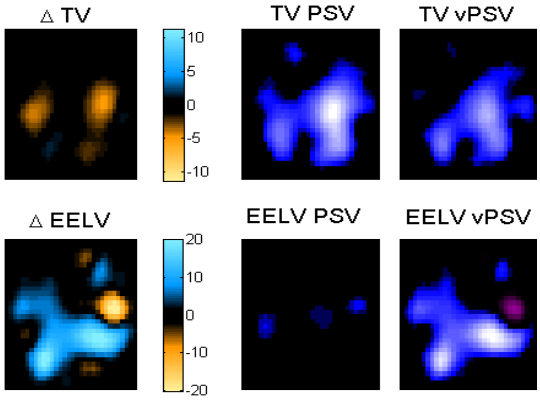

Figure 1: EELV and TV of one patient during PSV and vPSV. Volume loss is marked in orange and volume gain is marked in blue (vPSV minus PSV).

Table 1: Regional distribution of TV and ΔEELV

	PSV	vPSV
ΔEELV (%)	38% (173%)	
ΔTV (%)	99% (17.5%)	
GI	0.37 (0.04)	0.39 (0.07)
CoV	47.5% (10%)	48.5% (7%)

Percentage changes of EELV and TV were referenced to the amplitude of TV during PSV.

4 Discussion and conclusion

This is a running prospective study using EIT to assess vPSV in ARDS patients. Based on the preliminary results, positive ΔEELV during vPSV and ventilation redistribution towards dorsal regions were found in most of the patients. This partially coincided with a previous case report [7]. Due to the small number of the subjects explored up to now, no statistical significance was found. The vPSV might improve regional lung mechanics increasing aeration and ventilation homogeneity. Interquartile ranges of ΔEELV were relatively high. The previous case report suggested a possible recruitment effect, which may not be always the case.

References

[1] A Esteban, *et al. Am J Respir Crit Care Med*, 177: 170-7, 2008
[2] D Varelmann, *et al. Crit Care Med*, 33: 1968-75, 2005
[3] B Suki, *et al. Nature*, 393:127-8, 1998
[4] PM Spieth, *et al. Am J Respir Crit Care Med*, 179: 684-93 2009
[5] AR Carvalho, *et al. J Appl Physiol*, 110:1083-92, 2011
[6] M Miedema, *et al. Am J Respir Crit Care Med,* 194: 116-8, 2016
[7] T Mauri, *et al. Am J Respir Crit Care Med,* in press, 2017
[8] I Frerichs, *et al. Am J Respir Crit Care Med,* 174: 772-9, 2006
[9] Z Zhao, *et al. Intensive Care Med,* 35: 1900-6, 2009

Monitoring Ventilation and Perfusion in the liquid-ventilated lung

Étienne Fortin-Pellerin[1], Michaël Sage[1], Philippe Micheau[2], Julien Mousseau[2], Jonathan Vandamme[2], Mathieu Nadeau[2], Jean-Paul Praud[1], Andy Adler[3]

[1]Dept. of Pediatrics, Université de Sherbrooke, Canada, Etienne.Fortin-Pellerin@usherbrooke.ca
[2]Dept. of Engineering, Université de Sherbrooke, Canada
[3]Systems and Computer Engineering, Carleton University, Ottawa, Canada

Abstract: Total liquid ventilation (TLV) of the lungs provides lung lavage and gentle ventilation. EIT could provide real-time monitoring and allow precise control of TLV parameters. We report a preliminary EIT study in lambs of ventilation and perfusion during TLV perflubron filling. Results suggest more homogeneous ventilation with TLV and rapid blood flow redistribution to limits ventilation-perfusion anomalies.

1 Introduction

Total liquid ventilation (TLV) uses liquid perflubron instead of air for gas exchange. Since perflubron is dense ($\rho \approx 2$) it helps keep open dependent lung regions which would otherwise be collapsed (atelectatic) in pathologic conditions such as ARDS (adults) or hyaline membrane disease (neonates)[3]. Transition from air to liquid ventilation has many potential pitfalls. As Ventilated lung regions change from non-dependent to dependent, there is a risk of acute lung distention from the combined presence of air and liquid and blood redistribution to the ventilated area must occur.

We are motivated by the vision that EIT-based monitoring can identify and help avoid risks in the use of TLV. Our objective is to study the distribution of the volumes of air, perflubron and blood perfusion within the lungs using EIT. Our previous report studied EIT measurements of air and liquid volumes in one animal during the induction phase[1].

2 Methods and Results

Eight lambs (aged 2.4 ± 0.4 days, 3.2 ± 0.8 kg) were anesthetized and ventilated in a supine position using pressure controlled gaseous ventilation. Sixteen EIT electrodes were attached around the thorax and data acquired at 4.7 frames/s using the Sigmatome II EIT device. TLV was introduced using the Inolivent liquid ventilator prototype[2]. Perfusion was measured by a venous injection of a bolus of 7.9% saline solution during an apnea (Fig. 1).

Results were analysed to study the rate at which tidal ventilation and perfusion redistribute after the instillation of TLV. Representitive Ventilation (gas and TLV) and perfusion images from one lamb are shown in Fig. 2. Waveforms of global and vertical slices of ventilation are shown, along with images of tidal ventilation (V) and perfusion (P).

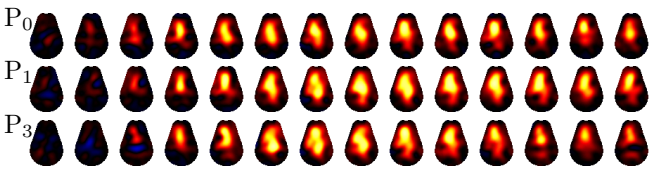

Figure 1: Time sequence of images of perfusion bolus through heart and lungs. Time progresses left to right with 400 ms between images.

3 Discussion

The distribution of ventilation/perfusion may be seen from these images by comparing images V_0/P_0 (gaseous ventilation), V_1/P_1 and V_3/P_3 (for liquid ventilation). Ventilation/perfusion matching is good and happens immediately after filling. However, the risk of overdistention was confirmed by this data and a slower filling protocol is now being used avoid this problem.

References

[1] A Adler, *et al*. Proc. EIT2016, Stockholm, p. 168, 2016.
[2] M Nadeau, *et al*. IEEE T Biom Eng, DOI:10.1109/TBME.2017.2671741
[3] MR Wolfson, TH Shaffer. *Paediatric anaesthesia*, 14:15–23, 2004.

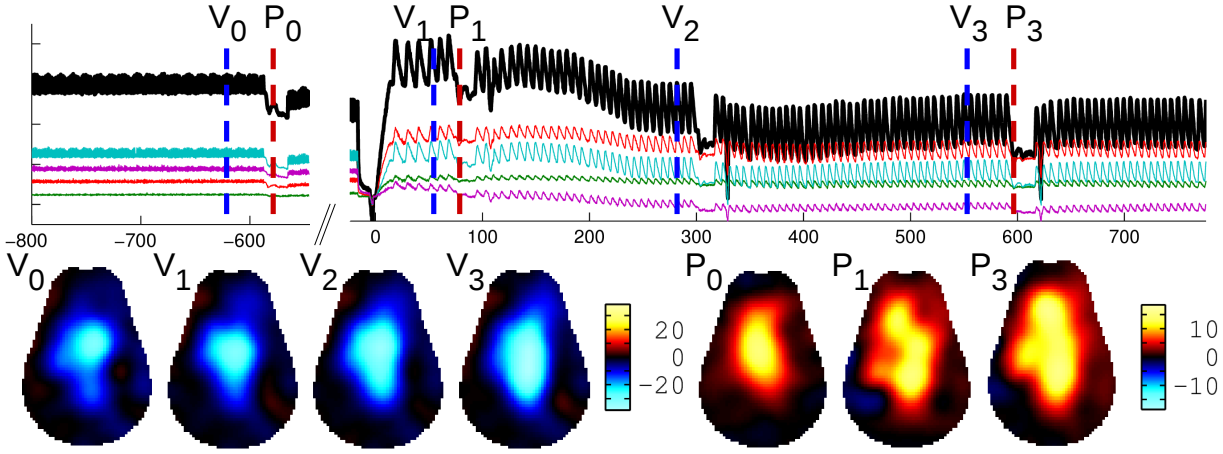

Figure 2: Example EIT waveforms and functional images showing the distribution of ventilation and perfusion in a slice of the thorax. Waveforms (vs. time (s) after the start of liquid ventilation) show global amplitude (black), and layers: green (ventral), red, blue, purple (dorsal). Images (blue, $\downarrow \sigma$, and red, $\uparrow \sigma$) show tidal ventilation (V) and perfusion (P) at the time instants shown.

Focusing EIT reconstructions using two electrode planes

Bartłomiej Grychtol[1], Johannes Peter Schramel[2], Ulrike Auer[2], Martina Mosing[3], Christina Braun[2], Andreas Waldmann[4], Stephan Böhm[4], Andy Adler[5]

[1]Fraunhofer PAMB, Mannheim, Germany
[2]Vetmeduni Vienna, Anaesthesiology and Perioperative Intensive Care Medicine
[3]School of Veterinary and Life Sciences, Murdoch University, Perth, Australia
[4]Swisstom AG, Landquart, Switzerland
[5]Systems and Computer Engineering, Carleton University, Ottawa, Canada, Andy.Adler@Carleton.ca

Abstract: EIT of the thorax has traditionally used a single electrode plane, and is sensitive to contrasts above and below the plane. It may be possible to improve (focus) the sensitivity using a two-plane placement of EIT electrodes. In this work, our objective is, first, to understand the impact of electrode placement and reconstruction parameter choices in simulations, and then to study these in experiments in horses. Pilot results show good images and slice sensitivity.

1 Introduction

Most clinical and experimental EIT studies for lung imaging have used a single plane of electrodes[1], which is sensitive to conductivity changes within about $\frac{1}{2}$ of the body diameter. This can interfere with EIT interpretation if image regions represent an average over a large volume, or if images are sensitive to out-of-plane effects such as movement of organs in the abdomen. To address both effects, 3D EIT reconstruction using two planes shows promising results [2, 3]. However, such work for lung EIT has mostly given example images, and not systematically evaluated how to choose various configuration details, or their robustness. Our *hypothesis* is that a 2-plane electrode placement for EIT can give improved 2D cross-sectional images, versus a single plane placement of the same number of electrodes. Here, we do not focus on 3D imaging; instead, we seek to take a first step: to see if two-plane electrode placement can give better 2D images.

We evaluated data measured from a horse model (Fig. 1A). Due to their size and specific anatomy, horse lungs are more exposed to gravity-related pressure changes during anaesthesia, and their large abdominal organs with huge amounts of gas lie, in a diagonal fashion, directly ventral to main parts of the lung. Thus, as the diaphragm moves backwards and forward during inspiration and expiration, air is moved in and out of the plane of interest. Clinically, equine asthma is a very common disease with enormous diagnostic challenges, which introduces patchy inhomogeneous changes to lung function. Better resolution would make EIT an improved diagnostic tool.

2 Methods and Results

For a pilot study, an EIT electrode belt was developed to allow combined placement of both: (1×32) 32 electrodes in a single plane, and (2×16) two planes of 16 electrodes, each separated by 12 cm from the single plane and arranged in a "square" pattern[2]. Using the Swisstom BBVet system, data were acquired during quiet tidal breathing and reconstructed with GREIT[2] for 1×32 (Fig. 1B), and then 2×16 (Fig. 1C).

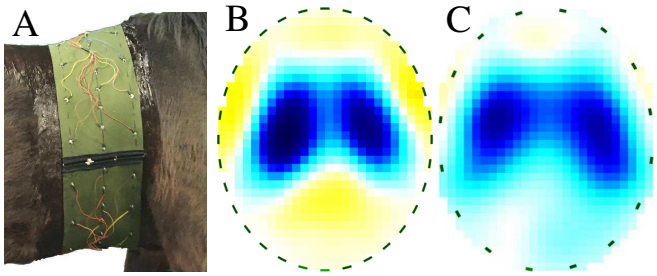

Figure 1: Horse with electrode belt system (A) and tidal ventilation images with 1×32 (B) and 2×16 (C) electrode configurations.

To understand the behaviour of a two-plane EIT, many details of the configuration need to be investigated, including: *1*) separation between planes, *2*) electrode stimulation and measurement pattern, *3*) regularization hyperparameter (via the noise figure, NF), and *4*) penalty for off-plane targets in the reconstruction. In Fig. 2, we study details *#1* and *#3*.

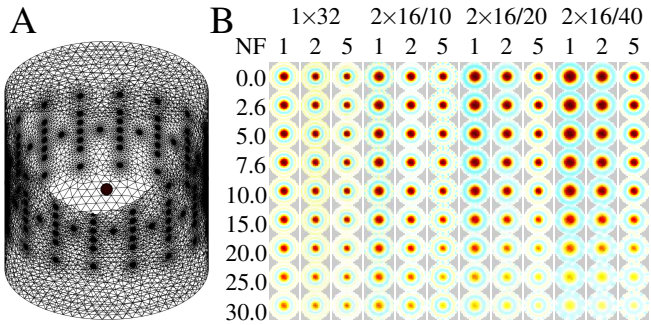

Figure 2: Off-plane rejection as a function of plane spacing (10, 20, 40 cm) and the hyperparameter (NF), using GREIT [2], and skip 4 square pattern. Images (B) show the central slice between the electrode planes in reconstructions of a small spherical target at various distances (in cm) above the cylindrical model centre (A) (h=100 cm).

We find that the 2×16 arrangement offers better off-plane contrast rejection than 1×32, with greater electrode plane separation producing greater improvement. At the same time, for the same NF, greater separation results in lower resolution.

3 Conclusion

Here, we study whether a 2×16 electrode configuration can outperform the traditional 1×32. Initial results appear promising, both in terms of robust images and improved rejection of off-plane contrasts.

References

[1] I Frerichs *et al Thorax*, 72:83–93, 2017.
[2] B Grychtol, B Müller, A Adler *Physiol Meas* 37:785–800, 2016.
[3] J Wagenaar, A Adler *Physiol Meas*, 37:922–937, 2016.

Detection of the aorta in electrical impedance tomography images without the use of contrast agent

Sarah Buehler[1], Karin H. Wodack[1], Stephan H. Böhm[2], Andreas D. Waldmann[2], Michael F. Graessler[1], Sarah Nishimoto[1], Florian Thürk[3], Eugenijus Kaniusas[3], Daniel A. Reuter[1], Constantin Trepte[1]

[1]Department of Anaesthesiology, Centre for Anaesthesiology and Intensive Care Medicine, University Medical Centre Hamburg-Eppendorf, Hamburg, Germany, s.buehler@uke.de

[2]Swisstom AG, Landquart, Switzerland

[3]Institute of Electrodynamics, Microwave and Circuit Engineering, Vienna University of Technology, Vienna, Austria

Abstract: After detecting the aorta by aortic saline bolus injections, we now focused on characterizing aortic pixels in EIT images of cardiac-related impedance changes. We inspected the aortic regions within EIT images of ten pigs using isoconductivity lines. High pulsatility out to the 50% isoconductity level is a possible attribute to distinguish the aortic regions from the edges with low pulsatility.

1 Introduction

While time-based methods [1] and time- and space-based localization of the aorta during injection of a hypertonic saline bolus into the aortic arch [2] have proven to be successful, in particular the latter method is not suitable for clinical routine. However, due to the cyclic cardiac activity, EIT pixels representing the descending aorta undergo pulsatile changes in conductivity. For localizing the aorta without contrast media we aimed to characterize the pulsatile changes within the pixels formerly identified as representing the aorta by saline bolus injection (see Buehler et al. in this conference edition).

2 Methods

2.1 Study protocol

The study was approved by the local authorities for animal care (approval no. 70/11). The ten pigs analyzed in our study were part of a larger project. In those anesthetized and mechanically ventilated animals, EIT data obtained with the EIT Pioneer Set (Swisstom AG, Landquart, Switzerland) during short phases of apnea and CT images of the thorax were available. Heart rhythm was continuously assessed by electrocardiography (ECG).

2.2 Image reconstruction and aorta localization

For each animal we used a segmented CT image taken at the electrode plane to build an individual finite element model. Image reconstruction parameters of the Graz consensus reconstruction algorithm for EIT (GREIT, [3]) were tuned to the specific requirements of aorta localization (see abstract of Buehler et al. in this conference edition). We used a prominence peak method [2] to localize the aorta during bolus injection. These aortic pixels were further inspected during phases of apnea without the presence of intravascular contrast media.

2.3 Isoconductivity lines

The cross-sectional appearance of the aorta on the EIT-images during apnea was explored by identifying isoconductivity lines at the 95%, 90% and 50% level of the previously defined aortic pixel. As a reference we 1) inspected the signal from pixels on the far edges of the thorax and 2) checked for synchrony of the pulsatility around the aortic pixel and the ECG signal (figure 1).

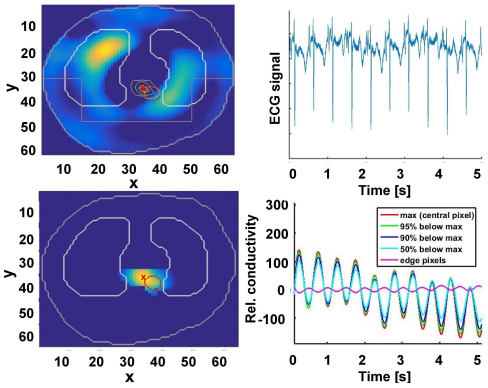

Figure 1: Top left: representative EIT image during apnea of one animal. Thorax and lung contours from CT segmentation are drawn in grey, the anatomical position of the aorta is delineated by the red circle. The aortic pixel identified by the bolus injection is shown as a red cross. The dark grey line shows the reference area of "edge pixels". Top right: ECG of the animal. Bottom left: prominence image. For markers see top left panel. Bottom right: Mean conductivity in the areas between the isoconductivity lines as well as in the edge pixels.

3 Results and Conclusions

We found closely spaced contours around the aortic pixel in all animals. The frequency of the observed pulsatility was in the same range as the ECG signal (figure 1). The difference between the mean conductivity within the 50% isoconductivity level and the edge pixels was significant ($p<0.05$). Knowledge of this characteristic appearance of the aorta is a prerequisite for an automated detection of the aortic pixels on EIT images without the use of intravascular contrast media.

References

[1] Sola S, Adler A, Santos A *Med Biol Eng Comput*, 49:409–415, 2011

[2] Thuerk F, Waldmann DA, Wodack KH *Conf 16th ICEBI & 17th EIT*, p.121, Stockholm, Sweden, Jun 2016 Jun 2016

[3] Adler A, Arnold JH, Bayford R *PhysiolMeas,* 30:35–55, 2009

Measurement Strategies for Heart Focused Dual Belt EIT

Jakob Orschulik, Tobias Menden, Steffen Leonhardt, Daniel Teichmann

Philips Chair for Medical Information Technology, Helmholtz Institute for Biomedical Engineering, RWTH Aachen University, Aachen, Germany, orschulik@hia.rwth-aachen.de

Abstract: In this paper, we present the results of a simulation study to determine measurement strategies for dual belt electrical impedance tomography. The idea is to use two electrode belts with 16 electrodes per belt to reconstruct images at different heights. Additionally, we aim to use an adjusted injection and measurement pattern in order to focus the sensitivity of the impedance measurements to specific regions of interest.

1 Introduction

In current setups, EIT images are recorded using one electrode belt positioned at a defined height, typically in the intercostal space between the 4^{th} and the 6^{th} ribs. The number of electrodes varies from 8 to 32 electrodes. Additionally, current systems usually use the *adjacent* injection and measurement pattern which has two main problems: First, it has been shown before that the sensitivity of this pattern is high close to the surface and low in the center of the body making the reconstruction challenging [1]. Second, images are only reconstructed in one image plane at the height of the electrode belt. These two points can be addressed using two electrode planes leading towards 3D-EIT. For this, studies regarding injection and measurement pattern as well as image reconstruction were performed [2–5]. In this paper, we present the results of a simulation study in which we aim at focussing dual belt EIT measurements to the heart region.

2 Methods

Our evaluation criteria are based on the term of the electrical sensitivity. In general, the sensitivity S of a single four-terminal measurement i in a given point ν can be calculated as

$$S_i(\nu) = \vec{J}_{LE,i}(\nu) \cdot \vec{J}_{LI,i}(\nu), \tag{1}$$

where $\vec{J}_{LE,i}(\nu)$ is the normalized current density distribution of the lead field and $\vec{J}_{LI,i}(\nu)$ the normalized current density distribution of the measurement electrodes [6]. The sensitivity can be both positive and negative. In areas with positive sensitivity, an increase in conductivity results in a lower measured impedance and vice versa. Each measurement i has an individual sensitivity distribution. In EIT, however, typically $l = n \cdot (n-3)$ bioimpedance measurements are performed in systems with n electrodes. Nevertheless, we are interested in determining the best overall sensitivity distribution for a given injection and measurement pattern. Thus, we define the overall sensitivity in a given point ν of a complete EIT measurement as the sum of the absolute sensitivities:

$$S_{EIT}(\nu) = \sum_{i=0}^{l} |S_i(\nu)|. \tag{2}$$

Next, we define the selectivity for a given Region of Interest (ROI):

$$Sel_{ROI} = \frac{\sum_{\nu \in ROI} S_{EIT}(\nu)}{\sum_{\nu} S_{EIT}(\nu)}. \tag{3}$$

Here, the ROI was chosen to be the heart (see Fig. 1, left).

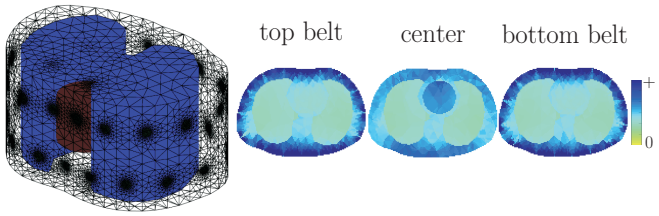

Figure 1: Finite-Element model used in this study (left) and sensitivity distribution in three image planes (right).

3 Results and Discussion

The results were computed using the EIDORS framework [7]. A total of 64 sensitivity distributions were calculated for both single and dual belt configurations. The best selectivity in the heart area was achieved using a skip-14 dual belt configuration in which the top and bottom belt were rotated to each other, as shown in Fig. 1, left. Fig. 1, right, shows the sensitivity distribution in three image planes. Compared to the single belt *adjacent* pattern, the heart selectivity was amplified by a factor of 14.2. However, restrictions apply to these results. First of all, no noise or other disturbances such as electrode displacement or conductivity changes were modeled. Furthermore, in order to perform a successful image reconstruction, not only the total sensitivity distribution of a complete EIT measurement, but also the sensitivity distributions of the l single impedance measurements have to be analyzed.

4 Conclusions

In this paper, we showed that a amplification of the cardiac signal can be achieved in EIT by using adequate injection and measurement pattern. While restrictions apply, we are convinced that different pattern than the *adjacent* method should be used to achieve high sensitivities in the central body areas.

References

[1] Adler A, Gaggero PO, Maimaitijiang Y. *Physiological Measurement* **32**(7):731–744, 2011
[2] Metherall P, Barber DC, Smallwood RH, et al. *Nature* **380**(6574):509–512, 1996
[3] Graham BM, Adler A. *Physiological Measurement* **28**(7):S29–S44, 2007
[4] Wagenaar J, Adler A. *Physiological Measurement* **37**(6):922–937, 2016
[5] Grychtol B, Müller B, Adler A. *Physiological Measurement* **37**(6):785–800, 2016
[6] Geselowitz DB. *IEEE Trans Biomed Eng* **18**(1):38–41, 1971
[7] Adler A, Lionheart WRB. *Physiological Measurement* **27**(5):S25–S42, 2006

Rapid Generation of Subject-Specific Thorax Forward Models

Andrew Tizzard[1] and Richard Bayford[1]

[1]Faculty of Science and Technology, Middlesex University, Hendon, London, UK, a.tizzard@mdx.ac.uk

Abstract: For real-time monitoring of lung function using accurate patient geometry, shape information needs to be acquired and a forward model generated rapidly. This paper shows that warping a cylindrical model to an acquired shape results in meshes of acceptable mesh quality, in terms of *stretch* and aspect ratio.

1 Introduction

Work has previously been undertaken on generating subject-specific meshes for EIT of brain function [1, 2], breast imaging [3] as well as investigating the effects of geometry for lung function [4]. Moreover, work has also been undertaken to develop a wearable device for real-time shape acquisition [5] . This paper presents some initial results for rapidly generating subject-specific forward models potentially in real-time, with minimal reduction in mesh quality. Mesh quality can be defined in a number of ways, e.g. σ and τ [6]. Historically, *stretch*, has been also used as a quality measure:

$$s = \sqrt{24}/\sigma = \sqrt{24}\left(r_i/l_{max}\right) \quad (1)$$

where r_i is the inscribed radius of the element and l_{max}, the maximum edge length. The scaling factor normalises the value to between 0 and 1. Another quality measure is *aspect ratio*, τ, often used by stress analysts, and is the ratio of longest to shortest edge lengths; a significant number of elements with values of $\tau > 5$ is generally considered unacceptable [7].

2 Methods

A surface model of a neonate thorax was generated using methods similar to those described in [8] and the resulting Non-Uniform Rational B-Spline (NURBS) surface used for warping cylindrical and elliptic cylindrical meshes to the surface, which were generated using *Netgen*.

Cylinder position and dimensions were determined by averaging points on the NURBS surface to estimate major and minor axes of the ellipse or the radius of the cylinder. Cylinder height was restricted to the proposed size of the wearable device: from the base of the model to just beneath the arms or 100 mm. The boundary nodes (excluding top and bottom planes) were orthogonally projected to the surface using the algorithm described in [2] and [9] to determine displacements for the mesh warping described in [2] to be carried out (Figure 1).

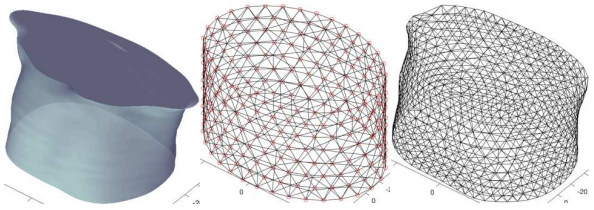

Figure 1: Surface, elliptical cylinder and warped mesh.

Three cylindrical meshes with 60, 477 and 2547 elements and three elliptical meshes with 282, 1924 and 8231 elements were used The quality parameters s and τ were measured before and after warping.

3 Results

Table 1: Statistics for cylindrical element quality. Medians (η) before and after warping and the median of differences (Diff η) with Wilcoxon p values compared to hypothesised median of 0.

	N	τ		s		Wilcoxon τ		Wilcoxon s	
		η	Max	Min	η	Diff η	p	Diff η	p
before	60	1.670	2.276	0.526	0.659	0.115	<0.001	-0.030	0.001
after		1.758	2.733	0.472	0.619				
before	477	1.556	2.100	0.443	0.726	0.082	<0.001	-0.031	<0.001
after		1.630	2.270	0.376	0.696				
before	2547	1.458	2.333	0.428	0.755	0.076	<0.001	-0.03	<0.001
after		1.532	3.653	0.313	0.728				

Table 2: Similar statistics for elliptical elements

	N	τ		s		Wilcoxon τ		Wilcoxon s	
		η	Max	Min	η	Diff η	p	Diff η	p
before	282	1.630	2.819	0.321	0.653	0.016	0.011	-0.004	0.17
after		1.690	2.769	0.252	0.635				
before	1924	1.508	2.300	0.420	0.732	0.033	<0.001	-0.012	<0.001
after		1.537	2.457	0.376	0.723				
before	8231	1.499	2.296	0.436	0.743	0.032	<0.001	-0.011	<0.001
after		1.528	2.670	0.363	0.731				

4 Conclusions

Results show that while the difference in medians (Diff η) before and after warping for both τ and s are mostly significant ($p < 0.05$, Wilcoxon), there is minimal change to the maximum τ and minimum s after warping, indicating an acceptable mesh quality, particularly when using elliptical geometry.

5 Acknowledgements

This work is supported by the CRADL project with funding from the EU Horizon 2020 programme 2014-2018 under grant agreement No. 668259.

References

[1] A Tizzard, L Horesh *et al*. *PhysiolMeas* 26:251-261,2005
[2] A Tizzard, R Bayford *PhysiolMeas* 28:163-182,2007
[3] A Tizzard, A Borsic *et al*. *JPhysics:Conf Series* 224,2010
[4] R Bayford, P Kantartzis *et al*. *PhysiolMeas* 29:125-138,2008
[5] J Khor, A Tizzard *et al*. *PhysiolMeas* 35:1149-1161,2014.
[6] V Parthasarathy, C Graichen *et al*. *FiniteElemAnalDes*. 15:255-261,1994
[7] JT Mottram, CT Shaw, Using Finite Elements in Mechanical Design. McGraw-Hill,1996.
[8] A Adler, J Arnold *et al*. *PhysiolMeas*. 30:35-55, 2009
[9] S Hu, J Wallner *ComputAidedGeomDesig*, 22:241-260,2005.

Combination of Electrical Impedance Tomography and Forced Oscillation Technique: a new pulmonary diagnostics tool?

Chuong Ngo[1], Carlos Munoz[1], Steffen Leonhardt[1]

[1]Philips Chair of Medical Information Technology, Aachen, Germany, ngo@hia.rwth-aachen.de

Abstract: We investigated a new measurement modality by combining forced oscillation technique (FOT) and electrical impedance tomography (EIT). A measurement system which can perform both modalities simultaneously was developed. Measurements was conducted on male test subjects. Data analysis of the signal proposed the potential of this modality in regional pulmonary diagnostic.

1 Introduction

Forced oscillation technique (FOT), first introduced by Dubois et al. [1], is a pulmonary test to assess lung parameters over a frequency rang of 5 to 30 Hz [3]. Electrical impedance tomography is a noninvasive, real-time imaging technique which provides dynamical information about ventilation distribution of the lungs [2]. We investigated the combination of the both modalities for additional information which might be useful in pulmonary diagnostics.

2 Methods

We developed a measurement system consisting of a FOT device (Philips Respironics, Pittsburgh, Pennsylvania, USA), a PulmoVista 500 (Dräger, Lübeck, Germany), and a linear pneumotach 370 (Hans Rudolph, Kansas, USA) including flow and pressure sensors. Sinusoidal waves were generated to have an amplitude of $4\,\mathrm{cmH_2O}$ and frequencies between 3 and 20 Hz. Simultaneously, EIT data as well as flow and pressure at the airway opening were captured by the PulmoVista 500 and the pneumotach, respectively. Measurements were performed on lung healthy male subjects.

Measured EIT data were synchronized and scaled by pneumotach data. Fast Fourier transform was applied to investigate the frequency spectrum of the EIT signals. A damping coefficient $E_{\mathrm{os}}(f_{\mathrm{os}})$ was derived as the ratio between the FFT oscillation peak in EIT and flow sensor signal, scaled by that ration during spontaneous breathing. To investigate the regional response of the lungs on the high frequency oscillation, a restrictive bandpass-filter was applied on the EIT signals.

3 Results

Figure 1 shows the fast Fourier transform of the EIT response on a 5 Hz wave applied by FOT. This indicates the ability of EIT to capture fluctuation at higher frequency. The damping coefficient $E_{\mathrm{os}}(f_{\mathrm{os}})$ reaches its maximal value in the frequency rang 4-6 Hz and falls sharply after 10 Hz.

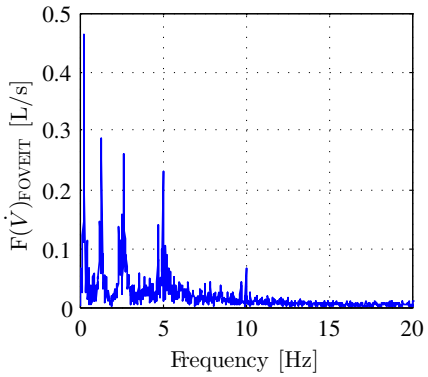

Figure 1: Fast Fourier transform of an EIT response on a FOT fluctuation at 5 Hz. The peak at 5 Hz indicates the visibility of the oscillations.

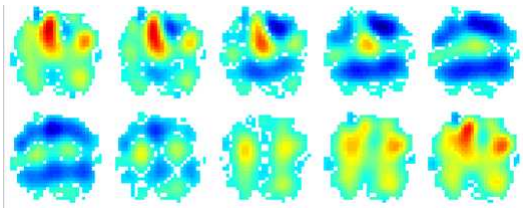

Figure 2: A sequence of bandpass-filtered EIT data.

Figure 2 illustrates a sequence of the EIT data measured on a test subject at 5 Hz FOT frequency. The result demonstrates different phases of the ventilation distribution in the lungs. While left-right homogeneity can be observed during one phase, ventilation seems to be strongly inhomogeneous in the other phase.

4 Conclusions

A combination of EIT and FOT may provide new aspect of regional diagnostics. The fluctuations at higher frequencies are visible in EIT data. Bandpass-filtered EIT images might become new tool for the investigation of regional lung mechanics at higher frequencies.

References

[1] A. DuBois, A. Brody, D. Lewis, and B. Burgess. Oscillation mechanics of lungs and chest in man. *Journal of Applied Physiology*, 8:587–594, 1956.

[2] S. Leonhardt and B. Lachmann. Electrical impedance tomography: the holy grail of ventilation and perfusion monitoring? *Intensive care medicine*, 38(12):1917–1929, 2012.

[3] E. Oostveen, D. MacLeod, H. Lorino, R. Farré, Z. Hantos, K. Desager, and F. Marchal. The forced oscillation technique in clinical practice: methodology, recommendations and future developments. *European Respiratory Journal*, 22(6):1026–1041, 2003.

Cardio-Respiratory Gated Electrical Impedance Tomography for Monitoring Stroke-Volume

Saaid H. Arshad[1], Ethan K. Murphy[1], and Ryan J. Halter[1,2]

[1]Thayer School of Engineering, Dartmouth College, Hanover, NH, USA, eit2017@dartmouth.edu
[2]Geisel School of Medicine, Dartmouth College, Hanover, NH, USA

Abstract: This work explores a novel breath-gating technique to reconstruct electrical impedance tomography (EIT) images of the heart without requiring a breath-hold. Data was collected on healthy volunteers performing breath-holds and regularly breathing. Reconstructions were compared between the breath-hold and regular breathing data sets for visual and quantitative validation.

1 Introduction

Stroke volume (SV) is the volume of blood pumped out by the heart every beat and is an important indicator of cardiovascular health [1]. Current methods of monitoring SV do not provide the capability of easy long-term and continuous monitoring to yield reliable information for clinicians to deliver proactive healthcare. An Electrical impedance tomography (EIT) device is proposed that can non-invasively monitor SV and meet the aforementioned criterion. Previous work has demonstrated the sensitivity of this device to clinically significant changes in SV through a simulation study [2]. The objective of this work is to demonstrate a novel breath-gating technique that will allow for passive monitoring of SV using EIT without requiring patients to perform a breath-hold.

2 Methods

2.1 Data Collection

Data was collected on 5 healthy volunteers. EIT data was collected using a 32-channel SwissTom Pioneer Set with electrodes positioned on the thorax two inches above the nipple plane (T4). Heart-rate data was collected using a pulse oximeter (PO). 3D reconstructions are computed with a standard Gauss-Newton EIT algorithm using the dual-mesh method.

2.2 Breath-Gating

The PO signal was synchronized with the EIT data using an external trigger and localized where end-diastole (ED) and end-systole (ES) occurred in the EIT data. Figure 1a shows the data used for breath-gating. The measure of SV is defined as a scaled version of the change in EIT-based heart area between ED and ES, shown by the high conductivity yellow regions in the top center-left of Figures 1b, 1c, and 1d. A simulated model was used to model blood perfusion into and out of the heart and lungs at ED and ES. The difference reconstruction is shown in Figure 1b. Figure 1c shows a visually similar image reconstructed from data collected on a human volunteer performing an exhaled breath-hold. To produce the image in Figure 1d, all ED and ES points in a data set are found, as shown in Figure 1a. Instead of differencing an ED and ES EIT frame, as is done for data in an exhaled breath-hold, each ES frame is matched with an ED frame that falls closest to it in the breathing cycle, meaning the smallest average voltage difference on the blue curve in Figure 1a.

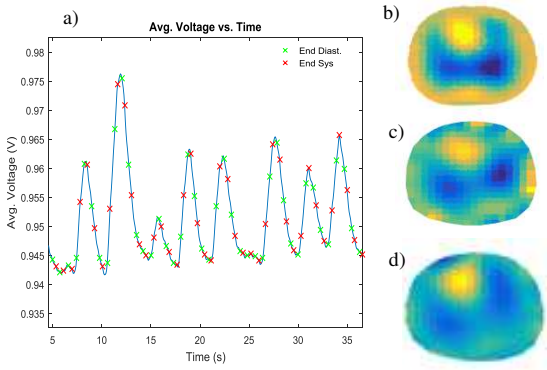

Figure 1: a) The blue curve represents the average voltage across all electrodes on the thorax and approximates a volunteer's breathing. ED and ES are localized from the PO data. The ED and ES points that minimize the average voltage difference are used to reconstruct images representing SV. b) A SV image from a simulated model. c) A SV image from volunteer 3's exhaled breath-hold data. d) A SV image from volunteer 3's regular breathing data after breath-gating.

3 Conclusions

The number of reconstructions possible for each data set depended on the number of ED and ES localized. 'Good' quality reconstructions were visually, manually classified as those that approximated Figure 1b, and that also fell within a consistent conductivity range of -3E-4 and 3E-4 S/m. Figures 1c and 1d show some ideal reconstructions from real data. On average over volunteers 1, 3, and 4, ~30% of the reconstructions possible from the regular breathing data yielded reconstructions that resembled Figures 1b-1c and fell within the aforementioned conductivity range.

4 Acknowledgements

This study was financially supported by Funding Source: NSF (SCH-INT) 1418497.

References

[1] Alhashemi, J. a, Cecconi, M., & Hofer, C. K. (2011). Cardiac output monitoring: an integrative perspective. *Critical Care (London, England)*, *15*(2), 214. https://doi.org/10.1186/cc9996

[2] Arshad, S. H., Murphy, E. K., & Halter, R. J. (2016). Respiratory-gated electrical impedance tomography: A potential technique for quantifying stroke volume. *Progress in Biomedical Optics and Imaging - Proceedings of SPIE*, *9788*, 0–3. https://doi.org/10.1117/12.2216595

Electrical impedance tomography in on-chip integrated microtubular fluidic channels

Sonja M Weiz[1], Mariana Medina-Sánchez[1], Kyounghun Lee[2] and Oliver G Schmidt[1,3]

[1]Institute for Integrative Nanosciences, IFW Dresden, Dresden, Germany, m.medina.sanchez@ifw-dresden.de

[2]Department of Computational Science & Engineering, Yonsei University, Seoul, Korea

[3]Material Systems for Nanoelectronics, Chemnitz University of Technology, Chemnitz, Germany

Abstract: A tubular electrical impedance tomograph (EIT) with micrometric dimensions was fabricated by using rolled-up nanotechnology. This approach gives access to EIT devices with tunable sizes in the sub-100 µm range. EIT images of silicon dioxide microparticles were obtained as proof of principle. These devices could enable the impedimetric analysis of biological micro-scale objects, such as single cells or small cell clusters.

1 Introduction

In recent years, there has been a growing interest in the analysis of single cells. Single-cell studies give valuable insights in the variability of biological cells in one and the same cell population, and can give new information about their fundamental properties.[1] Impedance measurements are especially well-suited for these analyses, as they are label-free and non-destructive. Tomographic measurements in particular are of interest since they can additionally provide spatial information in real time.

EIT studies of single cells call for appropriate measurement chambers, whose sizes should be similar to that of the object to be studied. This can easily be achieved using rolled-up nanotechnology.[2]

2 Methods & Results

Tubular EIT devices with diameters of approximately 35 µm and an integrated array of electrodes on the inner tube circumference were fabricated from strain-engineered thin films (see Fig. 1a). Successive steps of 2D photolithography and e-beam depositions were carried out to pattern a germanium sacrificial layer, a strained titanium dioxide bilayer, a chrome/gold electrode layer and a final insulating silicon dioxide layer which defines the active electrode areas. By selectively removing the sacrificial layer in a diluted hydrogen peroxide solution, the strained layer bends and rolls, resulting in a tubular configuration.

The tubular geometry provides a number of advantages. Firstly, the confinement mimics the cell's physiological environment, thus leading to *in vivo*-like measurement conditions.[3] Furthermore, compared to a planar layout an increase in electrode sensitivity is observed.[4,5] Additionally, the geometry lends itself readily for integration into microfluidic channels.

Measurements were carried out using an 8-channel EIT system (Sciospec Scientific Instruments). The samples were immersed in 1X PBS, and an SiO_2 microparticle with a diameter of approximately 15 µm was introduced into the rolled-up EIT device with a micromanipulator. The time-difference EIT image which is shown in Fig. 1b was obtained using a fidelity-embedded regularization (FER) method[6] with adjacent current injection (20 µA at 10 kHz).

The EIT image shows that the presence of the particle in the microtube can be detected. There is a slight deviation from the spherical particle shape, which is attributed to the asymmetry of the microtube, leading to a deformation of the measurement chamber. Design and fabrication optimization is being carried out to ensure a straight rolling in future devices.

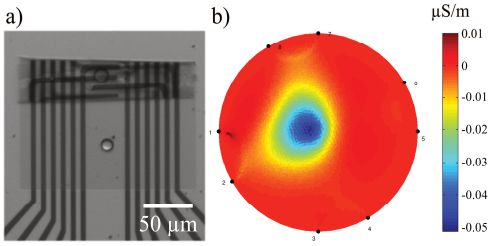

Figure 1: a) Optical microscopy image of an SiO_2 microparticle inside a rolled-up EIT device. b) EIT image of the particle showing the relative conductivity change.

3 Conclusions

An EIT image was obtained for an SiO_2 microparticle phantom employing a micrometer-scale EIT device fabricated by rolled-up nanotechnology. Further experiments will be required to determine the device's spatial resolution and determine the optimum frequency range. In the future, measurements will be carried out to study the behavior of single cells towards external stimuli, e.g. drugs or implant materials.

4 Acknowledgements

The authors would like to express their gratitude to Barbara Eichler, Dr. Helmut Siegel, Holger Günther, Sandra Nestler and Ronny Engelhard for technical support.

References

[1] S. J. Altschuler, L. F. Wu, *Cell* 141:559-563, 2010

[2] O. G. Schmidt, K. Eberl, *Nature* 410:168, 2001

[3] B. Koch, A. K. Meyer, L. Helbig, S. M. Harazim, A. Storch, S. Sanchez, O. G. Schmidt, *Nano Lett.* 15:5530-5538, 2015

[4] C. S. Martinez-Cisneros, S. Sanchez, W. Xi, O. G. Schmidt, *Nano Lett.* 14:2219-2224, 2014

[5] M. Medina-Sanchez, B. Ibarlucea, N. Perez, D. D. Karnaushenko, S. M. Weiz, L. Baraban, G. Cuniberti, O. G. Schmidt, *Nano Lett.* 16:4288-4296, 2016.

[6] K. Lee, E. J. Woo, J. K. Seo, *arXiv:1703.01821 [math.AP]* 1-16, 2017.

A wearable EIT system based on cooperative sensors

Michael Rapin[1,2], Fabian Braun[1,3], Josias Wacker[1] and Olivier Chételat[1]

[1]CSEM SA, Neuchâtel, Switzerland, mir@csem.ch
[2]ETHZ, Laboratory for Orthopaedic Biomechanics, Zürich, Switzerland
[3]EPFL, Signal Processing Laboratory (LTS5), Lausanne, Switzerland

Abstract: Most of the currently available EIT systems are limited by the number of electrodes, their position and/or the stimulation pattern. In view of overcoming these limitations we have developed a fully wearable EIT system based on cooperative sensors which allows for (a) a variable number and positioning of the electrodes, (b) an adjustable stimulation pattern, (c) fully parallel current injections, (d) synchronous ECG recording. Its feasibility is demonstrated on preliminary measurements on a healthy volunteer.

1 Introduction

Cooperative sensors (CS) are a novel measurement architecture for acquiring biosignals based on active electrodes [1]. CS benefit from simplified connection requirements (no shielded or complex multi-conductor cables, no central electronic unit), which significantly simplifies their connection and integration in a garment and increases the wearing comfort. In this paper, we present a wearable CS system used to measure lung EIT signals synchronously with an ambulatory ECG.

2 Methods

As shown in Fig. 2, the CS architecture has three different types of sensors: 1) the master sensor, 2) type I sensors for EIT current injections and 3) type V sensors for measuring voltages. All sensors are linked together with two unshielded connections called reference wire (ref. wire) and communication wire (com. wire). The ref. wire sets the common reference potential for all sensors. Voltages (v_1 to v_{n-1}) are amplified, filtered and digitized onsite by the electronic circuit embedded in each type V sensor. Type V sensors simultaneously measure the ECG signal (between 0.05 and 150 Hz) and bioimpedance signals resulting from the EIT current injections (~50 kHz).

The com. wire is used for communication between the CS. Communication from the master sensor to the other sensors is performed via small high-frequency voltage impulses (~2 MHz) sent by u_{sync} and received as u_1 to u_n. Moreover, current sources i_1 to i_{n-1} allow the type V sensors to communicate with the master sensor to transfer the digitized signals [2]. Data are sent as current impulses and are read as i_{com}.

Fig. 1 shows an example of a wearable EIT monitoring system based on CS consisting of the master sensor (black sensor) and an EIT belt with 16 CS (8 for current injections and 8 for voltage measurements). In the present configuration, 64 impedance channels are measured at 80 fps and fully in parallel (via frequency multiplexing).

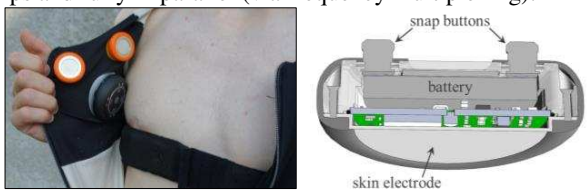

Figure 1: Wearable EIT belt integrated in a vest (left) and example of integration of a CS (right) with a diameter of 38 mm.

3 Results

This system was tested on one healthy male subject. Fig. 3 shows an EIT image sequence acquired during a normal breathing cycle and reconstructed using GREIT [3].

4 Conclusion

We presented a novel EIT system which is highly flexible (electrode position/number, stimulation pattern, parallel measurements, synchronous ECG). The system is fully wearable thanks to cooperative sensors, which are linked together with only two unshielded wires. While we have exemplified the capability of the system for lung EIT, future applications may include ECG-gated cardiovascular EIT or the continuous ambulatory monitoring of other organs.

References

[1] M Rapin, et al., *PhysiolMeas*, 36.4:767–783, 2015.
[2] M Rapin, et al., *MOBIHEALTH*, London, UK, 2015.
[3] A Adler, et al., *PhysiolMeas,* 30.6:S35, 2009.

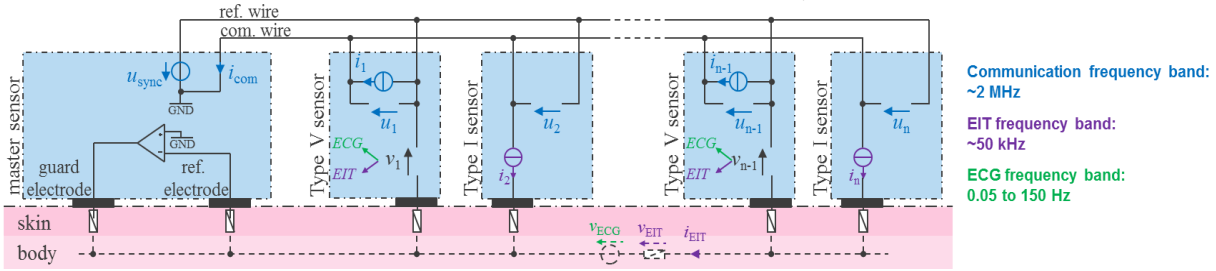

Figure 2: Architecture of the wearable EIT monitoring system based on CS.

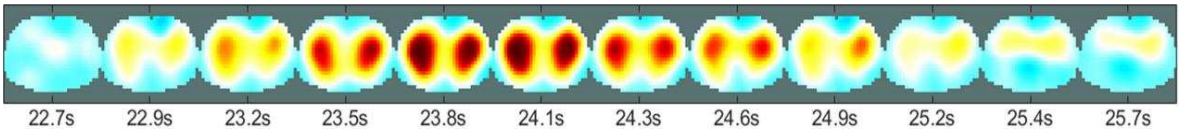

Figure 3: EIT impedance image sequence measured with the wearable EIT monitoring system during a normal breathing cycle.

Torso shape detection to improve lung monitoring

Serena de Gelidi[1], Andy Bardill[1], Yu Wu[2], Andreas Demosthenous[2], Andrew Tizzard[1], Richard Bayford[1]

[1]Middlesex University, London, United Kingdom, s.degelidi@mdx.ac.uk
[2]University College London, United Kingdom

Abstract: Two methodologies are proposed to detect the patient-specific boundary of the chest, aiming to produce a more accurate forward model for EIT analysis. Thus, a passive resistive and an inertial prototypes were prepared to characterize and reconstruct the shape of multiple phantoms. Preliminary results show how the passive device generates a minimum scatter between the reconstructed image and the actual shape.

1 Introduction

Preterm infants featuring lung immaturity require continuous monitoring in intensive care units. Therefore, the CRADL project is introducing the EIT technology as supportive care of the most common causes of paediatric respiratory failure (http://cradlproject.org/). Previous studies demonstrated that an accurate boundary form of the forward model is important to minimize artefacts in the reconstructed images [1]. The present study aims at assessing the patient-specific boundary of the torso without involving any radiation exposure. Thus, two different approaches are explored: the first is based on passive resistive devices, while the second adopts inertial sensors. Hence, the boundary shapes of some phantoms have been reconstructed by means of a specific algorithm for each approach. Lastly, the patient orientation is investigated by the inertial prototype.

2 Methods

Aiming to place the sensors around the torso of the infants, the prototypes have been designed like belts. Multiple phantoms have been created to model multiple chest cross-sectional areas.

2.1 Passive resistive prototype

The first prototype includes 4 conductive ink bend sensors (Flexpoint Sensor Systems Inc, US), arranged in a series and covering the entire length of the belt (320 mm). The sensors were biased by a voltage source. After amplification and digitization, the sensor outputs were sent to Matlab for further processing. In previous work [2], it was shown that a minimum of 8 bend sensors are required to generate an acceptable reconstruction of an ellipse. Thus, the algorithm has been optimized to reduce the number of sensors. Each bend sensor estimated a curvature radius, which is used by the Matlab algorithm to reconstruct the perimeter of the phantoms.

2.2 Inertial prototype

The second prototype uses inertial measurement units (IMU). Each IMU is a 9 degrees of freedom sensor utilising the LSM9DS1 system. Each IMU is addressed using an Inter-Integrated Circuit (I2C) data bus, via an 8 channel TCA9548A I2C Multiplexer. The I2C communication and data collection is enabled by an Arduino microcontroller, which passes the data to a pc via a serial link.

3 Results

The boundary shape detected by the passive resistive prototype is shown in Figure 1.

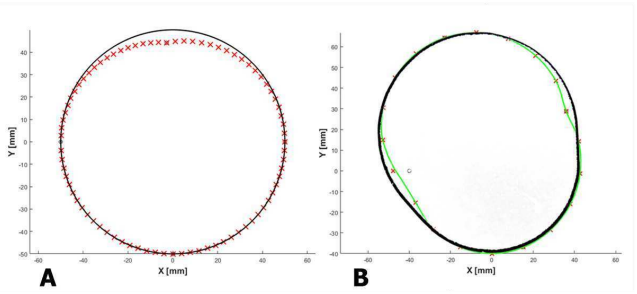

Figure 1: Boundary shape reconstruction (red crosses) obtained by means of the passive resistive prototype of A) circular and B) asymmetric phantoms (solid black lines). Green line represents a spline.

4 Discussion

Despite the limited number of bend sensors, the scatter between the actual shape and the reconstructed one is within few *mm* (Figure 1). A comparison between the results obtained by the two approaches will be addressed on the same sample. As an additional outcome of the study, an attempt to understand the patient orientation, without adding any other sensors, is going to be explored.

5 Acknowledgements

This work is supported by the CRADL project which has received funding from the European Union's Horizon 2020 research and innovation programme 2014-2018 under grant agreement No 668259. The authors would like to thank Mr Piotr Nowicki for assisting with the prototype development, Mr Joe Connick and Mr Kagan Rustem for preparing the phantoms.

References

[1] Bayford R H, Kantartzis P, Tizzard A, Yerworth R, Liatsis P, Demosthenous A. *Physiol Meas*, 29:S125–38, 2008

[2] Khor J M, Tizzard A, Demosthenous A, Bayford R H. *Physiol Meas*, 35:1149–61, 2014

Improved amplitude estimation of lung EIT signals in the presence of transients: Experimental validation using discrete phantoms

Wrichik Basu*[1], Michael G. Crabb[2], Peter M. Green[1], Paul Wright[1], and William R. B. Lionheart[2],
wrichik.basu@postgrad.manchester.ac.uk
[1]School of Electrical and Electronic Engineering, [2]School of Mathematics, University of Manchester, Manchester, UK

Abstract: In EIT systems that use a multiplexed excitation scheme, measured signals contain significant transients at switching. Typical Fourier methods for amplitude estimation of such signals incur extra time for settling and reduced accuracy. This paper presents results from an experimental validation of a novel method that achieves efficient and accurate amplitude estimation using model-based fitting.

1 Introduction

Lung EIT systems use an array of electrodes attached to the body surface at multiple positions along the torso. The double layer formed under each electrode and the dry skin immediately beneath it, together act as an R-C circuit in series with the electrode [1], as shown in Fig 1.

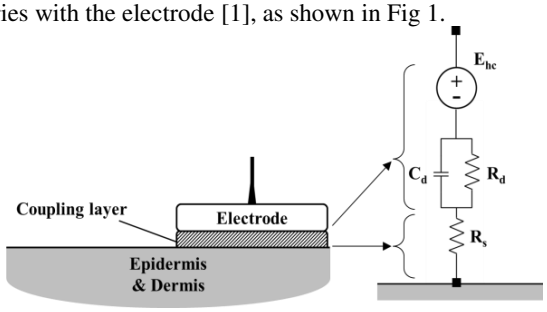

Figure 1: R-C model of skin-electrode interface impedance

As the current source is switched from one electrode pair to another [2], these effective R-C networks at the interfaces cause transients in the measured voltage signals. Since a typical mathematical model of EIT uses steady state data, these transients need to be eliminated from the measured signals before the voltage values can be input to a reconstruction algorithm. Traditionally, this has been done by allowing a period of settling time between switching and the onset of signal collection, and treating the subsequently collected signal as effectively steady state. Such an approach wastes valid sinusoidal signal information contained in the initial cycles, necessitates longer acquisition times by acquiring more than what is eventually used, and lacks accuracy since the used cycles are not truly free of transients. A method to estimate the transient and steady-state components through model-based fitting over the entire signal duration has been proposed [3], and this paper attempts to validate it with the help of data obtained from experiments performed on discrete phantoms.

2 Method

2.1 Experimental setup

A compact, FPGA-based, 6 channel prototype EIT system capable of simultaneous sampling is used for the experiments. The phantoms used in this study are of the common wheel architecture along with R-C networks in series with each channel to mimic the effect of skin-electrode interfaces, as shown in Fig 2. Values of R and C used in the interface models are selected in accordance with [1]. Adjacent pairwise excitation pattern [2] is used along with simultaneous sampling of differential voltages across all channels.

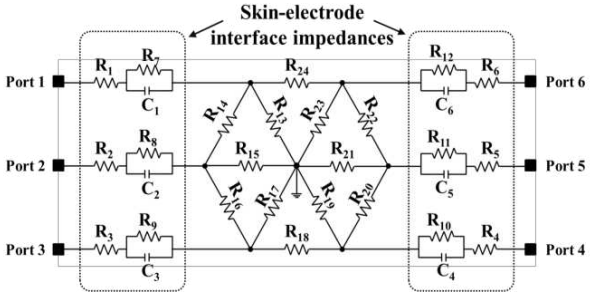

Figure 2: Wheel phantom with skin-electrode interface impedances modelled as R-C networks

2.2 Amplitude estimation

Due to bandwidth constraints, ADC output time-series values of the voltage signals are not available from the FPGA. After on-board processing of buffered samples, the output stream from the FPGA contains the following parameters for each measured cycle: D = DC component, I = in-phase component at frequency of excitation, Q = quadrature component at frequency of excitation, and S = RMS value. Assuming exponential transients, analytical expressions for the above are derived in terms of A = sinusoidal amplitude, φ = phase, B = transient magnitude, and τ = time constant. Next, an optimization problem is set up to solve for A and B, using a polynomial/exponential model as described in [3]. The solutions are then benchmarked against expected values as well as observed steady state values after settling, and compared against results from standard methods.

3 Conclusions

The model based estimation method is seen to estimate amplitudes and time constants satisfactorily with data from phantom experiments. Next steps in this project would be to carry out performance assessment *in vivo* and inference of electrode contact status from estimated interface impedances.

References

[1] YM Chi, T Jung, G Cauwenberghs *IEEE Rev Biomed Eng,* 3:106–119, 2010
[2] B H Brown, A D Seagar *Clin Phys Physiol Meas,* 8:A91-A97, 1987
[3] Crabb M, Green P, Wright P, Lionheart W *Conf 16th ICEBI & 17th EIT*, p.110, Stockholm, Sweden, Jun 2016

Influence of multiplexers and cables on bio-impedance measurements

Tobias Menden, Jakob Orschulik, Susana Aguiar Santos, Toni Tholen, Steffen Leonhardt, Marian Walter

Philips Chair for Medical Information Technology, Helmholtz-Institute for Biomedical Engineering, RWTH Aachen University, Pauwelsstr. 20, D-52074 Aachen, Germany, menden@hia.rwth-aachen.de

Abstract: Bioimpedance measurements may be afflicted with measurement errors due to common-mode voltage, stray capacitances and contact impedances [1]. This work investigates the influence of stray capacitances from cables and multiplexers, which are frequently used in Electrical Impedance Tomography (EIT)-setups these days. We show that the measurement error increases significantly with frequency, cable length and load.

1 Introduction

Nowadays, EIT systems with up to 64 electrodes and an increased frequency range up to 1 MHz are desirable [2]. Especially in multi-frequent EIT (mfEIT) systems, the phase of the signal may be measured under various frequencies. Semi-parallel and serial EIT systems use multiplexers to switch between injecting and measurement electrodes. This can result in a frequency- and load-dependent amplitude- and phase-shift, which may affect the mfEIT measurements. In this paper, we quantify and evaluate this influence for a 32 electrode system.

2 Simulation of 4-terminal measurements

The setup described in the introduction has been simulated in Simscape (with Simulink v8.7, MATLAB R2016a).

2.1 Simulation setup

The simulation consist of an ac current source (10 mA), which feeds multiplexers, cables and an ohmic load Z_{load}, as depicted in fig. 1.

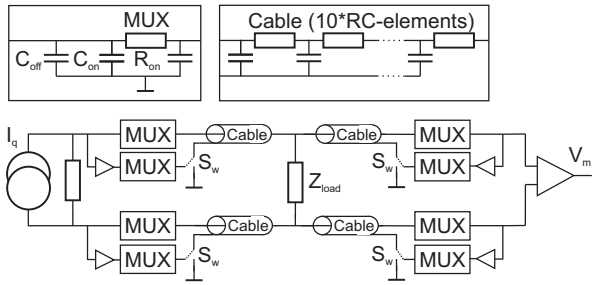

Figure 1: Model of a 4-pole measurement including cables and multiplexers. The cable-shield can either be grounded or driven by an active guard.

Each path of the 4-pole measurement is influenced by a multiplexer, the off-capacitance of the remaining 31 electrodes C_{off} and a cable. As an example we have chosen the ADG1404 multiplexer from analog devices and use equivalent resistance and stray capacitances given in the datasheet. Likewise we used a Belden RG174 coaxial cable, which is approximated with a series of RC-elements ($0{,}32\,\frac{\Omega}{\mathrm{m}}; 100\,\frac{\mathrm{pF}}{\mathrm{m}}$).

To solely consider the influence of cables and multiplexers, an ohmic resistance is used as the load Z_{load}. The influence of multiplexers and cables has been analyzed individually with different Z_{load} and cable length l in a frequency range from 10 kHz to 1 MHz. In addition, the switch S_w has been used to connect the shield to ground or to use an active guard. This paper focuses on the resulting phase shift, which is especially relevant for mfEIT.

2.2 Amplitude and Phase Error

Results for a load of $25\,\Omega$ and $75\,\Omega$ are shown in fig. 2. With a cable length of 0 m, multiplexers are the only modeled influence. The phase error increases rapidly from $0{,}8°$ to $8{,}2°$ in the range from 100 kHz to 1 MHz (solid line). Under a load of $75\,\Omega$ the effect is even bigger with an increase from $2{,}1°$ to $20{,}2°$ (dash-dot line). The increasing phase shift with an increasing load is reasonable under the assumption that the stray capacitances are parallel to the load. The additional phase shift caused by 1 m cable is in the range of 1 to $2{,}5°$ and increases slightly with load. An active guard could compensate most of the cable based errors down to $0{,}05°$.

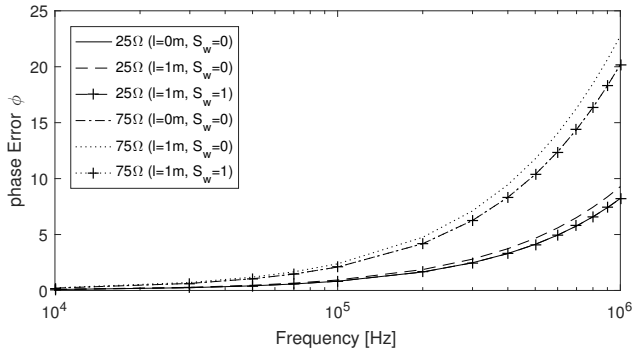

Figure 2: Phase error for $25\,\Omega$ (solid) and $75\,\Omega$ (dash-dot) load at 0 m and 1 m cable length (dashed, dotted) and active guard (+).

3 Conclusions

Multiplexers add a large frequency-dependent phase shift to bio-impedance measurements. In our simulation, the phase differences were between $0{,}8°$ and $20{,}2°$ from 100 kHz to 1 MHz. Hence, a measurement setup with multiplexers as described here may show significant errors in mfEIT. The usage of an active guard could reduces cable based errors significantly. In the future, different measurement approaches should be evaluated to calibrate or compensate this error.

References

[1] McEwan A, Cusick G, Holder DS. *Physiological Measurement* **28**(7):S197–S215, 2007

[2] Halter RJ, Hartov A, Paulsen KD. *IEEE Transactions on Biomedical Engineering* **55**(2):650–659, 2008

Cardiac Function Analysis using Electrocardiogram, Seismocardiogram and EIT Images

Hyuntae Choi[1], Junhwan Park[2], Tong In Oh[1] and Eung Je Woo[1]

[1]Department of Medical Engineering, Graduate school, Kyung Hee University, Seoul, Korea, tioh@khu.ac.kr

[2]Department of Biomedical Engineering, Graduate school, Kyung Hee University, Yongin, Korea

Abstract: Seismocardiogram (SCG) is represent vibration of the chest wall by the heart contraction and blood ejection. SCG signal is associated with cardiac function information that can be used to derive diagnostic relevant information about cardiovascular and cardiopulmonary health. On the EIT side, simultaneous measurement and analysis of SCG and ECG Signals are expected to present a new clinical direction for cardiac function.

1 Introduction

Continuous monitoring of cardiovascular system in a patient is important. Additionally, home health care requires the remote monitoring of physiological parameters for a normal subject. For these reasons, we have commonly used electrocardiogram (ECG) and seismocardiogram (SCG) to diagnosis of cardiac functions [1, 2]. Each signal has analysed with physiological events in the electrical and mechanical aspects of the heart function. Fast EIT images can provide the regional information related with blood perfusion changes in the heart and lung region. It would be very helpful to analyse cardiac function when interpreting ECG, SCG and conductivity changes together. In this study, we developed the multi-modal sensors and measurement module operated with KHU Mark2.5 EIT system to monitor cardiac function non-invasively [3].

2 Methods

Recent advances in technology have simplified the measurement and evaluation of SCG and ECG signals and can be easily detected with low-noise accelerometers and biopotential amplifiers. Multi-modal sensors and measurement module consists of low power ADC integrated Analog front-end circuits (ADS1291, Texas Instruments, USA), high sensitive accelerometers (MPU-9250, InvenSense, USA) and communication controller implemented in a FPGA as shown in Fig 1. Each signal is sampled at 250 SPS and transferred to the EIT system through the communication controller. Inside the communication controller, there were data arbitrator and double buffered memory. KHU Mark2.5 EIT system was operated with 50 frames/s. This module was positioned on the sternum where similar as other studies [4]. The location of electrodes for EIT images was in the 4th intercostal space. For this measurement, z corresponded to the dorso -ventral, y to the head-to-foot, and x to the right-to-left lateral components of the SCG.

3 Results

The amplitude of SCG is related to the function of left ventricle. Specially, Stroke volume and cardiac output influence the SCG signals. ECG can explain physiological events of the heart. In Fig 2, we displayed ECG waveform and SCG signal in the z direction synchronously. Those signals and EIT images were obtained while not breathing.

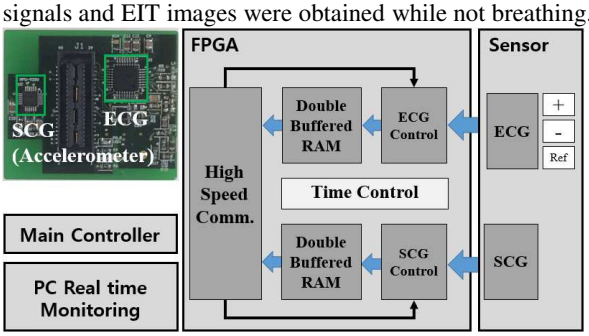

Figure 1: Multi-modal sensors and measurement module integrated with EIT system.

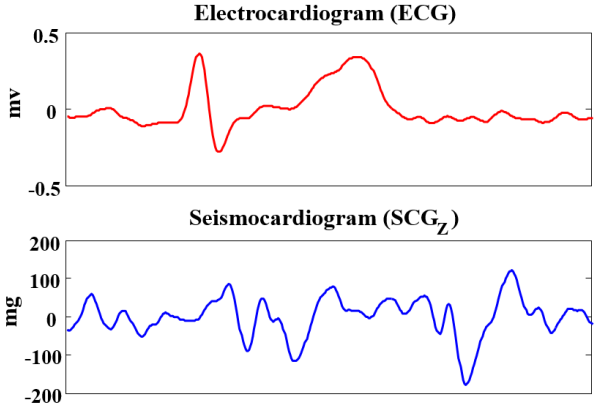

Figure 2: Simultaneously acquired Lead I ECG waveform and dorso-ventral axis seismocardiogram.

4 Conclusions

Fast EIT images was correlating with ECG and SCG waveforms and provided the regional information of blood perfusion in the heart. Integrated measurement parameters can be used as indexes to pre-screen patients for cardiac resynchronization therapy.

5 Acknowledgements

Research supported by Korean Health Technology R&D Project, Ministry of Health and Welfare, Republic of Korea (HI14C0743).

References

[1] Omer T. Inan, et.al *IEEE Journal of Biomedical and Health Informatics*, 99:1-1, 2015

[2] D T Nguyen, et.al *Physiol. Meas*., 33:695–706, 2012

[3] H. Wi, H. Sohal, L. M. Alistair, E. J. Woo and T. I. Oh *IEEE Trans Biomed Circuits Syst.* 8:119-128, 2014

[4] M. Di Rienzo, et.al *IEEE Annu. Int. Conf. Eng.Med, Biol. Soc*., 4263–4266, 2011

An Experimental Study for Magneto-Acousto Electrical Impedance Tomography using Magnetic Field Measurements

Keivan Kaboutari[1], Ahmet Önder Tetik[1], Elyar Ghalichi[1], Mehmet Soner Gözü[1], Reyhan Zengin[2], Nevzat Güneri Gençer[1]

[1]Department of Electrical and Electronics Engineering, Middle East Technical University, Ankara, Turkey ngencer@metu.edu.tr
[2]Department of Electrical and Electronics Engineering, Selçuk University, Konya, Turkey

Abstract: In this work, magneto-acousto electrical impedance tomography method is investigated experimentally. Experiments are conducted to measure conductivity gradient of bodies using magnetic measurements. A linear phased array transducer is used to generate pressure inside a phantom in a static magnetic field. Magnetic field intensity generated due to induced Lorentz currents is sensed using a coil. The pick-up voltages are on the order of mV.

1 Introduction

Magneto-Acousto Electrical Tomography (MAET) is one of the multiphysics method to image the electrical conductivity of biological bodies [1–3]. This is a hybrid imaging method based on electrical impedance and ultrasound imaging. In this method, body is in static magnetic field. An acoustic pressure is applied and Lorentz currents are induced in the body. The coils placed near the body are used to sense the resultant magnetic field intensity.

In this study, we prepared an experimental setup to measure the electrical conductivity gradient of an inhomogeneous phantom. Using a 16-element linear phased array (LPA) ultrasonic transducer (IMASONIC), acoustic pressure is generated inside the phantom in the existence of a static magnetic field. As a result of this, Lorentz currents are induced in the phantom. The magnetic field intensity is sensed by a coil placed near the phantom.

2 Methods

The experimental setup consists of a 16-element LPA ultrasonic transducer, a body phantom, a static magnetic field generator, a coil, a two-stage amplifier and a data acquisition system (Fig. 1 (a)). The transducer is driven with a 1 kHz burst signal. Each burst is 5 period of sinusoidal voltage (50 V_{pp} at 1 MHz). The resultant pressure amplitude is 500 kPa. The phantom consists of a conductive solution (70 S/m) and sunflower oil ($\approx$ 0 S/m) inside a cylindrical Plexiglas tube. The solution and oil are placed at the bottom and top of the Plexiglas tube, respectively (Fig. 1 (b)). Neodymium permanent magnets surrounded by a U shape iron core are used to produce inhomogeneous magnetic field distribution [4]. At the interface in the phantom, magnetic field is homogeneous and its value is 0.56 Tesla. Two layer coil has 4.15 cm mean diameter, 59 mm length and 33 turn number. This coil is connected to a two-stage amplifier with a high input impedance. Total gain of the amplifier is 100 dB. An oscilloscope (Agilent DS06014A, $R_{in} = 1M\Omega$, $C_{in} \approx 11pF$) used as data acquisition system.

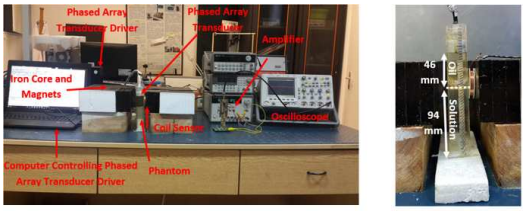

Figure 1: (a) Experimental setup for MAET method (b) Phantom.

3 Results

The distance between the surface of the transducer and oil-solution interface is 46 mm. Measuring sunflower oil's acoustic speed (1453 m/s), acoustic wave is expected to reach to the interface at 32 μs. Output signal of the coil is shown in Fig. 2. In this figure, MAET signal is at 32 μs which is consistent with the expectation.

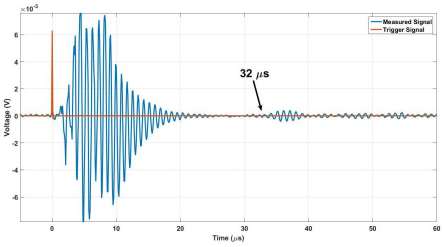

Figure 2: MAET signal from oil-solution interface at 32 μs.

4 Conclusions

Consequently with this setup, an inhomogeneity at a depth of 46 mm can be detected. The maximum voltage amplitude sensed by the coil is 0.8 mV. However, this signal level is obtained when conductivity of inhomogeneity was 70 S/m. Further studies are required to acquire data from more realistic body phantom.

5 Acknowledgements

This work is supported by The Scientific and Technological Research Council of Turkey (114E184) and COST Action BM1309 (EMF-MED).

References

[1] Montalibet A, Jossinet J, Matias A and Cathignol D, *Med. Biol. Eng. Comput.*, 39, 15–20, 2001.
[2] Guo L, Liu G and Xia H, *IEEE Trans. Biomed. Eng.* , 62, 2114–24, 2015.
[3] Zengin R and Gencer N G, *IOP Physics in Medicine and Biology*, 61, 5887-5905, 2016.
[4] Tetik A Ö, Ghalichi E, Kaboutari K, Gençer N G, *20th National Biomedical Engineering Meeting (BIYOMUT) (to be published)*, 2016.

MR-based Current Density Imaging during Transcranial Direct Current Stimulation (tDCS)

Nitish Katoch[1], S.Z.K Sajib[1], B.K Choi[1], Hyung Joong Kim[1], Oh In Kwon[2], and Eung Je Woo[1]
[1] Department of Biomedical Engineering, Kyung Hee University, Seoul, South Korea, ejwoo@khu.ac.kr
[2] Department of Mathematics, Konkuk University, Seoul, South Korea

Abstract: Estimation of current density distribution by electrical current stimulation inside anisotropic brain region can provide an alternative way for understanding the neuro-modulatory effect during transcranial direct current stimulation (tDCS). In this study, we reconstructed current density distribution of *in vivo* canine brain by combining the directional information obtained from a DTI-MRI scan and MREIT technique.

1 Introduction

Transcranial direct current stimulation (tDCS) is a neuro-modulatory technique for treating neuro-psychiatric diseases and neurological disorders. During tDCS, DC current is injected into the head through a pair of electrodes attached on the scalp. Therefore, imaging of the current density play an important role to understand the therapeutic effects. Lately, a proposed method [1] to visualize the current density distribution by combing directional information obtained from DT-MRI scan with the measured magnetic flux density data. In this paper, we report the results of animal experiment of current density imaging during tDCS.

2 Method

In this study, we perform the canine head imaging experiment. We anesthetized canine, after clipping hair we attached a pair of carbon-hydrogel electrodes and positioned inside the 8-channel knee coil equipped with our 3 T MRI scanner (Phillips Achieva, The Netherlands). We then collect the B_z data induce by 2 mA current injection at three slice position using T1-mFFE pulse sequence. The imaging parameters were set to TR/TE = 200/2.2 msec, echo spacing = 2.2 msec, voxel size = 1.1×1.1×4 mm^3. We also obtained DTI data with b-values of 1000 sec/mm^2 at the same three slice position using single-shot spin-echo EPI (SS-SE-EPI) sequence with TR/TE= 3000/67 msec.
The proposed method first estimate the model predicted current density ($\mathbf{J}^0$) and its corresponding z-component of the magnetic flux density (B_z^0) by solving the Laplace equation. In this step, the electrical conductivity tensor ($\mathbf{C}$) is assumed to be a scaler multiple of the water diffusion tensor($\mathbf{D}$), $\mathbf{C} = \eta_0\mathbf{D}$, where $\eta_0 = 0844$ S•sec/mm^3[2] comparing the error differences between the measured and the computed magnetic flux density data the proposed method iteratively update the current density distribution.

$$\mathbf{J}^{n+1} = \mathbf{J}^n + \frac{1}{\mu_0}\left(\frac{\partial(B_z - B_z^n)}{\partial y}, -\frac{\partial(B_z - B_z^n)}{\partial x}\right) \quad (1)$$

2.1 Results

Fig.1 (a)-(b) shows the acquired MR magnitude and B_z image induced due to 2mA current injection at the centre slice. The reconstructed color-coded fractional anisotropic map obtained from the DTI experiment was displayed in Fig.1(c). The reconstructed current density using equation (1) was shown in Fig. 1(d).

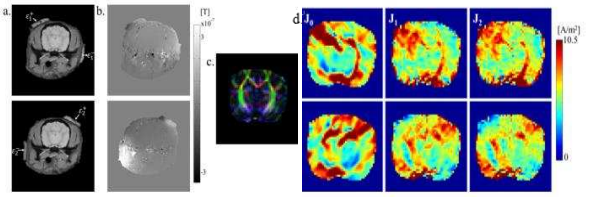

Figure 1: MR magnitude image (a) and acquired $\mathbf{B_z}$ data (b) induced by tDCS current injection. Colour coded fractional anisotropy map (c) obtain from DT-MRI. Reconstructed current density (d) at axial slice positions for electrode montage $\boldsymbol{\varepsilon_1^{\pm}}$ and for electrode montage $\boldsymbol{\varepsilon_2^{\pm}}$.

The measured current density values with in the chosen ROIs (Fig.2) at three different slice position and two different electrode montage were summarized in table-1.

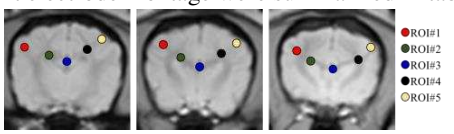

Figure 2: ROI assignment to measure the current density values

Table 1: Measured current density at five different ROIs (Fig.3) at two slice positions.

Slice	Electrode montage $\varepsilon_1^{\pm}$					Electrode montage $\varepsilon_2^{\pm}$				
	ROI#1	ROI#2	ROI#3	ROI#4	ROI#5	ROI#1	ROI#2	ROI#3	ROI#4	ROI#5
#1	7.37 ±0.85	7.92 ±1.20	6.49 ±1.64	7.08 ±1.65	5.40 ±1.17	4.03 ±0.49	5.67 ±0.50	5.63 ±1.11	7.40 ±1.73	8.22 ±1.01
#2	6.74 ±0.96	7.63 ±1.18	7.33 ±0.94	5.36 ±0.76	3.52 ±1.12	3.94 ±0.58	6.10 ±0.73	5.96 ±0.77	6.49 ±0.60	6.08 ±1.39
#3	8.05 ±1.20	4.51 ±0.97	6.50 ±1.95	4.40 ±0.86	5.10 ±0.86	4.98 ±0.72	4.90 ±0.81	7.39 ±0.89	4.35 ±0.48	7.33 ±1.06

3 Conclusion

For ensuring the clinical applications, effects of tDCS can be enhanced by localizing current flow and pathway into the targeted anatomical structure of the brain. Quantitative visualization of induced current density distribution in the brain will play an important role in monitoring the tDCS treatment.

4 Acknowledgement

This work was supported by the National Research Foundation (NRF) of Korea grants (No. 2014R1A2A1A09006320, 2015R1A5A1037656, 2015R1D1A1A09058104).

References

[1] Kwon O. I. *et al.*, *IEEE Trans. Biomed. Eng.*, article in press, 2015..
[2] Tuch D.S. et al., *Proc. Natl. Acad. Sci.*, 98, 11697-701, 2001.

Magnetic Flux Density Comparisons Between MREIT and FE Models

Christopher Saar[1], Aprinda Indahlastari[1], Aditya Kumar Kasinadhuni[2], Kevin Castellano[2], Casey Weigel[1], Bakir Mousa[1], Munish Chauhan[1], Thomas H Mareci[2], and Rosalind Sadleir[1]
[1]Fulton School of Engineering, Arizona State University, Tempe, AZ, USA rosalind.sadleir@asu.edu
[2]University of Florida, Gainesville, FL, USA

Abstract: MREIT can be used to recover *in-vivo* current density images from measured B_z data. Sensitivity studies based on these images can be used to validate computational model results. Our preliminary results here suggest that electrodes a quarter of the size suggested by electrode surface area, in combination with high skin conductivity values, produced the best match in B_z profile lines between MREIT results and tACS simulations.

1 Introduction

Many finite element modeling (FEM) studies attempt to model current distribution from transcranial alternating current stimulation (tACS) in the human head. but only a few have been validated against experiments [1-4]. Sensitivity studies can been used to compare FEM models to experimentally measured potentials, and to identify appropriate model tissue conductivity values [1-3]. Magnetic Resonance Electric Impedance Tomography (MREIT) can recover magnetic flux density (B_z) distributions in vivo [5]. These data can be compared with B_z data generated from models. Here we present a comparison of B_z distributions between MREIT in a human subject and FE models derived from the same subject, and determine the best combination of electrode-scalp contact areas and skin conductivity values to minimize differences.

2 Methods

MREIT and T1-weighted imaging were performed using a 3T scanner at the McKnight Brain Institute, University of Florida. MREIT data was acquired with a modifed Philips mFFE-ssfp pulse sequence in three axial slices (224x224, 2.24 mm resolution and 5mm thickness). During MREIT acquisitions, 1.5mA amplitude current pulses at 10 Hz were passed between two MRI safe 25cm^2 carbon electrodes placed at T7 and T8. Phase images from MREIT were processed and rescaled to B_z [4].

A realistic head model derived from the T1-weighted MRI dataset (256x256x256, 1mm^3 isotropic resolution) was segmented into ten tissue types following [4]. Each model was simulated in COMSOL-MATLAB Livelink interface using conductivity values typically used for tACS/tDCS FEM [4]. Three electrode sizes: large, medium and small with surface areas of 25, 16, 9 cm^2, respectively, were manually segmented in Simpleware, centered on original electrode locations. Three skin conductivity values were also modeled: 0.01 S/m [3] (C1), 0.43 S/m [4] (C2) and 0.8 S/m [1] (C3). Simulated B_z results were registered to MREIT B_z in MATLAB. B_z values were compared by drawing a profile line in each B_z distribution from anterior to posterior of the head. RMS values were calculated between MREIT and simulated B_z.

3 Results

Calculated RMS values were: $RMS_{L,C1}$=4.52nT, $RMS_{L,C2}$=0.91nT, $RMS_{L,C3}$=1.00nT, $RMS_{M,C1}$=4.73nT, $RMS_{M,C2}$=0.93nT, $RMS_{M,C3}$=0.98nT, $RMS_{S,C1}$=2.80nT, $RMS_{S,C2}$=0.93nT, and $RMS_{S,C3}$=1.04nT.

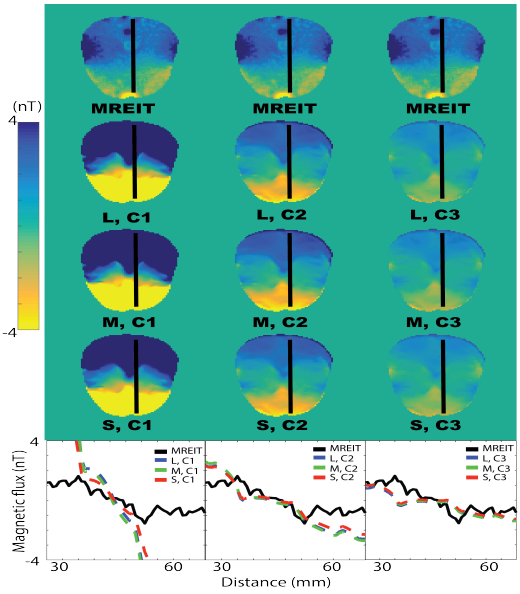

Figure 1. Comparisons of Bz between MREIT and simluation. Profile lines denoted by black lines drawn bottom to top overlaying the central slices of MREIT and FE models were compared. FE models were modified with a combination of small (S), medium (M) and large (L) electrode sizes and varied skin conductivity values (C1, C2, C3)

4 Conclusions

We compared MREIT B_z with simulated B_z with varying electrode surface areas and skin conductivity values. Reduction to electrode-scalp contact areas did not produce a considerable change while varying skin conductivities affected simulated B_z range. The smallest RMS values and closest profile lines were for simulation with C2 and C3 regardless modeled electrode size. This study provided an insight to previously modeled electrode areas and skin conductivity values in tACS. Further, B_z processing can produce current density and conductivity reconstructions. Thus our preliminary study can contribute to improvements in FEM predicting tACS and can be applied to other inverse source imaging applications.

References

[1] Huang Y, et al. *eLife*, **6**: 2017
[2] Santos L, et al. *IEEE 38th Annual EMBC* Aug 2016
[3] Parazzini M, et al. *IEEE Transactions on Biomedical Eng.* **58**:6:2011
[4] Indahlastari A, et al. *IEEE 38th Annual EMBC* Aug 2016
[5] Woo E, et al. *Physiological Measurement* **29**:10:2008

In-vivo Projected Current Density Reconstruction: Comparisons Between MREIT and FE Models

Aprinda Indahlastari[1], Christopher Saar[1], Aditya Kumar Kasinadhuni[2], Kevin Castellano[2], Casey Weigel[1], Bakir Mousa[1], Munish Chauhan[1], Thomas H Mareci[2], and Rosalind Sadleir[1]
[1]Fulton School of Engineering, Arizona State University, Tempe, AZ, USA rosalind.sadleir@asu.edu
[2]University of Florida, Gainesville, FL, USA

Abstract: MR electrical impedance tomography (MREIT) has been developed over the last decade to recover current density *in-vivo* from an induced magnetic field (B_z). In this study, we computed projected current density (J^P) distribution from MREIT B_z in a single subject during tACS session. Calculated J^P was compared to finite element models predictions derived from the same subject.

1 Introduction

Current injection during transcranial alternating current stimulation (tACS) can be captured *in-vivo* by using MREIT-CDI [1]. Recovered B_z from MREIT measurements can be converted to J^P by using a priori information in a uniform finite element model (FEM) derived from the imaged object [2]. We generated three-dimensional FE isotropic and anisotropic models of the human head to compute signal levels of electromagnetic fields from externally injected tACS currents [3]. In this study, we present a comparison of B_z and J^P in a single human head obtained from MREIT-CDI experiment and FEM simulation.

2 Methods

T1-weighted, DTI and MREIT datasets were acquired using a Philips 32-channel head coil in a 3T MRI Philips Achieva scanner at the AMRIS Facility at the UF McKnight Brain Institute. T_1-weighted and diffusion weighted MR data were used for generation of isotropic and anisotropic FE models.

For MREIT acquisitions, we employed a modified Philips `mffe` protocol to produce TTL-logic pulses that triggered a constant current (DC-STIMULATOR MR, neuroConn, Ilmenau, Germany) synchronously with the sequence. A total of 1.5 mA current pulses alternating at 10 Hz frequency was employed between a pair of MRI safe carbon electrodes (25 cm^2) in T_7-T_8 and F_{pz}-O_z configurations.

FEM of the subject's head were constructed from the T1-weighted MRI (256x256x256, $1mm^3$ isotropic resolution) following [3]. Each model was simulated in COMSOL-MATLAB Livelink interface using literature referenced conductivity values ($Wm_{isotropic}$=0.38S/m, GM=0.1 S/m, Eyes=0.5 S/m, Blood=0.67 S/m, Fat=0.025 S/m, Bone=0.0109 S/m, Muscle=0.16 S/m, CSF=1.8 S/m, Air≈0 S/m, Skin 0.43 S/m) [4]. In anisotropic model, the T1-weighted and DTI data were registered manually, and the anisotropic white matter conductivity tensor was reoriented following DTI information [3].

3 Results

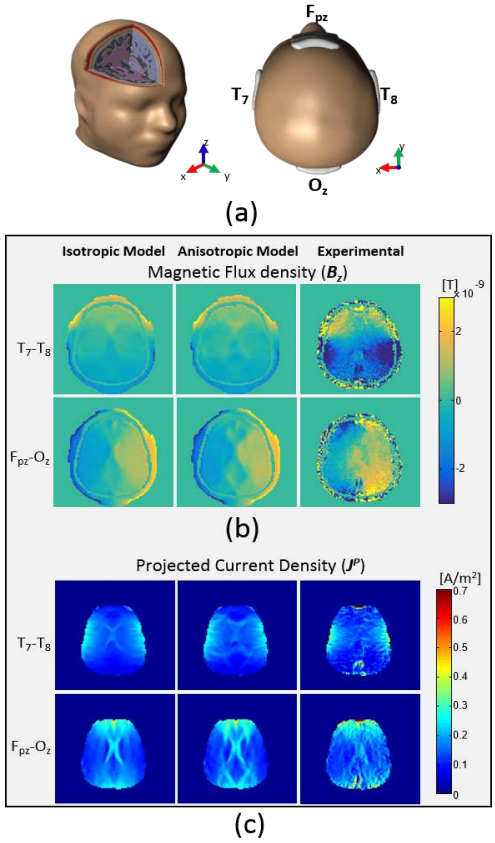

Figure 1. Comparisons of B_z and J^P between MREIT and FEM. (a) 3-D human head model with different tissue types (left), attached surface electrodes (right), (b) Computed B_z from isotropic FEM, anisotropic FEM and acquired experimental phase, from left to right, respectively, and (c) Computed projected current density for above B_z data.

4 Conclusions

We compared MREIT B_z and J^P data and its counterpart predicted from isotropic and anisotropic FEM. Maximum J^P values were found to be of the order of 0.7 A/m^2. Predicted and reconstructed J^P distributions showed high values in ventricle regions and near the electrodes for both montages. Ventricles were more visible for FPz-Oz placement compared to T7-T8, suggesting extension of current in subcortical tissue. Our J^Pcalculation can be further processed to reconstruct conductivity values.

References

[1] Seo, J.K. & Woo, E.J. 2014
[2] Nam, H.S. & Kwon, O 2008
[3] Indahlastari A, et al., 2016
[4] Sadleir RJ, et al., 2010

Carbon electrodes for MREIT imaging of DBS current distributions

Neeta Ashok Kumar[1], Munish Chauhan[1] and Rosalind J. Sadleir[1]

[1]School of Biological and Health Systems Engineering, Arizona State University, Tempe, AZ, USA.

Rosalind.Sadleir@asu.edu

Abstract:

Deep brain stimulation (DBS) involves the surgical implantation of electrodes that inject pulsed currents to reduce abnormal activity of neural networks. Conventional DBS uses Platinum-Iridium (e.g. Medtronic DBS 3387/3389) electrodes. However, MR artifacts caused by Pt-Ir are worse at higher magnetic field strengths and faster imaging sequences (e.g. Gradient echo and EPI). We propose carbon as an alternative to Pt-Ir for use in DBS. MR artifacts associated with carbon were reduced in strong MR fields and fast imaging sequences without compromising the effectiveness of current injection.

1 Introduction

Deep brain stimulation (DBS) is a landmark procedure performed to alleviate debilitating symptoms of neurological disorders such as Parkinson's disease, essential tremor and dystonia. Commonly used brain targets are ventral intermedius nucleus (VIM) of the thalamus, subthalamic nucleus (STN) and the internal globus pallidus (GPi) [1].

The superior biocompatibility and reduced MR artifacts of carbon enables carbon electrodes as an alternative to the typical use of Pt-Ir for current delivery in DBS. The objectives of this study were to quantify and compare the extent of MR artifacts between Pt-Ir and carbon electrodes, and to compare current flow patterns caused by Pt-Ir and carbon electrodes in a uniform gelatin phantom.

2 Methods

1. Electrodes We used two-contact carbon electrodes (2-C) that had a similar geometry to conventional DBS leads. The 2-C electrodes were constructed by insulating carbon fiber bundles by coating them with solutions of nafion in isopropanol and polyvinylidene fluoride (PVDF) in acetone. A pair of these bundles were then secured together with PVDF in acetone to form the final electrode (Figure 1a-right). We also used a quadripolar Medtronic DBS 3389 lead (Figure 1a-left).

2. Experimental set-up : Bruker Biospec 7T MRI was used for spin-echo and gradient-echo acquisitions of a cylindrical gelatin phantom (σ = 0.29 S/m) (Figure 1b).

a. Spin echo (SE): A SE-MREIT sequence was used with ±1 mA orthogonal current injection pairs after 90 and 180 degree pulses respectively. SE-MREIT scan parameters were FOV: 80 x 80 mm^2, Matrix size = 128 x 128, Repetition/Echo time = 1000/20 ms, Slice thickness = 4 mm, Averages = 2.

b. Gradient echo (GE): Scan parameters were same as SE except for Repetition/Echo Time = 500/10 ms.

3. Processing: The impedance of 2-C electrodes was measured in saline solution (Z = 20**Ω**) using an impedance analyzer HP4192A at 1 kHz. Artifacts were compared by computing ratios of electrode diameters observed on magnitude images to actual electrode sizes.

3 Results

The impedance of 2-C measured 1.5kΩ at the lower contact whereas both contacts together measured 3 kΩ at 1 kHz. An overall smaller artifact using carbon electrodes with further reduction in GE acquisitions was observed (Figures 1c and 1d). MR artifact using 2-C measured 1.20 and 1.80 times larger in GE and SE respectively. Whereas, the artifact using Pt-Ir was 8.23 and 2.69 times larger in GE and SE respectively. Induced magnetic flux density (B_z) [2] and current density (J^P)[3] due to current injection from Pt-Ir/2-C to reference surface electrode are shown in (Figures 1e/g and 1f/h).

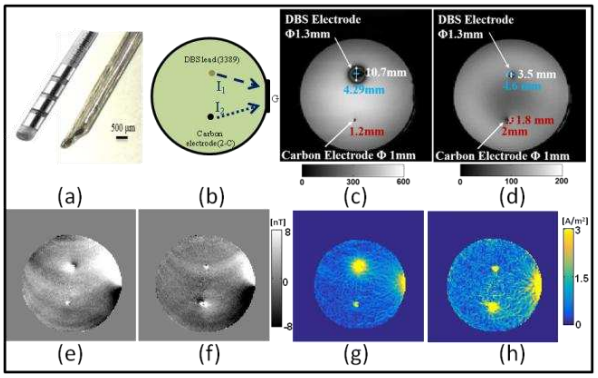

Figure 1: (a) Quadripolar 3389 DBS lead and two-contact carbon (2-C) electrodes (b) Phantom set up (c) Artifacts in GE (d) Artifacts in SE (e) B_z due to current (I_1) (f) B_z due to current (I_2) (g) J^P due to current (I_1) (h) J^P due to current (I_2).

4 Conclusions

In general, MR artifacts around carbon electrodes were significantly smaller in extent compared to Pt-Ir electrodes. The further reduction of artifacts around carbon in gradient-echo acquisitions makes it a suitable candidate for fast imaging sequences such as EPI-MREIT.

5 References

[1] Guo, et al 2015
[2] Woo, et al 2005
[3] Kim et al. 2013

Computer Simulation of Fast Neural EIT in Isolated Retina

Danyi Zhu[1], Calvin Eiber[2], Alistair McEwan[1]

[1]School of Electrical and Information Engineering, The University of Sydney, Sydney, Australia, danyi.zhu@sydney.edu.au
[2]Center of Excellence for Integrative Brain Function, Save Sight Institute, The University of Sydney, Sydney, Australia

Abstract:

This paper reports a computer simulation of EIT in isolated retina tissue through finite element modelling and image reconstruction. Recent development in system design and data processing of fast neural EIT are addressed in this work. Conductivity perturbations were reconstructed with acceptable accuracy in the transverse plane. Future work should focus on improving SNR without eliciting a neural response from the EIT current.

1 Introduction

EIT has been shown to image fast neural activity in the rat somatosensory cortex and peripheral nerves with spatial resolution < 200 μm over millisecond timescales [1]. These recent successes motivated us to study the feasibility of imaging impedance changes during neuronal depolarization in retinal tissue. EIT has the unique ability to image focal activation in the isolated retina with high spatial and temporal resolution and without causing unwanted neural activation of the light-sensitive retina, as can occur using optical methods. Thus EIT could be potentially be a novel approach for imaging focal activation of retina tissue for fundamental neuroscience and vision prosthesis research.

2 Methods

A 1-million tetrahedral finite element mesh was generated using the Netgen Mesh Generator and solved in EIDORS. The geometry (12 * 4 * 0.5mm) was based on a continuum healthy retinal model [2]. The conductivity profile corresponding to ganglion, inner plexiform, inner nuclear, outer plexiform, outer nuclear and photo-receptor layers was taken from published measurements of macaque retinal conductivity [3]. A 32-channel platinum epiretinal electrode array and a subretinal reference electrode were modelled using the complete electrode model. Focal activation was simulated as a disk (r = 200 μm, h = 50 μm) conductivity increase of 0.5% in the five layers of the retinal slice. Sequential injected currents were simulated through electrode pairs at 10 μA, and single-ended voltages were measured. Simulated Gaussian noise was added to the forward solution voltages for image reconstruction [4]. The inverse problem was assumed to be linearized and isotropic. Image reconstruction was regularized with zeroth-order Tikhonov prior on a coarser mesh with 160k elements. The hyper-parameter was chosen using Generalized Cross Validation method.

3 Results and Conclusions

Conductivity perturbations can be identified in the reconstructed images in the absence of noise with a position error < 0.2 μm in the transverse plane. The depth profile of the disk perturbation was not identified as the sensitivity decays exponentially with a planar array in half-space imaging. A clear image could not be reconstructed when $2\mu V_{RMS}$ system noise was added. This might be improved by increasing the injection current or the change in conductivity of the tissue. Lowering the frequency injection current leads to larger measurable impedance change in neuronal depolarization (1% maximum) but a lower amplitude threshold for unwanted electrical neural stimulation (measured as 76nC in feline retina [5]). However, there are technical challenges other than the trade-off between SNR and unwanted cell activation. At the present stage, it is not clear how retinal degeneration and cell death would impact EIT as the conductivity profile for finite element modelling are not yet available. The photoreceptor mosaic of the retina has high degree of conductivity anisotropy, as well as appreciable permittivity. Our current research objective is not to obtain EIT images, but to utilize the unique dynamic EIT signal as a novel way of study the activation in vision prosthesis and retinal neuroscience.

Ongoing research includes accurate modelling of isolated retina and designing electrode arrays to reduce charge densities. Combining subretinal stimulating electrodes with an epiretinal array is expected to improve sensitivity as the imaging domain becomes determined. An optimum current injection and measurement protocol must be determined when stimulating locations are known, but tentatively consists of a combination of maximum traverse electrode pairs.

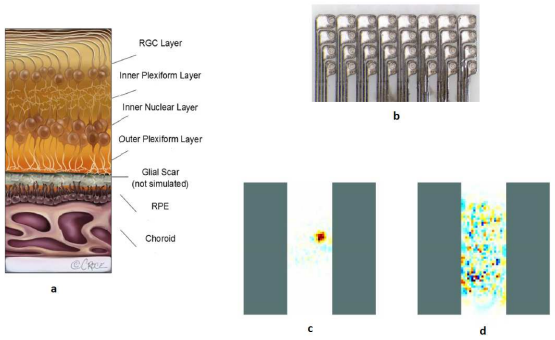

Figure 1: a) Cross section of continuum retina model (reprinted from [2]), b) 32 channel platinum planar electrode array, c) Reconstructed image slice with no noise, d) with uncorrelated system noise.

References

[1] K Y Aristovich et al. *Neuroimage*, 124:204-213, 2016
[2] S A Joarder et al. *J. Neural Eng.*, 8:066006, 2011
[3] H Heynen and D Van Norren *Vision Res.*, vol. 25, no.5, pp.709-715, 1985
[4] J Avery et al. *Sensors*, 17(2), 280, 2017
[5] Y T Wong et al. *Vision Research*, 49:825-833, 2009

Feasibility of recording epilepsy changes with EIT and depth electrodes

Anna Witkowska-Wrobel, Kirill Aristovich, James Avery, Mayo Faulkner, David Holder

Department of Medical Physics and Biomedical Engineering, University College London, UK

anna.witkowska-wrobel.14@ucl.ac.uk

Abstract: Measurement of epileptic activity using EIT with depth electrodes implanted for clinical purposes was proved successful in computer simulations. The location error within depth electrodes was significantly better with EIT than with EEG inverse source modelling, which can be explained by EIT not being sensitive to the orientation of a dipole signal generator. Therefore, EIT can potentially help in localising epilepsy onset in patients.

1 Introduction

Epilepsy surgery is a standard of care for preselected patients with drug-resistance partial epilepsy [1]. The localisation and extent of the epileptogenic zone is defined with MRI, video-telemetry EEG, clinical and psychological assessment, and intracranial electrodes. Intracranial EEG has the highest spatiotemporal resolution among methods currently used in clinics but signal coverage is limited to the immediate surroundings of the electrodes and source orientation. EIT can overcome these limitations. Previous studies in animals [2] and humans [3] suggest that obtaining a sufficient EIT signal for imaging epileptic activity requires the use of intracranial electrodes. Therefore, a comparison of the detection of epileptic changes with EIT, spike recognition and inverse source modelling was assessed in simulations prior to clinical measurements on epileptic patients.

2 Methods

The location accuracy and shape error of reconstructed changes were simulated in 3 subjects with 48 to 72 depth electrode contacts and 32 scalp electrodes with EIT (1), EEG inverse source modelling (ISM) (2), and spike detection on depth electrodes (SEEG), with a threshold for a clinically detectable spike of 250 µV (3).

Three meshes of ~9 million tetrahedral elements were generated from joint CT-MRI imaging [4]. EIT and inverse source reconstructions were performed on ~30000 hexahedral element meshes with zeroth order Tikhonov regularisation and noise-based image weighting [5]. 30 spherical (10/mesh, 5 within depth electrodes coverage, 5 in the opposite hemisphere), 5 mm radius realistic perturbations of 10% local conductivity change imitated the epilepsy onset in EIT. A single dipole (n=30, the same locations as for EIT) in varying orientations over 190 solid angles was used as a signal generator for spike detection and inverse source modelling. For EIT, all depth and scalp electrodes were used to measure voltages and current of amplitude 50 µA (depth electrodes) or 250µA (scalp electrodes) was injected.

3 Results and Conclusions

Localisation accuracy was best with EIT. For perturbations placed within the depth electrode region, it was <5 mm for EIT and 46.2±25.8 mm for ISM with radially oriented sources. For SEEG, 7/15 radially oriented source did not reach 250µV as they were >11mm distant from the nearest electrode (Fig. 1). For the sources placed in the opposite hemisphere, it was 26.1±36.2, 54.0±26.2 mm and 0/15 for EIT, ISM and SEEG.

Work is in progress to assess the detection of epilepsy onset with EIT and depth electrodes in patients.

References

[1] Elger et al., *Epilepsy & Behavior*, 2008
[2] Vongerichten, et al., *NeuroImage*, 2016
[3] Fabrizi, et al., *Physiol Meas*, 2006
[4] Jehl, et al., *Physiol Meas*, 2016
[5] Aristovich, et al., *Physiol Meas*, 2014

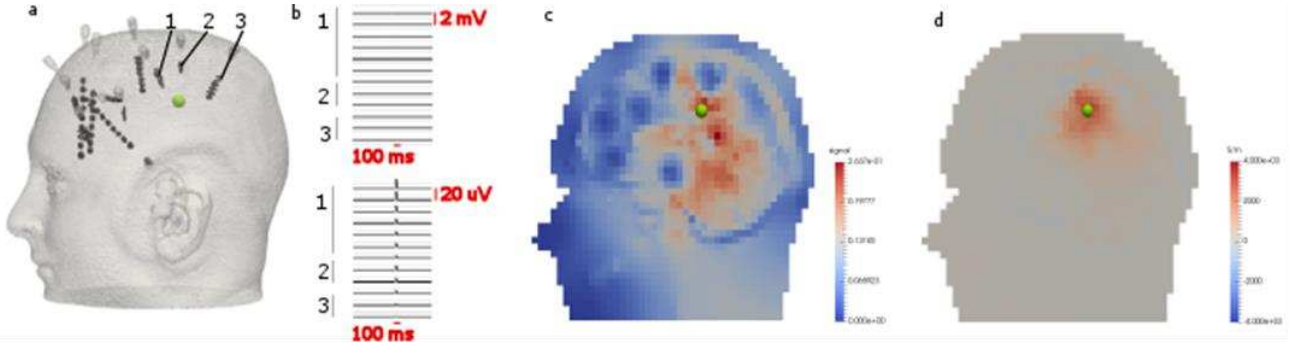

Figure 1. Illustration of an example of unsuccessful detection with SEEG (panel b) and inverse source modelling (panel c), even though EIT protocol using only depth electrodes (panel d) still reconstructed the perturbation <5mm. The real location of the epileptic perturbation (green sphere) and selected representative depth electrodes (black dots with numbers) are shown in panel a. The highest spike recorded was 16 µV on the closest electrode, which was 18mm away.

Imaging Epileptic Activity in the Rat Brain with Three-Dimensional Electrical Impedance Tomography

Sana Hannan[1], Mayo Faulkner[1], Kirill Aristovich[1], James Avery[1] and David Holder[1]

[1]Dept. Medical Physics and Biomedical Engineering, University College London, UK, sana.hannan.14@ucl.ac.uk

Abstract 3D Electrical Impedance Tomography (EIT) has been used to image fast neural impedance changes in the rat brain during ictal activity in the cortical stimulation model of epilepsy. Preliminary images show reproducible patterns of spread of fast electrical activity during ictal discharges. Current and future work is aimed at examining the potential of EIT to image the spatiotemporal propagation of these changes through cortical layers.

1 Introduction

Epilepsy, one of the most prevalent chronic neurological disorders worldwide, is characterised by recurrent seizures, episodes of abnormal, hypersynchronous activity of neuronal networks in the brain. 20-40% of individuals with epilepsy are treatment-resistant and may benefit from neurosurgery [1]. In conjunction with conventional EEG monitoring methods, EIT holds therapeutic potential to improve localisation of epileptogenic tissue prior to its surgical resection in patients with focal epilepsies. Using epicortical electrode arrays, EIT of fast neural activity in the rat cortex can be undertaken with a resolution of 2 ms and <200 µm during evoked potentials [2] and interictal spikes in rat epilepsy models [3]. Additionally, the 4D spatiotemporal propagation of activity in the somatosensory cortex during vibrissae stimulation has been determined [2]. The purpose of the current work is to utilise a similar approach to image fast neural activity during ictal discharges and evaluate the possibility of establishing the propagation pattern of this activity through cortical layers.

2 Methods

Adult female Sprague-Dawley rats weighing 300 to 450 g were used for all experiments. Anaesthesia was induced with isoflurane and, following completion of surgery, maintained with a combination of continuously-infused intravenous fentanyl and isoflurane. A large craniotomy was performed on one hemisphere before implanting a 15x9 mm^2 57-electrode array, fabricated from stainless steel and silicone rubber, on the cortical surface. Epileptic seizures were induced by electrically stimulating the sensorimotor cortex with a 5-s train of 1-1.5 mA biphasic, charge-balanced square-wave pulses at 100 Hz. For EIT recordings, a 50 µA sine-wave was injected at 1.7 kHz through a single electrode pair per seizure. Subsequent offline analysis involved setting trigger markers at the peak amplitude of ictal discharges in the EEG trace to enable averaging, demodulating the EIT signal with a ±500 Hz bandwidth and reconstructing the processed voltages to produce images.

3 Results

Epileptic seizures, comprising a characteristic electrographic pattern of ictal discharges, were reliably elicited by cortical stimulation in 6 rats. Single-channel impedance measurements of ictal discharges averaged within separate seizures consistently showed a maximum negative impedance change of -0.31 ± 0.06 % (c. 20 ms) and slower positive impedance changes of 0.24 ± 0.19 % (c. 100 ms) (n = 87 seizures, 5 rats). Preliminary data from reconstructed images have shown a distinct fast neural impedance pattern during ictal spikes, beginning in the somatosensory cortex and projecting in a posterior and lateral direction (Figure 1, n = 60 seizures, 2 rats).

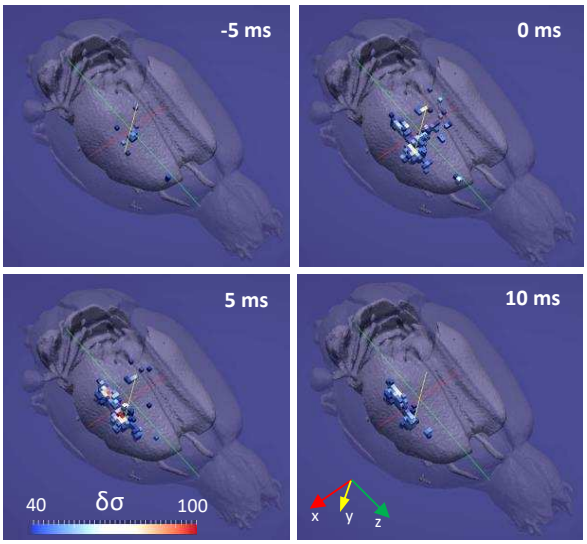

Figure 1. EIT image showing fast neural impedance changes during an averaged ictal discharge. Time is given with respect to the peak amplitude of the ictal spike in the EEG. δσ represents t-score of conductivity changes.

4 Conclusions

Qualitative visual inspection of the image sets obtained to date of fast neural activity during ictal discharges in this epilepsy model may suggest a role of distinct neural pathways projecting from the site of electrical stimulation to the somatosensory cortex in generation of epileptiform events. Work in progress includes examining the spatiotemporal propagation of activity through cortical layers by reconstructing images using a FEM tetrahedral mesh segmented into layers orthogonal to the somatosensory cortex and computing 4D trajectories. This information may enable assessment of functional connectivity between cortical layers, which has the potential to provide insights into the pathophysiology of this common pattern of epileptic activity.

References

[1] Nair DR et al. *Continuum (Minneap Minn)* 22: 157-172, 2016
[2] Aristovich KY et al. *Neuroimage* 124: 204-2013, 2016
[3] Vongerichten AN et al. *Neuroimage* 124: 813-823, 2016

In-vivo EIT imaging of spontaneous phasic activity in peripheral nerves

Kirill Aristovich[1], Matteo Donega[2], Justin Perkins[3], Catherine Fjordbakk[3], James Avery[1], and David Holder[1]

[1]Dept of Medical Physics and Biomedical Engineering, University College London, London, UK,
[2]Neural Interfacing Group, Bioelectronics R&D, GlaxoSmithKline, UK
[3]Structure & Motion Laboratory, The Royal Veterinary College, UK
k.aristovich@ucl.ac.uk

Abstract:
EIT has been employed to image spontaneous phasic activity in sheep vagus nerve in-vivo, using cardiac (ECG) and pulmonary (End Tidal CO2, EtCO2) output for ensemble averaging of the amplitude envelopes at high frequencies to avoid mechanical artefacts related to nerve shape changes. Reproducible significant EIT signals reflected the mechanical stretch receptors' activity. Further work is to reconstruct and validate the images.

1 Introduction

EIT allows imaging of neural activity in peripheral nerves and brain during evoked activity [1,2]. Currently the SNR is insufficient to reconstruct the spontaneous activity without averaging. Measurements also may be contaminated with mechanical artefacts due to changes in shape. The purpose of this study was to develop a method for EIT imaging of spontaneous phasic fast neural activity in peripheral nerve. It employed natural ECG and breathing activity for triggered ensemble averaging and simultaneous minimisation of mechanical artefacts.

2 Methods

Three healthy Romney sheep were anaesthetised and mechanically ventilated. A 30-contact EIT platinised stainless steel array (3mm x 0.1mm square contact) was placed around the right vagus nerve. ECG, EtCO2 and EIT at 100uA and 9kHz were recorded, with 16 independent current injections lasting 120s each, resulting in 32 mins per imaging data set.

Demodulated impedances traces, *dZ,* were then demodulated further to obtain set of high-frequency (>100Hz) spectrograms per *dZ*. The frequency amplitudes were examined for correlation with the physiological signals, and best-correlated frequency band was selected (Figure 1).

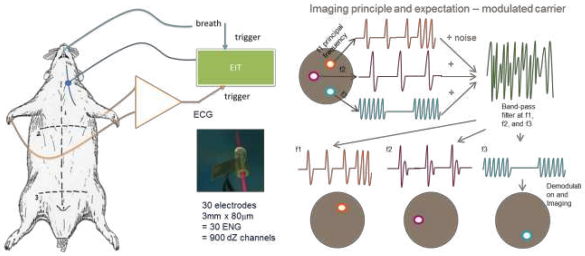

Figure 1. Method of extracting the phasic high-frequency neural activity using EIT.

Amplitude traces over the best frequency band were then ensamble averaged using a physiological signal, either breath intake or peak ECG as a trigger.

3 Results

Reproducible significant (P<0.001, N >500, n=3 sheep) amplitude envelopes were obtained at high (>100Hz) frequencies of the impedance change, correlated to both ECG (average 800 dB/Hz, P<0.001) and pulmonary (average 1500 dB/Hz, P<0.01) activity (Figure 2).

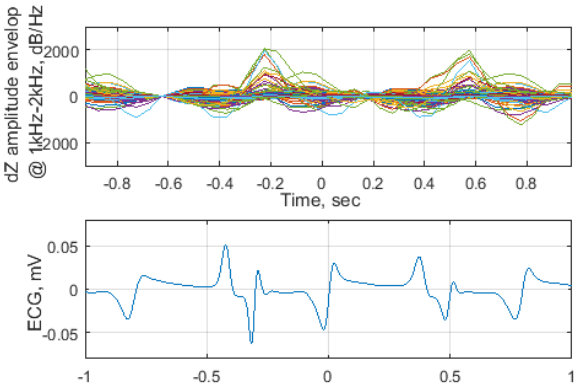

Figure 2. Example of average *dZ* amplitude envelops (N=38 for each trace) for cardiac-related EIT traces (top), and ECG trace (bottom). Two complete cardiac cycles are shown, centred around P-wave (0 sec.). P-wave is also at -0.8 and 0.8 sec respectively.

4 Conclusions and further work

The EIT signals correlated to cardiac and pulmonary activity and passed a variety of controls to ensure the validity of the recordings. The behaviour of the traces corresponded with the expectations of the phasic activity of afferent stretch receptors [3]. The cardiac-related activity had relatively large peak straight after the QRS complex. Pulmonary activity also increased in magnitude during stretching of the lungs.

Work is in progress to reconstruct images of the activity and perform independent cross-validation with evoked activity. The accuracy of the method is being corss validated in similar studies in the rat sciatic nerve.

References

[1] K Aristovich, B Packham, R Koo, GS dos Santos, A McEvoy, DS Holder *Neuroimage*, 124:204–213,2016
[2] K Aristovich, J Avery, C Blochet, D Holder *EIT 2016 Proceedings*, 2016
[3] Kubin L, Alheid G F, Zuperku E J and McCrimmon D R. *J. Appl. Physiol*. 101 618–27,2

Highly Reliable Iridium Oxide Electrodes for Electrical Impedance Tomography Imaging of Fast Neural Activity in the Brain

Min H Kim, Seonhye Han, Montrey D. Freeman, Obadiah K. Koech and Hargsoon Yoon

Neural Engineering and Nano-Electronics Laboratory, Norfolk State University, Norfolk, VA, USA

Abstract: It is important to develop reliably performing electrodes for imaging of fast neural activity with electrical impedance tomography in the brain. In this research, vertically aligned iridium oxide (IrO_x)/gold (Au) nanowire electrode array have been developed on a flexible polymer substrate. We tested long term reliability by applying sinusoidal current with 50 µA amplitudes for 1 million cycles and monitoring impedance changes. This research showed gradual decrease of impedance up to 500k cycles and stable values for the rest of cycling periods without any performance degradation, which confirms high reliability of electrode performance.

1 Introduction

Developing highly performing and reliable electrodes for electrical impedance tomography (EIT), especially for fast neural imaging in the brain is challenging, because many different design factors should be considered such as size, biocompatibility and long term stability [1]. The electrode size should significantly be reduced down to few hundreds micron in diameter to minimize brain tissue damage, when the electrode array is implanted. To overcome the impedance increase issue resulting from the electrode size reduction, vertically aligned IrOx/Au nanowire electrodes are applied in this research [2]. Iridium Oxide is also a favourable material for implantable EIT imaging because of its biocompatibility and high charge injection capacity [3]–[5]. In this research, IrO_x /Au nano-electrodes array were developed on a flexible polymer substrate and their long term stability were tested with 1 million cycles of sinusoidal current injection.

2 Methods

Vertically aligned IrO_2/Au nanowire electrodes were fabricated using nano/micro fabrication processes. First, gold nanowires (AuNW) were grown on a gold-coated polyimide substrate by electrochemical deposition on a nanopored polycarbonate membrane [2]. After patterning of electrode array, IrOx was electrochemically deposited on AuNW electrodes as shown in Figure 1 [6].

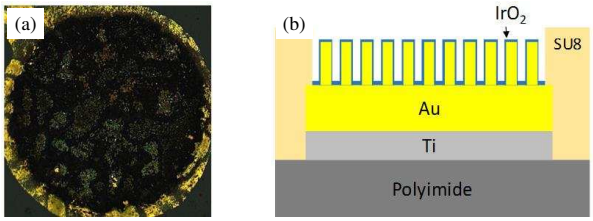

Figure 1: a) In image of 280µm diameter IrO2/Au nanowire electrodes and b) a cross section diagram of the electrode

For characterization, iridium oxide electrodes were tested in 100 mM phosphate buffered saline. Electrodes were connected to a current source and a multiplexer for current injection as well as voltage recordings by a data acquisition system. Sinusoidal current with 50 µA amplitude at 1725 Hz frequency was applied [7] and the current supply was switched clockwise for one complete cycle. This cyclic current injection between electrode pairs was repeated for 1 million cycles and the impedance of electrodes was monitored throughout the 1 million cycles. The reliability testing set-up was controlled by Lab-View software (National Instrument, Austin, TX). Results showed gradual decrease and saturation of impedance to around 500k cycling periods and stable impedance values for the rest of cycling periods without any significant change, as shown in Figure 2. This presents high reliability of electrode performance.

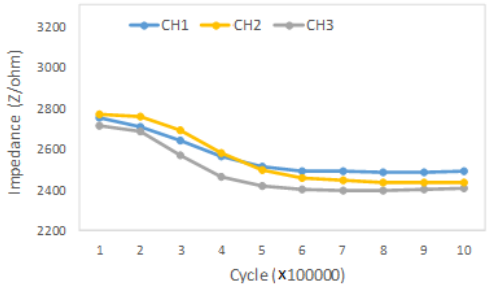

Figure 2: Impedance changes during 1 million cycles of sinusoidal current injection.

3 Conclusions

For EIT imaging of fast neural activity, vertically aligned iridium oxide/gold nanowire electrodes have been developed on a polymer substrate. Long term stability of electrodes was tested with 1 million cycles of current injection. Test results showed gradual decrease of impedance to around 500k cycling periods and stable values for the rest of periods without any performance degradation. This research demonstrated that iridium oxide/gold nanowire electrode array can operate with high reliability for neural imaging in the brain.

4 Acknowledgements

This work is partially supported by the NSF-RISE Grant (HRD 1345215).

References

[1] C. Venkatratnam and N. Farrukh IFMBE Proc., 56:1-3,2016.
[2] H. Yoon, P. Hankins, S. Oh, R. E. Haubaugh, V. K. Varadan, J. Nanotech. Engineering Medicine, 1(2): 021006, 2010.
[3] S. F. Cogan Annu. Rev. Biomed. Eng., 10:275–309,2008.
[4] R. D. Meyer, S. F. Cogan, T. H. Nguyen, and R. D. Rauh IEEE Trans. Neural Syst. Rehabil. Eng., 9(1):2–11, 2001.
[5] S. Kakooei, M. C. Ismail, and B. A. Wahjoedi *Int. J. Electrochem. Sci.*, 8:3290–3301, 2013.
[6] Yamanaka, K. Japanese Journal of Applied Physics., 28(4), 632-637, 1989.
[7] D. Holder, K. Astrovish, M. Faulkner, Personal Communication, Aug. 12, 2016.

Recording thalamic impedance changes to assess feasibility of 3D EIT

Mayo Faulkner[1], Sana Hannan[1], Kirill Aristovich[1] and David Holder[1]

[1]Department of Medical Physics and Biomedical Engineering, University College London, UK

mayo.faulkner@ucl.ac.uk

Abstract: EIT has the potential to track the propagation of activity throughout the brain. The magnitude of impedance changes occurring in thalamic nuclei were directly measured to assess the feasibility of detecting such deep activity when only recording with cortical electrodes. Impedance changes were present in the thalamus but were too small to be detected with cortical electrodes alone.

1 Introduction

EIT can image fast neural activity throughout the rat cortex with a temporal and spatial resolution of 2 ms and 200 µm respectively, and has the potential to concurrently image activity occurring in deeper structures such as the thalamus [1]. Recent simulations have shown that when implementing arrays of cortical electrodes, an impedance change of 10% should occur in the thalamus in order to be imaged accurately.

The purpose of this work was to quantify the size of the impedance change occurring in target thalamic nuclei following somatosensory forepaw stimulation. This was intended to allow the feasibility of imaging such activity with cortical electrodes alone to be assessed.

2 Methods

Female Sprague-Dawley rats weighing between 320 – 400g were used for experiments. Anaesthesia was induced using isoflurane and maintained with 0.1% α-chloralose. A craniotomy was performed on the right hemisphere of the brain and a 57 channel electrode array was placed on the exposed cortex. An additional 16 channel depth probe was placed in the ventral posterolateral (VPL) nucleus of the thalamus.

The contralateral forepaw was stimulated at 2 Hz using a monophasic electrical pulse of duration 500 µs and amplitude 10 mA. Single channel impedance measurements were recorded using the ScouseTom EIT system [2] by injecting current between two electrodes on the cortical array. A range of current amplitudes (50 µA – 400 µA) and frequencies (1 kHz – 10 kHz) were explored.

3 Results

Thalamic evoked potentials and impedance changes following forepaw stimulation were recorded in N = 3 rats. The magnitude of both responses was found to be highly sensitive to the position of the depth probe. In two out of three rats the probe position deviated from the target nuclei and evoked potentials of 21.2 ± 4.1 µV (mean ± S.E) and impedance changes of -0.005 ± 0.002 % at 6725 Hz were detected (n=11, N=2). In one rat, the probe was accurately placed in the target nucleus and an evoked potential of 176 ± 19 µV and an impedance change of -0.09 ± 0.02 % at 6725 Hz were recorded (n=6, N=1). In this rat a comprehensive sweep of frequencies between 1kHz and 10 kHz was conducted and the largest impedance change was -0.60 ± 0.07 at 1325 Hz, figure 1. This impedance trace along with the corresponding evoked potential (176 ± 27 µV) are shown in figure 2.

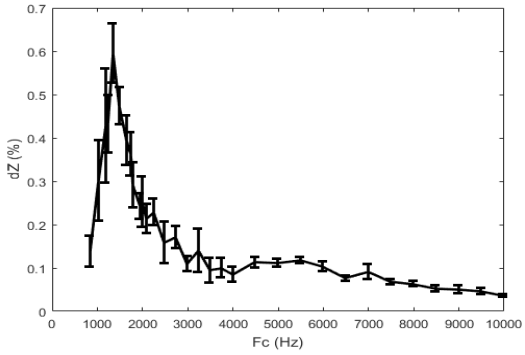

Figure 1: Magnitude of impedance change dZ (%) with carrier frequency Fc. Peak amplitude of -0.60 ± 0.07 % observed at 1325 Hz.

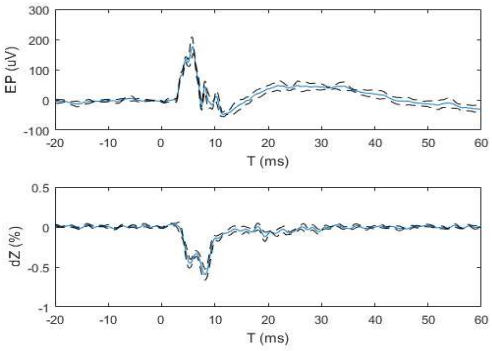

Figure 2: Evoked potential (top row) and impedance change at 1325 Hz (bottom row) measured on 16 channel depth probe following stimulation of forepaw at 2Hz. Solid line shows mean and dashed lines ± S.E (n =6, N=1).

4 Discussion and Conclusion

The maximum thalamic impedance change occurring during contralateral forepaw stimulation was -0.6 %. A comprehensive sweep of all frequencies has only been obtained in one subject and work is in progress to repeat measurements to confirm the optimum frequency. Once this has been ascertained attempts to image the deep activity will be conducted. The early indication is that the magnitude of the impedance change is between 1 and 2 orders of magnitude smaller than that would be required to image the thalamic activity when using cortical electrodes alone. It could, however, be imaged if additional depth electrodes are implemented.

References

[1] Aristovich, K. Y et al (2016). *NeuroImage*, *124* (2016), 204–213

[2] Avery, J et al (2017). *Sensors* **2017**, *17*(2), 280

The UCLH Stroke EIT dataset

Nir Goren, James Avery, Anna Witkowska-Wrobel and David Holder

Department of Medical Physics, University College London, London, UK, n.goren@ucl.ac.uk

Abstract: An extensive multi frequency EIT dataset MFEIT was collected in stroke patients at University College London Hospital. Recordings were made in 30 patients and 10 healthy subjects, at 17 frequencies between 5 Hz and 1.7 kHz. Whilst reconstructions were not successful with current MFEIT methods, all data is available to the community to encourage continued research in this area the data.

1 Introduction

Multi-frequency EIT has the potential to expedite stroke type classification, decreasing the time to treatment and improving patient outcomes [1]. Whilst the potential has been demonstrated in simulation [2], the methods have yet to be tested experimentally. Further, the lack of quality MFEIT data has made it difficult to asses the robustness of these methods to experimental errors.

2 Methods

Data were collected using 32 EEG electrodes and the UCL ScouseTom EIT system [4] with a 31-injection pair protocol, yielding 930 voltage measurements. Current was injected at 17 frequencies between 5 Hz and 2 kHz, encompassing the range using in previous simulation studies [2]. The current amplitude varied at each frequency in accordance with IEC 60601. The protocol was repeated three times over the course of 20 minutes. An additional dataset using a subset of three frequencies, was collected for 60 frames over 25 minutes. Both of these recordings constitute a single "Multi Frequency" dataset.

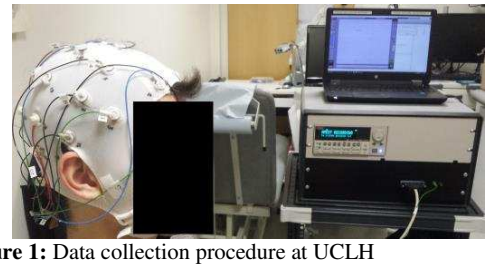

Figure 1: Data collection procedure at UCLH

In some cases, for clinical reasons, a further CT or MRI was required. In which case a second EIT dataset was also collected to capture any potential changes in pathology such as haemorrhagic transformation. This constitutes a "Time Difference" dataset. In total of 30 recordings in 23 patients were collected at the Hyper Acute Stroke Unit (HASU) at University College London Hospital, approved by NHS/HSC R&D (IRAS ID: 168765). Datasets were also recorded in 10 healthy subjects.

For each patient, a corresponding MRI or CT scans were obtained alongside any relevant clinical records. The patients could be divided into 5 broad categories based on diagnosis, Table 1.

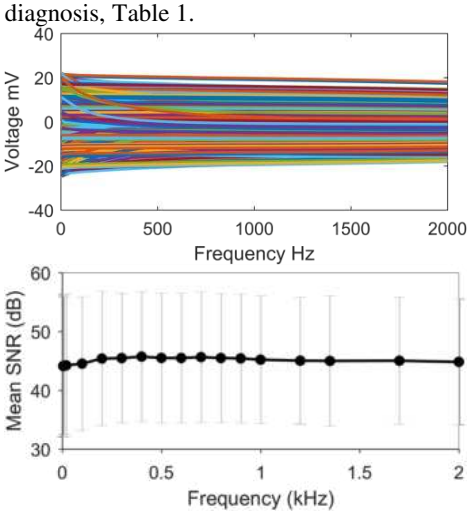

Figure 2: Top: Example dataset from ICH patient Bottom: SNR across frequency in all recordings

3 Results and Conclusions

Across all recordings, the SNR did not show any significant frequency dependence ($P < 0.05$) with the exception of 5 Hz, figure 2 b. Increased patient movement resulted in an SNR decrease from 46.5 ± 4.14 dB to 41.6 ± 7.9 dB compared to healthy subjects. This is half the noise observed in the most comparable study [1]. The measurements in this study constitute the most comprehensive stroke EIT dataset in the literature, and is available to the community. Whilst MFEIT reconstructions have not been successful with current methods, it is our hope that this dataset will form the basis of future research in this area. Further, work is currently in progress to reconstruct the time difference data, whilst correcting for electrode movement [5].

4 Acknowledgements

This work was funded by the EPSRC and the MRC.

References

[1] Romsauerova, A. et al., *Physiological Measurement*, 27(5) 2006
[2] Malone, E. et al., *Physiological measurement*, 35(6) 2014
[3] Oostenveld, R. et al., *Clinical neurophysiology*, 112(4), 2001.
[4] Avery, J et al. Sensors 2017, 17(2), 280
[5] Jehl, M. et al., *Physiological Measurement*, 36(12), 2015.

Table 1: Number of patients in each diagnostic grouping, total number of recordings in parenthesis

	Ischaemia		Haemorrhage			
Data Type	Large Territory	Small	Large	Small	Other	Healthy Subjects
Multi Frequency	7 (8)	3 (4)	4 (5)	2 (2)	10 (11)	10 (20)
Time Difference	2 (2)	1 (1)	1 (1)	-	2 (2)	10 (10)

EIT-based TBI Monitoring with Active and Passive Intracranial Electrodes

Ryan J Halter and Preston Manwaring

Thayer School of Engineering, Dartmouth College, Hanover, NH, USA, ryan.halter@dartmouth.edu

Abstract: There is an interest in developing new clinical imaging modalities to better monitor patients with severe traumatic brain injury (TBI). We have explored using EIT with 8 scalp electrodes and 1 intracranial electrode (ICE) for TBI monitoring. Simulation and animal model data were used to demonstrate the benefit of using an ICE in passive or active mode as compared to not using an ICE.

1 Introduction

Current clinical practices using continuous intracranial pressure (ICP) monitoring along with CT images acquired every few hours to monitor patients with TBI unfortunately do not provide clinicians with early enough warning to adequately treat evolving injury. Electrical impedance tomography (EIT) is a method by which intracranial pathology can be safely and continuously monitored in patients with TBI. We have used an approach that couples scalp electrodes with an intracranially positioned electrode to help overcome challenges in brain imaging associated with 1) sensing voltages within the intracranial space and 2) overcoming the large skull impedance making it difficult for current to penetrate within the intracranial space. Here, we explore through simulations and an animal model the benefits attributable to an intracranial electrode acting in either passive (voltage sensing only) or active (voltage sensing and current driving) modes.

2 Methods

We instrumented 3-4 week old piglets (~10kg, 8 pigs) with eight circumferentially located scalp electrodes and an ICE/ICP sensor inserted through a burr hole drilled into the cranium of the pig above the right lateral ventricle[1]. A contralateral paramedian burr-hole was created above the left ventricle to induce traumatic events. These events included: 1. Inflation of a parenchymal balloon (Fogarty catheter) with 150 ml of CT contrast for 10 minutes followed by deflation and 2. injection of a total of 1 mL of arterial drawn, unclotted blood.

EIT data is recorded from baseline (prior to balloon inflation and blood injection) and is used as the reference data set for producing conductivity (σ) images. EIT frames are recorded at ~100 frames/second and shown on screen in real-time. ICP measurements are recorded in tandem with EIT. The results presented here are based on off-line analysis of the data; however, on-line real-time display would be the intended clinical deployment method.

In addition to the animal experiments, we conducted several simulations to evaluate the utility of an intracranial electrode (ICE) acting in passive mode (i.e. voltage sense only) or active mode (i.e. voltage sense and current drive) as compared to not using an ICE.

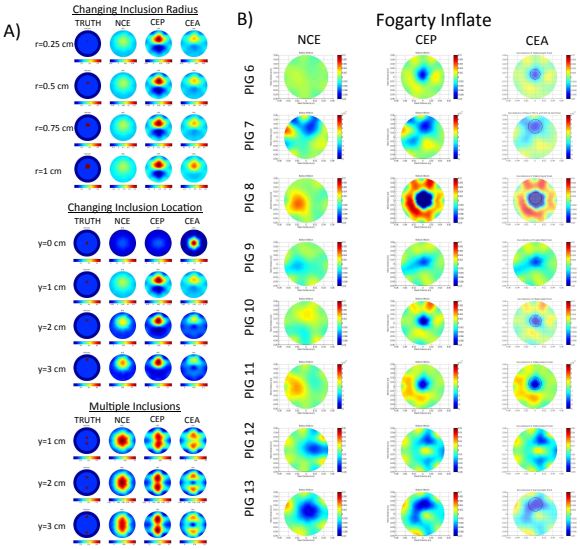

Figure 1. Benefit of central electrode. A) Simulations and B) in vivo animal images demonstrating that the central electrode provided enhanced imaging when used in either active or passive mode. Expect lowered σ at balloon location, NCE = no central electrode, CEP = central electrode – passive, CEA = central electrode – active. Note that both CEP and CEA perform better than NCE in both simulation and in vivo animal studies.

3 Results

As expected, simulations demonstrated that an active intracranial electrode provides the best resolution and accuracy when compared to no intracranial electrode and an intracranial electrode active in passive mode only. That said, the passive ICE provides enhanced resolution and accuracy as compared to not using an ICE. These observations were also evident in the animal model experiments. Regions of low conductivty associated with Fograty inflation were observed in images of all 8 animals when an active or passive ICE was used. The correct ballon effect (decreased conductivty) was only noted in 4 of the 8 cases when no ICE was used.

4 Conclusions

We have demonstrated through simulations and animal model experiments that a central electrode significantly improves imaging accuracy Further, we have shown that the central electrode acting in either active mode (driving/sinking currents) and passive mode (sensing voltage only) will outperform a system consisting of only scalp electrodes.

References

[1] Manwaring P *et al* Anesthesia and Analgesia, 2013

Simultaneous reconstruction of EIT and EEG

James Avery, Kirill Aristovich, Thomas Dowrick and David Holder

Department of Medical Physics, University College London, London, UK, j.avery@ucl.ac.uk

Abstract: Simultaneous reconstructions of a colocated current dipole and impedance contrast were performed using EEG inverse source modelling and Frequency Division Multiplexed EIT (FDM-EIT). Using four injection pairs, FDM-EIT reconstructions had less localisation error than EEG inverse, despite an order of magnitude smaller signal amplitude. Work is currently in progress on a combined EIT and EEG reconstruction.

1 Introduction

By imaging both the fast neural and cell-swelling changes, EIT has the potential to improve localisation of epileptic foci, compared to EEG based methods, due to increased sensitivity in deeper structures [1]. Conventional EIT methods are not suitable in this application due to artefacts when switching injection pairs, and the short duration of the signals [2]. By injecting current continuously at multiple pairs of electrodes at different frequencies, FDM-EIT removes any switching artefacts, providing uncorrupted EEG recordings. The time resolution of these images is then limited by the demodulation bandwidth, as opposed to the switching speed of the hardware.

EEG has considerably higher SNR than EIT, particularly when measured on the scalp. EEG signals range from 0.5 μV to 100 μV [3] compared to expected changes of 0.01% [4] to 0.35% [5] in EIT, dependent upon application. However, EIT has advantages in a greater number of independent measurements, and is insensitive to the orientation of the source, unlike EEG. Given the reduced number of possible injection pairs, and consequent limitations in Jacobian size, it is not well understood whether the benefits of EIT over EEG are conferred to FDM-EIT.

2 Methods

Experiments were performed in a neonatal head tank with skull, filled with 0.4 S/m saline [6]. Voltages were recorded on all 32 electrodes in parallel using an ActiChamp EEG system, sampling at 100 kHz. To obtain the FDM-EIT data, current was injected between four pairs of electrodes, with 100 μA amplitude, and 513 Hz spacing starting at 2.5 kHz. The five signals (EEG + four EIT) were retrieved through simple band pass filtering.

A voltage to simulate EEG was generated with a current dipole constructed from a differential Howland current pump and two 1 mm diameter Ag ball electrodes, spaced 10mm apart. Pulses of a 10 Hz sine wave were generated with a current amplitude sufficient to generate 100 μV RMS signals averaged across all electrodes. A 10mm sponge of 10% contrast was used as a biologically representative perturbation for the EIT measurements. The RMS change in FDM-EIT signal, *dZ*, was 10.7 μV or 0.47 %. These two colocated perturbations approximate the spike and cell swelling expected during a seizure.

The resultant frame rate after all processing steps, was 250 Hz. Reconstructions were made in a c. 250,000 element hexahedral mesh using cross validated zeroth-order Tikhonov regularisation with noise based correction [7]. Images of the current density magnitude and conductivity changes were reconstructed independently, using the EEG and FDM-EIT signals respectively.

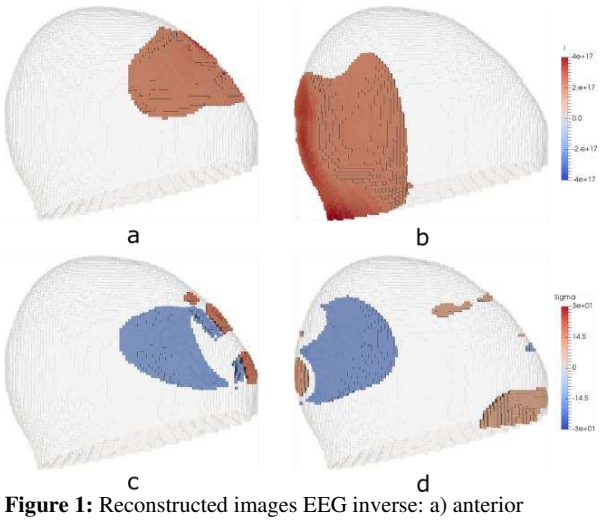

Figure 1: Reconstructed images EEG inverse: a) anterior location, radially orientated, b) posterior location, tangentially orientated. FDM-EIT: c) anterior d) posterior.

3 Results and Conclusions

FDM-EIT and EEG inverse images were obtained simultaneously. This demonstrates the potential of FDM-EIT as a modality adjunct to conventional clinical EEG. Even with as few as four injection pairs, FDM-EIT localisation was equal to or better than EEG inverse (Fig 1). This was most pronounced when the dipole was oriented tangentially to the surface electrodes (Fig. 1b), when the localisation error was 8.4% compared to 4.1% with FDM-EIT. However, there were more artefacts present in the EIT images (Fig 1d), with noise error values > 10%. Work is currently in progress to create a combined EIT and EEG inverse solver, which may take advantage of the higher SNR of EEG whilst benefiting from the greater number of independent measurements in EIT.

4 Acknowledgements

This work was funded by the EPSRC and DARPA

References

[1] Fabrizi, L, et.al (2006) Phys Meas, 27(5), S163-S174
[2] Vongerichten, et al., *NeuroImage*, 124, 2016
[3] Teplan, M., *Measurement Science Review*, 2(2), 2002.
[4] Abascal, J.-F.P.J. et al., *NeuroImage*, 43(2), 2008
[5] Romsauerova, A. et al., *Physiological Measurement*, 27(5), 2006
[6] Avery, J et al., *Physiological Measurement,* 2017
[7] Aristovich, K.Y. et al., *Physiological measurement*, 35(6), 2014

Model of impedance change in unmyelinated fibres

Ilya Tarotin[*1], Kirill Aristovich[1] and David Holder[1]

[1]Dept of Medical Physics and Biomedical Engineering, University College London, London, UK,
ilya.tarotin.14@ucl.ac.uk

Abstract: Simple Hodgkin-Huxley and complex C-fibre 3D FEM models were developed to simulate apparent impedance changes (dZ) during action potential propagation. In contrast to the expected decrease in dZ falling with frequency, there were its peak decreases at 2 kHz for HH and 6 kHz for C-fibres, and an increase at <4 kHz for both fibre types. This was due to a superposition of changes in membrane currents and impedance.

1 Introduction

EIT can be used to image fast impedance changes accompanying depolarization in brain or nerves [1]. One way to evaluate if experimental changes are genuine is to compare them to those produced by a realistic biophysical model. We expected that all changes simulated would be decreases, as the resistance of nerve membranes falls during the action potential as ion channels open. The purpose of this study was to develop a model of unmyelinated fibres, to simulate the dZ under various alternating currents and to study the principles underlying the observed impedance changes. This was the first step towards construction of an accurate model of the whole nerve to be employed in optimising fast neural EIT.

2 Methods

Nerve fibres were modelled as 1D cables in a 3D space using FEM. Each fibre contained active ion channels modelled via HH equations [2] or HH-type C-fibre equations [3]. Membrane potential and external field were simulated simultaneously so that extracellular action potentials could be recorded together with the intracellular ones. The injection of the EIT current and recording of the electric field were done through external electrodes. The main equations used in the model were:

$$\frac{r_{ax}}{2\rho_i}\left(\frac{d^2V_m(x,t)}{dx^2}+\frac{d^2V_e(x,t)}{dx^2}\right)=C_m\frac{dV_m}{dt}+\sum I_{ion}(V_m) \quad (1)$$

$$I_m|_\Gamma=\sigma\nabla V|_\Gamma=\frac{r_{ax}}{2\rho_i}\left(\frac{d^2V_m}{dx^2}+\frac{d^2V_e}{dx^2}\right), on\ \Gamma \quad (2)$$

$$-\nabla\left(\sigma_e(\nabla V_e)\right)=0, in\ V \quad (3)$$

where $V_{m,e}$ are membrane and extracellular potentials, r_{ax} – fibre radius, ρ_i – intracellular resistivity, C_m – membrane capacitance, $\sum I_{ion}$ – membrane ionic currents according to the used model [2,3], σ_e – extracellular conductivity, Γ – fibre boundary, V – external volume.

Simulations were carried out at frequencies from 1 to 15 kHz and "safe" current amplitudes where dZ linearly depended on the current (10-100 µA for HH axon and 0.5-1 mA for a C-fibre).

To find a biophysical explanation of the recorded apparent dZ, changes in the sum of sodium (Na), potassium (K) and capacitive (C) membrane currents, dI_m and internal membrane impedances $dZ_m=dV_m/dI_m$ in the HH model were studied during activity.

3 Results

The maximum absolute impedance decrease for the HH axon was at 2 kHz (fig 1a). For a C-fibre, the highest negative dZ was at 1 kHz falling with frequency; however, a peak at 6 kHz was observed (fig 1b). Impedance increase was simulated for both fibres below 4 kHz (fig 1c,2a).

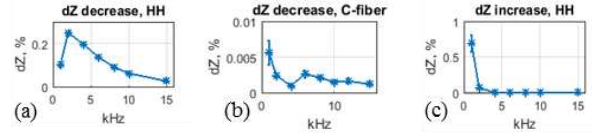

Figure 1: dZ decrease: (a) HH model (50 µA/cm^2), (b) C-fibre (150 mA/cm^2); (c) dZ increase in HH model (50 µA/cm^2)

Investigation of the membrane parameters in the HH model showed that the recorded apparent dZ was determined not only by membrane internal impedance change, dZ_m but also by a change in the membrane currents, dI_m, which change differently at different frequencies (fig 2).

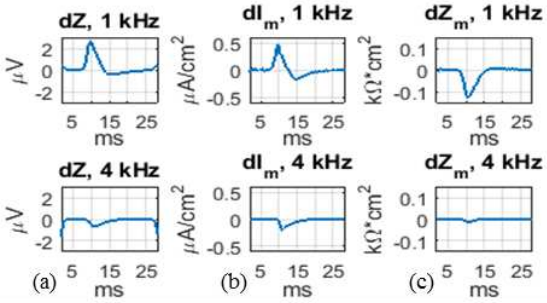

Figure 2: Change during activity: dZ (a), membrane currents (b), internal membrane impedance (c) (1 kHz, 50µA/cm^2)

4 Conclusions and further work

Active ion channels play a vital role in the determination of the apparent impedance change during activity as otherwise there would be a constant decrease from DC. The apparent increase in dZ seen at lower frequencies supported previous experimental findings [4]. The recorded dZ were shown to be a superposition of dZ_m and dI_m which alters with frequency.

The developed model forms a basis for future model of the whole nerve with unmyelinated and myelinated interacting fibres. With the model, it would be possible to better understand the physiology of the recorded dZ and optimize fast neural EIT.

References

[1] K Aristovich, B Packham, R Koo, GS dos Santos, A McEvoy, DS Holder *Neuroimage*, 124:204–213,2016
[2] AL Hodgkin, AF Huxley *J. Physiol* 117.4:500, 1952
[3] J Tigerholm, ME Petersson, O Obreja, A Lampert, R Carr, M Schmelz, E Fransén *J Neurophysiol*, 111.9: 1721-1735, 2014
[4] A Vongerichten *PhD thesis* UCL, 2014.

Cerebral perfusion imaging using EIT

Andy Adler[1], Mayo Faulkner[2], Kirill Aristovich[2], Sana Hannan[2], James Avery[2], David S. Holder[2]

[1]Systems and Computer Engineering, Carleton University, Ottawa, Canada, Andy.Adler@Carleton.ca
[2]Medical Physics and Biomedical Engineering, University College London, UK

Abstract: Imaging of cerbral perfusion is understood to provide rich information on cerebral processes. This study explores whether EIT is able to image perfusion in the brain. In a single rat, a bolus of hypertonic saline was introduced into an arterial catheter during two activity states, and EIT images reconstructed. Results suggest that changes in perfusion pattern are visible in EIT images.

1 Introduction

In functional MRI imaging, the Blood-oxygen-level dependent (BOLD) signal allows imaging of the "hemodynamic response", a process by which active neurons with higher metabolic rates induce delivery of additional blood (perfusion). Cerebral imaging using fMRI now plays an important role in functional studies involving the brain.

EIT has been used to image perfusion in the lungs using a venous injection of a bolus of hypertonic saline[2], where the contrast agent flows through the heart and then the lungs increasing conductivity in proportion to blood flow. We were motivated to explore whether EIT is able to measure perfusion in the brain, as this could potentially provide rich functional imaging possibilities, especially given EIT's ability to image small volumes with high temporal resolution.

To explore this possibility, a pilot experiment was conducted in a single rat. EIT measurements were performed during injection of the contrast bolus in two conditions to provide a within-subject control.

2 Methods

A single white Sprague-Dawley rat was anesthetized and ventilated. A craniotomy was performed and an array of 57 EIT electrodes placed on the cortical surface. Using the Scouse-Tom EIT system[1], data were collected at 5 frames/s and a total of 903 stimulation/measurement pairs acquired. A heuristic protocol aimed at maximizing sensitivity throughout the cortex was implemented and current of amplitude 50μA and 2 kHz was injected.

A contrast bolus of 10% NaCl (w/v) of size $500\,\mu$L was used. First, the bolus was injected through a venous injection via the femoral vein. As expected, no clear cerebral perfusion signal was seen, likely because the conductivity contrast became diffuse while travelling through the pulmonary vasculature. Next, an arterial catheter was inserted via the femoral artery and placed at the aortic arch (as verified by the pressure waveform). EIT recording was initiated before the arterial bolus injection for two conditions (repeated twice): (C) control condition (no stimulation) and (S) electrical stimulation of the forepaw (and thus the S1 forepaw somatosensory cortex)[3].

3 Results

Time-difference EIT images were reconstructed using a one-step GN algorithm and the slices of the volumetric image or the cortex studied as a function of time (Fig. 1). In all recordings, there was a clear signal which corresponded to the expected arrival time of the bolus.

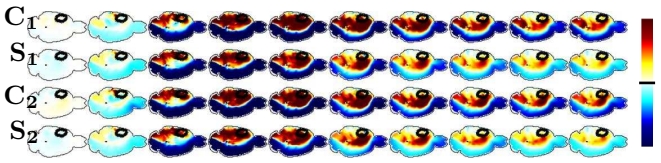

Figure 1: Time sequence of EIT images of a horizontal slice (Red $\uparrow\sigma$, Blue $\downarrow\sigma$), from left to right; images spaced by 600 ms. C_1, C_2) control (no stimulation). S_1, S_2) with forepaw stimulation.

In order to explore whether EIT detected differences between groups, the maximum images are shown in Fig. 2. Some differences in the spatial pattern appear visible, and are repeatable between the repeated protocols.

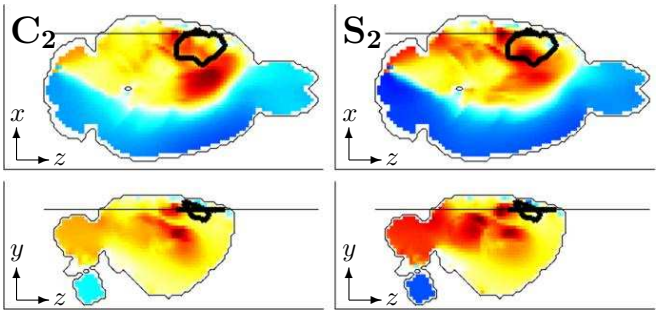

Figure 2: EIT images of maximum signed voxel value for C) control, and S) forepaw stimulation. Region outlined in black is the S1 forepaw cortex. Coronal (top) and Saggital (bottom) slices shown.

4 Discussion

Our goal was to explore the possibility of creating EIT images of cerebral perfusion using an injected bolus contrast. Results in a single rat are show consistent images corresponding to the expected arrival time of cerebral perfusion. Additionally, there are interesting spatial differences between the control and stimulation protocols which are suggestive of underlying functional changes.

References

[1] J Avery, T Dowrick, M Faulkner, N Goren, D Holder. *Sensors* 17:280, 2017

[2] I Frerichs, J Hinz, P Herrmann, G Weisser, G Hahn, M Quintel, G Hellige. *IEEE T Med Imag* 21:646, 2002.

[3] N Van Camp, M Verhoye, A Van der Linden *NMR Biomed* 19:10, 2006.

A Novel Tissue-Mimicking Material for Phantom Development in Medical Applications of EIT

Barry J McDermott, Emily Porter, Marggie Jones and Martin O'Halloran

Translational Medical Device Lab, National University of Ireland Galway, b.mcdermott3@nuigalway.ie

Abstract: A solid Tissue-Mimicking Material (TMM) with adjustable conductivity properties, which can be matched to those of biological tissue, is presented. TMM models of breast fat and gland matching the conductivity of real tissue over the frequency range of 100 kHz–250 kHz are shown. These TMMs are incorporated into an anatomically accurate breast phantom. This TMM will be useful for phantoms used in EIT for clinical research.

1 Introduction

TMMs that have appropriate conductivity over a selected frequency range are used in phantoms, and can be used as pre-clinical, experimental test platforms. Solid TMMs have the advantage of being robust, mechanically and electrically stable over time, and moldable into the anatomy of interest [1]. This paper presents the development of a novel EIT-oriented TMM. This type of TMM, previously used in microwave imaging studies, is composed of graphite, carbon black and polyurethane. Adjusting the ratio of ingredients allows adjustment of the conductivity profile to model any tissue of interest [2-4] Here we present and validate TMMs models of breast fat and breast gland over the frequency range of 100 kHz – 250 kHz. This range is chosen as it matches that of the Swisstom Pioneer, a commercial research-targeted EIT device [5] and that of the impedance analyzer used, the Agilent 4395A. A simple hemispherical aggregate model of the breast combining the fat and gland TMMs is also shown, demonstrating the ease of creating anatomically accurate phantoms with these materials.

2 Methods

The breast fat and gland TMMs are made from mixtures of graphite, carbon black and polyurethane, with proportions adapted from [3] and [4]. An impedance analyzer is used to measure the conductivity of the two TMMs over the range 100 kHz – 250 kHz. These values are compared to reference conductivity values for the tissues over the same frequency range [6]. Figure 1 plots the measured and reference conductivities, showing that the range of properties obtained by the TTMs easily cover those of the tissues. Figure 2 shows a simple hemispherical breast phantom created using a heterogenous mixture of the two tissues, in proportions of 30% gland and 70% fat. The two tissues are distributed in discrete locations within the structure. This simple phantom demonstrates the ease of developing more anatomically precise models with this solid, moldable TMM.

3 Conclusions

This study has demonstrated a TMM that can model the conductive properties of biological tissues over the frequency range of interest for EIT medical applications. Further, the material is mechanically and electrically stable over time, and is easily moldable to create precise anatomical structures. As such, this TMM will be a valuable tool for EIT studies involving biological tissues and organs.

4 Acknowledgements

The research leading to these results has received funding from the European Research Council under the European Union's Horizon 2020 Programme/ ERC Grant Agreement BioElecPro n.637780, and from the Hardiman Research Scholarship, NUIG.

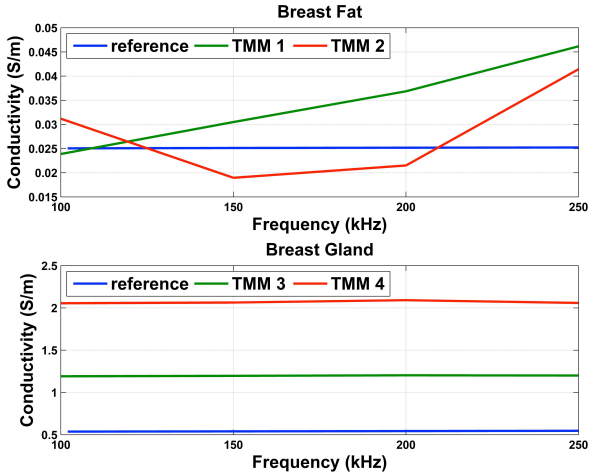

Figure 1: Plots of conductivities for the breast fat (top) and breast gland (bottom) TMM mixtures versus reference values.

Figure 2: Simple hemispherical anatomically accurate breast phantom created using heterogenous mixture of the two tissues.

References

[1] A.T. Mobashsher, *IEEE Mirocw. Mag.,* July, pp 42-62 2015
[2] J.Garrett and E.Fear, *IEEE Antennas Wirel. Propag. Lett.,* vol. 13, pp 599-602, 2014
[3] A.Santorelli, O.Laforest, E.Porter and M.Popovic, *European Conference on Antennas and Propagation (EuCAP)*, 2015
[4] J.Garrett and E.Fear, *IEEE Trans. Antennas Propag.,* vol. 63, no. 4, pp 1693-1700, 2015
[5] *Swisstom.com*, [Online]. Available: http://www.swisstom.com/en/products/pioneer-set. [Accessed: 05-Dec-2016]
[6] H.PA, F. DiGennaro, C.Baumgartner, E.Neufeld, M.Gosselin, D.Payne, A. Klingenböck and N.Kuster, 2015. [Online]. Available: www.itis.ethz.ch/database [Accessed 06-Dec-2016]

DICOM for EIT

Rebecca J Yerworth[1] and Richard Bayford[2]

[1]Dept. Medical Physics and Biomedical Engineering, University College London, UK, r.yerworth@ucl.ac.uk

[2]Middlesex University London, UK

Abstract: With EIT starting to be used in routine clinical practice [1], it important that the clinically relevant information is portable between hospital data management systems. DICOM formats are widely used clinically and cover many imaging modalities, though not specifically EIT. We describe how existing DICOM specifications, can be repurposed as an interim solution, and basis from which a consensus EIT DICOM 'Supplement' (an extension to the standard) can be written.

1 Introduction

One of the messages from Keynote speakers at EIT2016 was the need to present EIT findings in clinically relevant ways, to speed the adoption of EIT in to clinical practice. There already exists a consensus EIT file formats, implemented and managed in EIDORS (sourgeforge.net/projects/eidors3d/). This serves a vital role in enabling data and code sharing between EIT researchers but is largely impenetrable to clinical facing users.

DICOM (dicom.nema.org) is recognised internationally as the standard to adhere to for many imaging modalities, each with one or more Information Object Definitions (IODs), built mainly from agreed standard building blocks ('Modules'). Though originally designed for digitally sharing clinical images, it has expanded to cover waveforms (e.g. EEG) and handle relevant patient and technical data associated with these images as well as clinical reporting. It is designed primarily as a clinical tool, and patients are assigned a unique identifier, which enables all the data and reports etc., from different modalities, and different dates to be linked in a patient information system (PIS).

To create EIT specific IODs would necessitate a Supplement and the setting up of a Work Group to develop it. This takes time, effort and agreement from a consortium of manufacturers and clinical users.

This paper reports on whether DICOM is the way forward for clinical EIT, and whether existing IODs can be repurposed, for EIT use, as an interim solution.

2 Methods

Clinical colleagues were consulted as to the types of EIT data that is clinically meaningful: Images would be useful, but mainly for expert users and researchers; derived parameters as waveforms, very likely especially as similar format to other information on intensive care wards; boundary voltages are considered unnecessary.

A survey of the existing IODs, combined with advice from the DICOM Standards Committee identified those which were likely candidates for repurposing.

Matlab (Mathsworks.com) imaging tool box DICOM functions were used with a custom Matlab script to read Swisstom *.zri files and export the selected images in DICOM Secondary capture format. Derived parameters, including global and regional tidal impedance change (rel. ΔZ) [1,2] were exported as DICOM Waveform Information Object. These were then opened using freely available DICOM viewers and checked for accuracy.

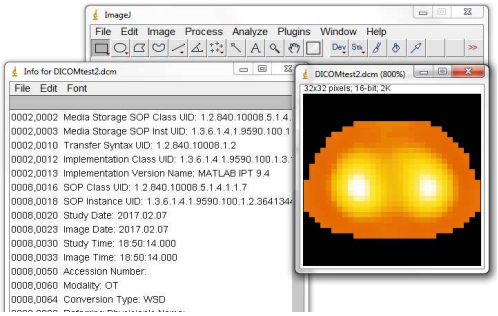

Figure 1: screen shot of EIT image loaded with ImageJ, a popular free DICOM viewer (https://imagej.nih.gov)

3 Conclusions

EIT images and derived waveforms can be exported in DICOM compatible formats by repurposing existing DICOM IODs.

There IODs are not perfect for EIT and we recommend that creation of an EIT specific DICOM Supplement be a longer term goal of the EIT community.

However, these existing IODs can provide an excellent interim solution, speeding up the clinical uptake of EIT, as well as forming a starting point from which to develop a new Supplement.

We recommend that DICOM is adopted as the preferred clinical facing EIT format. To this end we encourage developers to make their clinically relevant outputs available DICOM compatible.

4 Acknowledgements

This project has received funding from the European Union's Horizon 2020 research and innovation programme 2014-2018 under grant agreement No 668259

The authors would like to express their gratitude to the rest of CRADL project team for their insights and advice.

References

[1] Frerichs I, Amato MB, van Kaam AH, Tingay DG, Zhao Z, Grychtol B, Bodenstein M, Gagnon H, Böhm SH, Teschner E, Stenqvist O, Mauri T, Torsani V, Camporota L, Schibler A, Wolf GK, Gommers D, Leonhardt S, Adler A; TREND study group. Thorax 2017;72:83-93

[2] Frerichs I, Becher T, Weiler N. Curr Opin Crit Care. 2014;20:323–32.

EIT based Natural Sleep Monitoring for Obstructive Sleep Apnea Patients

Young Eun Kim[1], Ghazal Ayoub[2], Sang Wook Kim[3], Tong In Oh[1] and Eung Je Woo[1]

[1]Department of Medical Engineering, Graduate school, Kyung Hee University, Seoul, Korea, ejwoo@khu.ac.kr
[2]Department of Biomedical Engineering, Graduate school, Kyung Hee University, Yongin, Korea
[3]Department of Otorhinolaryngology, Gyeongsang National University Hospital, Jinju, Korea

Abstract: There is a growing prevalence of obstructive sleep apnea (OSA) among middle-aged or aged men and women. There exist unmet clinical needs to evaluate OSA effectively in terms of both accuracy and cost. We conducted pilot experiments for OSA patients to detect obstructive apnea, hypopnea and central apnea in the upper airway during natural sleep using an electrical impedance tomography (EIT) system. The time series of reconstructed conductivity images provide diagnostic information about airway collapse for effective treatment planning.

1 Introduction

Obstructive sleep apnea (OSA) is a sleep disorder in which upper airway obstruction over 10 seconds occurs more than 5 times per hour [1]. OSA patients are increasing in prevalence due to ageing and obesity. Polysomnography (PSG) is the current standard method for its diagnosis [2]. However, it requires the sleeping in the special monitoring room with attaching multiple sensors on the body. Usually, the subjects are difficult to sleep naturally because of the first night effect and stress from the large number of sensors [3]. In this study, we propose a new natural sleep monitoring method for the diagnosis of upper airway obstruction using electrical impedance tomography(EIT). Despite of low spatial resolution and low sensitivity due to the intrinsic ill-posed condition and non-linearity, EIT can produce high temporal conductivity images corresponding to the obstruction of upper airway. We conduct preliminary experiments for OSA patients to detect OSA in real time during natural sleep.

2 Methods

We recruited normal subjects and OSA patients. To detect OSA, we used KHU Mark2.5 EIT system [4]. 16 electrodes were attached to the boundary of the upper airway occlusion portion. We obtained the specific model from the 3D scanner (Sense, 3D systems, USA). In order to detect the upper airway obstruction, imperceptive current (1 mA, 10 kHz) was injected to a human body and the induced voltage was measured at a rate of 50 frames/s. PSG signals were recorded simultaneously to analyse EIT data for detecting upper airway obstruction.

3 Results

Fig 1(b) presents conductivity changes in the upper airway region calculated from EIT images and PSG signal. When the PSG signal and the conductivity change were compared, the percentile conductivity was different in hypopnea and obstructive apnea. Fig 1(c) shows time series of conductivity images at the specific time points.

4 Conclusions

EIT can provide the diagnosis information of obstructive apnea and hypopnea in real time during natural sleep. Further validations with cine-MR or videofluoroscopy are required in our future study.

5 Acknowledgements

Research supported by Korean Health Technology R&D Project, Ministry of Health and Welfare, Republic of Korea (HI14C0743).

References

[1] T. Young, P. E. Peppard and D. J. Gottlieb *Am J Respir Crit Care Med.*, 165:1217–1239,2002
[2] Sher, Aaron E., Kenneth B. Schechtman, and Jay F. Piccirillo *Sleep* 19.2: 156-177, 1996.
[3] Lee, Da-Hye, et al. *Psychiatry investigation* 13.2: 203-209, 2016.
[4] H. Wi, H. Sohal, L. M. Alistair, E. J. Woo and T. I. Oh *IEEE Trans Biomed Circuits Syst.* 8:119-128, 2014

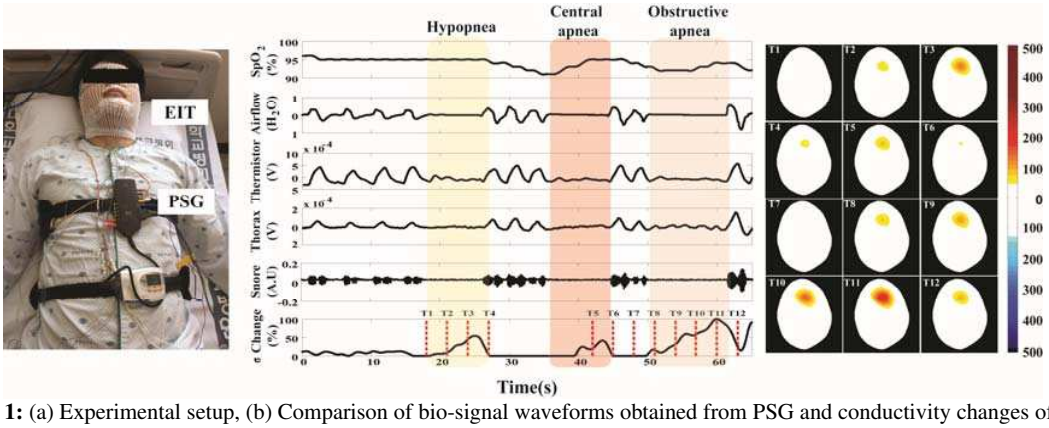

Figure 1: (a) Experimental setup, (b) Comparison of bio-signal waveforms obtained from PSG and conductivity changes of upper airway region calculated from time series of reconstructed EIT images, (c) Time series of conductivity images.

Quantification of subcutaneous fat thickness using static EIT: experimental validation using ultrasound

Hyeuknam Kwon[1,*], Seward B Rutkove[1], Benjamin Sanchez[1]

[1]Department of Neurology, Beth Israel Deaconess Medical Center, Harvard Medical School, Boston, MA 02215-5491, USA.

[*]hyeuknamkwon@gmail.com

Abstract: Here, we evaluate our novel static electrical impedance tomography (EIT) method to quantify subcutaneous fat thickness [1]. The feasibility of the approach is validated through simulations and experiments on volunteers.

1 Introduction

Electrical impedance tomography (EIT) has two fundamental drawbacks for static imaging: (i), the technique is extremely sensitive to forward modeling errors caused by boundary geometry artifacts, and (ii), the absence of reference data required to solve the conventional linear system. As a consequence, the application of minimization-based algorithms is restricted to those situations where the geometry is exactly known, e.g. circular phantoms [2]. To overcome this limitation, we developed a novel static EIT method that uses experimental reference-like data gathered from special current injection patterns [1]. In doing so, the effects of boundary geometry errors on the reconstruction algorithm can be mitigated without requiring exact information of the geometry. Here, we evaluate the feasibility of the approach through simulations and experiments on volunteers using ultrasound. The results reported confirm the feasibility of the technique to detect and estimate the thickness of subcutaneous fat tissue.

2 Methods

We define the measured voltage difference $U_{k,l} := u_k(p_{l^+}) - u_k(p_{l^-})$ for $(k^+, k^-, l^+, l^-) \in \mathcal{P}$, where u_k is the electric potential and $\mathcal{P}$ denotes the set of inject-measure electrodes' indexes (k^+, k^-, l^+, l^-). Note the boundary geometry effects on $U_{k,l}$ can be mitigated by introducing the voltage difference $V_{k,l}$ when the admittivity $\gamma = 1$. To do so, we define the geometry-free data $G_{k,l} := \frac{V_{k,l}}{U_{k,l}}$. We then use the difference of $G_{k,l}^{-1}$ to compensate forward modeling errors introduced by $V_{k,l}$, namely $B_{k,l,k',l'} := G_{k,l}^{-1} - G_{k',l'}^{-1}$. By assuming $\gamma = \gamma_0$ constant in the subcutaneous fat region $\Omega_f \subset \Omega$ and $\partial\Omega \subset \overline{\Omega_f}$, its influence on muscle can be removed as follows

$$B_{k,l,1,2} = -\int_{\Omega \setminus \Omega_f} \frac{\nabla v_l \cdot \beta \nabla u_k}{V_{k,l}} - \frac{\nabla v_2 \cdot \beta \nabla u_1}{V_{1,2}}\, d\mathbf{r}, \quad (1)$$

where $\beta(\mathbf{r}) = (\gamma(\mathbf{r})/\gamma_0 - 1)/I$, and v_k is the electric potential when $\gamma = 1$.

3 Simulation and experiment results

We simulated a two-layer cylindrical model including subcutaneous fat and muscle tissues (see detail in Fig.1 left). The cumulative intensity plots in Fig.1 (right) confirm the feasibility to estimate accurately the subcutaneous fat thickness.

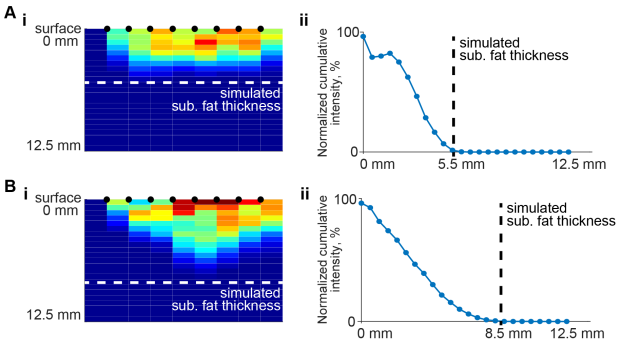

Figure 1: (i) Reconstructed image using 8 electrodes positioned over the subcutaneous fat (in black circles). The white dashed lines show the separation between subcutaneous fat and muscle tissues considering two subcutaneous fat thicknesses: 5.5 mm (A) and 8.5 mm (B). (ii) Cumulative intensity plots.

Fig.2 shows the result of measuring the biceps femoris muscle of a volunteer. The subcutaneous fat thickness was determined using ultrasound (Terason t3000, Teracorp Inc, Burlington, MA, USA).

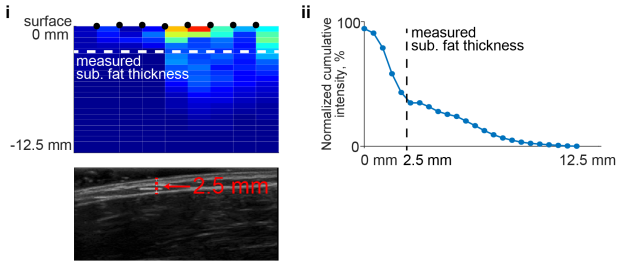

Figure 2: (i) Reconstructed image. The ultrasound image is shown below. (ii) Cumulative intensity plot.

4 Conclusions

Here we presented the cumulative value of the reconstructed image as a simple quantitative metric to estimate the skin and subcutaneous combined thickness. Numerical simulation results confirm the viability of the approach considering different thicknesses of subcutaneous fat tissue. The experimental results are also in good agreement with those obtained with simulation. Future work will focus on studying more robust metrics, for example, by detecting changes in the cumulative slope.

References

[1] H Ammari, H Kwon, S Lee, J K Seo *SIAM Journal on Imaging Sciences (SIIMS)*, Accepted, 2017.

[2] E Murphy, A Mahara, R Halter *IEEE Transactions on Medical Imaging*, 35:1593–1603, 2016.

Application of electrical capacitance tomography on thrombus detection in blood extracorporeal circulation systems

Jianping LI[1]*, Daisuke Kikuchi[1], Madoka Koishi[1], Achyut Sapkota[2], Masahiro Takei[1]
[1]Graduate School of Mechanical Engineering, Division of Artificial System Science, Chiba University, 1-33 Yayoi, Inage, Chiba, 263-8522 Japan; Email address: jianpingli2013@gmail.com
[2]Department of Information and Computer Engineering, National Institute of Technology, Kisarazu College, 2-11-1 Kiyomidai-Higashi, Kisarazu, Chiba, 292-0041 Japan

Abstract: Electrical capacitance tomography (ECT) is applied for the detection of thrombus formation in extracorporeal circulation systems. An ECT sensor with eight electrodes was manufactured and placed around the blood circulation tube. ECT images got from the experiments indicate that: from t=0 min to t=10 min, the capacitance of blood goes up; after that, the capacitance of blood falls down continuously.

1 Introduction

Blood extracorporeal circulation systems are widely utilized in medical science, such as left ventricular assist devices (LVAD), extracorporeal membrane oxygenation systems (ECMO) and artificial hemodialysis systems. However, the patients with blood extracorporeal circulation systems are always facing the critical threat of thrombosis [1]. Generally, the patients receive regular and ration antithrombotic therapy which brings troubles to patients and sometimes causes the haemorrhage. Therefore, it is of great significance to develop the online thrombus detection technology in order to offer efficient antithrombotic medicine only at the well needed time [2].

In this study, electrical capacitance tomography is applied to the online detection of thrombus formation due to its advantages of high speed, compact size and reliability. A compact ECT sensor is wrapped around the blood tube; hence, the ECT images of the blood tube cross section are obtained. From the variation of the capacitance images, the thrombus formation process is monitored visually.

2 Methods

2.1 Electrical capacitance sensor

Fig. 1 illustrates the construction of the proposed ECT sensor. It consists of the earth electrodes (EE), the flexible print circuit (FPC), the blood tube, the measurement electrodes (ME), the screen electrode (SE) and the public ground electrodes (GE). During the experiments, the blood is stored inside the blood tube which is coated with heparin. Eight measurement electrodes and eight earth electrodes are placed around the blood tube to measure the capacitance of blood and generate the ECT images.

2.2 Experimental conditions

Fresh swine blood with 1/10 tri-sodium citrate solution (3.28%) was used for the experiments. The hematocrit of the swine blood was measured by the centrifuge (3220; Kubota Corporation) at 12000 rpm for 5 minutes, and the value was H=43%. During the experiments, 30 mL swine blood and 0.45 mL $Cacl_2$ solution (2%) were mixed together inside the ECT sensor. The applied voltage for the compact ECT sensor was U=18 V, and the frequency of this AC voltage signal was f=160 kHz, the measurement speed was 75 points/s. This voltage signal was generated and measured by the ACECT system (ACECT-2000; ECT Instrument Corporation). Normalization of measured capacitance was utilized to obtain better ECT images according to the following equation [3]:

$$C_{\mathrm{r}} = \frac{C^{\mathrm{m}} - C^{\mathrm{L}}}{C^{\mathrm{H}} - C^{\mathrm{L}}} \tag{1}$$

where C^{m} is the measured capacitance; C^{L} is the low capacitance obtained by NaCl solution with a concentration of 9g/L; C^{H} is the high capacitance measured by pure water.

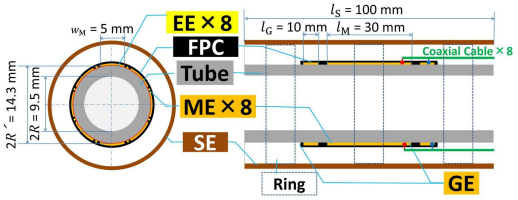

Figure 1: Structure of the proposed compact ECT sensor

3 Results and Conclusions

Fig. 2 shows the ECT images of the thrombus formation during the experiments. The red colour means high capacitance, and blue colour represents low capacitance. It can be seen that, at the beginning, the capacitance of blood is low; and then, from time t=0min to t=10min, blood capacitance increases to high value; after that, blood capacitance decreases slowly.

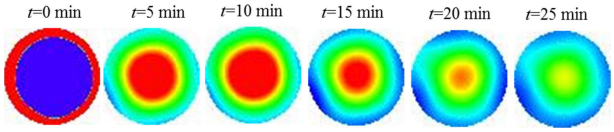

Figure 2: ECT images during thrombus formation

This study generates the possibility of the online thrombus detection method based on electrical capacitance tomography. It is of great significance for the efficient therapy to patients with extracorporeal circulation systems.

4 Acknowledgements

This work was supported by JSPS KAKENHI Grant Number JP16H02312 and 16F16368.

References

[1] D. N. Huu, D. Kikuchi, O. Maruyama, A. Sapkota, M. Takei *Flow Measurement and Instrumentation*, 53: 172-179, 2017.
[2] A. Sapkota, T. Fuse, M. Seki, O. Maruyama, M. Sugawara, M. Takei *Flow Measurement and Instrumentation*, 46:334-340, 2015.
[3] Z. Ren, W. Yang *IEEE Sensors Journal*, 15: 3037-3049, 2015.

Total Variation and L_1 Joint Regularization for High Quality Cell Spheroid Imaging Using EIT

Yunjie Yang, Hancong Wu and Jiabin Jia

Agile Tomography Group, School of Engineering, University of Edinburgh, Edinburgh, UK, jiabin.jia@ed.ac.uk

Abstract: A total variation and l_1 joint regularization method is proposed for cancer cell spheroid imaging on a miniature EIT sensor. High spatial resolution and low noise reconstruction results are obtained in the experiment. The method can be applied in long-term cell culture and cell-drug interaction monitoring.

1 Introduction

Real-time and long-term cell spheroid imaging is requisite for study of cell culture process and cell-drug interaction [1]. As a potential candidate, the challenges of applying EIT for imaging cell spheroids include improving spatial resolution for accurate geometry estimation of tiny targets and distinguishing the targets from artefacts and noises. Therefore, to facilitate quantitatively analysis regarding the cell dynamics from the reconstructions, stable and high quality image reconstruction based on the noisy, weak measurement signals is an essential.

In this work, a Total Variation (TV) and l_1 joint regularization method is proposed to produce tomographic images on tiny objects with high spatial resolution and improved noise reduction performance. The work is based on time-difference measurements $\Delta\mathbf{V}$ and the linearized EIT model, as expressed by

$$\Delta\mathbf{V} \approx \mathbf{J}\Delta\boldsymbol{\sigma} + \mathbf{e} \tag{1}$$

where $\boldsymbol{J}$ is the Jacobian matrix; $\mathbf{e}$ is additive noise. $\Delta\boldsymbol{\sigma}$ is the conductivity change with respect to a homogeneous background in the sensing domain.

2 TV-L_1 Joint Regularization Method

The isotropic TV regularization [2] and l_1 regularization [3] are combined together to promote a sparse conductivity estimation with a clear boundary. The resulting optimization problem can be formulated as

$$\Delta\hat{\boldsymbol{\sigma}} = \arg\min \frac{1}{2}\left\|\Delta\mathbf{V} - \mathbf{J}\Delta\boldsymbol{\sigma}\right\|_2^2 + \lambda_1\left\|\Delta\boldsymbol{\sigma}\right\|_{\mathrm{TV}} + \lambda_2\left\|\Delta\boldsymbol{\sigma}\right\|_1 \tag{2}$$

where $\|\Delta\boldsymbol{\sigma}\|_{\mathrm{TV}}$ is the TV norm of $\Delta\boldsymbol{\sigma}$; λ_1 and λ_2 are the regularization factors. In spite of the non-differentiability of Eq. (2) at origin point, by introducing the sub-gradient of l_1 norm, gradient-based method such as Newton's method can be applied to trace a local minimum of Eq. (2). The iteration form can be formulated as

$$\Delta\boldsymbol{\sigma}_{x,y}^{i+1} = \Delta\boldsymbol{\sigma}_{x,y}^{i} - \alpha^i\left\{\nabla_{x,y}L(\Delta\boldsymbol{\sigma}^i) + \lambda_2\nabla_{x,y}\left(\left\|\Delta\boldsymbol{\sigma}^i\right\|_1\right)\right\} \tag{3}$$

where (x, y) denotes the coordinate of a pixel; α^i is the iteration step size; and

$$\nabla_{x,y}L(\Delta\boldsymbol{\sigma}^i) = \mathbf{J}^{\mathrm{T}}(\mathbf{J}\Delta\boldsymbol{\sigma}^i - \Delta\mathbf{V})\big|_{x,y} + \lambda_1\nabla_{x,y}\left(\left\|\Delta\boldsymbol{\sigma}^i\right\|_{\mathrm{TV}}\right) \tag{4}$$

where the gradient of TV norm can be easily calculated by using proper relaxation. More details can be found in [1].

The sub-gradient of l_1 norm can be defined as

$$\nabla_{x,y}\left(\left\|\Delta\boldsymbol{\sigma}^i\right\|_1\right) = \begin{cases} sign(\Delta\boldsymbol{\sigma}_{x,y}^i), & \left|\Delta\boldsymbol{\sigma}_{x,y}^i\right| \geq \varepsilon \\ 1, & \left|\Delta\boldsymbol{\sigma}_{x,y}^i\right| < \varepsilon, \nabla_{x,y}(L(\Delta\boldsymbol{\sigma}^i)) < -\lambda_2 \\ -1, & \left|\Delta\boldsymbol{\sigma}_{x,y}^i\right| < \varepsilon, \nabla_{x,y}(L(\Delta\boldsymbol{\sigma}^i)) > \lambda_2 \\ 0, & \left|\Delta\boldsymbol{\sigma}_{x,y}^i\right| < \varepsilon, \left|\nabla_{x,y}(L(\Delta\boldsymbol{\sigma}^i))\right| \leq \lambda_2 \end{cases} \tag{5}$$

where ε is the relaxation factor 1e-7 in this work.

3 Experiment Results on MCF7 Cells

Two imaging experiments on MCF7 cell spheroid with a diameter of 700 μm were carried out on a miniature EIT sensor with 15 mm diameter, as illustrated in Fig. 1. MCF7 cells are human breast cancer cells, which are provided by the Tissue Culture Lab at the University of Edinburgh. The reconstructed images are compared with those only using the l_1 regularization. The comparison confirms that the proposed algorithm can provide cell spheroid images with higher spatial resolution and better noise reduction performance.

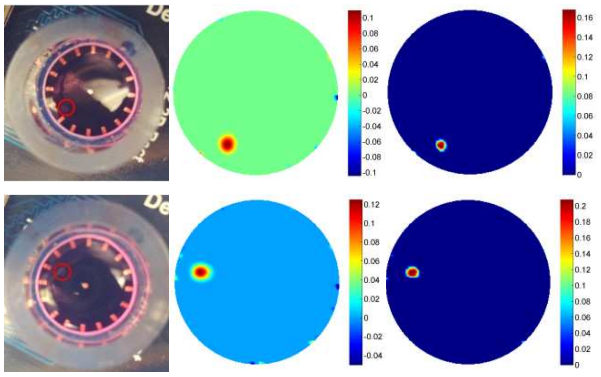

Figure 1: Experiment results. Note that the second column is based on l_1 regularization and the third are the TV-L_1 results.

4 Conclusions

The TV-L_1 joint regularization method demonstrates high quality cancer cell spheroid imaging results on a series of miniature sensor experiments. The method is promising in conducting long-term cell culture process and cell-drug interaction monitoring.

5 Acknowledgements

The authors would like to thank 2015 IEEE I&M Society Graduate Fellowship Award for supporting the work.

References

[1] Y Yang, J Jia, S Smith, et al *IEEE Sens. J*, 17.2: 514–523, 2017
[2] D Strong, T Chan *Inverse problems* 19: S165, 2003
[3] Y Mamatjan, A Borsic, D Gürsoy, A Adler *Physiol Meas*. 34: 1027, 2013

Using a two plane EIT-System to reconstruct conductivity change in lung lobes

Benjamin Schullcke, Sabine Krueger-Ziolek, Bo Gong and Knut Möller
Institute of Technical Medicine, Furtwangen University, Villingen-Schwenningen, Germany
benjamin.schullcke@hs-furtwangen.de

Abstract: Information about the lung anatomy has been used to combine voxels in 3D-EIT according to the shape of the lung lobes. This dimension reduction in the image reconstruction process leads to stable and easy interpretable data of conductivity change in lung lobes and might be useful for applications where knowledge about the performance of particular lung lobes is beneficial, e.g. during endobronchial valve placement for COPD patients.

1 Introduction

The placement of endobronchial valves is one of the surgical options for the treatment of severe emphysema in patients with chronic obstructive lung disease (COPD). Thereby a one-way valve is implanted into a bronchus to occlude a lung lobe and allow the air to exit during expiration. However, not all COPD patients with emphysema are suitable to be treated with endobronchial vales. Typically the severity and distribution of the emphysema is assessed by high resolution CT [1], whereas endobronchial valves seem to be most beneficial for heterogeneous emphysema.

In this paper we describe how the advantages of EIT might be used as an alternative imaging method for patient selection, to monitor the correct functioning of the valves and to identify the target lobe for endobronchial valve placement.

2 Methods

2.1 Simulation model

Lung lobes of a COPD patient were manually extracted from CT-scans captured at end-expiration and end-inspiration. Based on these datasets two 3D FEM models of the thorax were generated and voxels were assigned to the respective lobes, as visualized in Figure 1(a). 2x16 electrodes were placed equidistantly around the thorax in two layers at the 3rd and 7th intercostal space. Boundary voltages were simulated for end-expiration and end-inspiration by changing the conductivity of 'lung-voxels' between $\sigma_{exp} = 120mS/m$ and $\sigma_{insp} = 60mS/m$, respectively. Voxels not assigned as lung tissue were modelled with a constant conductivity of $\sigma_{bkg} = 480mS/m$. Spots of different size were arbitrarily placed in the lobes to model different amount of emphysema and trapped air. In the spots the conductivity remained at $\sigma_{exp} = 120mS/m$ during simulated inspiration. Figure 1(b) depicts one of 100 arbitrary patterns of simulated emphysema and trapped air.

2.2 Lobe reconstruction

A standard one-step GN algorithm was used for reconstruction of the conductivity change in the lobes. The Jacobian $\mathbf{J}$ was modified [2], resulting in $\mathbf{J}_{lobe} = \mathbf{JL}$, with

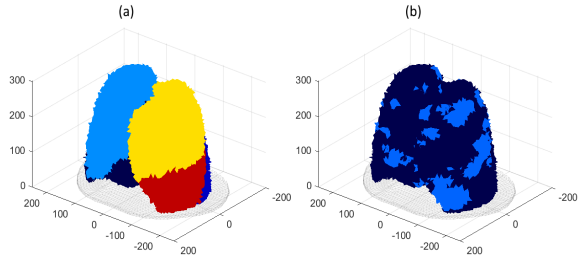

Figure 1: (a) fem model of the lung with separated lobes. (b) arbitrary obstruction pattern sprinkled in the lobes to simulate heterogeneous emphysema and mucus plugging.

$$L_{i,j} = \begin{cases} 1, & if\ element\ i\ belongs\ to\ lobe\ j \\ 0, & else \end{cases} \quad (1)$$

With this reduced dimension of the Jacobian no regularization is needed and the conductivity change in the lobes was estimated from simulated voltage differences $\Delta\mathbf{v}$ according to

$$\Delta\hat{\boldsymbol{\sigma}}_{lobe} = (\mathbf{J}_{lobe}^{\mathrm{T}}\mathbf{J}_{lobe})^{-1}\mathbf{J}_{lobe}^{\mathrm{T}}\Delta\mathbf{v} \quad (2)$$

Simulations of 100 patterns of emphysema have been carried out, with models including excursion of thorax and lung lobes during inspiration. The capability of the described EIT configuration to identify the lobe which is most severely affected by emphysema has been evaluated.

3 Conclusions

The correct classification of a severely affected lobe depends on the amount of emphysema compared to the remaining lobes. If the conductivity change in the severely affected lobe is only 70% or less of the mean conductivity change in the remaining lobes, the proposed method is able to detect the affected lobe with a specificity of more than 77%. The sensitivity of the correct classification of lobes differs, whereby the right upper lobe has the lowest and the left upper lobe has the highest sensitivity. Results reveal that EIT is able to determine affected lobes which might be used during endobronichal valve placement or for long-time monitoring in various diseases.

4 Acknowledgements

This work was partially supported by the Federal Ministry of Education and Research (BMBF) grant 03FH038I3 (MOSES).

References

[1] R Eberhardt et al., *Int J Chron Obstruct Pulmon Dis,* 2147-2057, 2015
[2] B Schullcke et al., *Med Phys*, 426-436, 2017

Combined electrical and thermal simulation of EIT to detect lesion formation in RF ablation using internal electrodes

Duc M Nguyen[1], Danyi Zhu[1], Tony Barry[2], Pierre Qian[2], Alistair McEwan[1]

[1]School of Electrical and IT, Sydney University, Sydney, Australia, minh.d.nguyen@sydney.edu.au

[2]Department of Cardiology, Westmead Hospital, Sydney, Australia

Abstract: Electrical Impedance Tomography (EIT) has the potential to measure direct information of lesions during a Cardiac Radiofrequency (RF) ablation. In this study, we examined combined electrical and thermal simulations to study the use of internal electrodes and the amplitude threshold for constraining suspected lesions. The volume could be tracked better but less precise than the depth, i.e. 10-15% over a wider range versus within 5% over shorter.

1 Introduction

Radiofrequency (RF) ablation is used widely in treating some Arrhythmias [1]. However, none of the current online monitoring methods can provide doctors with dynamic lesion information such as depth or volume, which is vital for the cardiologist to understand the on-going ablation. Electrical Impedance Tomography (EIT) may be feasible in measuring such information [2], although it suffers from ill-posedness and hence low resolution. In this study, we tested EIT's feasibility in RF ablation simulations with the use of external electrodes and one internal electrode and constrained the lesion using an amplitude threshold.

2 Methods

2.1 Simulation

We simulated RF ablation in a block of liver tissue within a tank using COMSOL 5.1 and bioheat model (constant ablation voltage of 40V), then converted the temperature to conductivity and simulated voltages using Matlab R2016b and EIDORS (Fig.1). The temperature-conductivity (T-C) relationship was based on realistic values provided in [3] with fast heating ratio. To avoid the inverse crimes we used two different FEM models for the forward and inverse problem. The Jacobian was only calculated inside the tissue, which produces more accurate answer then the whole-model Jacobian [4]. This assumed that the geometry was pre-known and the burning area was defined within the tissue only. There were 16 external electrodes (2 rings) and 1 internal electrode (all 64 electrodes of MEA was combined as a single electrode [5]). The best pattern of stimulation and measurement was chosen based on the z-score evaluation [6] explored fully in [7]. Finally, the NOSER algorithm was used for reconstruction.

2.2 Lesion constraint

The lesion was defined as a region consisting of necrotic tissue after its temperature exceeded 50°C. The volume and the depth of the lesion were tracked as these are of most interest to the cardiologist. Some previous studies like [2] re-converted the conductivity change into a temperature change. However this is difficult to achieve because of the ill-posedness and the uncertainty of the termperature-conductivity relationship of real tissue. Instead, we used an amplitude threshold of 20% of the maximum value to constrain the suspected lesions.

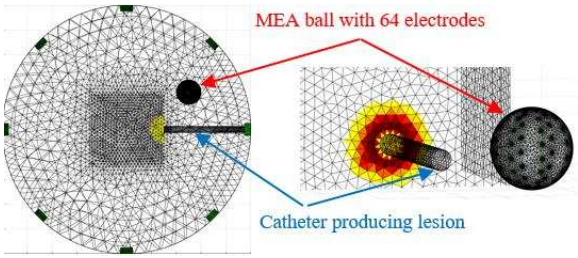

Figure 1: EIT model with MEA ball (64 electrodes combined as one) and an example of a simulated lesion.

3 Results and Conclusions

To the best of our knowledge this study is the first to combine the bioheat model and EIT. It provides researchers with a flexible tool to evaluate EIT performance in ablation, before experiments in vitro and in vivo.

As shown in Table 1, the amplitude-threshold-based lesion solution, with the support of internal electrode, was able to track the lesion size at a reasonable level, but the depth was much less sensitive. However this method could be useful if a target threshold was set at e.g. at 6.2mm depth and 600mm^3. This also suggests such thresholds may only accurate be for a small number of cases. In the future, an adaptive multiple thresholds solution could be considered for a more accurate measurement.

References

[1] H Calkins, et al. *Circ Arrhythm Electrophysiol,* CIRCEP-108.824789,2009
[2] KD Paulsen, et al. *INT J HYPERTHER*, 12.5:573-591,1996
[3] EG Macchi, et al. *J. Phys. D: Appl. Phys.*, 47.48:485401,2014
[4] L Miao, et al. *IEEE Trans. Instrum. Meas.*, 63.12:2903-2910,2014
[5] D Zhu, et al. *Biomed Phys Eng Express*, 3.1:015007,2017
[6] A Adler, et al. *Physiol Meas*, 32.7:731,2011
[7] Minh DN, et al. *Biomed Eng (BME-HUST), Int Conf on IEEE,* p.36, Hanoi,Vietnam, Oct 2016

Table 1: The best results in measuring the depth (minimum error: < 5%) and the volume (minimum error: 10-15%) over 90 seconds.

Maximum / Best matched depth (mm)	Matched period (second)	Overall error: mean / std (mm)	Maximum / Best matched volume (mm^3)	Matched period (second)	Overall error: mean / std (mm^3)
7.7/ 5 and 6.2 (mm)	32-40 and 61-66 (s)	0.03/1.17 (mm)	690/520-640 (mm^3)	58-76 (s)	111/35 (mm^3)

Various electrode configurations for in-depth detection of electrical impedance mammography

Min Xu, Xiao-Qian Chen, Gerald Sze, David Barber and Wei Wang

Micro Image Biotech Ltd, Cambridge, UK, w97wang@yahoo.co.uk

Abstract: With optimized planar and backplane configuration and driver-receive patterns, the combined planar and backplane electrode configuration (CPBEC) is analysed. To evaluate different electrode distributions, this paper gives the calculation method of sensitivity, resolution and contrast. The optimization of electrode arrangement is verified by simulation showing that the detectable depth reaches 38mm when the SNR is 58dB.

1 Introduction

This paper mainly discusses electrode configurations and its optimization, the common electrode arrangements include: planar electrodes, backplane electrodes and its deformation [1-5].

2 Methods

2.1 Theory

The pseudo-inverse of sensitivity matrix S_n of EIT could be expressed as:

$$S_n^+ = (S_n^t S_n + \gamma_1 \alpha^2 I)^{-1} S_n^t \quad (1)$$

Where γ_1 is the first eigenvalue of $\mathbf{S_n^t S}_n$,α is a weighting factor and $\boldsymbol{I}$ is an identity matrix.
The sensitivity matrix of the EIM system is defined as R:

$$R = (SN^tSN + sv\alpha^2 I)^{-1} SN^tSN \quad (2)$$

The sum of the R column is sensitivity, and the maximum value over the column is contrast. The resolution diameter is described as imaging sensitivity divided by the contrast.

2.2 Electrode configuration discussion

Figure 1 shows the CPBEC configurations. The planar configuration has 85 electrodes, and the drive and receive pattern is exactly same to [4]. The number of backplane electrodes is selected as 18 and the drive and receive electrode pairs spacing one electrode, similar to [6]. A 3D mesh is used for image reconstruction, the location of backplane electrodes must on the mesh node. In this system, the electrodes are placed at the first and forth layer when there are five layers (height is 38mm) according to simulation.
Fig. 2 shows the sensitivity and contrast value of CPBEC are increased compared to the planar plane. And the resolution values of each layer are obvious decreased, which means the quality of reconstructed images, especially the top slice image, should be improved.
The breast model and reconstructed images are shown in Fig.3, the conductivity of adipose, stroma and tumour are set to 0.449, 0.787, 3.917ms/cm at 50kHz [7]. The diameter of the model is 191.5mm and the thickness is 38mm. SNR of 58dB white Gaussian and random noise are added. Both of tumours are 9mm in diameter. The simulation shows that both configurations can detect the object on the second layer, but for the object on the top, CPBEC has better sensitivity, while the planar configuration cannot detect this object.

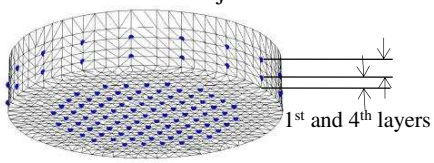

Figure 1: Combined Backplane and Planar electrode configuration

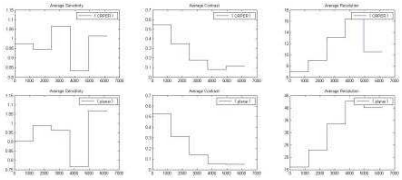

Figure 2: Sensitivity, contrast and resolution of electrode configurations. The 1st row is by CPBEC, 2nd row is by planar

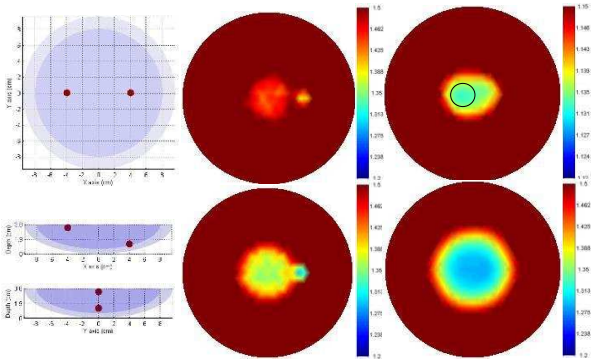

Figure 3: Reconstructed images of simulation. The 1st row is reconstructed images by CPBEC, 2nd row is by planar

3 Conclusions

The combination of planar and backplane electrode configuration can increase the sensitivity of the planar electrodes. The height of backplane electrodes should be selected based on the detecting depth of planar electrodes or the detecting depth of planar combined with backplane. The detection depth of planar is influenced by layer numbers. 18 is an appropriate number of electrodes on the backplane, since excessive number cannot bring much improvement but results with much more artefact.

References

[1] W. Wang, et al *Conf 20th IEEE*, p2: 1042-1043,IEEE,1998
[2] W. Wang, M. Tang, et al *PhysiolMeas*, 22(1): 39, 2001
[3] G. Sze, *Dissertation*, Univ. Sussex, 2012
[4] X. Zhang, W. Wang, G. Sze, et al *IEEE*, 33(12): 2223-2241, 2014
[5] G. Ye, et al, *Microwave and Optical Techn Let*, 50:3261-3271, 2008
[6] A. Adler, et al, *Physiol Meas*, 32(7): 731,2011
[7] J. Jossinet, *Physiol Meas*, 19(1): 61, 1998

EIT of muscle contraction: A preliminary study

Seward B. Rutkove[3], Ethan Murphy[1], and Ryan J Halter,[1,2]

[1]Thayer School of Engineering, Dartmouth College, Hanover, NH, USA, ryan.halter@dartmouth.edu
[2]Geisel School of Medicine, Dartmouth College, Hanover, NH, USA
[3]Beth Israel Deaconess Medical Center, Boston, MA, USA srutkove@bidmc.harvard.edu

Abstract: To date, there are no good tools to assess muscle contraction in real time, outside of the evaluation of force, which provides only a non-specific output. Given the short time scale of electrical impedance measurements, its use for assessing muscle contraction in real time is a logical application. Here, we evaluate EIT data during a muscle contraction in preparation for studies in patients with neuromsucular diseases.

1 Introduction

The assessment of muscle contraction in real time remains a remarkably challenging proposal. Standard methods such as force output are nonspecific and do not provide any information on the geometrical or stress-related changes within the muscle itself. Standard imaging modalities such as MRI and CT are generally slow and inconvient or, like ultrasound, are challenging to quantify. Needle electromyography only evalutates the depolarization of the muscle fibers and not the contraction itself. EIT could potentially be applied in this way to assist in wholistically evaluating changes in the muscle structure and strain during a contraction. It is anticipated that in disease, the normal contractile patterns will be disrupted, causing atypical stresses in the muscle which may produce irregular alterations in the EIT signal. Here, we explore muscle contraction in a healthy population as a means to obatin early proof-of-concept data for future use in patients with neuromuscular disease.

2 Methods

We designed and fabricated a 4x5 rigid electrode array with 5 mm x 5 mm electrodes, interfaced the array to our EIT data acquisition system, and recorded real-time impedance data at 10 kHz from three healthy volunteer's biceps under different loading conditions (Figure 1). Specifically, the arm was bent at ~45^o and weights of 5 lbs, 10 lbs, and 15 lbs were used to load the bicep. A FEM mesh was created to model the bicep volume below the electrode array and an open-domain algorithm was used to reconstruct 3D conductivity images for the different loads. Data recorded from an unloaded arm held at a 45^o angle (same pose as Figure 1) was used as a reference data set. Difference images were computed between the unloaded and loaded conditions.

3 Results

Data was collected from 3 healthy subjects (only one subject is displayed here). An increase in conductivity associated with increased load was observed both in the coronal and axial views of the biceps (blue region). Other areas of reduced conductivity were also identified, more apparent on the axial sections. Maximum changes in conductivty in both the positive and negative direction were ~0.15 S/m when loaded with 15 lbs.

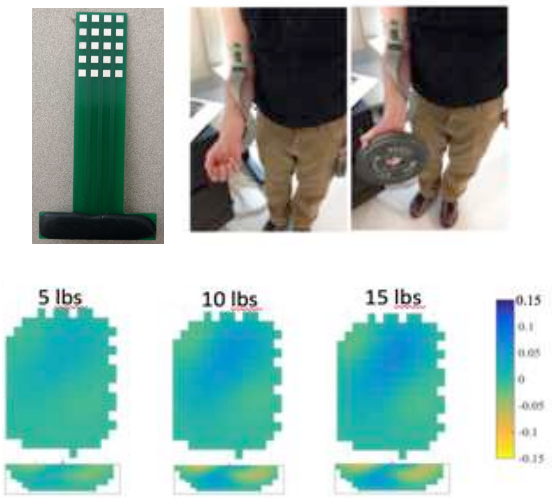

Figure 1. Real-time EIT data from healthy volunteer contracting biceps with different weights (as indicated in left photos). These coronal and axial impedance images are "difference images" comparing at rest values with active contraction. Note increasing conductivity region (blue) with increasing force generation on coronal images, likely related to increasing muscle fiber size and tissue swelling with active isometric contraction. Smaller regions of decreased conductivity are also observed on the axial images.

4 Conclusions

This is the first study to attempt an EIT image of muscle during contraction. The data suggest that alterations in the muscle are detectable and these changes are force dependent. The exact nature of what underlies these alterations is unknown, but may reflect alterations in muscle fiber size with contraction or changes in blood flow. Further study of this novel approach to muscle imaging may be valuable for clinical diagnostic assessment and for assessing the effects of therapy.

References

[1] Khan S, Manwaring P, Borsic A, Halter RJ, "FPGA Based Voltage & Current Dual Drive System for High Frame Rate Electrical Impedance Tomography," IEEE Transactions on Medical Imaging, 34(4): 888-901, 2015.

[2] Murphy E, Mahara A, Halter RJ, "A Novel Regularization Technique for Microendoscopic Electrical Impedance Tomography," IEEE Transactions on Medical Imaging, 35(7):1593-603, July 2016

Preliminary volunteer experiment with an EIM system

Gerald Sze[1], Min Xu[1], Zhao Song[1], Weibo Zhang[2] and Wei Wang[1,2]
[1]Micro Image Biotech Ltd, Cambridge, UK, w97wang@yahoo.co.uk
[2]Institute of Acupuncture, Chinese Academy of TCM, Beijing, China, w97wang@yahoo.co.uk

Abstract: This paper demonstrates volunteer experimental results that acquired from an EIM system that adopts the planar electrode configuration [1]. We have measured three volunteer subjects in different ages with a fixed depth of saline in 28mm. Different regularization factors and the use of variable layer thickness method are analysed on the reconstructed images of the three volunteers.

1 Introduction

An electrical impedance mammography (EIM) system [1] using 85 planar electrodes has been developed for breast cancer detection. Recently volunteer trials have been carried out and presented here, with two ad-hoc methods that improve the quality of the reconstructed images.

2 Methods

2.1 Regularization factor

Below is the general equation of EIT that solving a solution of conductivity distribution with an array of known impedance and calculated sensitivity matrix:

$$\Delta c = S^{-1}\Delta v \quad (1)$$

Since the inverse of S, S^{-1}, is very ill-conditioned, the formal solution to this would be:

$$\Delta c = |S^t S + \propto^2 I|^{-1} S^t \Delta v \quad (2)$$

In this case the inverse exists and is well-conditioned provided the regularization factor $\propto$ is not too small.

2.2 Variable layer thickness

The first plane of image is always noisy. This is because the voltage gradients close to the electrode plane are poorly modelled by the mesh. All data that presented in this paper are measured from a saline tank with 28mm depth. Reconstructed images are displayed as four layers, as such the depth of each layer is 7mm. The variable layer thickness (VLT) method uses thinner layers close to the electrodes and thicker layers further away. The first layer was replaced with 4 layers, the second with 2 layers. The depth co-ordinate for the layer surfaces is calculated using an exponential model. The first 4 layers were combined by taking average after reconstruction as one layer.

2.3 Volunteer

Three healthy volunteer subjects in different ages are involved. We expect different age represent different distribution of stroma and adipose tissue in breast.

Table 1: Volunteer details

Volunteer ID	Age
F0001	32
F0002	28
F0003	45

3 Results

Results are displayed as resistivity images. Red represents higher resistivity and blue represents lower.

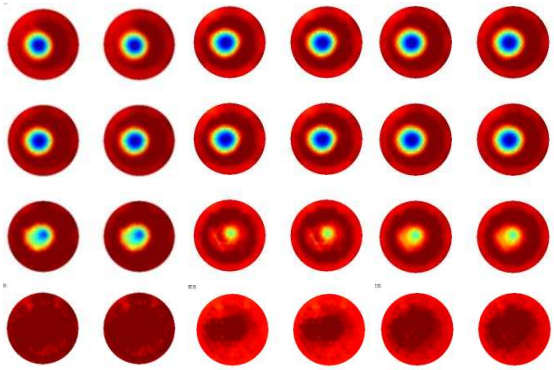

Figure 1: F0001 results. From left to right columns: right breast without VLT,∝=0.05; Left breast without VLT,∝=0.05; Right breast with VLT,∝=0.05; Left breast with VLT,∝=0.05; Right breast with VLT and ∝=0.1; Left breast with VLT and ∝=0.1

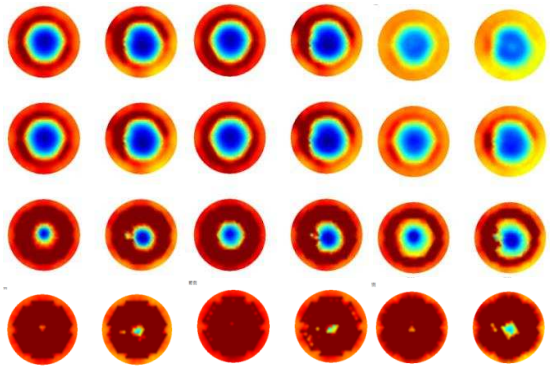

Figure 2: F0002 results

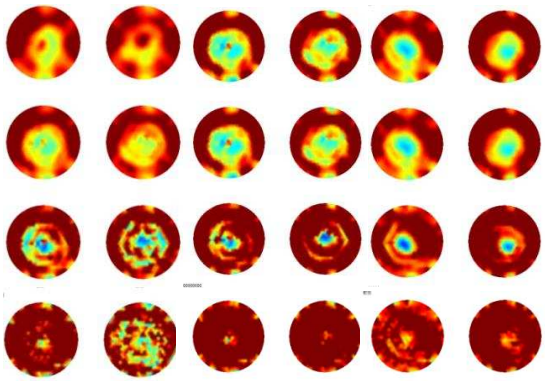

Figure 3: F0003 results

4 Conclusions

Better results of F0001 and F0002 were reconstructed by using VTL and ∝=0.05. F0003 has less stroma (blue region in image) because it belongs to older age group, better results could be found by using VTL and ∝=0.1.

References

[1] G. Sze, *Dissertation*, Univ. Sussex, 2012

Nanoparticle Electrical Impedance Tomography

Richard Bayford[1], Sven Nordebo[3], Ivan Roitt[1], Tom Rademacher [1], Rui Damaso[1], Yu Wu[2], Nima Seifnaraghi[1], and Andreas Demosthenous[2]

[1]Dept. Natural Sciences, Middlesex University UK, [2]Dept. Electronic and Electrical Engineering, University College London, UK, Dept. Physics and Electrical Engineering, Linnaeus University, 351 95 Växjö, Sweden.

Abstract: We have developed a new approach to imaging with electrical impedance tomography (EIT) using gold nanoparticles (AuNPs) to enhance impedance changes at targeted tissue sites. This is achieved using radio frequency (RF) to heat nanoparticles while applying EIT imaging. The initial results using 5-nm citrate coated AuNPs show that heating can enhance the impedance in a solution containing AuNPs due to the application of an RF field at 2.60 GHz.

1. Introduction

Gold nanoparticles provide a potentially viable mediator for hyperthermia tumor treatment using laser and radio frequency (RF) excitation. Aspects of nanoparticle chemistry, which affect thermal dissipation, include the hydrodynamic diameter of the particle, the oxidation state and related magnetism of the core, and the chemical nature of the ligand shell. It is possible to use RF to heat nanoparticles (Nordebo *et al.,* 2017). The appropriate RF frequency is linked to the size of the nanoparticles and materials used to construct them. Magnetic field hyperthermia can be made more effective by the use of biocompatible super paramagnetic nanoparticles, principally iron nanoparticles. In principle these particles help heat cancerous tissue by creating oscillations that produce heat from friction. Hypothermia of cancer cells could also be mediated by gold nanoparticles, which have the advantage that they are biocompatible allowing a range of ligands to be attached to them. Gold nanoparticles, nanorods and nanoshells have been applied with visible laser sources that excite the particles at or near their plasmon resonance frequency; this mechanism has been well studied. Gold is favoured in the construction of nanoparticles as it is hydrophobic although normally gold is paramagnetic which can cause issues when they are used as contrast agents. It is also worth noting that extensive efforts have been made to synthesize and characterize nanoparticles at sizes smaller than 6-nm, which includes the core and attached ligands, as this is the maximum size that will pass through the kidney.

The use of heating to destroy cancer cells can also be exploited for imaging. It has been reported that cancer cells can be destroyed when elevated to 42 degrees C, noting however that normal cells will still be viable at this temperature. Aspects of RF, which may affect thermal dissipation, include power, frequency and antenna designs that emphasize relative strength of magnetic or electric fields. It is possible to control the thermal gradient to elevate the medium the nanoparticles occupy by just a few degrees C which would permit the enhancement of imaging without the need to destroy the cells. This can be achieved by using AuNPs to target cancer cells by attaching ligands to the surface of the AuNPs which will bind to the specific biomarkers associated with the target cancer cells. Our initial pilot studies demonstrate that we can elevate the temperature of a medium by a few degrees using an RF filed at 2.599 GHz with AuNPs approximately 5-nm in diameter. The rate of this elevation increases in the presence of AuNPs.

2. Methods

A small set of 32 electrodes (figure 1) was positioned in an RF field and 20 µl of a suspension of 0.06 mg/mL 5nm AuNP's coated with citrate (milli-Q supplied by ClineScientific) in the ion exchange solution, were placed in the central ring of the electrodes. Measurements were taken over a period on one hour every few minutes with and without the active RF field of 5 W.

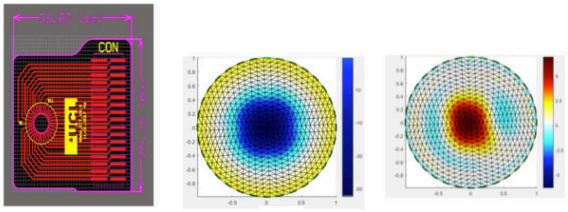

Figure 1: a) Printed circuit board of EIT electrode system; b) EIT image with AuNPs and RF at 1 second; c) image of EIT with RF at one hour.

3. Conclusion

The use of RF to heat AuNPs over exposure of one hour suggests that targeted AuNPs could be used as a contrast agent in EIT to provide difference images, which would track the path and location of the particles. Similar results could be obtained using 13.5 MHz. In practice it would be possible to achieve similar results with other types of nanoparticle such as iron, but AuNPs have considerable advantages in term of the biochemistry and acceptability for clinical use.

References

[1] S. Nordebo, M. Dalarsson, Y. Ivanenko, D. Sjöberg, and R. Bayford. On the physical limitations for radio frequency absorption in gold nanoparticle suspensions. J. Phys. D: Appl. Phys., 50(15), 1–12, 2017.

Heat Analysis in Magneto-Acousto Electrical Impedance Tomography

Elyar Ghalichi[1], Reyhan Zengin[2], Nevzat G. Gençer[1]

[1]Electrical and Electronics Engineering, Middle East Technical University, Ankara, Turkey, ngencer@metu.edu.tr
[2]Electrical and Electronics Engineering, Selcuk University, Konya, Turkey,

Abstract: In this study, heat analysis in Magneto-Acousto Electrical Impedance Tomography method is investigated numerically for a two-dimensional simplified breast model. The breast model is excited with a 16-element transducer at 1 MHz under 1 T static magnetic field for one second. The acoustic pressure wave absorption and resistive power dissipation are the sources for heat problem. During the excitation, the temperature increase in the breast tissues is 0.62 °C.

1 Introduction

Magneto-Acousto Electrical Impedance Tomography (MAET) is a hybrid imaging method for electrical conductivity of bodies [1–3]. Acoustic pressure is applied to a conductive object in existence of a static magnetic field, then Lorentz currents are induced in the object. The resultant magnetic field intensity is sensed by coils placed near the body or the resultant surface voltages are measured by electrodes. In this study, heat analysis in MAET is investigated due to absorption of acoustic pressure and resistive power dissipation.

2 Methods

To analyze the heat changes in MAET, a numerical breast model is developed with Comsol Multiphysics (Fig.1).

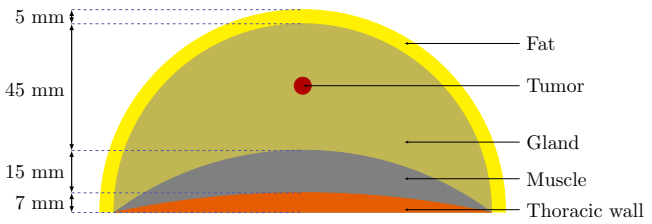

Figure 1: 2D simplified breast geometry. The geometry consists of subcutaneous fat, gland, tumor, muscle and thoracic wall [4].

The breast model is excited by a 16-element linear phased array (LPA) transducer and maximum 1.7 MPa pressure is generated in the model. In the electric problem, displacement and induced currents due to Lorentz current are calculated. In heat problem, acoustic intensity and total current density are defined as heat sources in Penne's bioheat equation [5]:

$$\rho C_p \frac{\partial T}{\partial t} = \nabla \cdot (k \nabla T) + Q_{bio} + Q - \rho_b C_b \omega_b (T - T_b) \quad (1)$$

$$\mathbf{n} \cdot (k \nabla T) = \epsilon \sigma_{S-B} (T^4_{ambient} - T^4) + h(T_{ambient} - T) \quad (2)$$

$$Q_{acoustic} = 2\alpha I, \; Q_{electric} = \frac{1}{\sigma} |\mathbf{J}|^2 \quad (3)$$

Here T is temperature, ρ is density, C_p & C_b are specific heat capacity of tissues and blood respectively, k is Boltzmann constant, Q_b & Q are metabolic and external sources, ω_b is blood perfusion rate, $\mathbf{n}$ is normal unit vector on boundaries, ϵ is emissivity, σ_{S-B} is Stefan-Boltzmann constant, h is heat transfer coefficient for convective and evaporative losses, α is acoustic attenuation, I is acoustic intensity, σ is electrical conductivity and $\mathbf{J}$ is total current density.

Surface to ambient radiation condition is defined for the boundary between breast tissue and air in (2). On thoracic wall, constant temperature boundary condition is utilized as 37 °C. Due to inclusion of metabolic heat sources, surface radiation and blood perfusion, first the steady state heat distribution is calculated for an ambient temperature of 20 °C. Then this distribution is set as initial condition for the case where acoustic and electric heating sources are added to (1).

3 Results

Due to surface radiation, the temperature of the outer surface of the tissue is lower than inside (Fig. 2). The temperature distribution after the transducer excitation for one second is given in Fig. 2. The maximum increase in temperature is below 0.5 °C.

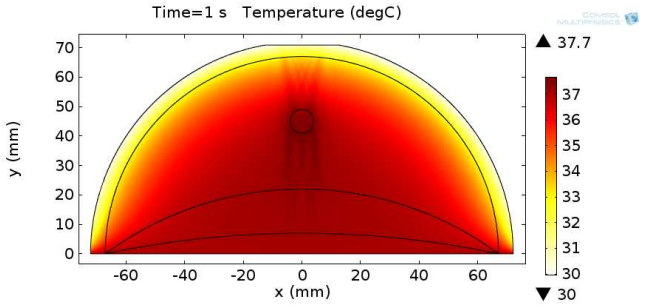

Figure 2: The temperature distribution after one second of sinusoidal excitation at 1 MHz.

4 Conclusions

The heat analysis in MAET method is investigated. The pressure below the safety limits was applied to the breast tissue. Acoustic sources are the dominant sources of heat generation. If the pressure is applied for one second, the temperature rise does not pose a threat to the tissues.

References

[1] Montalibet A, Jossinet J, Matias A and Cathignol D, *Med. Biol. Eng. Comput.*, 39, 15–20, 2001.
[2] Guo L, Liu G and Xia H, *IEEE Trans. Biomed. Eng.* , 62, 2114–24, 2015.
[3] Zengin R and Gencer N G, *IOP Physics in Medicine and Biology*, 61, 5887-5905, 2016.
[4] Sudarshan MN M, Ng E Y K, and Teh S I, *Computer Methods in Biomechanics and Biomedical Engineering*, 2, 3, 187–199, 1995.
[5] Deng Z S, Liu J, *Transactions of the ASME*, 124, pp. 638-649, 2002

Estimation of Thorax Shape for Forward Modelling in Lungs EIT

Nima Seifnaraghi[1] ,Andrew Tizzard[1], Serena de Gelidi[1], Davood Khodadad[2], Sven Nordebo[2], Anton Van Kaam[3], Inez Frerichs[4], Andreas Waldmann[5], Erich Sorantin[6], Sebastian Tschauner[6],Andreas Demosthenous[7], Stelios Christofides[8], Richard Bayford[1]

[1]Department of Science and Technology, Middlesex University, London, UK nima.seifnaraghi@mdx.co.uk [2]Department of Physics and Electrical Engineering, Linnaeus University, Vaxjo, Sweden [3] Faculty of Medicine, University of Amsterdam, Amsterdam, The Netherlands [4]Department of Anaesthesiology and Intensive Care Medicine, University Medical Centre Schleswig-Holstein, Kiel, Germany 5Swisstom AG company, Landquart, Switzerland [6]Department of Radiology, Medical University of Graz, Graz, Austria [7] Department of Electronic & Electrical Engineering, UCL, London, UK [8] Department of Medical Physics, Nicosia Generel Hospital, Nicosia, Cyprus

Abstract: The thorax models for pre-term babies are developed based on the CT scans from new-borns and their effect on image reconstruction is evaluated in comparison with other available models.

1 Introduction

The lung application of Electric Impedance Tomography (EIT), reveals the air distribution in lungs, providing regional information on lung function [1].

The inverse problem of reconstructing the impedance distribution depends on the ability of the forward problem to predict the voltages on boundary electrodes knowing exciting current patterns and conductivity map. In addition the forward model should be able to provide the electric field in the interior volume of the domain under study. This can be done numerically using Finite Element Method (FEM). Therefore, the physical geometry should be modelled considering the real dimensions, the exact boundary shapes, the electrode sizes and their contact surfaces with the outer boundaries of the thorax [2].

Some of the FEM models of the thoracic section which are in use for forward modelling at the moment are achieved by down scaling the available adult chests models to the desired scale for the new-borns and preterm-born babies. However the shape of the thorax go through an evolution process from the early ages to adulthood, changing its shape from being relatively round in new-borns to a more flat shaped in adults. Due to the advert radiation effect of imaging techniques such as CT scan, typically the thoracic images of new-borns are very rare. Fortunately, as a partner of CRADL project the Medical University of Graz provided the CT scan images of 63 patients with 23 of them being below 2 years of age.

2 Method

The cross sectional images of thorax were taken at different heights along the longitudinal axis. The area and circumference (considering the voxel actual sizes) of the thorax cross sections of each patient were used to categorize the patients into different groups. These values were calculated as an average between the sixth-seventh intercostal space (corresponding to nipple line where the electrodes would later be placed) and the two neighbouring images of above and below. The sternum and vertebra were segmented out on every image in order to create reference ventral-dorsal line. Subsequently the rotated images were aligned using these reference points. Furthermore, the outer boundaries of each cross sectional image were detected using edge detection algorithms and the achieved contours were averaged within each group to yield the final contour maps at specific heights. The final three-dimensional model was built by importing the contours to a commercial CAD software. Figure 1 depicts the models created from two categories with the mean age of 0.12 and 5.5 years. Later the effect of the models on the reconstruction images will be evaluated.

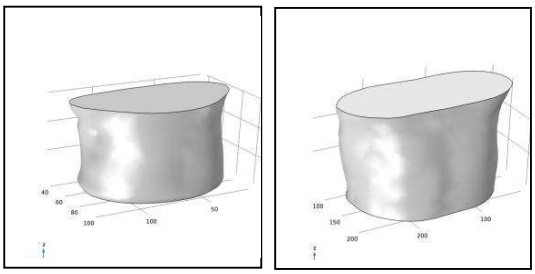

Figure 1: Thorax models (a) 0.12 years, (b) 5.5 years

3 Acknowledgements

This work is supported by the CRADL project which has received funding from the European Union's Horizon 2020 research and innovation programme 2014-2018 under grant agreement No 668259.

References

[1] I. Frerichs *PhysiolMeas,* 21(2):R1–21,2000

[2] A. Adler et al. *PhysiolMeas,* 30(6):S35–55,2009

Localizing the aorta by electrical impedance tomography within regions of interest

Sarah Buehler[1], Karin H. Wodack[1], Stephan H. Böhm[2], Andreas D. Waldmann[2], Michael F. Graessler[1], Sarah Nishimoto[1], Eugenijus Kaniusas[3], Florian Thürk[3], Constantin Trepte[1], Daniel Reuter[1]

[1]Department of Anaesthesiology, Centre for Anaesthesiology and Intensive Care Medicine, University Medical Centre Hamburg-Eppendorf, Hamburg, Germany, s.buehler@uke.de

[2]Swisstom AG, Landquart, Switzerland

[3]Institute of Electrodynamics, Microwave and Circuit Engineering, Vienna University of Technology, Vienna, Austria

Abstract: As a first step towards EIT-based assessment of cardiovascular function we used a prominence peak algorithm on predefined regions of interest (ROI) to detect the aorta on EIT images of ten pigs during saline bolus injection. Image reconstruction parameters were tuned to these specific requirements. No significant differences between EIT-based and CT-based anatomical location of the aorta were found.

1 Introduction

Reliable localisation of the aorta using EIT is a necessary prerequisite for further EIT-based assessment of cardiovascular performance. Time-based approaches [1] as well as a time- and space-based method using the most prominent peak during the injection of a hypertonic saline bolus into the aortic arch [2] were proposed. Here, we present a development based on the latter method to localize the aorta of ten pigs using constraints on the ROI.

2 Methods

2.1 Study protocol

The study was approved by the local authorities for animal care (approval no. 70/11). The ten pigs analyzed here for which CT scans were available were part of a larger project. In those anesthetized and mechanically ventilated animals, the EIT Pioneer Set (Swisstom AG, Landquart, Switzerland) was used for EIT measurements. At the beginning of the study protocol, a saline bolus (10 ml, 20 %) was injected into the descending aorta to increase regional conductivity contrast.

2.2 Image reconstruction

We modified the linearized differential GREIT algorithm [3], primarily developed for pulmonary monitoring, and adjusted it for the detection of the aorta. We used CT images segmented at the EIT electrode plane to build an individual finite element model for each animal and calculated the reconstruction matrix. Target size, desired radius and noise figure for our training data set were iteratively adjusted and a uniform background was used [4]. Reference images were constructed for each animal by averaging over several heartbeats prior to bolus injection.

2.3 Aorta detection

On the low-pass filtered 64x64 pixel images (n=10, f_{cutoff} =0.5 Hz) conductivity changes in each pixel were analyzed during bolus injection. A "prominence image" showing local maxima at a minimum distance of half the duration of the bolus injection was calculated and the peak with the largest relative height was identified as the central pixel of the aorta. We restricted the search to the dorsal regions as 70% of our images showed a bolus-like detection in the ventral region, most possibly originating from the reflux of the saline solution into the heart.

3 Results and Conclusions

In all animals we found the aorta to be located on the EIT images close to its anatomical location derived from CT images (figure 1). Offsets in the x- and y-direction averaged to -3.1±6.3 px and 1.1±3.2 px respectively. A two-sample t-test showed no significant differences between the anatomical location and EIT imaging ($p>0.05$). Using ROIs, the aorta can be localized on EIT during saline bolus injection.

References

[1] Maisch S, Bohm SH, Sola J *CritCareMed*, 39:9, 2011

[2] Thuerk F, Waldmann AD, Wodack KH *Conf 16th ICEBI & 17th EIT*, p.121, Stockholm, Sweden, Jun 2016

[3] Adler A, Arnold JH, Bayford R *PhysiolMeas,* 30:35-55, 2009

[4] Grychtol B, Adler A R *PhysiolMeas,* 35(6):1035-50, 2013

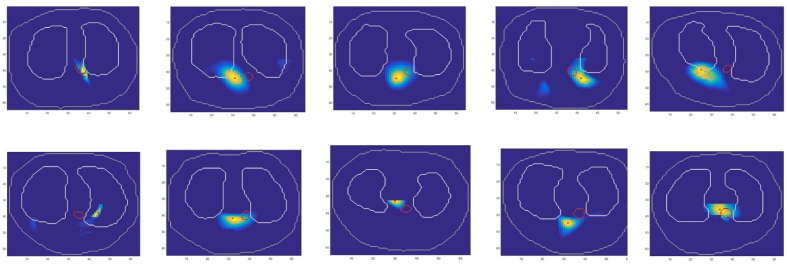

Figure 1: Prominence images from EIT analyses showing the aorta location (red cross) and its profile. The anatomical location of the aorta from CT images is circled in red, grey lines show anatomical contours of the thorax and lungs.

An Embedded System for Impedance Imaging of Permafrost Changes

Alistair Boyle[1] and Andy Adler[2]

[1]University of Ottawa, Ottawa, Canada, aboyle2@uottawa.ca
[2]Carleton University, Ottawa, Canada

Abstract: Permafrost is permanently frozen soil in the near-surface. Impedance imaging techniques may enable monitoring of increased seasonal variation in land movement and slope stability wrought by climate changes. We explore the constraints on an open-hardware embedded system for long-term remote monitoring of permafrost enabling preventative action prior to a catastrophic infrastructure failure.

1 Introduction

Permafrost is a layer of permanently frozen soil ($< 0°$C for 2 years) which covers 24% of the landmass in the North to a depth of 1.5 km in some locations [1]. Changing climatic conditions have led to structural changes in permafrost: seasonal heaving of formerly stable land upon which civil infrastructure resides. A key indicator of these changes are the formation of "ice wedges" as well as sub-surface pooling of melt water. Electrical Impedance Tomography (EIT), or equivalently Electrical Resistivity Tomography (ERT), is a promising technique for monitoring these localized changes in structure [2]. In warmer conditions, EIT systems tend to be designed for relatively low frequencies (1 Hz) and are often designed to be sensitive to humid soils and conductive ores. Frozen soils have much lower conductivities and temperature dependent permittivity, meaning current will propagate poorly unless stimulation frequencies in the 10's or 100's of kHz are used [3]. This means that the hardware design experience in the biomedical EIT community can be relevant to designing a multi-frequency system for permafrost EIT measurement. We explore the design constraints for an embedded system to be used in remote, long-term monitoring of seasonal changes in the resistivity of permafrost layers.

We have interviewed a number of hardware experts from the EIT community regarding their experiences designing EIT systems. We briefly summarize the design considerations identified during these interviews below.

2 Design Considerations Identified

An impedance imaging system can be broken down into a number of components as shown in (fig. 1). Audio frequency analog circuits, low frequency A/D converters, and millivolt-range measurements imply a straight-forward design. The components are relatively well understood but are deceptively challenging to implement well at 100kHz frequencies [4, 5]. In implementing these functional blocks, design choices and trade-offs must be made: frequencies of operation, noise tolerance, complexity, and reliability.

For products manufactured at a commercially viable scale or remote installations where on-site maintenance costs can be very high, reliability plays a key role. How much calibration, testability, and repeatability should be built into a system or be available in some adjacent system?

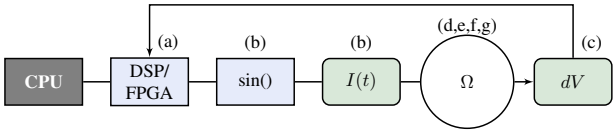

Figure 1: Block diagram of typical EIT hardware, consisting of (a) a storage and communication solution, typically some form of microcontroller or embedded processor and storage connected to the outside world, (b) digital frequency synthesis and modified Howland current source, (c) quadrature differential measurement, (d) analog signal chains for amplification, buffering, and filtering, (e) switching, (f) wiring, and (g) electrodes

Design decisions imply different cost, sensitivity to noise and interference, robustness and calibration requirements. Key challenges are to address drive, connectivity, and measurement needs while limiting interactions that complicate calibration. Quality of excitation is determined by quantization errors, current source matching, output impedance, and frequency range. Wiring, muxing and electrodes may limit system performance: crosstalk, stray capacitance, and leakage currents may be controlled with shielding. Electrode polarization can be managed through appropriate measurement strategies and careful control of excitation. Differential measurements are typically limited by Common Mode Rejection Ratio (CMRR). Measurement accuracy and speed is further limited by filter structures, A/D dynamic range, time source jitter and phase accuracy at measurement demodulation. Equipment must be able to report on the quality of measurements, as well as the measurements themselves. Increasing circuit complexity in an attempt to solve some of these issues tends to lead to increased calibration challenges.

3 Discussion

There are challenges in implementing an EIT system under new constraints. We aim to bring together the experiences of many in the EIT and ERT communities in designing these systems by working towards an open-hardware platform as a focal point for discussion of design constraints and trade-offs.

Acknowledgements

We would like to thank the following individuals for the time generously spent in describing their design choices, and their open-ness in sharing their implementation details: Ryan Halter (Dartmouth), Paul Wright (Manchester), David Holder & Kirill Aristovich et al. (UCL), Hervé Gagnon (Carleton), Peter Kramer (Swisstom), Jonathan Chambers & Paul Wilkinson et al. (British Geological Survey). We look forward to many more such discussions with those of you we have not had a chance to sit down with yet.

References

[1] Zhang T, Barry R, et al. *Polar Geography* **23**(2):132–154, 1999
[2] Kneisel C, et al. *Permafrost and ...* **19**(2):157–178, 2008
[3] Watt A, Maxwell E. *J Res NBS* **64D**(4):357–363, 1960
[4] McEwan A, Cusick G, et al. *Physiol Meas* **28**(7):S197–S215, 2007
[5] Langlois P, Wu Y, et al. *Physiol Meas* **36**(6):1337–1350, 2015

Improvement of an EIT backprojection image using a bilateral filter

Miguel-Ángel San-Pablo-Juárez[1], Eduardo Morales-Sánchez[1], Fernando Ireta-Moreno[2], Raúl-Alejandro Ávalos-Zúñiga[1], José-Joel González-Barbosa[1], Joaquín Salas[1]

[1]Centro de Investigación en Ciencia Aplicada y Tecnología Avanzada unidad Querétaro, Instituto Politécnico Nacional, Qro., México, miguelangel.sanpablo@ieee.org

[2]División Ingenierías campus Irapuato-Salamanca, Universidad de Guanajuato, Gto., México

Abstract: A bilateral filter for the improvement of an electrical impedance tomography (EIT) image is presented in this work. The filter was applied to a backprojection image using OpenCV. Results were compared with respect to a typical Gaussian filter. The applied bilateral filter made it possible to observe the smoothing of the image with preservation of edges. There was an improvement on the Normalized Mean Square Error with respect to a typical Gaussian filter.

1 Introduction

The objective of this work is to improve the EIT backprojection images for a better visualization of the spatial separation between regions applying a bilateral filter. Most used filters are Gaussian low-pass filters, where if the noise level is assumed to be high, an algorithm will smooth (or blur) the image to suppress such noise. However, if data have low levels of noise, it is appropriate to let the algorithm reduce blurring which allows better spatial separation of image regions [1]. The problem of the border recognition and the determination of a functional region of interest (ROIs) that represents lungs is required to solve in medical analysis of pulmonary and non-pulmonary tissues [1]. Therefore in this work it is proposed a bilateral filter that smooths the EIT images without blurring the regions that delimit contours.

2 Methods

A bilateral filter is a non linear filter that preserves borders and reduce noise while smooths an image. It does not produce ghost colors through the edges in color images and reduce them when they appear in the image. The definition of the bilateral filter is presented in equation (1) [4]:

$$BF[I]_p = \frac{1}{W_p} \sum_{q \in S} G_{\sigma_s}(\| p - q \|) G_{\sigma_r}(| I_p - I_q |) I_q \quad (1)$$

$BF[I]$ is the output of the bilateral filter F applied to the image I, S is the spatial domain, R the range domain and p the pixels. The weight for pixel q is defined by a Gaussian part $G_{\sigma_s}(p, q)$, σ is a parameter defining the neighborhood size. The terms $G_{\sigma_r}(I_p, I_q)$ and W_p denote the range weight and a normalization respectively. The backprojection was made using C language and the filter was implemented by the OpenCV library. Measured data were taken from [2]. A comparison between bilateral and Gaussian filters is shown in Figure 1, a) shows the image with the Gaussian filter and b) shows the image with bilateral filtering.

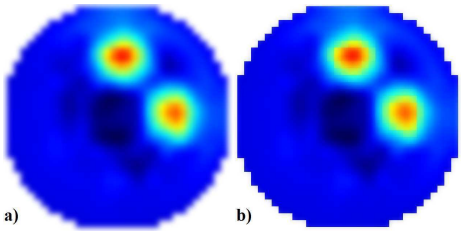

Figure 1: a)Image with Gaussian filter b)Image with bilateral filter.

Figure 2 shows a comparative performance between the used filters. A Normalized Mean Square Error was computed using the method of [3] and it was possible to observe a smaller error with the bilateral filter.

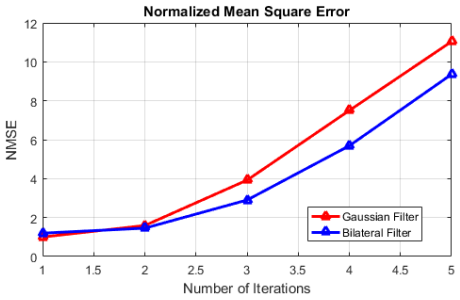

Figure 2: Normalized Mean Square Error (NMSE) of Gaussian and Bilateral filters.

3 Conclusions

When the bilateral filter is used, there is an improvement in the spatial separation between regions of EIT images, this is proved because the NMSE is smaller than in the typical Gaussian case.

4 Acknowledgements

The authors thank to Instituto Politécnico Nacional for the support given in SIP20171461 project and to CONACYT for scholarship 350051/237150.

References

[1] I. Frerichs *et al.* Online supplement 2 eit raw images: Chest electrical impedance tomography examination, data analysis, terminology, clinical use and recommendations: consensus statement of the translational eit development study group. *Thorax*, 2016.

[2] C. Gómez-Laberge. Electrical impedance tomography for deformable media. Master's thesis, University of Ottawa, 2006.

[3] E. Michel, M. Cho, and S. Lee. Geometric nonlinear diffusion filter and its application to x-ray imaging. *BioMedical Engineering OnLine*, 2011.

[4] C. Tomasi and R. Manduchi. Bilateral filtering for gray and color images. In *Proceedings of the 1998 IEEE International Conference on Computer Vision, Bombay, India*, 1998.

Optimal Design of a Planar Miniature EIT Sensor for 3D Cell Imaging

Yunjie Yang, Hancong Wu and Jiabin Jia

Agile Tomography Group, School of Engineering, University of Edinburgh, Edinburgh, UK, jiabin.jia@ed.ac.uk

Abstract: This work presents a comparison study of planar miniature EIT sensors with different electrode layouts for 3D cancer cell spheroid imaging. The dynamic range of measurement, sensitivity distribution and image reconstruction errors are evaluated and corresponding simulation results are illustrated.

1 Introduction

Cell culture widely exists in biological, pharmaceutical industries and research laboratories. Study of biological behaviour and control of chemical environment of cell culture process makes real-time 3D quantitative imaging ability an essential, among which cellular morphology and cell-drug interaction monitoring in real time are regarded as particularly helpful [1]. EIT demonstrates great potential on such purposes. In this work, we focus on the optimal design of a planar miniature EIT sensor for 3D cell spheroid imaging. Four sensors with different electrode layouts are compared in simulation, from the aspects of dynamic range of measurement, sensitivity and 3D image reconstruction errors.

2 Sensors and Evaluation Criteria

Fig. 1 illustrates four planar EIT sensors with different electrode layouts. The diameter of each sensor is 12 mm and the height is 3 mm. Each has 16 circular electrodes and one grounding electrode on the base of the sensor.

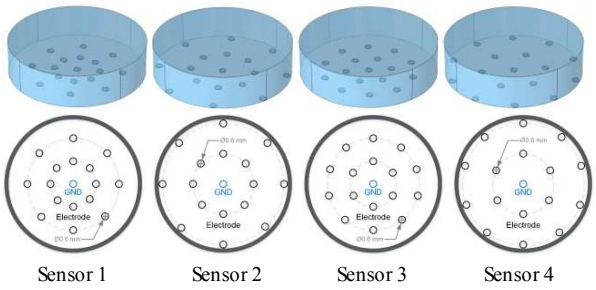

Figure 1: Four planar EIT Sensors. The first row is the 3D view. The second row is the electrode layouts.

Three criteria are adopted to evaluate the performance, i.e., dynamic range of measurement, sensitivity and reconstruction image error. Dynamic range is defined as

$$D = \frac{V_{\max}}{V_{\min}} \tag{1}$$

where, $V_{\max}$ and $V_{\min}$ are the maximum and minimum voltage measured across the electrodes on a homogeneous background, respectively. A smaller D is better EIT measurement.

The sensitivity is calculated by the row summation of the Jacobian matrix. The images are reconstructed by the one-step Gaussian-Newton method with Laplacian filter regularization [2] and the image error is defined as

$$E = \frac{\|\sigma - \sigma_t\|}{\|\sigma_t\|} \tag{2}$$

where σ and σ_t are the estimated and true conductivity distribution respectively. Note that when calculating the image error, σ and σ_t are firstly normalized to [0 1]. Small dynamic range D, large sensitivity and small image error E are always preferable for EIT imaging.

3 Results

Fig. 2 shows the dynamic range of each sensor and Fig. 3 shows the sensitivity (vertical slice in the y direction) and image reconstruction errors regarding three test phantoms. Sensor 1 has smallest dynamic range, largest sensitivity and smallest image error among four layouts, which suggests that sensor 1 has the best performance.

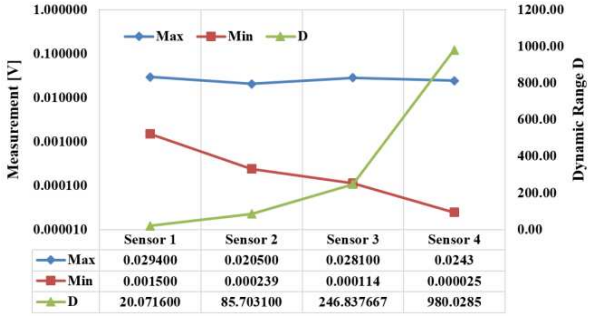

	Sensor 1	Sensor 2	Sensor 3	Sensor 4
Max	0.029400	0.020500	0.028100	0.0243
Min	0.001500	0.000239	0.000114	0.000025
D	20.071600	85.703100	246.837667	980.0285

Figure 2: Dynamic range of each sensor.

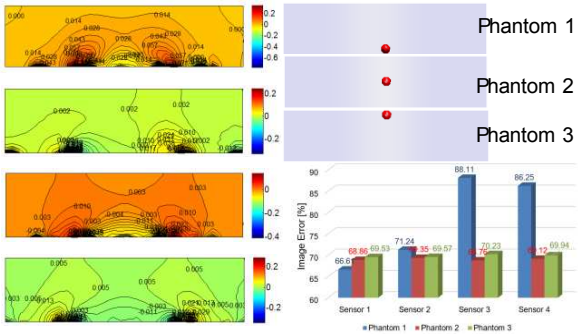

Figure 3: Sensitivity and image error analysis of each sensor. The left part is the vertical slice of sensitivity (from top to bottom: sensor 1 to sensor 4). Right top shows side views of three phantoms. Right bottom shows the image errors.

4 Conclusion

This paper proposed and evaluated four planar miniature EIT sensors. The suggested sensor electrode layout is expected to achieve better performance for the assessment of dynamics such as cell-drug interaction.

References

[1] Y Yang, J Jia, S Smith, et al *IEEE Sens. J*, 17.2: 514–523,2017
[2] A Adler, T Dai, W R B Lionheart *PhysiolMeas*, 28: S1, 2007

EIDORS Version 3.9

Andy Adler[1], Alistair Boyle[1], Fabian Braun[2], Michael G. Crabb[3], Bartłomiej Grychtol[4,5], William R. B. Lionheart[3], Henry F. J. Tregidgo[3], Rebecca Yerworth[6]

[1]Carleton University, Ottawa, Canada [2]Centre Suisse d'Électronique et de Microtechnique, Neuchâtel, Switzerland [3]University of Manchester, Manchester, UK [4]Fraunhofer Project Group for Automation in Medicine and Biotechnology PAMB, Mannheim, Germany [5]University of Heidelberg, Mannheim, Germany [6]University College London, UK

Abstract: This paper announces the release of version 3.9 of the EIDORS software suite. We review its new features, and discusses its growth and citations.

1 Introduction

We proudly announce the release of EIDORS version 3.9, for the 18th Int. Conf. on Biomedical Applications of EIT, in June 2017. The software is available at eidors.org and licensed under the GNU GPLv2 or GPLv3. Archived versions are now available on Zenodo [1] (and v3.8 [2]).

EIDORS aims to provide free software algorithms for forward modelling and inverse solutions of Electrical Impedance and (to some extent) Diffusion-based Optical Tomography, in medical, industrial and geophysical settings and to share data and promote collaboration.

2 New Features

Release 3.9 of EIDORS builds upon a strong foundation in reconstruction algorithms, adding and improving a number of aspects.

- Faster forward solve times for real conductivity distributions
- Improved support for GREIT reconstructions in 3D [3]
- New hyperparameter selection approaches [4]
- Interface to "Regularization Toolbox" [5]
- Gmsh-based human 3D model interface [3]
- Correction of artefacts caused by low frame rates [6]
- Improved support for mixed point and CEM electrode models
- Support for $2\frac{1}{2}$D solvers (including a rank-1 $2\frac{1}{2}$D movement Jacobian) [7]
- Forward solve supporting model reduction (i.e. efficient precalculation of out-of-field regions) [8]
- Improved testing framework esp. for core solver algs
- Improved support for geophysical FEM models
- Improved support for Octave
- Updated ability to load recent device file formats including auxiliary data (Dräger and Swisstom formats)
- Expanded shape library

3 Growth

EIDORS-related citations continue to grow. Current citation results are shown in table 1. The EIDORS code-base is growing (fig. 1) with significant effort being applied to improving test coverage, refining performance and implementing new features. In 2012, a `dev` (development) staging area was created for contributions in progress.

Table 1: EIDORS Citations (May 2017, scholar.google.com).

Paper	Date	Citations
[9] A MATLAB package for the EIDORS project ...	2001	207
[10] Image reconstruction algorithms for ...	2002	127
[11] A Matlab toolkit for three-dimensional ...	2002	367
[12] EIDORS: Towards a community-based ...	2005	10
[13] Uses and abuses of EIDORS: An extensible ...	2006	334
[14] Simple FEMs aren't as good as we thought ...	2008	19
[15] EIDORS version 3.8	2015	4

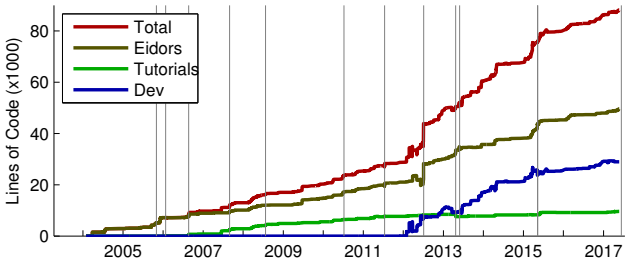

Figure 1: Lines of Code (LoC) in Matlab files in the EIDORS codebase vs. time; Total (red), Eidors (i.e. release branch, brown), Tutorials (green), development code (blue). Releases are indicated by gray bars.

4 Discussion

The structure of EIDORS has been relatively stable due, in part, to some early design choices: a modular framework and data structure, cross-platform support, integration of meshing, tutorials, and the contributed data repository. These aspects, along with an open source code-base, have enabled EIDORS to maintain research relevance. Presenting version 3.9!

Acknowledgements

Recent funding for EIDORS development thanks to NSERC Canada and EPSRC UK.

References

[1] Adler A *et al*, "EIDORS v3.9", DOI:10.5281/zenodo.583266, 2017.
[2] Adler A *et al*, "EIDORS v3.8", DOI:10.5281/zenodo.17559, 2015.
[3] Grychtol B, Müller B, Adler A, *Physiol Meas*, 37:785–800, 2016.
[4] Braun F, Proença M, Solà J *et al*, IEEE T Biomed Eng, 2017.
[5] Hansen PC, *Numerical algorithms*, 46.2:189–194, 2007.
[6] Yerworth R, Frerichs I, Bayford R, J Clin Monit Comput, 2016.
[7] Boyle A, Adler A, *Proc EIT2016*, p.100, Stockholm, 2016.
[8] Adler A, Lionheart WRB, *Proc EIT2016*, p.116, Stockholm, 2016.
[9] Vauhkonen M, Lionheart WRB *et al*, *Physiol Meas*, 22:107–111, 2001.
[10] Polydorides N, *Ph.D. thesis*, U Manchester, UK, 2002.
[11] Polydorides N, Lionheart WRB, *Meas Sci Tech*, 13:1871–1883, 2002.
[12] Adler A, Lionheart WRB, *Proc EIT2005*, London, UK, 2005.
[13] Adler A, Lionheart WRB, *Physiol Meas* 27:S25–S42, 2006.
[14] Adler A, Borsic A *et al*, *Proc EIT2008*, Hannover, NH, USA, 2008.
[15] Adler A *et al*, *Proc EIT2015*, p.19, Neuchâtel, Switzerland, 2015.

A simplified calibration method for multi-frequency EIT system

Hancong Wu, Yunjie Yang and Jiabin Jia

Agile Tomography Group, School of Engineering, University of Edinburgh, Edinburgh, UK, jiabin.jia@ed.ac.uk

Abstract: The present paper introduces a simplified calibration method for multi-frequency EIT system. This method reduces the complexity of calibration but maintains a high calibration performance.

1 Introduction

Multi-frequency EIT is a novel method in monitoring human diseases and biological cells through impedance measurement. The measurement error caused by stray impedance on the hardware circuitry directly affects the quality of the reconstructed images. One approach to compensate the measurement error is to apply calibration for each current source and voltmeter [1, 2]. However, this calibration procedure is complex and the calibrator is unavailable for the other EIT systems. A simplified and effective calibration method is presented for a 16-channel multi-frequency EIT system in this paper.

2 Methods

2.1 Single channel calibration

Based on the principle of EIT measurement, a calibration model is developed as shown in fig.1. In the model, the current source is connected with a pair of electrodes while the voltmeter is connected to its adjacent electrode pair. R_c is used to simulate the contact impedance between the electrode and the medium while R and C are the equivalent impedance of the medium. A total of 8 combinations of R and C values are used to calculate the calibration factors. Current with different frequency components is stimulated from the current source, and the corresponding voltages are measured through the voltmeter. The measured voltage matrix is defined as:

$$V_m \angle \varphi_m = \alpha V_t \angle (\varphi_t + \beta) \quad (1)$$

where V_m and V_t are the magnitude of the measured voltage and the theoretical voltage; $\angle\varphi_m$ and $\angle\varphi_t$ are the phase shift of the measured voltage and the theoretical voltage with respect of the phase of stimulation current.

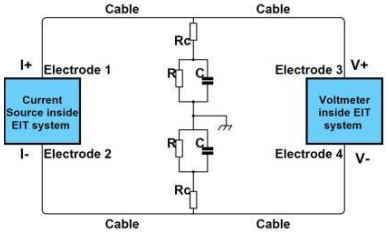

Figure 1: Circuit diagram for single channel calibration.

Because the difference between measured voltage and the theoretical voltage is caused by the system error on hardware system, the calibration is performed by compensating the magnitude and phase using calibration factor α and β at all frequencies:

$$\alpha = \underset{\alpha}{arg\,min} \|WV_m - \alpha W V_t\| \quad (2)$$

$$\beta = \overline{\angle(\varphi_m - \varphi_t)} \quad (3)$$

where W is the weight matrix to normalize the voltage matrices V_m and V_t.

2.2 Channel consistency evaluation

A 16-channel conformal resistor network [3] is connected with the electrodes of the system. The electrode pairs for current stimulation and voltage measurement are switched sequentially (1-2-3-4, 2-3-4-5 … and 16-1-2-3) and the impedance is measured and compared with the first measurement at electrode 1-2-3-4. If the difference between two values is lower than 5%, the channel consistency can be considered as high and the calibration factors for electrode pair 3-4 calculated in section 2.1 can be directly applied to other electrode pairs. Otherwise, new calibration factors should be calculated independently.

3 Results

Fig. 2 shows that most of the error on magnitude and phase is compensated after calibration. In fig.3, background noise in reconstructed images using uncalibrated data is reduced after calibration.

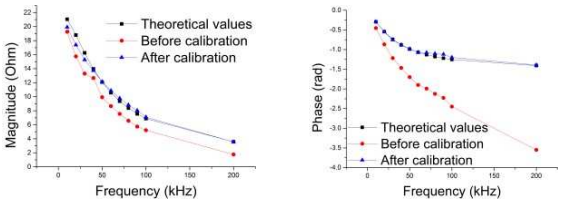

Figure 2: Comparison before and after magnitude and phase calibration.

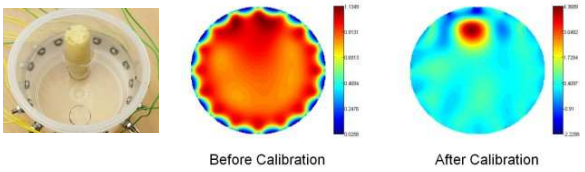

Figure 3: Frequency-difference real part image between 10kHz and 80kHz for saline-potato phantom before and after calibration.

4 Conclusions

The simplified multi-frequency EIT system calibration method through single channel calibration and channel consistency evaluation is feasible and effective. It provides an alternative method for the calibration of multi-frequency EIT research.

References

[1] O. Tong In, et al, *Physiological Measurement,* vol. 28, pp. 1175-1188, 2007.

[2] H. Wi, et al, *IEEE transactions on biomedical circuits and systems,* vol. 8, pp. 119-128, 2014.

[3] M. Wang, et al, *IEEE Sensors Journal,* vol. 5, pp. 289-299, 2005.

Realistic 3D Finite Element Mesh of the Adult Human Pelvis for Electrical Impedance Tomography

Eoghan Dunne[1], Emily Porter[1], Brian McGinley[1], and Martin O'Halloran[1]

[1]Translational Medical Device Lab, National University of Ireland Galway, e.dunne13@nuigalway.ie

Abstract: The finite element method is a numerical technique used to solve forward models for electrical impedance tomography. To date, realistic finite element models (FEMs) have been created for the head and thorax, but pelvic models for bladder imaging are lacking. This paper presents a high quality, first-order, tetrahedral FEM of 25004 nodes and 129157 elements for the adult male pelvis, with mean and standard deviation stretch values of 0.752 and 0.082, respectively.

1 Introduction

The finite element method is commonly employed in the forward problem of electrical impedance tomography (EIT). To resolve the ill-posed problem within EIT, the finite element model (FEM) provides information on the geometry of the region of interest. The position and the geometry of the attached electrodes are included in the FEM when in use for a specific forward problem.

Realistic 3D FEMs for EIT applications have been created for the head [1] and the thorax [2]. However, to date, a model for the pelvic region does not exist. Applications such as bladder volume monitoring using EIT have instead employed cuboid [3], circular [4] and cylindrical [5, 6] FEMs for the boundary of the pelvis. Li et al. [4] based their 2D FEM for patient bladder volume monitoring using a single slice from a CT scan.

Discrepancies between the FEMs and the geometry of the true subject can significantly and negatively affect the reconstructed image, with inconsistency between the boundary of the subject and the FEM leading to potential image artefacts [1, 7].

This paper presents a realistic 3D FEM of the adult male pelvis to support applications in EIT bladder imaging.

2 Methods

Computed tomography (CT) slices of the adult male pelvic anatomy were gathered from the Visual Human Project [8]. Slices were selected from above the genitals to the top of the navel. The slices were taken at 10 mm increments, imported into the computer aided design software, AutoDesk^{TM} Fusion 360, and stacked at 10 mm spacings in order to create the surface model.

The procedure used to form the surface model was similar to one used for the head model by Tizzard et al. [1]. The procedure involved placing points on the boundary of each image and using splines to interpolate through the points to form the curved contours. The 3D surface model was then formed by lofting the curve contour profiles and exported in Initial Graphics Exchange Specification (IGES).

The first-order, tetrahedral mesh was created in SimScale [9]. SimScale is a Salome-based numerical simulator that operates in the cloud, allowing for faster mesh generation.

3 Results

The generated mesh of the male pelvic anatomy consists of 25004 nodes and 129157 tetrahedral elements. The number of elements of the mesh is greater than the recommended minimum of 10^6 elements for 3D FEMs [7]. The model is 20 cm in height. The stretch values are between 0.292 and 0.989 with a mean and standard deviation of 0.752 and 0.082, respectively. The mesh is illustrated in Figure 1.

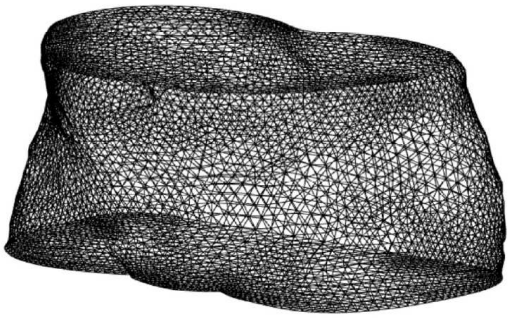

Figure 1: The generated first-order, tetrahedral mesh of a male adult pelvis, from above the genitals to the top of the navel.

4 Conclusions

A realistic 3D FEM of an adult male human pelvis has been developed for EIT image reconstruction. This work has the potential to benefit bladder imaging applications in EIT.

5 Acknowledgements

This research was supported by funding from the European Research Council under the European Union's Horizon 2020 Programme/ ERC Grant Agreement BioElecPro n. 637780 and the charity RESPECT and the People Programme (Marie Curie Actions) of the European Union's Seventh Framework Programme (FP7/2007-2013) under REA Grant Agreement no. PCOFUND-GA-2013-608728.

References

[1] A Tizzard et al. *Physiol Meas*, 26:251-261, 2005
[2] A Adler et al. *Physiol Meas*, 30:35-55, 2009
[3] W He et al. *Comput Math Methods Med*, 2012
[4] R Li et al. *J Med Biol Eng*, 36(1):71-79, 2016
[5] T Schlebusch et al. *Conf 35th IEEE EMBS*, Osaka, Japan, Jul 2013
[6] T Schlebusch et al. *Physiol Meas*, 35(9):1813-1823, 2014
[7] A Adler et al. *Conf 9th EIT*, Dartmouth College, New Hampshire, Jun 2008
[8] M J Ackerman *Proc. IEEE*, 86:504-511, 1998
[9] *Simscale.com,* [Online]. Available: www.simscale.com [Accessed Feb 2017]

Upper Arm Imaging based on Electrical Capacitance Tomography

Marlin R Baidillah[1,2*], Al-amin S Iman[1,2], Yue Sun[1] and Masahiro Takei[1]

[1]Graduate School of Engineering, Dept. Mechanical Eng. Div. Fundamental Engineering, Chiba University, Chiba, JAPAN
mr.baidillah@chiba-u.jp

[2]Dept. Research & Development, CTECH Labs Edwar Technology, Tangerang, INDONESIA

Abstract: The study proposes a new sensing method for ECT to allow imaging of biomedical tissue. A conventional ECT sensing method uses one electrode capacitance measurement to charge the inspected object. Meanwhile, our study uses two-electrodes capacitance measurement with different polarity. A numerical study by using an upper arm permittivity distribution shows the proposed ECT sensing method has the potential change.

1 Introduction

Among of electromagnetic tomography techniques, Mutual Inductance Tomography (MIT) and Electrical Impedance Tomography (EIT) are quite comprehensively developed for biomedical imaging compare with Electrical Capacitance Tomography (ECT) [1]. This is due the permittivity range of biological tissue is very high compare to industrial applications object as a common object interest of ECT. It makes the inhomogeneity of object interest in biomedical application is difficult to ascertain based on capacitance measurement of ECT. Commonly, capacitance measurement of ECT operates below of f = 2.5 MHz [2]. In this frequency range, the permittivity value of such biological tissue is in the range more than ε_r > 500 [-]. Therefore, the current ECT technique is not gaining acceptance among of biomedical application users.

The conventional ECT sensing method employs one or more than two electrodes as transmitter with similar polarity voltage to charge the inspected object. Based on this technique, the current data acquisition system of ECT does not designed to measure high induced voltage due to high permittivity distribution. Our study proposes a new ECT sensing method by using two electrodes that have different polarity to allow imaging of high permittivity distribution with low voltage and low frequency measurement.

2 Methods

A numerical study was conducted using 2D upper arm with diameter D = 80 mm as shown in Figure 1. The permittivity value of each components as shown in the figure. Non-contact 16 capacitive electrodes are attached in the cylindrical vessel. Two electrodes are defined as a transmitter with Vi^+ = +10V and Vi^- = -10V with frequency measurement is f = 1 MHz. For conventional ECT technique, a transmitter electrode uses Vi = 20 Volt and frequency measurement f = 1 MHz.

To solve the normalization stage prior to reconstruction, a homogenous potato pulp is used (ε_r = ±700 [-] at f = 1 MHz) instead of using homogenous water (ε_r = ±78 [-] at f = 1 MHz). Because the measured voltage is directly related to the capacitance of inspected object, then the normalization stage can be rewritten based on the following equation

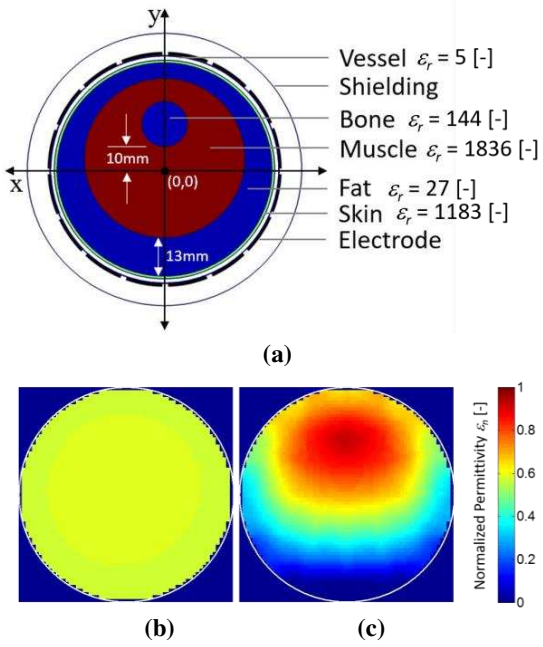

Figure 1. (a) Upper arm phantom, (b) reconstructed image of ECT conventional and (c) reconstructed image of the proposed ECT.

$$V_n = (V_m - V_{ref})/V_{ref} \quad (1)$$

where V_n is the normalized voltage [-], V_m is the inspected object voltage [Volt], and V_{ref} is the homogenous potato pulp voltage as the reference object [Volt]. An image reconstruction algorithm based on Generalized vector sampled pattern matching (GVSPM) technique is used [3].

3 Conclusions

In this study, we showed the feasibility of ECT as biomedical imaging tool as an alternative of EIT and MIT. The conventional ECT is design for low capacitance measurement where the permittivity medium is commonly below of er < 80 [-]. The proposed ECT sensing method makes high permittivity distribution can be acquired by using low voltage and low frequency measurement.

4 Acknowledgements

This works was supported in part by JSPS (Japan Society for the Promotion of Science) Grants-in-Aid for Young Scientists 16J08769.

References

[1] M Wang, *Industrial Tomography: systems and applications* Elsevier, 2015
[2] DX Chen, X Deng, WQ Yang, *Rev. Sci. Instrum,* 81(3):2-5,2010
[3] M Takei, Y Saito, *Meas. Sci. Technol.* 15:1371-1381,2004

Using EIT derived parameters for the detection of changes in work of breathing during spontaneous breathing

Sabine Krueger-Ziolek, Benjamin Schullcke, Bo Gong and Knut Moeller

Institute of Technical Medicine, Furtwangen University, 78054 Villingen-Schwenningen, Germany

krue@hs-furtwangen.de

Abstract: Electrical Impedance Tomography (EIT) was applied to determine differences in relative impedance changes within the thorax depending on the work of breathing during spontaneous breathing. Results indicate that EIT might be suitable to identify variations in breathing efforts.

1 Introduction

Besides the determination of global lung parameters such as functional residual capacity, residual volume and total lung capacity, body plethysmography allows to assess the specific airway resistance (sRaw). sRaw does not reflect the actual airway resistance, rather it depicts the volume- and resistance-dependent work of breathing which is necessary to generate respiratory flow [1]. Previously our group introduced a novel measurement system combining Electrical Impedance Tomography (EIT) with body plethysmography that allows simultaneous measurements of regional and global lung parameters [2].

The aim of this preliminary study was to investigate the relationship between ventilation related impedance changes within the thorax and work of breathing (WOB) during spontaneous breathing. An artificial airway resistance which enables unimpaired inspiration, but causes impaired expiration was built to simulate variations in breathing effort. We hypothesized that EIT derived parameters may be used to detect changes in WOB.

2 Methods

EIT and body plethysmographic measurements were conducted simultaneously on one lung-healthy volunteer during normal tidal breathing. Ten different settings of the artificial airway resistance were applied. EIT data were acquired at the 5th intercostal space with an electrode belt comprising 16 electrodes and a frame rate of 40 Hz.

2.1 Data processing and evaluation

EIT data reconstruction was performed by utilizing a Finite Element Method based linearized Newton-Raphson reconstruction algorithm. EIT images were generated with a resolution of 32 × 32 pixels. To filter out the cardiac activity, a low-pass filter with a cut-off frequency of 45 min^{-1} was employed.

The global ventilation related impedance signal of one tidal breath was normalized to the maximum impedance value at end-inspiration and the lowest impedance value at end-expiration (Figure 1). In addition, impedance signals of all 1024 pixels were normalized to those impedance values occurring at the time of end-inspiration and end-expiration of the global signal. Differences between the normalized global impedance signal and the normalized impedance signal of a pixel were calculated. Differences were squared and summed. Each pixel in a generated functional EIT image represents the sum of the squared differences.

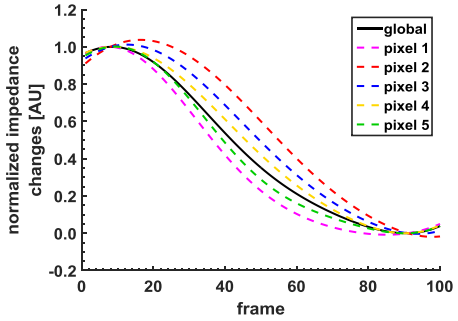

Figure 1: Example of a normalized global impedance signal as well as normalized impedance signals of five selected pixels of one tidal breath.

To assess the variation in pixel values within this functional EIT image, a slightly modified version of the global inhomogeneity index (fGI) [3] was applied. Five tidal breaths were analyzed for each setting of the artificial airway resistance. The mean of the five resulting fGI indices was calculated for each setting and depicted in dependency of sRaw (Figure 2).

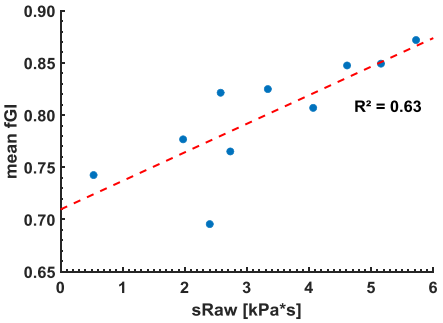

Figure 2: Mean fGI index in dependency of sRaw.

3 Conclusion

The mean fGI index increased with rising WOB of the subject indicating that EIT may be suitable to trace changes in WOB during spontaneous breathing.

4 Acknowledgements

This work was partially supported by the Federal Ministry of Education and Research (MOSES, Grant 03FH038I3).

References

[1] C. P. Criée, S. Sorichter, H. J. Smith, *et al.*, Respir Med, 105(7):959-71, 2011.

[2] S. Krueger-Ziolek, Z. Zhao, K. Moeller, Biomed Tech, 58 (Suppl. 1), 2013.

[3] Z. Zhao, K. Möller, D. Steinmann, *et al.*, Intensive Care Med., 35(11):1900-6, 2009.

Microelectrode array EIT in the deep brain: a feasibility study

Calvin Eiber[1], Danyi Zhu[2], Alistair McEwan[2]

[1]Centre of Excellence for Integrative Brain Function, Save Sight Institute, University of Sydney, Sydney, Australia
[2]School of Electrical and Information Engineering, The University of Sydney, Sydney, Australia

Abstract: This simulation study explores the feasibility of generating EIT images or functional recordings based on a NeuroNexus microelectrode array placed intra-cortically.

1 Introduction

Electrical Impedance Tomography (EIT) is an emerging technique for non-invasive imaging of neural activity on millisecond timescales. Currently, however, the spatial resolution achievable by EIT is insufficient to non-invasively interrogate specific brain structures. In principle, EIT can also be applied to systems involving implanted microelectrode arrays, sacrificing non-invasiveness for improved spatial resolution in a region of interest. This communiqué explores the feasibility of using EIT to record transient neural activity in deep brain structures, in particular the lateral geniculate nucleus (LGN) of the common marmoset monkey, *callithrix jacchus*.

2 Methods

The 3-dimensional profile of one hemisphere of a marmoset brain was extracted from coronal sections [1] from 2.3 mm to 7.3 mm anterior to the intra-aural plane, along with the profile of the LGN. The extracted geometry was meshed in Comsol (COMSOL AB, Sweden, V5.0.0) to form a tetrahedral mesh with 563,000 elements. No distinction was made between gray matter and white matter of the brain. The brain was assigned a conductivity of 0.3 $\Omega^{-1}\,\mathrm{m}^{-1}$ [2] and the LGN a conductivity of 0.15 $\Omega^{-1}\,\mathrm{m}^{-1}$. An implanted electrode array with dimensions matching a NeuoNexus 2x16 array (50 µm separation between recording sites, 500 µm between shanks) was simulated at two different locations, as shown in figure 1. A 7% conductivity change within the LGN was simulated in Comsol. Every choice of current source and sink such that the source and sink site were on opposite shanks was included in the overall imaging stimulus set. The (linearized, isotropic) inverse problem was solved using a 1-step Gauss-Newton procedure using EIDORS V3.8. Image reconstruction was regularized with a Laplace prior on a coarse 2-dimensional mesh with 1016 elements; a hyperparameter of 0.003 was selected empirically.

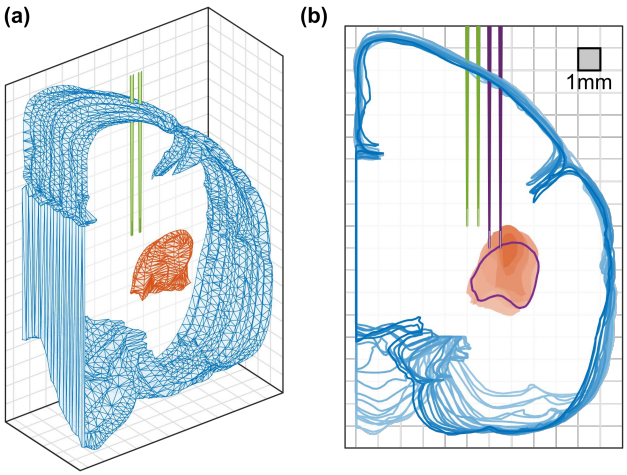

Figure 1: A: Isometric and B: Coronal view of simulated geometry and electrode array placement. Red body is LGN.

3 Results

Figure 2 shows simulated conductivity images for each of the simulated locations. In both cases, the direction from the array to the LGN can be clearly identified in the absence of noise. In order to achieve an acceptable SNR to generate figure 2(a), a minimum of 30-50 passes (assuming a recording noise RMS of 3.5 µV and a probe current of 2 µA [3]) would be necessary and the stimulus pulses would exceed 1.5 V through a 600 kΩ electrode (typical for the simulated NeuroNexus device). These values are achievable on modern electrophysiology equipment.

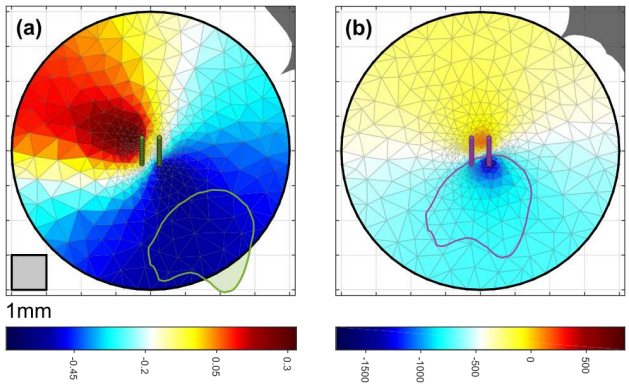

Figure 2: Image reconstructions for simulated change in LGN conductivity

4 Conclusions

These preliminary results are promising, although there is room for improvement for the image reconstruction. Impedance changes in different nearby structures could potentially be distinguished. Given a detailed conductivity map of the tissue and knowledge of the electrode array position (confirmed in vivo with either EIT or other imaging techniques, or post vivo with sectioning and staining), the inverse solution techniques of EIT can also be used for the interpretation of local field potentials by solving the inverse problem of determining the distribution of sources in the surrounding tissue.

References

[1] G Paxinos, C Watson, M Petrides, M Rosa, H Tokuno *The marmoset brain in stereotaxic coordinates* Elsevier: AP, 2012
[2] C Gabriel, A Peyman, and E Grant *Phys Med Biol* 54:4863-78, 2009
[3] M Histed, V Bonin, C Reid. *Neuron* 63:508-522, 2009

Improvements to the ScouseTom EIT System Arising From Noise Analysis

Thomas Dowrick[1] , James Avery[1] and David Holder[1]

[1]Department of Medical Physics, University College London, London, UK, t.dowrick@ucl.ac.uk

Abstract: In order to identify the hardware components of the ScouseTom EIT system which will most benefit from improvement, a noise analysis of the system has been undertaken. By measuring across a range of frequencies, amplitudes and loads, the noise of each individual component (current source, electrodes, voltage recording) was identified, with the current source being the dominant source of noise (~0.1% current noise), followed by electrode related noise (1-10µV). Work is underway to produce a next generation current source which can be incorporated into the ScouseTom system and future EIT experiments.

1 Introduction

Fast neural EIT requires hardware which can reliably measure voltage changes as small as several microvolts, over millisecond timescales. The most recent UCL EIT system [1] has been successfully employed in a range of human and animal experiments, imaging in both brain and nerve, but the noise performance is not sufficient for all applications. In order to develop the next generation of UCL EIT system, a noise analysis of each component of the EIT system was carried out and any bottlenecks were identified.

2 Methods

The three main components of the ScouseTom EIT system (Keithley 6221 current source, ActiChamp EEG recorder and platinum black electrode arrays) were analysed and their contributions to the overall noise of the system was calculated. Noise variations with measurement frequency (1kHz -10kHz), current amplitude (10µA - 200µA) and load impedance were considered. The broadband noise across the entire measurement range (100kHz) was first calculated for each component, and then the signal processing pipeline for a typical EIT experiment was followed in order to calculate the noise in the band of the EIT signal, depending on the bandwidth of the expected impedance change.

Data was collected using resistor phantoms, head tanks, human EEG electrodes, and in-vivo during brain and nerve imaging experiments.

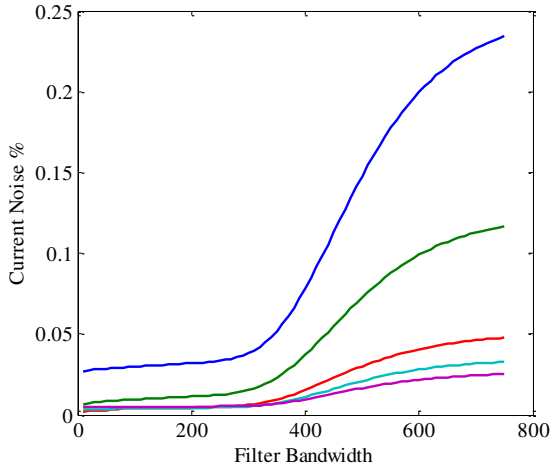

Figure 1: Current source noise as a % of the injection current vs bandwidth, measured on resistor phantom. Current amplitudes between 10µA and 200µA were used, at a frequency of 5kHz.

3 Conclusions

The dominant noise source in the system was identified as the current source (Figure 1/Table 1), providing a multiplicative noise which is proportional to the magnitude of the injected current. Noise in the current signal is especially problematic is it is magnified in all parts of the system by the electrode impedance. In order to improve on this aspect of the system, new implementations are being considered, including microcontroller, PCB and IC based solutions. An additional motivation in this area is to move to a more portable, battery operated current source, rather than the mains operated Keithley, which will be beneficial in clinical environments. The second largest noise source was introduced by the interface between electrodes and biological tissue. However, platinum black is currently considered to be the optimal electrode material, and there is limited scope for improvement in this area.

4 Acknowledgements

This work has been funded by a combination of GlaxoSmithKline and DARPA.

References

[1] Avery, J., Dowrick, T., Faulkner, M., Goren, N. and Holder, D. Sensors, 2017.

Table 1: Summary of noise in EIT components

Component	Noise contribution	Additive/Multiplicative
ActiChamp	0.5-5µV	Additive
Electrodes	1-10µV	Additive
Keithley 6221	0.02-0.2% of injected current amplitude (10-100µV)	Multiplicative

Electrical Impedance Tomography Image Explorer

Florian Thürk[1], Daniel Mudrak[1], Stefan Kampusch[1], Stefan Böhme[2], Helmut Prosch[3] and Eugenijus Kaniusas[1]

[1]Institute of Electrodynamics, Microwave and Circuit Engineering, TU Wien, Vienna, Austria
[2]Department of Anesthesia, Pain Management and General Intensive Care Medicine, Medical University of Vienna, Vienna, Austria
[3]Department of Biomedical Imaging and Image-guided therapy, Medical University of Vienna, Vienna, Austria

Abstract: We introduce the Electrical Impedance Tomography Image Explorer (EITIE), a web-based image browser that enables researchers, clinicians and students to interactively explore the impact of different reconstruction algorithms and settings. The purpose of this work is to improve the understanding about the dependency of EIT-images and derived physiological parameters (e.g., center of ventilation) on the applied reconstruction method.

1 Introduction

Electrical impedance tomography (EIT) is a cheap and non-invasive imaging modality that can be applied directly at the bedside. Small currents are injected into the body and the corresponding voltages are measured. From these surface measurements, the impedance or conductivity distribution within the domain can be reconstructed. Since the mathematical problem behind this process is highly ill-posed, no unique solution exists and the obtained impedance image will depend on prior assumptions about the domain and parameters of the reconstruction algorithm (e.g., regularization) [1]. Consequently, this affects also the post-processed physiological EIT parameters [1,2].

In this work, a web-based image visualization tool is proposed to demonstrate this issue not only to well-trained engineers, but also to clinicians and students who might not be aware of this issue. With our implemented tool, users can upload their own images and explore the impact of different reconstruction algorithms and settings, e.g., GREIT [3] or Gauss Newton (GN).

2 Methods and Results

EITIE is based on Python and the web framework Django, and is available at eitie.emce.tuwien.ac.at. For demonstration and teaching purposes, we provide two initial image collections, obtained from EIDORS [4,5] and from experimental measurements (ethics approval ETK_01082015).

2.1 Web Framework

A graphical interface is dynamically generated according to the uploaded data set and its specific reconstruction settings (Fig. 1). After selection of a parameter combination (see 2.2.), the corresponding EIT-image is shown and physiological parameters, i.e., center of ventilation and right-left ratio of ventilation distribution, are calculated. In addition, a threshold can be defined to identify regions with specific impedance changes.

Even though we dedicated this tool to the evaluation of reconstruction parameters, the dynamic generation of the user interface provides the means to investigate any kind of image attributes (e.g., PEEP trials or patient id).

2.2 Initial Data Set

Finite element models with individual anatomical boundaries were created from computed tomography images. Reconstruction models were then generated for GREIT and GN using different permutations of reconstruction settings [6]. Specifically, we varied target size, weighting radius for GREIT, and priors for GN. Common parameters for both algorithms were noise figure, the weight of lungs and heart as well as the thorax shape. Inspiration and expiration were detected in the raw voltage data and the corresponding difference as well as normalized difference voltages were used for the reconstruction.

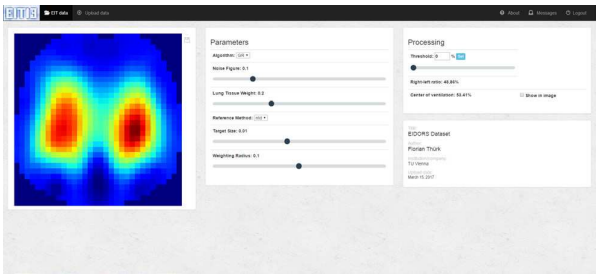

Figure 1: User interface of the EIT Image Explorer. The displayed image is updated according to the selected reconstruction parameters.

3 Conclusions

The presented web-framework provides an online platform for explorative EIT-image analysis. Although this first approach intents to provide a qualitative assessment of different reconstruction algorithms, we additionally provide basic analysis of physiological EIT parameters. Not only has Python the potential to include more sophisticated analysis methods in the future, MATLAB wrappers also could allow direct integration of existing code such as the EIDORS tutorials.

4 Acknowledgements

This study has been funded by the Vienna Science and Technology Fund (WWTF) through project LS 14069.

References

[1] B. Grychtol, et al. *PloS One* 9.8 (2014): e103045.
[2] Z. Zhao, et al. *Physiological measurement* 35.6 (2014): 1083.
[3] A. Adler, et al. *Physiological measurement* 30.6 (2009): S35.
[4] A. Adler and W.R.B. Lionheart. *Physiological measurement* 27.5 (2006): S25.
[5] R. Guardo et al. *IEEE T Biomed Eng* 38: 617−627, (1991)
[6] F. Thürk, et al. *Current Directions in Biomedical Engineering* 2.1 (2016): 511-5

Quantitatively Assess Breast Density as a Cancer Risk Prediction Factor Using Electrical Impedance Spectrums

Ali Zarafshani[1], Sreeram Dhurjaty[2], Shanshan Tang[1], Liangzhong Xiang[1] and Bin Zheng[1]
[1] Stephenson Cancer Research Center, School of Electrical and Computer Eng., Uni. of Oklahoma, Norman, OK, USA
[2] Dhurjaty Electronics Consulting LLC, Rochester, NY, USA
a.zarafshani@ou.edu

Abstract: Breast density as an important risk factor of developing breast cancer is visually assessed by radiologists from mammograms based on BI-RADS guidelines. This subjective determination is often unreliable due to the large inter-reader variability. We investigated a breast density assessment method based on measuring the electrical impedance spectrum of different breast locations to quantitatively assess asymmetric in breast density.

1 Introduction

Asymmetric bilateral breast density has been recognized as an important risk factor of developing breast cancer. Radiologists visually assess asymmetric bilateral breast density from mammograms based on BI-RADS breast density guidelines, namely (1) almost entirely fatty, (2) scattered fibrous-glandular density with a regional focal density areas denoted by dashed line, (3) heterogeneously dense and (4) extremely dense breast, respectively. Current approaches to assess mammographic density have several limitations i.e., the estimated mammographic density does not have a clinically acceptable discriminatory power at the individual level to determine which group of women should be currently screened and/or which imaging screening modality should be applied [1] also the reproducibility of mammographic density is lower in both subjective ratings of radiologists and quantitative assessment of CAD schemes due to large inter-reader variability [2] and high sensitivity [3, 4]. Due to the concern of radiation exposure, imaging cost and high false-positive recalls, many women particularly young women (aged ⩽ 50 years) and underserved women do not participate in routine imaging screenings [5].

2 Methods

We propose a new low-cost, and safe technique to assess asymmetric breast density using electrical impedance spectrums (EIS). The EIS signals depend on the dielectric properties of different tissue types as a function of frequency, since fat, stroma, malignant and benign tissues have different extra and intra-cellular conductivities and membrane capacitance characteristics, RSC values. So, it can provide spectrums in regard to tissue electrical properties exists in different breast regions. We used an enhanced four electrode method (consists of five electrodes) to measure two combinations of electrical impedance spectrums where two electrodes are used to inject current and other three electrodes, two by two are applied to measure the differential voltage across the breast region under test. To overcome the low contact stability and the high electrode-skin impedance, we built a "breast cup" to cover the breast. In this "breast cup" the probes are placed along the eight segments as shown in Fig 1(a).

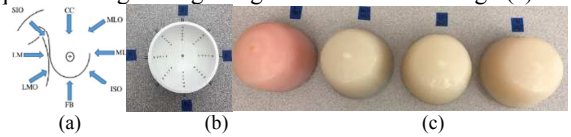

(a) (b) (c)

Fig 1: (a) breast density measurement locations, (b) its breast cup (c) breast density phantom cup with suggested different ratio of fat to dense tissue i.e.1) 90%-10%, 2) 55%-45%, 3) 40%-60% and 25%-75% to mimic BI-RADS breast density.

To detect EIS signals, we used a SR865 DSP Lock-In Amplifier with a custom mirror improved Howland current source [6] to inject current signals and collected electrical impedance signals at the breast phantoms. The Lock-in Amplifier is capable of generating a variety of waveforms with different amplitude fromto 10μV to 1Vppand phase differences, operates up to 2MHz, sensitivity of 1fA, 1nV.

3 Results

To validate EIS technique for breast density, we made four conductive not uniform distributed breast phantoms with different ratio of fibroglandular to fat tissues to be used as experimental models to mimic four breast density categories defined by BI-RADS, fatty tissue>75% and dense tissue ≤ 25%), 25% < dense tissue ≤ 50%), 50% < dense tissue ≤ 75%) and dense tissue > 75%, as illustrated in Fig 1(c). Results indicate the difference of breast density is significant in each breast phantoms.

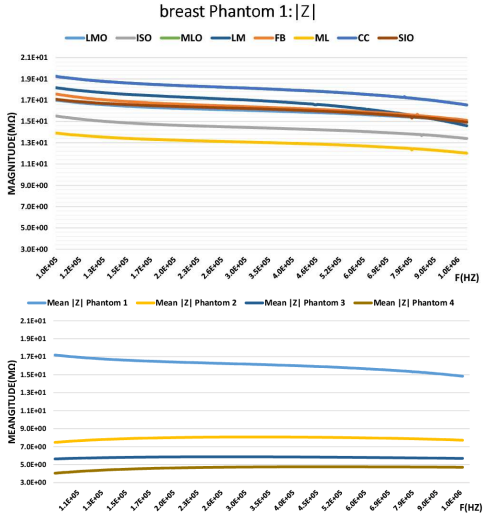

Fig 2: (a) Illustration of |Z| value of electrical impedance spectrums generated from eight transfer electrical impedance measurements in eight different locations, (b) Comparison of the mean value of the electrical impedance spectrum curves measured from four breast phantoms.

4 Discussion and Conclusions

In short, developing new detection methods to more accurately quantify breast density and the bilateral density asymmetry between the left and right breasts is important to significantly increase the discriminatory power in short-term breast cancer risk prediction. We presented a simple EIS application without imaging functionality to non-invasively quantify breast density. In future works, we intend to test the feasibility of using this EIS application by performing human studies.

References

[1] M. H. Gail and P. L. Mai, *J. Natl. Cancer Inst.,* vol. 102, pp. 665-668, May 19, 2010.
[2] W. A. Berg, C. Campassi, P. Langenberg and M. J. Sexton, *Am. J. Roentgenol.,* vol. 174, pp. 1769-1777, 2000.
[3] B. Zheng, R. Shah, L. Wallace, C. Hakim, M. A. Ganott and D. Gur, *Acad. Radiol.,* vol. 9, pp. 1245-1250, 2002.
[4] J. A. Harvey and V. E. Bovbjerg, *Radiology,* vol. 230, pp. 29-41, 2004.
[5] B. L. Sprague, R. E. Gangnon, V. Burt, A. Trentham-Dietz, J. M. Hampton, R. D. Wellman, K. Kerlikowske and D. L. Miglioretti, *J. Natl. Cancer Inst.,* vol. 106, pp. 10.1093/jnci/dju255. Print 2014 Oct, Sep 12, 2014.
[6] A. Zarafshani, T. Bach, C. Chatwin, L. Xiang and B. Zheng, Proc. SPIE, Medical Imaging 2017.

Preliminary test of mobile body composition analyser using AFE4300

Tae San Kim[2], Hyun Tae Choi[1], Geuk Young Jang[2], Tong In Oh[1] and Eung Je Woo[1]

[1]Department of Medical Engineering, Graduate school, Kyung Hee University, Seoul, Korea, ejwoo@khu.ac.kr

[2]Department of Biomedical Engineering, Graduate school, Kyung Hee University, Yongin, Korea

Abstract: Among BCA methods, bio-impedance analysis (BIA) is easy to measure with cheap and fast measurement speed and there is no risk of exposure to radiation. Using the AFE4300 (Texas Instruments, USA) impedance measurement chip from TI, the BCA was performed using the RC model and human body experimental data with a Cole plot analysis. We also compared calculated body composition value with data measured on a commercial BIA system (Inbody770, InBody CO., LTD, Korea).

1 Introduction

Body composition analysis using BIA has been studied for a long time due to the accuracy and convenience of measurement [1]. Various attempts have been made through regression analysis of BIA measurement variables (eg, frequency dependent resistance, phase, etc.) [2]. Measuring position, electrode status, water intake, meal, etc. affect the BIA measurement. Various IC chips are being developed to miniaturize size of the impedance measurement device. We used the AFE4300 to develop a mobile BCA device (mBCA1.0), evaluate its performance, and compare it with a commercial device [3].

2 Methods

2.1 Device

The mBCA1.0 consists of the BCA front-end and analog-to-digital converter (ADC) based on the AFE4300 (TI, USA) and is controlled via the Arduino module. The four-electrode method was used to reduce the influence of the electrode and the buffer was added to improve the input impedance of the voltage measurement device. For BIA measurements, the excitation source is 375uArms and measures 0 Ω to 2.8 kΩ. The maximum sample rate for a 16-bit ADC is 860 samples/second.

2.2 Measurement

mBCA 1.0 can be measured in two modes. (Full-wave rectifier, IQ mode). IQ mode was used for analysis using the Cole plot and the measured frequencies were 8 kHz, 16 kHz, 32 kHz, 64 kHz and 128 kHz. When the user takes a certain posture, mBCA1.0 scans the entire frequency and stores the data after a certain delay.

2.3 Performance evaluation

The RC model phantom was used to evaluate the measurement performance of mBCA1.0 and the comparative evaluation was performed using data from 100 subjects measured simultaneously with a commercial BCA device (Inbody770, Inbody Inc., Korea) [4].

3 Results

We evaluate the measurement module using with the RC phantom in figure 1. The average SNR of the in-phase was 56.58 dB and quadrature-phase was 48.25 dB. Table 1 shows SNR table of each frequency. Higher frequency results has worse repeatability.

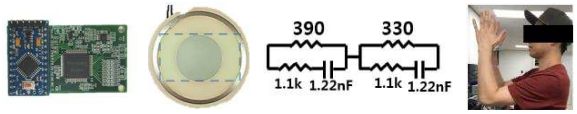

(a) (b) (c)

Figure 1: (a) measurement module in mBCA1.0, (b) Test RC-model (c) measurement posture (RA-LA)

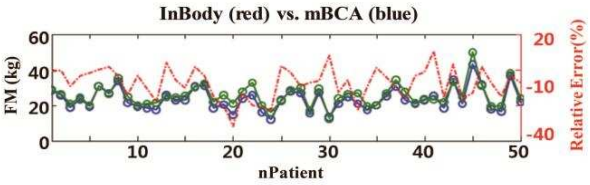

Figure 2: Comparison between Inbody770 and mBCA1.0

SNR [dB]	8kHz	16kHz	32kHz	64kHz	128kHz
In-phase	62.31	61.77	61.14	58.57	39.12
Quadrature	46.54	55.56	44.48	47.38	47.28

Table 1: Signal to noise ratio in 100 time measurement

We performed human experiment using the developed device and a commercial BIA system, called Inbody770 with 100 normal people. We use 50 person data to calculate regression equation. And others are used to evaluate the accuracy. As a results, the fat mass has 11.7% error, and 8.7% dispersion.

4 Conclusions and discussion

To simplify BCA measurements, we developed the "mBCA1.0" mobile body composition analyser based on the AFE4300. The SNR measured by the current system is about 50 dB. And we found that system has 88.3% accuracy with commercial BCA system. We plan to improve performance by using a small electrode to improve the interface and improve and correct the excitation current source.

5 Acknowledgements

References

[1] U. G. Kyle, Clinical Nutrition 23 (2004) 1226-1243, 1430–1453
[2] R Buendia et. al., Physiol. Meas. 35 (2014) 1373-1395
[3] AFE4300(doc.SBAS586B), Texax Instruments, , 2013
[4] Inbody770 manual, Inbody Inc., (www.inbody.com

Origins of Cardiosynchronous Signals in EIT

Andy Adler[1], Martin Proença[2], Fabian Braun[2,3], Josef X. Brunner[4], Josep Solà[2]

[1]Carleton University, Ottawa, Canada, Andy.Adler@Carleton.ca
[2]CSEM, Neuchâtel, Switzerland
[3]Ecole Polytechnique Fédérale de Lausanne, Switzerland
[4]Swisstom AG, Landquart, Switzerland

Abstract: EIT waveforms have components synchronous with cardiac activity, which are often assumed to originate from the blood perfusion. There are numerous other contributions to this signal. The goal of this paper is to provide a list of the factors which could be at the origin of these cardiac-related components, to help guide future research.

1 Introduction

As a functional imaging modality, EIT is understood to be sensitive to the movement of conductivity-contrasting gasses ($\downarrow\sigma$) and fluid ($\uparrow\sigma$). It is thus common to assume that the component of EIT images synchronous with breathing originates in the movement of air, and that the cardiac-frequency component originates from the perfusion of blood. The validity of these assumptions is important for the interpretation of EIT results. For example, simulations of chest-wall movement identified a breathing-frequency contribution to lung images [1], which contribute up to 20% of the signal due to ventilation, and depend on the geometry of chest wall movement. Thus, changing breathing movements (e.g. due to posture change) affects the ventilation-EIT signal relationship.

For the case of cardiosynchronous EIT signals, the problems of interpretation are more difficult. EIT is quite sensitive to heart activity, and measures of almost any part of the body show clear cardiosynchronous signals. In several publications, these signals have been called "EIT perfusion", suggesting the EIT signal is caused by blood flow. However, it is clear that continuous blood flow, by itself, cannot create EIT conductivity changes (Fig. 1). To avoid this problem various other terms have been proposed: 1) "perfusion-related EIT signals", which emphasizes that there is a relationship but not necessarily a correlation to blood flow, and 2) "pulsatilility" which emphasizes the relationship to the pulsatile signal. For a review of the terminology and its use, see [2]. Here, we recommend the neutral term "cardiosynchronous" EIT signals.

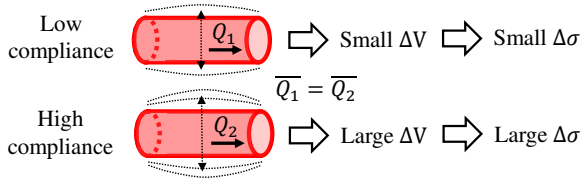

Figure 1: Arteries with equal perfusion (i.e. mean flow $\overline{Q_1} = \overline{Q_2}$) but different compliance lead to different conductivity changes $\Delta\sigma$.

Our goal in this paper is to collect a list of the possible sources for these cardiosynchronous signals. Some work has been done to model and understand the effect of heart deformation and displacement[3], and flow-induced blood conductivity changes[4], but a detailed list of the possible sources is not available.

2 Origin of Cardiosynchronous Signals

We first classify phenomena by their physical mechanism:
- Cardiosynchronous mechanical deformations: heart motion and the resultant movements of other structures.
- Blood volume changes: within the heart, a vessel or organ
- Red blood cell reorientation due to pulsatile blood flow [5]
- Reorientation of anisotropic structures: heart muscle, etc.

We then identify the possible sources and locations where the mechanisms listed might occur (Fig. 2).

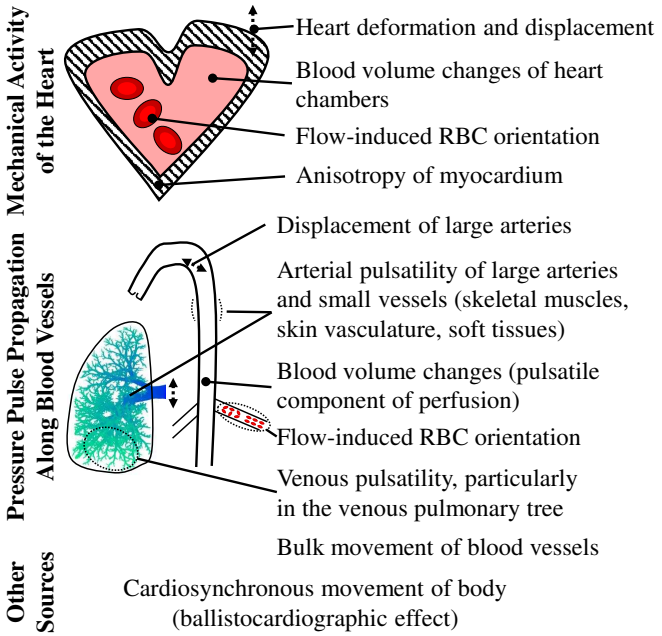

Figure 2: Diagram of possible sources of cardiosynchronous signals (by mechanism). The pressure pulse propagation is modulated by the pressures and compliances in the veins and arteries, and the compression and displacement of lung tissue due to lung arterial pulsatility and heart motion. Also, the pulsatile signal from venous return varies with intra-thoracic pressure. Finally, all factors will be affected by the spatial sensitivity of the EIT imaging system given the electrode positions and stimulation and measurement patterns.

EIT is sensitive to blood flow and many other cardiosynchronous effects, which we list here. Only some effects have been studied [4]. Our hope is that this list serves as a starting-point to better understand the origin and relative contribution of these signals, as a fraction of that from perfusion.

References

[1] A Adler, R Guardo, Y Berthiaume *IEEE T Biomed Eng* 43:414, 1996.
[2] I Frerichs, *et al Thorax*, 72:83, 2017.
[3] M Proença, *et al*, *Physiol Meas*, 36:1175, 2015.
[4] M Proença, *PhD Thesis*, EPFL, Lausanne, 2017
[5] R L Gaw, *PhD Thesis*, Queensland University of Technology, 2010.

Piezo-electric Nanoweb based Pressure Distribution Sensor for Detection of Dynamic Pressure

You Jeong Jeong[1], Tong In Oh[1], Kap Jin Kim[2] and Eung Je Woo[1]

[1]Department of Medical Engineering, Graduate school, Kyung Hee University, Seoul, Korea, tioh@khu.ac.kr
[2]Advanced Materials Engineering for Information & Electronics, Kyung Hee University, Yongin, Korea

Abstract: Recently, a fabric based flexible and soft pressure imaging sensor is required for ubiquitous lifecare monitoring. In this study, we developed the new fabric pressure distribution sensor for detecting dynamic pressure using piezo-electric nanoweb. We apply electrical source imaging technique to reconstruct the pressure distribution image from the measured voltage data at the boundary of the fabric sensor. We evaluated the performance of piezo-electric nanoweb imaging sensor and presented the preliminary results.

1 Introduction

To provide ubiquitous lifecare services and wearable healthcare monitoring requires the detection of pressure changing over a large area. Many studies on pressure distribution sensors covering a large area have used a large number of single-cell-based pressure sensors in a grid structure [1,2]. However, pressure sensor arrays were commonly thick and inflexible. Due to a large number of signal lines and manual manufacturing processes, there is a large crosstalk and high cost. In this study, we developed the pressure distribution sensor using PVDF (polyvinylidene fluoride) nanoweb and non-conductive fabric sheet for detecting dynamic pressure. Piezo-electric current is generated at the pressure point and we measure the piezo-electric signal at the boundary of fabric sensor. Since all materials of pressure distribution sensor are fabric, it is very flexible and breathable [3].

2 Method

We designed the dynamic pressure distribution sensor of 15×5 cm^2 size. We inserted the PVDF nanoweb fabricated by electro-spinning procedure (FTEnE, South Korea) between non-conductive fabric sheets as shown in Fig.1(b). Because the PVDF nanoweb included high density of β-crystal generated by the addition of TBAP (Tetrabutylammonium perchlorate) and metal nanoparticles ($AgNO_3$), our PVDF sensor can produce larger piezo-electric signal due to the compressive force than other PVDF nanoweb. We evaluated the basic performance of the fabric based pressure sensor using the customized testing equipment combining with applying dynamic pressure in Fig.1(a).

3 Result

We measured the piezo-electric output signal when applying the constant pressure in setting of Fig.1(a). For dynamic pressure distribution measurements, we did an additional experiment as shown in Fig.1(d). Two piezo-electric amplifiers were connected at the end of left and right sides (point A and B) of Fig.1(d). We were hammering with rubber stick from the end of left side to the end of right side during 10 seconds. Time points of T1-T4 were corresponding to the position of applying pressure. The maximum amplitude of piezo-electric signal was 1,350 mV_{pp} at A point and 1,270 mV_{pp} at B point. The amplitude was decreasing when increasing of distance between the position of hammering and the position of measurement.

4 Conclusions

The piezoelectric current of new sensor was increased by adding tetrabutylammonium perchlorate (TBAP) and metal nanoparticles ($AgNO_3$). The amplitude of measured signal was corresponding to the distance of pressure point.

5 Acknowledgements

Research supported by the Industrial Strategic Technology Development Program (10047976) funded by the Ministry of Trade, Industry, and Energy of Korea

References

[1] R. Wijesiriwardana, K. Mitcham, W. Hurley and T. Dias et al, *IEEE Sens. J.*, 5:989-994, 2005.
[2] A. Ueno, Y. Akabane, T. Kato, H. Hoshino, S. Kataoka, and Y. Ishiyama, *IEEE Trans Biomed Eng.*, 54, 2007.
[3] M. Feneberg, K. Thonke, T. Wunderer, F. Lipski and F. Scholz, *J. Appl. Phys.*,107:103517-103517-6, 2010.

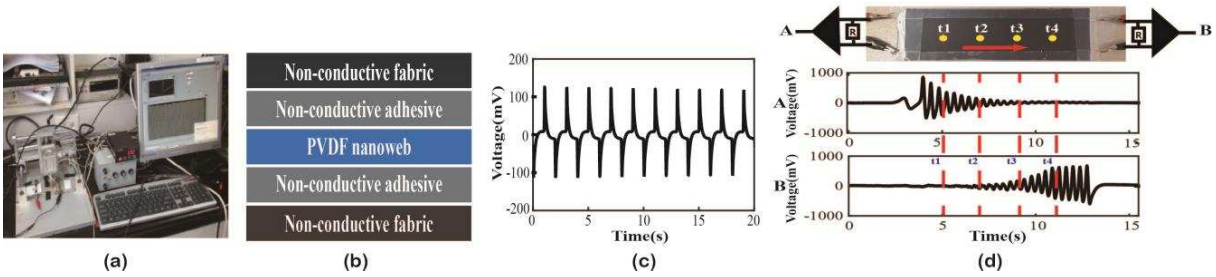

Figure 1: (a) Experimental setup for applying dynamic pressure, (b) Structure of piezo-electric pressure distribution sensor layered by PVDF nanoweb and non-conductive fabric, (c) piezo-electric output when applying the constant pressure, (d) output measured at the both end of point A and B when hammering with rubber stick from the end of left side to the end of right side of sensor (5 cm × 15 cm) during 10 seconds.

Efficient computations of the Jacobian matrix using different approaches are equivalent

Andy Adler[1], Alistair Boyle[2], William R.B. Lionheart[3]

[1]Systems and Computer Engineering, Carleton University, Ottawa, Canada, Andy.Adler@Carleton.ca
[2]School of Electrical Engineering and Computer Science, University of Ottawa, Canada
[3]School of Mathematics, University of Manchester, UK

Abstract: Two main approaches have been used to calculate the Jacobian, $\mathbf{J}$, or sensitivity matrix: the "adjoint field" method and differentiation of the system matrix. While some investigations have sought to test which is more efficient, we show the approaches are equivalent, and an efficient implementation of either produces the same underlying algorithm.

1 Introduction

The sensitivity matrix, $\mathbf{J}$, describes how small internal conductivity changes relate to measurements; it is key to image reconstruction and also to understanding the characteristics of EIT configurations. Efficient calculation of the $\mathbf{J}$ matrix is essential. Fig. 1 shows a body where data element $d_{i,j}$ is recorded using measurement $\mathbf{m}_i$ and current $\mathbf{c}_j$ patterns.

When a region k undergoes a change $\sigma_k \rightarrow \sigma_k + \delta\sigma$, the sensitivity is defined

$$\mathbf{J}_{i,j,k} = \frac{\partial}{\partial \sigma_k} d_{i,j} \tag{1}$$

Normally, $\mathbf{J}$ is represented as a matrix, by selecting rows corresponding to (i,j) pairs of (measurement, stimulation) in the order applied by the EIT hardware.

Numerical methods are used to solve the forward problem on arbitrary geometries, and the finite element method (FEM) is widely used because it facilitates refinement in regions of high electric field, such as near the electrodes. We assume piecewise-constant conductivity on each element.

Two approaches to the calculation of $\mathbf{J}$ have been used in EIT: adjoint-field methods[1, 3], and differentiation of the FEM system (admittance) matrix[5], which we call the "admittance matrix differentiation method". It is also possible to approximate $\mathbf{J}$ using a "perturbation Jacobian."

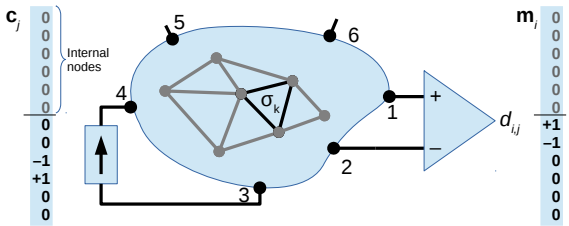

Figure 1: FEM with six electrodes and internal nodes, using current pattern $\mathbf{c}_j$ and measurement pattern $\mathbf{m}_i$. Electrodes nodes are enumerated after internal FEM nodes in this example.

2 Jacobian calculations

Measurements are $d_{i,j} = \mathbf{m}_i^\mathsf{T}\mathbf{v}_j$, using the notation: continuous values $\mathcal{V}$, values on FEM nodes $\mathbf{v}$, and values on nodes $\dot{\mathbf{v}}_k$ in region k. After choosing a ground node, the node voltages due to current pattern $\mathbf{c}_j$ are $\mathbf{v}_j = \mathbf{Y}^{-1}\mathbf{c}_j$ with admittance matrix $\mathbf{Y}(\boldsymbol{\sigma}) = \mathbf{C}^\mathsf{T}\mathbf{S}(\boldsymbol{\sigma})\mathbf{C}$, where $\boldsymbol{\sigma}$ is the vector of conductivities in each finite element, $\mathbf{C}$ is a connectivity matrix, and $\mathbf{S}(\boldsymbol{\sigma})$ is a block diagonal matrix with blocks $\sigma_k\mathbf{B}_k$ for each region k

$$[\mathbf{B}_k]_{\ell,m} = \int_k \phi_\ell \phi_m dA \tag{2}$$

integrated over the volume of region k, where ϕ_ℓ, ϕ_m are shape functions.

2.1 Adjoint-field method

The adjoint-field method calculates[1]

$$\mathbf{J}_{i,j,k} = \int_k \nabla\mathcal{V}_i \cdot \nabla\mathcal{V}_j dA, \tag{3}$$

where $\mathcal{V}_j, \mathcal{V}_i$ are the body voltages from applying a current $\mathbf{c}_j$ and $\mathbf{m}_i$ (interpreted as a current). Defining $\mathbf{v}_j = \mathbf{Y}^{-1}\mathbf{c}_j$ and $\mathbf{v}_i = \mathbf{Y}^{-1}\mathbf{m}_i$, eqn (3) may be represented as $\mathbf{J}_{i,j,k} = \dot{\mathbf{v}}_{k,i}^\mathsf{T}\mathbf{B}_k\dot{\mathbf{v}}_{k,j}$, where node voltages in region k are $\dot{\mathbf{v}}_{k,i} = \dot{\mathbf{C}}_k\mathbf{v}_i$, for a selection matrix $\dot{\mathbf{C}}_k$ (and similarly for j). The Jacobian is then efficiently calculated for each region k

$$\mathbf{J}_{i,j,k} = \left(\dot{\mathbf{C}}_k\mathbf{Y}^{-1}\mathbf{m}_i\right)^\mathsf{T}\mathbf{B}_k\left(\dot{\mathbf{C}}_k\mathbf{Y}^{-1}\mathbf{c}_j\right) \tag{4}$$

2.2 Admittance-matrix differentiation method

From (1) and $d_{i,j} = \mathbf{m}_i^\mathsf{T}\mathbf{v}_j = \mathbf{m}_i^\mathsf{T}\mathbf{Y}^{-1}\mathbf{c}_j$ [5],

$$\begin{aligned}\mathbf{J}_{i,j,k} &= \frac{\partial}{\partial\sigma_k}\mathbf{m}_i^\mathsf{T}\mathbf{Y}^{-1}\mathbf{c}_j = \mathbf{m}_i^\mathsf{T}\mathbf{Y}^{-1}\left(\frac{\partial}{\partial\sigma_k}\mathbf{Y}\right)\mathbf{Y}^{-1}\mathbf{c}_j \\ &= \mathbf{m}_i^\mathsf{T}\mathbf{Y}^{-1}\mathbf{C}^\mathsf{T}\left(\frac{\partial}{\partial\sigma_k}\mathbf{S}(\boldsymbol{\sigma})\right)\mathbf{C}\mathbf{Y}^{-1}\mathbf{c}_j \\ &= \left(\dot{\mathbf{C}}_k\mathbf{Y}^{-1}\mathbf{m}_i\right)^\mathsf{T}\mathbf{B}_k\left(\dot{\mathbf{C}}_k\mathbf{Y}^{-1}\mathbf{c}_j\right)\end{aligned} \tag{5}$$

where $\mathbf{B}_k$ is the only non-zero block in $\frac{\partial}{\partial\sigma_k}\mathbf{S}(\boldsymbol{\sigma})$, and $\dot{\mathbf{C}}_k$ is the corresponding reduced connectivity matrix.

3 Discussion

The equivalence of (4) and (5) illustrates that an implementation of both methods yields the same underlying calculation (see also [2], ch. 3). Efficient implementation strategies are also the same for both: pre-calculation of the matrices in parenthesis, and calculation of larger blocks $\mathbf{B}_k$ for model regions with the same parameter value in the inverse model.

References

[1] O Dorn, H Bertete-Aguirre, JG Berryman, GC Papanicolaou *Inverse Problems*, 15:1523–1558, 1999.
[2] WR Breckon , PhD Thesis, Oxford Polytechnic, UK, 1990.
[3] N Polydorides, WRB Lionheart. *Meas Sci Technol* 13:1871–1883, 2002.
[4] N Polydorides, WRB Lionheart *Proc WCIPT*, Banff, Canada, 2003.
[5] TJ Yorkey, JG Webster, WJ Tompkins, *IEEE T Biomed Eng* 11:843–852, 1987.

MRCI: a Matlab toolbox for Low-frequency Conductivity and Current Density Imaging using MRI

Nitish Katoch[1], B.K Choi[1], S.Z.K Sajib[1], Hyung Joong Kim[1], Oh In Kwon[2], and Eung Je Woo[1]

[1] Department of Biomedical Engineering, Kyung Hee University, Seoul, South Korea, ejwoo@khu.ac.kr

[2] Department of Mathematics, Konkuk University, Seoul, South Korea

Abstract: To facilitate experimental studies in potential clinical applications, we developed a software toolbox for low frequency conductivity and current density imaging methods. This includes magnetic resonance electrical impedance tomography (MREIT), diffusion tensor MREIT (DTMREIT) and magnetic resonance current density imaging (MRCDI).

1 Introduction

Low-frequency conductivity is an apparent conductivity value of a medium measured by using a low-frequency probing current. MRCDI and MREIT [1] provide current density and isotropic conductivity images, respectively, using current-injection phase MRI techniques. DT-MREIT produces anisotropic conductivity tensor images by incorporating diffusion weighted MRI into MREIT [2] [3].

2 Method

When low frequency current is injected to an electrically conductive object it induces voltage u, current density $\mathbf{J}$ and magnetic flux density $\mathbf{B}$ depending on the internal conductivity distribution $\boldsymbol{\sigma}$, which are described by the Maxwell's equation. In order to produce isotropic or equivalent isotropic conductivity distribution in MREIT, numerous algorithms has been reported, e.g. *J*-substitution algorithm, harmonic B_z, non-iterative harmonic B_z, etc. [1]. For estimating the current density distribution from the measured B_z data the projected current density method also developed [1]. At low frequency biological tissues like skeletal muscle, brain white matter shows anisotropic property due to the cellular membrane. For estimating the tissue anisotropic conductivity, DT-MREIT method has been developed [2] which combines the directional information from the DTI and MREIT, recover position depended scale factor to convert the water diffusion tensor to its corresponding conductivity tensor. In this Matlab toolbox, we implemented three current density image reconstruction algorithms for MRCDI, four isotropic conductivity image reconstruction algorithms using MREIT and two anisotropic conductivity tensor image reconstruction algorithms in DT-MREIT, which are summarized in the table-1.

Table 1: List of toolbox functions for Low-frequency conductivity and current density imaging using MRI.

Function	Algorithm
mrci_projected_current_density1.m	Projected current density type 1
mrci_projected_current_density2.m	Projected current density type 2
mrci_regional_projected_current_density.m	Regional projected current density
mrci_harmonic_bz.m	Harmonic Bz algorithm
mrci_J_substitution.m	*J*-substitution algorithm
mrci_JT_substitution.m	Transversal *J*-substitution algorithm
mrci_noniterative_harmonic_Bz.m	Non-iterative harmonic Bz algorithm
mrci_dtmreit_noniterative.m	Non-iterative DT-MREIT algorithm
mrci_dw_J_substitution.m	Diffusion weighted *J*-substitution algorithm

2.1 Results

We reconstruct the equivalent isotropic conductivity of an *ex-vivo* canine brain using harmonic B_z algorithm implemented as toolbox function, "*mrci_harmonic_bz*" which is displayed in Fig 1(b)-(c). Also current density distribution of the same animal subject using the toolbox function, "*mrci_projected_current_density_type2*" shown in Fig. 2(a)-(b) is reconstructed. Using the recovered current density distribution estimated from the measured B_z data, we then reconstruct the isotropic conductivity using non-iterative harmonic B_z algorithm implemented as toolbox function "*mrci_non_iterative_harmonic_bz*".

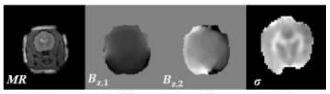

Figure 1: *ex-vivo* canine head image. (a) MR magnitude, (b)$B_{z,1}$ and (c) $B_{z,2}$ image.

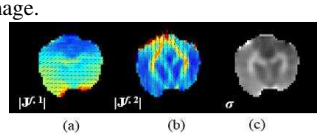

Figure 2: Horizontal (a) and vertical (b) component of projected current density vector. Reconstructed isotropic conductivity using non-iterative harmonic B_z algorithm(c).

Using the toolbox function *"mrci_dw_J_substitution"* we recover the position dependent scale factor (Fig. 3) and anisotropic conductivity distribution for the *in-vivo* canine brain (Fig. 3(b)-(d)).

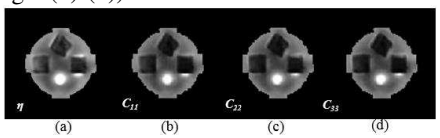

Figure 3: (a) Scale factor ($\boldsymbol{\eta}$), Diagonal component of conductivity tensor (b)-(d).

3 Conclusion

This paper introduces a novel MR conductivity imaging (MRCI) toolbox for Matlab (Math Works, USA) for experimental studies of these imaging methods. Together with experimental data sets, it is available at http://iirc.khu.ac.kr.

4 Acknowledgement

This work was supported by the National Research Foundation (NRF) of Korea grants (No. 2014R1A2A1A09006320, 2015R1A5A1037656, 2015R1D1A1A09058104).

References

[1] J. K. Seo, E. J. Woo, *IEEE TMBE Vol.*61, pp. 2955-74, 2014.
[2] O. I. Kwon, E. J. Woo, *Phys. ed. Bio. Vol. 59, pp.* 2955-74, 2014.
[3] W.C Jeong, S. Z. K. Sajib, N. Katoch H. J. Kim, O. I Kwon, E. J. Woo, *IEEE TMI Vol*. 36 pp. 124-131,2017

Imaging of Transient Hyperaemic Response (THR) by EIT

Taweechai Ouypornkochagorn[1], Hugh McCann[2], and Nick Polydorides[2]

[1]Faculty of Engineering, Srinakharinwirot University, Thailand, taweechai@g.swu.ac.th

[2]School of Engineering, University of Edinburgh, UK, {h.mccann, n.polydorides}@ed.ac.uk

Abstract: We report on a series of tests on human volumnteers aimed at assesing the performance of EIT in sensing, monitoring and imaging cerebral heamodynamic responses. Using our fEITER system we have observed systematic patterns indicating the expected response of cerebral haemodynamics to clamping of the carotid artery by means of the Transient Hyperaemic Response test.

1 Introduction

The establishment of EIT in cebebral diagnostics continuous to be hindered by challenges pertaining to the complexity of the models, the signal to noise ratio in the measurements, the uncertainty in in-vivo tissue conductivity, and often the muffled nature of the targeted neurophysiological change. We have recently been working to address some of the geometric modelling errors [1], as well as developing strategies to obtain more accurate estimates of in-vivo tissue conductivities from EIT data [2]. In this work, we focus attention in the application of Transient Hyperaemic Response (THR) that is known to trigger a cerebral conductivity change that is more profound in its amplitude and support, aiming to verify whether the neurophysiological effect can be sensed, localised and imaged using EIT. This test involves a phase (~5s) of carotid artery occlusion administered to the subject at the side of the neck, causing the vasodilation of small vessels, and in turn leading to a decrease of blood flow velocity (FV) during that period. Subsequenbtly the occlusion is released causing a brief increase of blood flow before the velocity returns to the normal rate.

2 Methods

A THR test was applied to the left side of the neck of a healthy male subject. The FV of middle cerebral artery was recorded by Transcranial Doppler ultrasound (TCD) on the both sides. ECG was also recorded during the test. EIT data aquisition was performed on 32 scalp electrodes using the fEITER machine [3], complying with IEC60601, recording at a speed of 100 fps. To model these measurements we have used a 3D head model with anatomical detail comprising 208000 tetrahedral elements and configured to the electrode positions, current and measurement patterns. For image reconstruction we have used a regularised, nonlinear conjugate gradient algorithm [4]. To suppress noise, the measured data were averaged over a cardiac cycle, effectively reducing the temporal resolution of imaging to about 1 frame per second.

3 Results and Discussion

A set of representative results from these measurements are illustrated in Fig. 1 and Fig. 2. The decrease of FV can is trivial to notice on the (left) occlusion side in Fig. 1a, and this appears to be consistent with the EIT data in that the increase of voltage implies drop in conductivity, conceivably linked to a decrease of blood flow, cf Fig. 2a and b. However, after releasing the occlusion, the brief increase of blood seems undetected by the EIT measurement and imaging, although this is captured in the TCD data. This may be due to the brief change duration is shorter than a REG cycle, or a lack of sensitivity from EIT. Meanwhile on the non-occlusion side, the small increase of blood can be interpreted from the EIT measurement during occlusion, see Fig.1b, which is in the similar interpretation from the TCD measurement. This increase is clearly depicted in the images Fig.2a and b. However, the large change in EIT measurements occuring after the occlusion is not exhibited in TCD, though the changes in several regions appear in images Fig. 2d.

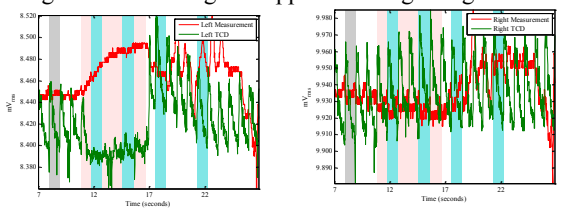

(a) (b)

Figure 1: TCD (green lines) and EIT (red lines) measurement on the left (a) and right (b) temple side. The occlusion period is indicated by the light red regions (11^{th} s – 17^{th} s). The profound change occurred on the occlusion (left) side on both signals.

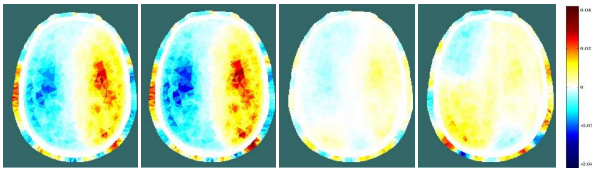

(a) (b) (c) (d)

Figure 2: Reconstructed difference images of THR (the left of the images is the position of the left ear). The reference period is shown in grey regions in Fig. 1 (before the occlusion). Image (a) and (b) are of the 1^{st} and 2^{nd} blue regions (during the occlusion), and (c) and (b) are of the 3^{rd} and 4^{th} blue region (after the occlusion).

4 Conclusions

Significant conductivity changes like those associated to accute haemodynamic phenomena, become suitable to monitor with EIT, although further clinical tests and methods validation might be necessary to fully understand and validate the images.

References

[1] T Ouypornkochagorn, H McCann, N Polydorides, *Conf EMBC2015*, Milan, Italy, 2015.

[2] T Ouypornkochagorn, H McCann, N Polydorides, *Conf 15th EIT2014*, Ontario, Canada, 2014.

[3] H McCann, ST Ahsan, JL Davidson, RL Robinson, P Wright, CJD Pomfrett, *EMBS2011*, Boston, USA, 2011.

[4] T Ouypornkochagorn, *PhD Thesis*, University of Edinburgh, 2016

Enhancement of EIM system with shifting drive-receive method

Gerald Sze, Min Xu and Wei Wang

Micro Image Biotech Ltd, UK, w97wang@yahoo.co.uk

Abstract: In order to enhance the resolution of an EIM system with limited number of planar electrodes, a shifting drive-receive method has been investigated in last few years. This method shifts the electrode plane horizontally, and the movement can mimic a multiplication of planar electrodes, as such the number of drive-receive pattern could be increased. Results showed that this method could greatly enhance the resolution of images.

1 Introduction

This paper presents the configuration and results of a method that enhances the resolution of image acquired from an electrical impedance mammography (EIM) system [1].

2 Methods

2.1 Shifting of electrodes

The 2D mesh applied in the reconstruction process was shown as below:

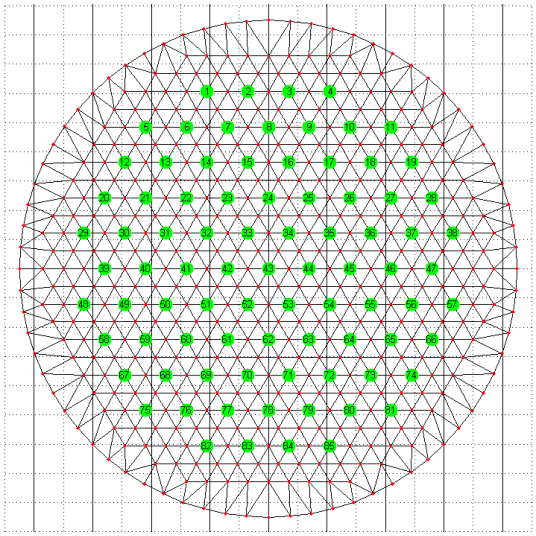

Figure 1: 2D mesh

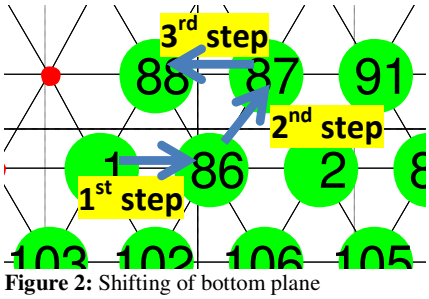

Figure 2: Shifting of bottom plane

The mesh consists of 780 triangular elements and 85 planar electrodes that located on the nodes in green. The proposed shifting method shifts the whole bottom plane together with all electrodes three times. Figure 2 presents the shifting of the bottom plane, as such the number of nodes of the mesh would be multiplied by 4. For example, After the first shift, node number 1 would be physically shifted to node number 86. Second shift to node number 87. Third shift to node number 88, then back to the original position. The number of drive-receive pattern are multiplied by 4.

2.2 Experimental setup

Here presents an agar experiment to compare the different between no-shift and shifting methods. Configuration of the experiment is as below: Depth of saline is 21mm; Saline conductivity 6000μs/cm; Agar object diameter 9mm; Located at 10mm from bottom plane and 10 o'clock position as shown in figure 3..

Figure 3: Agar experiment and object location

3 Results

Acquired data of no-shift method and shifting method at 10kHz are reconstructed as below:

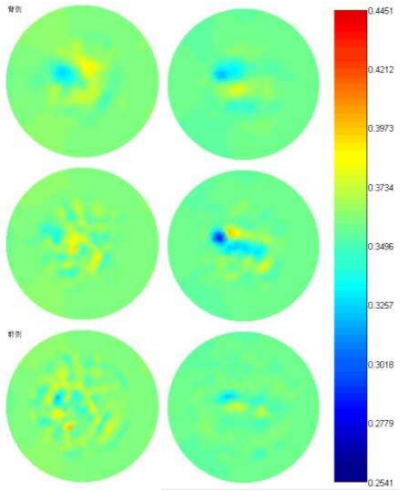

Figure 4: No-shift method image (left); Shifting method image (middle); Colorbar showing reconstructed resistivity of both methods (right)

The images are constructed as 3 layers 3D image. Top row represents the ventral layers, and bottom row represents the dorsal layers (where electrodes closes to). It could be seen that the agar object, that hanging in the saline tank could be displayed more clearly and precise location in the shifting method images.

References

[1] G. Sze, *Dissertation*, Univ. Sussex, 2012

Internal Diode for Frequency Selective EIT Contrasts

Alistair Boyle[1], Daniel Kyrollos[2], John Harvey[2], Andy Adler[2]

[1]University of Ottawa, Ottawa, Canada, aboyle2@uottawa.ca
[2]Carleton University, Ottawa, Canada

Abstract: Impedance imaging has low sensitivity in regions deep within the interior of a body. Inserting a current source, such as a capsule swallowed and then tracked through the gastrointestinal tract, would improve sensitivity near the source. We conducted simulation and tank-model experiments to evaluate whether harmonics from diode conduction would be detectable when used in a body.

1 Introduction

A circuit element with a non-linear V-I relationship, such as a diode, produces harmonics at multiples of the input frequency f when driven with sinusoidal inputs. Our concept is that harmonics could be detected in the measured voltages from a diode placed within the body using an EIT system. In this case, the diode will act as a source at the first harmonic $2f$, turning EIT into a source localization problem which can give higher resolution.

Since the harmonics are small, the EIT current sources would need to be sufficiently harmonically pure, in order to separate the the diode-produced harmonics from those of the current source. In this paper, our goal is to evaluate the feasibility of the concept; we study the harmonic to fundamental ratio v_{2f}/v_f which would be used to detect the source.

2 Simulations

We study an EIT measurement system with 16 electrodes around the circumference of a tank or chest operating at 1 kHz. 2D models were constructed in EIDORS using Netgen to estimate the voltage V across a diode located near the centre of a cylindrical domain (fig. 1). V was simulated for a range of geometries and EIT drive levels, as well as expected measurement amplitudes. The FEM system matrix $\mathbf{A}$ may be reduced to a minimal resistor network [1].

$$\begin{bmatrix} \mathbf{v}_a \\ \mathbf{v}_b \end{bmatrix} = \mathbf{A} = \begin{bmatrix} \mathbf{B} & \mathbf{C}^\mathsf{T} \\ \mathbf{C} & \mathbf{D} \end{bmatrix} \begin{bmatrix} \mathbf{i}_a \\ 0 \end{bmatrix} \tag{1}$$

The upper-left triangle of the reduced matrix, $\widetilde{\mathbf{A}} = \mathbf{B} - \mathbf{C}^\mathsf{T}\mathbf{D}^{-1}\mathbf{C}$, gives the resistor values between nodes: the four electrodes and two nodes at the ends of the diode. Resistor values were selected to minimize the fitting error between ideal resistor values and available values within tolerances ($\pm 0.1\%$). This procedure is available as an EIDORS tutorial [2].

3 Experiments and Results

A resistor mesh was constructed using resistance values from the tank simulation with a diode node spacing of 9 mm. Across nodes 1 and 2, a 1.0 kHz sine wave with varying amplitude was applied. A spectrum analyzer was placed across nodes 3 and 4 and the $1f$ and $2f$ harmonics were recorded. Different models of diodes were tested, these were selected based on their low forward voltage characteristics.

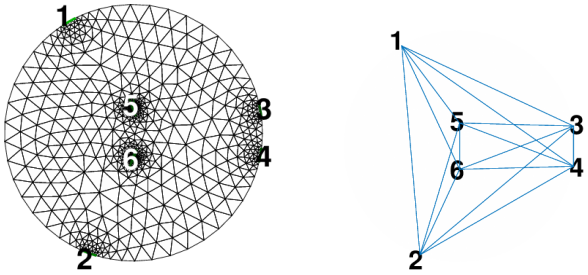

Figure 1: (left) 2D FEM simulation mesh and (right) reduced model as a 15 resistor (blue), 6 terminal (numbered) network, a diode is inserted between terminals #5 and #6 in the interior

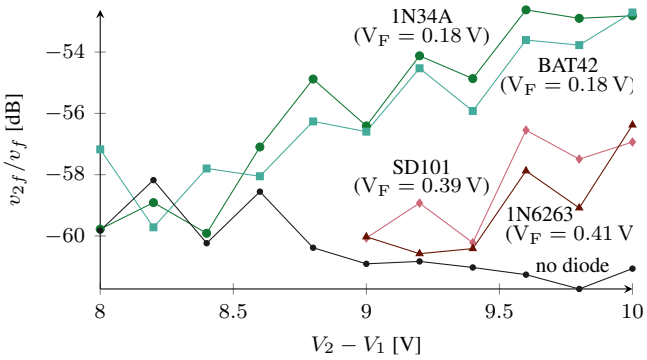

Figure 2: Difference between first and second harmonic compared to input voltage at 9 mm spacing for a variety of passive low-dropout diodes; 1N34A germanium and BAT42 Schottky diodes exhibit stronger second harmonics

Results show that although only small signals were produced by the diodes, it was still possible to detect the diode presence as long as input voltages were high enough. Signal strength increased with increasing applied EIT voltage, and decreasing diode forward voltage.

4 Discussion

Our study investigated whether the harmonics from internal diodes produce enough signal to distinguish them. Even for low-dropout (~0.2 V) passive diodes, the required boundary stimulation voltages was > 10 V, which limits its practical application in humans. Industrial or geophysics ECT/ERT have reduced electrical safety requirements that may allow sufficient forward voltage. Active circuits such as "super diodes" offer an alternative, but need a virtual ground and power which make their implementation challenging. Other passive components such as inductors or capacitors may also prove to be effective, but were not evaluated in this work.

References

[1] Adler A, Lionheart WRB *EIT2016* Stockholm, Sweden, 2016
[2] Boyle A, *eidors.org/tutorial/model_reduction*, 2017

Portable, Accessible Multi-Frequency Screen for the Prognosis of Neuromuscular Atrophy and Degeneration

Mary McCreary, Allison Garcia, Danya Hoban, Hyun Song, Taylor Barg and Ahmet Can Sabuncu

Lyle School of Engineering, Southern Methodist University, Dallas, TX, USA, mmccreary@smu.edu

Abstract: In the spirit of improving access to affordable, portable, and compatible medical diagnostics, this paper presents the design and Phase I implementation of an impedance system for the comparison of neuromuscular disease states. Using the novel configuration of multiple electrocardiogram-standard electrodes with the multi-frequency AD5933 impedance converter, 90 human subjects were screened for variations in the impedance profiles of their dominant biceps brachii muscle.

1 Introduction

EIT is most notably used for high-contrast conductivity imaging in thoracic cavities [1], but its potential for soft tissue distinction in extremities can be applied towards the critical early diagnosis and prognosis of irreversible neuromuscular degeneration [2]. By combining the techniques of electromyography and bioelectric impedance analysis [3], we aim to establish proof-of-concept that lumped electrical and demographic data can highlight physical anomalies in muscle composition. Conflation of the circumference, temperature, and force loading data of the accessible, cylindrical biceps brachii with patient demographic data such as body composition, body mass index, disease history, age, and gender allows for a comprehensive survey of minutia that skew the background impedance profiles for healthy skeletal muscle. By understanding the parasitic effects of fat, temperature, or muscle contractions on the impedance profile, a continuum of background data on many human body types can be applied to future disease models. This proof-of-concept is the first step towards the exclusion of scattered metrics, and consideration of these findings will advance the distinction of soft tissue composition in improved-resolution EIT images.

2 Methods

Each subject is surveyed for their disease and injury history or any implanted electrical devices. Their height, weight, body composition, body mass index, age, gender, and ethnicity is recorded. The temperature of the applied skin surface is scanned with an infrared thermometer and the dominant-arm resting and flexing circumferences of the biceps brachii are taken, marking the apex of the flexing muscle. The application surface is sterilized, and two ECG-standard electrodes were applied 5 cm apart axially, centred on the apex. Triplicate control measurements are taken for resting (180^o), angled (90^o), and angled-loading (90^o, 10 lbs) anatomical positions with a 10 kHz – 100 kHz frequency sweep on the HP 4194A Precision Impedance Analyzer. The triplicate measurements were repeated experimentally at the same frequencies on the software package from the AD5933 chip. The chip was calibrated by selecting precise resistors and capacitors that permitted tight experimental replication of control data from the precision analyser. Through this experiment, the impedance analysis function of the larger, more expensive desktop device was compacted into a mobile, low-cost chip.

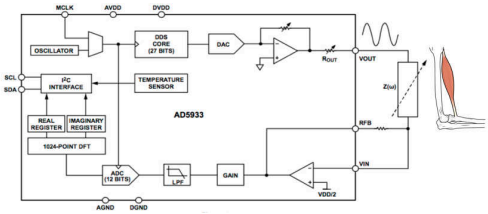

Figure 1: Electrical Block Diagram for AD5933 Chip.

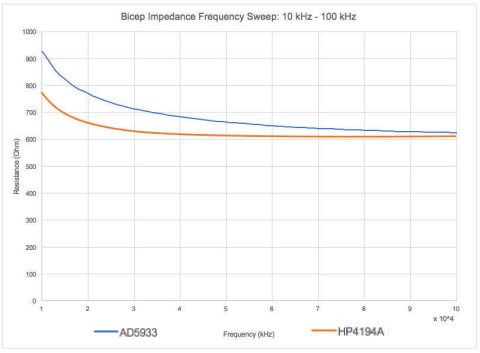

Figure 2: Comparison of Control and Experimental Calibrations.

The impedance data of HP4194A and AD5933 devices was corrected for the spurious effects of cables and fixtures using standard open-short-load compensation. Following the calibration the measured admittance is equal to,

$$Y_{sample} = G_{sample} + j\omega C_{sample} \quad (1)$$

where G is for conductance and C is for capacitance. The conductance and capacitance is reported over different frequencies.

3 Conclusions

In summary, we have shown that the inexpensive chip AD5933 is capable of obtaining accurate biceps brachii bioimpedance data as determined by the comparison with the precision impedance analyser HP4194A. The understanding of the scatter in the healthy subjects' bioimpedance data as a function of body composition, body mass index, disease history, age, and gender, is crucial for future application of EIT in muscle imaging.

References

[1] Brown B.H. (2003) "Electrical Impedance Tomography (EIT) – A Review". J. Med. Eng. Technol. 27(3): 97–108.

[2] Garmirian, LP; Chin AB; Rutkove SB (2008). "Discriminating neurogenic from myopathic disease via measurement of muscle anisotropy". Muscle and Nerve. 39 (1): 16–24.

[3] Sung M, Spieker AJ, Narayanaswami P, Rutkove SB (2013). "The effect of subcutaneous fat on electrical impedance myography when using a handheld electrode array: the case for measuring reactance". Clin Neurophysiol. 124: 400–4.

Focusing electrical current at depth for ablation

Andy Adler[1] and Pablo Nery[2]

[1]Carleton University, Ottawa, Canada, Andy.Adler@Carleton.ca
[2]University of Ottawa Heart Institute, Ottawa, Canada

Abstract: During ablation, current must penetrate deeply into tissue to deposit energy; to achieve this, electrodes must be spaced further apart, affecting more tissue than necessary. We propose a strategy to focus current at depth using multiple surface electrodes and an optimal current-drive strategy. Simulation results in 2D show promising improvements.

1 Introduction

Catheter ablation is a minimally invasive procedure to destroy abnormal tissue. This study is motivated by the use of radiofrequency catheters to apply electrical energy to arrhytmogenic sites on the endocardium, as a therapeutic technique for atrial fibrillation (AF).

Current catheters have two electrodes through which current is applied, and modern designs typically use advanced features such as open saline irrigation which cools the surface of the heart muscle[2]. To be effective current must penetrate sufficiently deeply into the tissue so energy reaches the entire ablation site. However, in order to penetrate sufficiently deeply, electrodes must be spaced further appart, and thus the width of the region to which current is applied is large.

This study is motivated by the need to achieve deep current penetration, while still maintaining a narrow width of application. Our proposed approach is to use multiple surface electrodes and calculation of an optimum pattern to produce current in a region of interest.

2 Methods and Results

Using EIDORS[1], a model of an homogeneous half space with 11 surface electrodes is created and the 2D plane vs. depth along the electrodes shown for an inner region (Fig. 1). A region of interest (ROI) is identified (green box) in which it is desired to have uniform current density magnitude, $|\vec{J}|$. On each side of the ROI, a region ROIx is identified in which it is desired to have zero current density, $\vec{J} = 0$.

Using these 11 electrodes, $11 \times 10/2 = 55$ pair-drive current patterns are possible. For each pattern, i, the forward model is solved to calculate $\vec{J}_i$ throughout the model. The magnitude $|\vec{J}_i|$ is shown for a few patterns.

In order to calculate an "optimal pattern", $\mathbf{c}$, we seek the value of current to be appled through each pattern, c_i. Thus if patterns 1,2 and 5 apply positive current through electrode #1, the optimal pattern will apply $c_1 + c_2 + c_5$ through this electrode. A Jacobian (sensitivity) matrix, $\mathbf{J}$ is calculated via vertical concatenation of each vector component of $\vec{J}$.

Vector $\mathbf{c} = \left(\mathbf{J}^t\mathbf{W}\mathbf{J} + \lambda\mathbf{I}\right)^{-1}\mathbf{J}^t\mathbf{W}\mathbf{d}$ is then calculated, where λ is a small Tikhonov regularization factor, $\mathbf{W}$ is a weighting of each element's importance (currently uniform) and $\mathbf{d}$ is 1 in ROI and 0 in ROIx (other areas are ignored).

Fig. 1 shows three bipolar patterns (with the classic depth-width trade-off) and the "optimized" pattern for the identified ROI. A clearly more uniform current in the ROI has been achieved, in this simplified, 2D model.

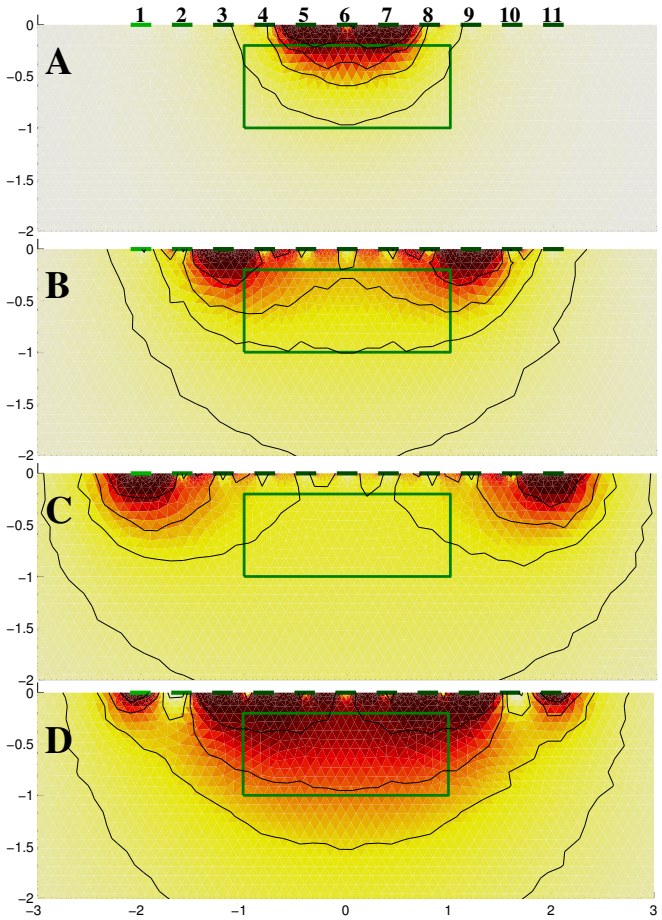

Figure 1: Current density vs. depth for four different current drive scenarios (darker colours indicate higher current). Contours indicate 5%,10%,15% and 25% of maximum. Electrodes: A) 5→7, B) 3→9, C) 1→11, D) optimized pattern (all electrodes).

3 Discussion

Previous data[3] show that bipolar ablation is feasible in vivo. However, current technology used in circular catheters is limited to ablation within the atria. The present model has the potential to improve ablation technology with linear ablation catheters, resulting in an increase ablation lesion size and depth with wide clinical applicability.

These simulation results are promising and suggest that it may be possible to achieve improved ablation performance using multiple electrodes with optimized current patterns.

References

[1] A Adler, WRB Lionheart *Physiol Meas* 27:S25-S42, 2006
[2] MC Wijffels, *et al*, *J Cardiovasc Electrophysiol* 10:1142–8, 2009
[3] H Nakagawa, *et al*, *Circulation* 98:458–65, 1998.

Barriers between chest EIT and its clinical users

Mei-Yun Chang[1] Yeong-Long Hsu[1], Hou-Tai Chang[1*] and Zhanqi Zhao[2]

[1] Division of Chest Medicine, Far Eastern Memorial Hospital, Taipei, Taiwan, *houtai38@gmail.com

[2] Institute of Technical Medicine, Furtwangen University, Villingen-Schwenningen, Germany

Abstract: Clinical studies indicate that EIT is able to monitor ventilation distribution at the bedside and may help to develop lung protective ventilation strategies. The main barriers between chest EIT and its clinical users are (1) the difficulties in result interpretation, (2) the lack of application protocols and (3) no established chargeable expense. Possible solutions to these issues were discussed.

1 Introduction

Clinical studies indicate that chest EIT is able to monitor ventilation distribution at the bedside and may help to develop lung protective ventilation strategies [1]. Several years have passed since the first launch of a commercial EIT device in 2012. The number of EIT devices installed in the clinics is still limited. For those who already bought a clinical approved EIT system, the major use of the device remains in research. We would like to discuss the main barriers during EIT promotion in the clinics and possible solutions based on our experiences in the Greater China Region.

2 Barriers and possible solutions

2.1 The difficulties of data/results interpretation

Issue: Real time and functional EIT images are new to intensivist, pneumologist, anesthetist and respiratory therapist. The following ideas are most profound for the clinical users to comprehend: relative impedance values; distorted thorax and lungs in the reconstructed images; the lens-shaped intra-thoracic volume that EIT measurement covered.

Solutions: A newly published review paper introduces fundamental as well as advanced topics in EIT that assist new users to get started [1]. Various EIT measures have been proposed to extract the information from EIT data, analogue to traditional clinical terms, such as compliance (regional), tidal volume (impedance variation), and pressure-volume (impedance) loop. Investigations on the issues in clinical settings, such as sources of interference [2] and influences of measurement planes [3], are appreciated. Forums and workshops in traditional pneumology and critical care conferences increase the exposal of EIT.

2.2 The lack of application protocols

Issue: Previous studies suggest that EIT is able to evaluate the efficacy of recruitment manoeuvre, to optimize titration of positive end-expiratory pressure (PEEP), along with other useful applications [1]. However, how to apply EIT for these purposes in clinical routine is unclear. There is no well documented, clinical validated protocol to follow. For example, many EIT measures were suggested for PEEP titration. Each measure has its requirements (e.g. the regional delay index runs with prolonged inspiration; regional compliance method requires a minimum number of PEEP steps). Only a few were prospectively evaluated with small number of subjects [4]. From the opinions we collected, instead of interpreting the EIT findings by themselves, clinical users want clear guidance on the procedures.

Solutions: Protocols should be defined for potential clinical applications. Multicenter, prospective randomized trials should be conducted to valid the protocols, so that the clinical users can follow.

2.3 The lack of established chargeable expense

Issue: Even if the clinical users find EIT device useful, normally it is not their decision to make if a EIT device should be purchased. Financial benefit is crucial, especially when EIT is not a life-saving device. Since EIT applications are new to the health insurance systems, the clinical users cannot charge the patients or the insurance companies for EIT usage. Although the profit models of two commercial EIT devices (Draeger Pulmovista 500 and Swisstom BB^2) are different, the cost of device use is considerable.

Solutions: Some clinics that in possess of EIT have already applied to establish chargeable items in the health and medical bureau. In our hospital, approval has been acquired to charge patients on a daily based. Other expense possibilities are also possible (e.g. hourly based or flat-rate covering entire stay). Besides, standardized print-out source documents are required for attending physician (Fig. 1), patient (similar to a print-out report of pulmonary function test). Reports have been designed for various purposes (weaning, recruitment, and PEEP titration, etc.).

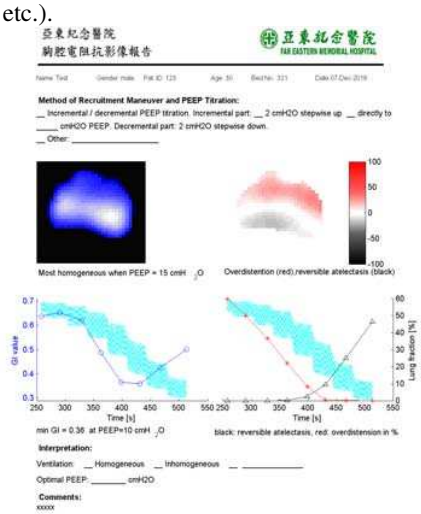

Figure 1: Example of a print-out report for PEEP titration.

References

[1] I Frerichs, *et al. Thorax*, in press, 2016
[2] I Frerichs, *et al. Physiol Meas*, 32:L1–10, 2011
[3] J Karsten, *et al. Crit Care*, 20:3, 2016
[4] GK Wolf, *et al. Crit Care Med*, 41:1296-304, 2013

Author Index

Thank you to the sponsors of EIT2017

scio spec
scientific instruments

NIH
National Institute of Biomedical Imaging and Bioengineering

swisstom
Now I can see.

Dräger

Physiological Measurement
iopscience.org/pmea

Kitware

IIRC
IMPEDANCE IMAGING RESEARCH CENTER

1867
THAYER SCHOOL OF ENGINEERING AT DARTMOUTH